TECHNISCHE UNIVERSITÄT WIEN

MedAustron Ion Therapy Center

DIPLOMARBEIT

Radiobiological considerations in proton beam therapy: Influence of different treatment planning optimization approaches on the dose-averaged linear energy transfer distribution

zur Erlangung des akademischen Grades

Diplom-Ingenieurin

im Rahmen des Studiums

Technische Physik

eingereicht von

Martina PALKOWITSCH

Matrikelnummer 01426198

Ausgeführt am
Atominstitut der Fakultät für Physik
der Technischen Universität Wien
und am
EBG MedAustron GmbH

unter der Anleitung von
Ao.Univ.Prof. Dipl.Ing. Dr. Christina STRELI,
Ass.Prof. Dipl.Ing. Dr. Karin POLJANC,
Priv.Doz. Dipl.Ing. Dr. Markus STOCK und
Dipl.Ing. Dr. Gabriele KRAGL

Wien, 16.12.2019

Martina Palkowitsch

Christina Streli

Contents

ABSTRACT

Purpose

Conventional radiotherapy applies photons and electrons. In the last years another treatment modality has been steadily gaining in importance – the proton therapy. The advantageous physical properties of protons lead to a global increase of the number of proton therapy centers. Since 2016 proton therapy has been available also in Austria, more precisely at MedAustron in Wiener Neustadt, Lower Austria. Due to their characteristic depth dose profile – most of the dose is deposited at the end of the particle range – protons are an excellent tool for treating tumors located close to critical, radiosensitive organs. Proton therapy makes it possible to deposit a large proportion of the dose in the diseased tissue while sparing the healthy tissue around. An additional advantage in relation to the conventional photon therapy is its slightly increased relative biological effectiveness (RBE). RBE is defined as the ratio of a dose of photons to a dose of any other ionizing radiation which produces the same biological effect. Even though studies show that the RBE for protons increases at the end of the range of the particles, commonly a constant proton RBE of 1.1 for planning and delivering clinical therapy is assumed. This simplification might not sufficiently describe the biological effect in clinical situations where it is inevitable to use beams stopping in front of organs at risk. Besides other factors, the enhanced RBE of protons at the end of range can be connected to the higher linear energy transfer (LET) with increasing depth. In the case of mixed particle fields, the dose-averaged LET (LET_d) over the entire particle spectrum can be used to quantify the beam quality. To illustrate RBE uncertainties, LET_d is in use as a surrogate for the biological effect. Within the scope of this work, LET_d-distributions resulting from different tumor localizations, tumor sizes as well as treatment plan optimization settings and strategies were assessed according to their ability of sparing organs at risk from high LET_d. The study was carried out at and in collaboration with the light ion beam therapy facility MedAustron.

Materials and methods

In a first step LET_d to water calculation using the Monte Carlo (MC v4.0) algorithm in the Treatment Planning System RayStation (RS v5.99.50, in the following briefly called RS, of RaySearch Laboratories AB, Sweden) was benchmarked against GATE8.0/Geant4.10.3 MC simulations. Plans with a target of (5x5x5) cm^3 centered at a depth of 6 and 30 cm in water and one 160 MeV pencil beam (range in water: 17.4 cm) were optimized in RS and recalculated with GATE/Geant4. By doing so a validated tool for further investigations was obtained. Different dose grids ((0.1x0.1x0.1) cm^3, (0.2x0.2x0.2) cm^3 and (0.3x0.3x0.3) cm^3) were used to investigate if the voxel size of the dose grid chosen for calculating LET_d distributions influenced the computed values.

Once the validation of RS by GATE8.0/Geant4.10.3 was completed, the actual RS simulations could be started. Initially, the dependence of LET_d on target depth, field size, irradiation angles and number of beams was studied. A (2x2x2) cm^3, a (5x5x5) cm^3 and a (10x10x10)) cm^3 water target were centered in the simulation at 8 cm, 18 cm and 28 cm depths in a water phantom to assess depth and field size dependence. Two SFO (Single Field Optimization) fields were separated by 0° to 180° in steps of 10° for a spherical target with 4 cm diameter centered in a cylindrical water phantom to study the angular dependence. The same target was used to gain information about the dependency on the number of beams by using one to ten beams.

Finally, one- and two-field plans were generated in RS for five clinical cases (two pediatric head tumors, one superficial tumor, one pediatric Ewing tumor and one pediatric ependymoma) and for the spherical phantom using different optimization strategies. The assessment of those strategies was made according to the ability of sparing surrounding tissue from high LET_d and consequently minimizing RBE uncertainties there. The effect of using two beams instead of one, of varying the number of distal energy layers, of limiting the maximum spot weights and of the

combination of the latter two strategies was tested from this perspective. In the case of two-field plans Single Field Optimization (SFO) was compared with Multiple Field Optimization (MFO) for two (almost) orthogonally arranged beams. Subsequently, Dose-Volume Histograms (DVHs) and LET_d-Volume Histograms (LET_d-VHs) in the target and in concentric shells around the target enabled to evaluate the influence of the investigated target anatomies and treatment planning optimization approaches on the LET_d distribution.

To gain an impression of the impact the difference in LET_d might have on the RBE the Wedenberg et al. model was employed.

Results

The relative deviation of LET_d computed with RS v5.99.50 from those calculated with GATE8.0/Geant4.10.3 was within ±5% for all evaluated profiles. These just slight differences confirmed to assume that RS v5.99.50 was computing a validated output. Moreover, no deviations of values computed with different voxel sizes were observed in the calculated longitudinal LET_d distributions. This led to the conclusion that the calculated longitudinal LET_d distributions did not depend on the chosen size of the dose grid´s voxels. Consequently, RS v5.99.50 could be used as a validated tool for further investigations.

Analysis of the field depth and size found the highest maximum LET_d ($LET_{d,max}$) for small superficial targets (16 keV/µm versus 12 keV/µm for targets of (2x2x2) cm^3 centered at 8 cm depth versus (10x10x10) cm^3 at 28 cm). Increasing the angle separating two SFO beams as well as the number of beams led to a decrease of $LET_{d,max}$ around the target (by e.g. 63% for two contralateral beams instead of one beam).

Looking subsequently at the clinical cases showed the following: When averaging over all clinical cases $LET_{d,max}$ in the shell from 0.0 to 0.5 cm around the target was reduced by 23% for plans with two beams compared to those of one, by 9% when using three distal energy layers and a limitation of maximum spot weight instead of one distal energy layer and no limitation, by 6% for plans with three distal energy layers compared to those with one, by 3% for plans with maximum spot weight limitation compared to plans without maximum spot weight limitation. Values of $LET_{d,max}$ obtained by applying SFO did not differ much from those using MFO. The change of average dose to the target was within 1% for all cases.

As expected when using the Wedenberg et al. model an almost linear relationship between LET_d and RBE was observed. When calculating the biological-weighted dose by using a constant RBE of 1.1 instead of a non-constant RBE, it was most potentially underestimated in the region surrounding the target.

Discussion and Conclusion

Investigating the angular dependence revealed the following: If two SFO beams which are separated by a rather large angle are used the peaks at the end of range are diluted by fields entering from the opposite direction. This results in a reduction of $LET_{d,max}$. A reason for a smaller $LET_{d,max}$ with increasing target depth might be the increasing impact of range straggling present when treating deep-seated targets. If the irradiated target is small, peaks cannot dilute each other to a great extent. The consequence is a rather large $LET_{d,max}$.

Computations of the RBE-weighted dose using the Wedenberg et al. model depicted a substantial effect of enhanced LET_d in the distal parts of the irradiation fields just in the target and in the directly adjacent shell, which was located from 0.0 to 0.5 cm around the target. Due to the relatively rapid reduction of physical dose after the target, shells further away from the target were scarcely affected.

Hence, a detailed study of LET_d distributions in clinical cases is particularly advisable whenever critical organs are right beside the target, i.e. at a distance of up to 0.5 cm from the target.

On average, the applied optimization settings decreased the $LET_{d,max}$ around the target. Nevertheless, for individual cases no reduction of $LET_{d,max}$ appeared. Actually, in some cases $LET_{d,max}$ around the target increased. This illustrates that it is difficult to make predictions concerning the LET_d distribution for the individual based on the average case. Implementing a function, which enables to optimize LET_d distributions, in the individual treatment planning process of each clinical case might provide a remedy here.

Finally, one has to keep in mind that characterizing the biological effect of a given dose only by a single parameter, i.e. LET_d, is not feasible. However, trying to reduce LET_d to critical structures is still suggested. This enables to reduce uncertainties in the prediction of the biological dose.

KURZFASSUNG

Intention

In der konventionellen Strahlentherapie finden Photonen und Elektronen Anwendung. Während der letzten Jahre gewinnt eine andere Strahlenmodalität stetig an Bedeutung – die Protonentherapie. Die vorteilhaften physikalischen Eigenschaften von Protonen führen zu einem weltweiten Anstieg der Anzahl an Protonentherapiezentren. Seit 2016 ist die Protonentherapie auch in Österreich, präziser am MedAustron in Wiener Neustadt in Niederösterreich, verfügbar. Aufgrund ihres charakteristischen Dosistiefenprofils – der größte Anteil der Dosis wird am Ende der Reichweite der Partikel deponiert – sind Protonen ein exzellentes Werkzeug für die Behandlung von Tumoren, die in der Nähe von kritischen, radiosensitiven Organen lokalisiert sind. Protonentherapie macht es möglich, einen großen Anteil der Dosis im krankhaften Gewebe zu deponieren bei gleichzeitiger Schonung des umgebenden gesunden Gewebes. Ein zusätzlicher Vorteil im Vergleich zu der konventionellen Photonentherapie ist die etwas erhöhte relative biologische Wirksamkeit (RBE). RBE ist definiert als das Verhältnis zwischen Photonendosis und der Dosis einer beliebigen anderen ionisierenden Strahlung, die denselben biologischen Effekt bewirkt. Obwohl Studien zeigen, dass der RBE von Protonen am Ende der Reichweite der Teilchen ansteigt, wird im Allgemeinen ein konstanter Protonen RBE von 1,1 für die Planung und Durchführung klinischer Therapien angenommen. Diese Vereinfachung beschreibt solche klinische Situationen, in welchen ein Stoppen des Strahls unmittelbar vor Risikoorganen unvermeidbar ist, möglicherweise nicht ausreichend genau. Der am Ende der Reichweite erhöhte RBE von Protonen kann, neben anderen Faktoren, mit dem ansteigenden linearen Energietransfer (LET) mit größer werdender Tiefe in Verbindung gebracht werden. Im Fall von gemischten Teilchenfeldern wird in der Literatur vorgeschlagen den über das ganze Teilchenspektrum in der Dosis gemittelten LET (LET_d) als Stellvertreter für den biologischen Effekt zu verwenden. Im Rahmen dieser Arbeit wurden LET_d-Verteilungen, die sich für verschiedene Tumorlokalisationen, Tumorgrößen sowie Bestrahlungsplanoptimierungseinstellungen und -strategien ergaben, nach ihrer Fähigkeit Risikoorgane vor hohen LET_d zu bewahren, bewertet. Die Studie wurde am und in Zusammenarbeit mit dem Leichtionentherapiezentrum MedAustron durchgeführt.

Materialen und Methoden

In einem ersten Schritt dienten GATE8.0/Geant4.10.3 MC Simulationen als Benchmark für die Berechnung des LET_d in Wasser mit dem Monte Carlo (MC) Algorithmus des Bestrahlungsplanungsystems RayStation (RS v5.99.50, im Folgendem kurz RS genannt, der RaySearch Laboratories AB, Schweden). Pläne mit einem Target von (5x5x5) cm^3 in 6 und 30 cm Wassertiefe und einem 160 MeV Pencil-Beam (Reichweite in Wasser: 17,4 cm) wurden in RS optimiert und mit GATE/Geant4 nachgerechnet. Auf diese Weise war es möglich, ein validiertes Werkzeug für weitere Untersuchungen zu erhalten. Verschiedene Dosisnetze ((0,1x0,1x0,1) cm^3, (0,2x0,2x0,2) cm^3 und (0,3x0,3x0,3) cm^3) wurden verwendet um zu untersuchen, ob die Größe des Volumenelements, die für die Berechnung der LET_d-Verteilungen gewählt wurde, die ermittelten Werte beeinflusste.

Nachdem die Validierung von RS durch GATE8.0/Geant4.10.3 abgeschlossen war, konnte mit den eigentlichen RS Simulationen begonnen werden. Zunächst wurde die Abhängigkeit des LET_d von der Targettiefe, der Feldgröße, den Bestrahlungswinkeln und der Anzahl an Strahlen untersucht. Ein (2x2x2) cm^3, ein (5x5x5) cm^3 und ein (10x10x10) cm^3 großes Wassertarget wurden in der Simulation in 8 cm, 18 cm und 28 cm Tiefe in einem Wasserphantom platziert, um die Tiefen- und Feldgrößenabhängigkeit feststellen zu können. Für die Untersuchung der Winkelabhängigkeit wurde ein sich mittig in einem zylindrischen Wasserphantom befindliches, kugelförmiges Target mit einem Durchmesser von 4 cm verwendet. Der Winkel zwischen zwei SFO (Einzelfeldoptimierungs-) Feldern wurde von 0° auf 180° in Schritten von 10° erhöht. Für

dasselbe Target wurden ein bis zehn Strahlen eigesetzt um Information über die Auswirkung der Anzahl an Strahlen zu erhalten.

Schlussendlich wurden Ein- und Zweifeldpläne für fünf klinische Fälle (zwei pädiatrische Kopftumore, ein oberflächlicher Tumor, ein pädiatrisches Ewing-Sarkom und ein pädiatrisches Ependymom) sowie für das sphärische Phantom Pläne in RS unter Verwendung verschiedener Optimierungsstrategien generiert. Die Beurteilung dieser Strategien erfolgte nach ihrer Fähigkeit, hohen LET_d in umliegendem Gewebe zu vermeiden und dort somit RBE Unsicherheiten zu minimeren. Unter diesem Gesichtspunkt wurde der Effekt der Verwendung von zwei Strahlen statt einem, der Variation der Anzahl an distalen Energieschichten, der Limitierung von maximalen Spot-Gewichtungen und der Kombination beider Strategien untersucht. Im Fall von Zweifeldplänen wurde Einzelfeldoptimierung (SFO) mit Mehrfeldoptimierung (MFO) für zwei (beinahe) orthogonal angeordnete Strahlen verglichen. Dosisvolumshistogramme (DVHs) und LET_d-Volumshistogramme (LET_d-VHs) im Target und in konzentrischen Schalen um das Target ermöglichten anschließend den Einfluss der untersuchten Targetanatomien und Planungsoptimierungs-Methoden auf die LET_d-Verteilung zu evaluieren.

Um einen Eindruck darüber zu erhalten, welche Auswirkung der Unterschied im LET_d auf den RBE haben könnte, fand das Wedenberg et al. Modell Anwendung.

Resultate

Die relative Abweichung des LET_d berechnet mit RS von jenen, welche mit GATE8.0/Geant4.10.3 ermittelt wurden, war innerhalb von ±5% für alle ausgewerteten Profile. Diese nur geringen Abweichungen bestätigten, dass RS einen validierten Output berechnete. Zudem wurde keine Abweichung der Werte, die mit verschieden Volumenelementgrößen des Dosisnetzes errechnet wurden, festgestellt. Somit wurde geschlussfolgert, dass keine Abhängigkeit der kalkulierten longitudinalen LET_d Verteilungen von der gewählten Größe des Volumenelements des Dosisnetzes bestand. Folglich konnte RS als validiertes Mittel für weitere Untersuchungen herangezogen werden.

Die Analyse der Feldtiefe und -größe fand den höchsten maximalen LET_d ($LET_{d,max}$) für kleine oberflächliche Targets (16 keV/µm versus 12 keV/µm für Targets von (2x2x2) cm^3 in 8 cm versus (10x10x10) cm^3 in 28 cm Tiefe). Eine Vergrößerung des Winkels zwischen zwei SFO Strahlen sowie eine Erhöhung der Anzahl an Strahlen führte zu einer Reduktion des $LET_{d,max}$ in Bereichen, die das Target umschlossen (um z.B. 63% für zwei kontralaterale Strahlen statt einem).

Der anschließende Blick auf die fünf klinischen Fälle zeigte Folgendes: Bei Mittelung über alle klinischen Fälle konnte der $LET_{d,max}$ in der Schale von 0,0 bis 0,5 cm um das Target um 23% für Pläne mit zwei statt einem Strahl, um 9% bei Verwendung von drei distalen Energieschichten und einer Limitierung der maximalen Spot-Gewichtung statt einer distalen Energieschicht und keiner Limitierung, um 6% für Pläne mit drei distalen Energieschichten statt einer und um 3% für Pläne mit maximaler Spot-Gewichtungslimitierung statt keiner Spot-Gewichtungslimitierung reduziert werden. Werte die aus der Verwendung von SFO resultierten, unterschieden sich nicht sehr von jenen, die in MFO Plänen erhalten wurden. Die Veränderung der durchschnittlichen Dosis im Target war innerhalb von 1% für alle Fälle.

Wie bei Verwendung des Wedenberg et al. Modells zu erwarten, zeigte sich ein beinahe lineares Verhältnis zwischen LET_d und RBE. Die biologisch-gewichtete Dosis wurde, wenn sie statt mit einem nicht konstanten, mit dem Wedenberg et al. Model berechneten, RBE mit einem konstanten RBE von 1,1 berechnet wurde, am meisten in den direkt ans Target anschließenden Gebieten unterschätzt.

Diskussion und Schlussfolgerung

Das Untersuchen der Winkelabhängigkeit verdeutlichte Folgendes: Wenn zwei durch einen relativ großen Winkel separierte SFO Felder eingesetzt werden, kommt es zur Abschwächung des Peaks am Ende der Reichweite des Strahles. Diese wird ausgelöst durch den Strahl, welcher von der gegenüberliegenden Richtung eintritt. Es kommt zu einer Reduzierung des $LET_{d,max}$. Ein möglicher Grund für den kleiner werdenden $LET_{d,max}$ mit größer werdender Targettiefe ist der größer werdende Einfluss der Reichweitenstreuung, die bei der Behandlung von tiefliegenden Targets auftritt. Wenn das bestrahlte Target klein ist, können sich die Peaks nur in geringem Ausmaß gegenseitig abschwächen. Die Konsequenz ist ein relativ großer $LET_{d,max}$.

Berechnungen der RBE-gewichteten Dosis, die das Wedenberg et al. Modell verwendeten, zeigten einen substantiellen Effekt der erhöhten LET_d Werte in den distalen Bereichen des Bestrahlungsfeldes ausschließlich im Target und in der direkt angrenzenden Schale, welche von 0,0 bis 0,5 cm um das Target lag. Aufgrund des relativ raschen Abfalls der physikalischen Dosis hinter dem Target, waren weiter vom Target entfernte Schalen kaum betroffen. Folglich ist eine detaillierte Untersuchung der LET_d Verteilungen in klinischen Fällen immer dann besonders ratsam, wenn kritische Organe direkt neben dem Target, d.h. im Abstand von bis zu 0.5 cm, liegen.

Im Durchschnitt konnten alle angewandten Optimierungsstrategien wie erwünscht den $LET_{d,max}$ um das Target verringern. Trotzdem trat für individuelle Fälle keine Reduktion, teilweise sogar eine Erhöhung des $LET_{d,max}$ auf. Dies verdeutlicht, dass es schwierig ist, Vorhersagen über die LET_d-Verteilung eines individuellen Falles basierend auf Durchschnittsergebnissen zu treffen. Die Implementierung einer Funktion, die das Optimieren von LET_d Verteilungen ermöglicht, in den individuellen Bestrahlungsplanungsprozess jedes klinischen Falls könnte hier Abhilfe schaffen.

Am Ende darf außerdem nicht außer Acht gelassen werden, dass es nicht möglich ist, den biologischen Effekt einer gegeben Dosis mit nur einem einzigen Parameter, z.B. LET_d, zu beschreiben. Dennoch wird empfohlen, LET_d in kritischen Strukturen zu reduzieren. Damit lässt sich die Unsicherheit in der Vorhersage der biologischen Dosis reduzieren.

ABBREVIATIONS

bp	Base pairs	**MCDS**	Monte Carlo damage simulation
CSDA	Continuous-slowing-down approximation	**MFO**	Multifield optimization
CT	Computed tomography	**MRI**	Magnetic resonance imaging
DNA	Deoxyribonucleic acid	**NTCP**	Normal tissue complication probabilities
D_{RBE}	RBE-weighted (absorbed) dose	**OAR**	Organ at risk
DSB	Double strand break	**PBS**	Pencil-beam scanning
DVH	Dose volume histogram	**PET**	Positron emission tomography
HU	Hounsfield units	**PTV**	Planning target volume
IMPT	Intensity modulated proton therapy	**RBE**	Relative biological effectiveness
LET	Linear energy transfer	**RS**	RayStation
LET_d	Dose averaged linear energy transfer	**SFO**	Single-field optimization
$LET_{d,max}$	Maximum LET_d	**SOBP**	Spread out Bragg peak
LET_d-VH	LET_d volume histogram	**SSB**	Single-strand breaks
LET_t	Track averaged linear energy transfer	**TCP**	Tumor control probability
LQ	Linear quadratic model	**TPS**	Treatment planning system
LS	Line scanning	**WEPL**	Water-equivalent path length
MC	Monte Carlo	**XRT**	Photon radiotherapy

1 INTRODUCTION

1.1 Proton beam therapy – General aspects

Cancer is one of the leading causes of death worldwide (World Health Organization - Cancer - Key facts, 2018). Besides surgery and chemotherapy, radiation therapy is one of the standard methods of cancer treatment (IAEA, Relative Biological Effectiveness, 2008, p. 1). In 2018 the number of new cancer cases worldwide was estimated to be 18.1 million and the number of cancer deaths to 9.6 million (Bray, 2018). All over the world about 1 in 6 deaths is related to cancer. More and more details of the evolution of cancer are known. The greater understanding may soon lead to more effective therapies. Nevertheless, the probability for radiation therapy to remain the most important, effective and cost effective treatment modality for all types of solid malignancies is envisioned to be high (IAEA, Relative Biological Effectiveness, 2008, p. 1).
As history has demonstrated major improvements in the efficacy of radiation therapy goes hand in hand with significant progress in technology (IAEA, Relative Biological Effectiveness, 2008, p. 2). Soon after their discovery by W.C. Roentgen in 1895, X-rays found application in therapy of malignant tissue. In the following years, therapy methods were further developed and improved. Finally, the use of heavy-charged particles like protons or heavier ions[1] was suggested (Kraft, 2000). Robert Wilson recommended the use of proton beams to treat deep-seated tumors in a paper published in 1946. The first treatment of a human with protons took place at the Lawrence Berkeley Laboratory in 1954. In the following years technologies important for further progress, like accelerators, magnetically scanned beams, treatment planning systems, computed tomographic imaging (CT) and magnetic resonance imaging (MRI) were developed. Nevertheless, technical difficulties, cost and lack of evidence of cost-competitiveness led to an only slow adoption of proton therapy. It was not until 2001 that commercial proton delivery systems came on offer. In comparison to the equipment of a comparable photon radiotherapy (XRT)[2], the equipment used in a proton therapy is still much more expensive. In the last years a huge step forward was made in spite of these circumstances. (Newhauser & Zhang, 2015). Currently, 81 proton therapy centers are in operation across the globe. More than 160 000 patients had been treated with protons worldwide by the end of 2017 (PTCOG, 2019).

When radiation passes through a tissue various atomic and nuclear interaction processes take place. To quantify the energy transfer and deposition in the tissue in those interactions the quantity *absorbed dose*, which is expressed in energy (Joule) absorbed per unit mass (kg) and measured in the unit of Gray (Gy) was introduced. Possible consequences for those, primarily with cellular deoxyribonucleic acids (DNA)[3], interactions are mutations or complete functional disruption (for example cell death). They depend on the number and spatial correlation of the interactions.

[1] In the following the term *ions* describes charged atoms, nuclei of atoms with some or all of the atomic electrons removed, accelerated to high energies in different types of accelerators (Kraft, 2000).
[2]Photons with energies of up to 30 MeV are applied in photon radiotherapy (Reiser, Kuhn, & Debus, 2004, p. 101).
[3]*Deoxyribonucleic acid* (DNA) is a macromolecule, in which deoxyribonucleoside are linked by phosphodiester bridges; the order of the purine bases (Adenin and Guanin) and of the pyrimidine bases (Cytosin and Tymin) encodes the genetic information of all living organisms with exception of the RNA viruses; the DNA is present as so-called double helix in more or less all plants and animals (with exception of single strand DNA viruses); it consist of two antiparallel single-stranded DNAs, which are linked by hydrogen bridge bonds between the purine and pyrimidine bases; these bonds as well as the interactions between the hydrophobic bases lead to a helical twisting of the DNA; the double helix contains hydrophilic rest sugar in the outer sides and hydrophobic bases in the inner sides. The fluctuations in DNA content of cells is significant in terms of size; most mammals contain about 4-8 pg/cell; the stretched DNA of a somatic cell would be about 1.8 m long; the DNA is present in the cell nucleus as chromatin and forms together with the histones a DNA superhelix, which is the structural basis for the chromosomes (definition according to (Reuter, 2007, p. 406)).

There is a wide variety of how to administer radiation – one can for instance choose the radiation modality, the applied doses and the beam directions. Eradicating cancerous tissue and minimizing the irradiation of healthy tissue at the same time are at the center of research and development of radiation therapy. A treatment of the designated target while not damaging any healthy structures would be ideal. This ideal scenario will stay out of reach due to numerous rationales like uncertain definitions of the target volume[4] or deliveries of the therapeutic dose as planned. In addition, in the case of an external beam radiation therapy a penetration through healthy tissue is often unavoidable if the target should be reached. Mathematical and physical formalisms are used for the optimization of the compromise between delivering a high and conformal dose to the target and limiting the doses to critical structures. The foundation of the definition of dose tolerance levels for critical structures and, additionally, for a variety of tumor types, is formed by many years of clinical experiences. An improvement of the ratio of the probabilities for tumor eradication and normal tissue complication is the principal aim of technological progress. It is achievable by, for instance, the use of a revised patient setup or tumor localization due to the application of improved imaging techniques or the use of another particle type – protons in place of photons or electrons.

What most distinguishes charged particles, and so also protons, from photons is their finite range. An extremely high part of the energy is deposited in the narrow peak. In the foremost entrance region the energy deposited by photon beams is built-up and then follows an exponential decay with increasing depth in tissue. If the treatable tumor is not located on the surface[5] but close to an organ at risk[6] it can only be treated by using multiple beam directions. Moreover, many different beam angles have to be used in order to gain a homogenous dose distribution. In the case of protons, the main contribution to the energy loss in tissue is their electromagnetic interacting with orbital electrons. Hence the energy transferred to tissue by protons shows an inverse proportionality to the proton velocity. A lower velocity of the protons means the amount of energy transferred to tissue per track length increases. In the case of a single proton a sharp peak at the end of its range, the so-called Bragg peak (*Fig. 1*), can be noticed. More than one proton track are included in a proton beam and those are statistically distributed. The consequence is a broadening into a peak, which is generally a few millimeters wide. (Paganetti, Proton Therapy Physics Series in Medical Physics and Biomedical Engineering, 2012, pp. xi-xii).

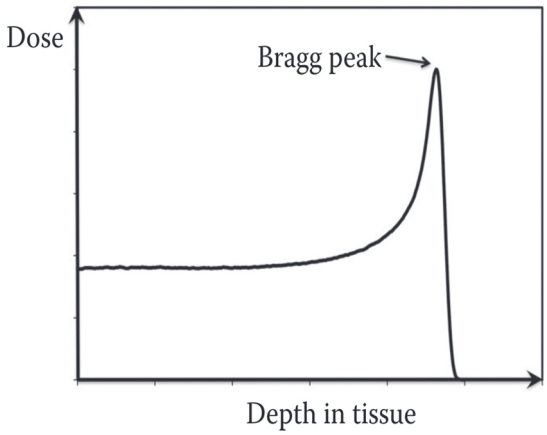

Fig. 1: *Energy deposition as a function of depth for a proton beam leading to the Bragg peak (Paganetti, Proton Therapy Physics Series in Medical Physics and Biomedical Engineering, 2012, p. xii)*

[4] A *target volume* is a 3-D object that is the intended target for the high dose part of the dose distribution. In section *1.5.1.4* different volumes are defined (definition according to (IAEA, Technical Reports NO. 430 - Commissioning and Quality Assurance of Computerized Planning Systems for Radiation Treatment of Cancer, 2004, p. 277)).

[5] In this context, s*urface* is understood to mean the skin of the patient (definition according to definition according to (IAEA, Technical Reports NO. 430 - Commissioning and Quality Assurance of Computerized Planning Systems for Radiation Treatment of Cancer, 2004, p. 276)).

[6] *Organs at risk* are normal tissues whose radiation sensitivity may significantly influence treatment planning and/or prescribed dose (definition according to (ICRU, International Commission on Radiation Units and Measurements, 1993, p. 18)).

Due to the characteristic depth dose profile[7] of ions it is possible to deposit a large proportion of the dose in the diseased tissue while sparing the healthy tissue around. Another advantage of using protons instead of photons for radiation therapy is their increased efficiency of cell killing as a result of their high density of energy depositions (Kraft, 2000).
The particle´s mass and charge, together with its initial energy determine the depth and magnitude of the Bragg peak. In the case of a monoenergetic beam of particles the Bragg peak is extremely narrow. Various techniques can be applied to modify the energy and consequently the range of the incident particles. By layering successive Bragg peaks with various intensities a so-called spread out Bragg peak (SOPB)[8] is created (*Fig. 2*). A spreading of high dose over a sufficiently wide region to surround a target volume (tumor) can be achieved. The average amount of energy deposited per unit length is called linear energy transfer (LET). The LET is, as it soon turns out, the quantity this master thesis is focusing on. By spreading of the Bragg peak the LET over the SOBP is decreased. However, in comparison to photons or particles in the entrance region of the beam this LET is still much higher.

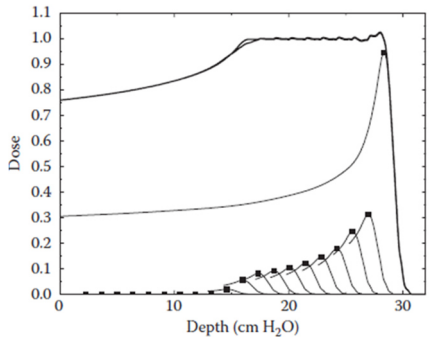

***Fig. 2**: Spread-out Bragg peak (SOBP) obtained by adding shifted, appropriately weighted Bragg Peaks (Paganetti, Proton Therapy Physics Series in Medical Physics and Biomedical Engineering, 2012, p. 24)*

As a consequence of what was mentioned so far ions are characterized by an improved and advantageous distribution of absorbed dose compared to photons (*Fig. 3*). By consideration of the

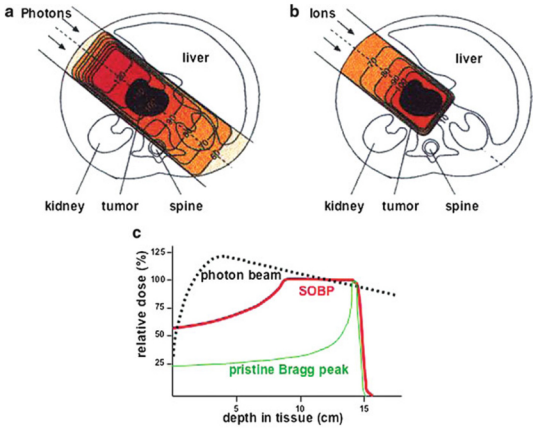

***Fig. 3**: Schematic view of depth-dose distributions of photons and ions.*
(a) megavoltage photon field,
(b) spread-out ion beam,
(c) depth–dose profiles of a and b along the central beam axis. The spread-out Bragg peak (SOBP) is the result of several stacked pristine Bragg curves
(Linz & al, 2012, p. 46)

[7] A *profile* in dosimetry is the dose measured along a line, typically across a beam (definition according to (IAEA, International Atomic Energy Agency, 2004, p. 275)).
[8] The *Spread-Out Bragg Peak* (SOPB) is defined as the extended uniform dose region in depth formed by the optimal stacking of multiple depth dose curves of pristine peaks of different energies (definition according to (Brady & Yaeger, 2013, p. 810)).
The depth dose curve for a broad beam of heavy charged particles is also known as the *Bragg curve* (definition according to (Mayles, Nahum, & Rosenwald, 2007, p. 1008)).

biological effect the superiority of protons is even more pronounced. Apart from affecting the absorbed dose distribution, high LET occurring at the end of the protons´ ranges also impacts the response of biological systems to that dose. High LET radiations are, for instance, more efficient in producing cell kills. Looking at the absorbed dose delivered to the cancer cell population this may be advantageous, looking at the dose absorbed in normal tissue it may be disadvantageous. Both aspects need to be considered.

For being able to accurately estimate the increased efficacy of ions, respectively high LET radiations, vis-à-vis photons, the concept of the relative biological effectiveness (RBE) has been introduced (*Fig. 4*). RBE is defined as the ratio of a dose of photons to a dose of any other particle to produce the same biological effect. The concept of RBE is simple. However, a unique definition for a given radiation is not possible – RBE strongly varies with the position within the treatment beam. The quantity is a function of many different parameters, like particle type, dose, dose per fraction, fraction number, degree of oxygenation, cell or tissue type, biological end point and local energy spectrum. With regard to ion irradiation RBE varies strongly depending on position (IAEA, Relative Biological Effectiveness, 2008, pp. 3-6). The term which is an appropriate description of the latter and is one of the indicators of the radiation quality is the above mentioned linear energy transfer (LET). Therefore, providing LET distributions additionally to the physical dose distributions is sensible. It might be a help for locating high LET regions – it is expected that RBE varies the most there – or even an estimation of RBE distributions. Nevertheless, it is important to be aware that RBE for sure neither depends exactly linearly on LET, nor depends solely on LET (Wilkens, 2003). Commonly, RBE rises with increasing LET till a maximum at approximately 100 keV/µm which corresponds to one ionization per 2 nm. 2 nm is also more or less the dimension of the diameter of a DNA strand. An LET of 100 keV/µm is consequently assumed to be the optimal value for cell killing. A higher LET leads to an overkill effect. The amount of energy deposition of a single particle is then far above what is required for killing a cell. As a consequence the number of cells a particle kills per absorbed dose is reduced (Chang, Lasley, Das, & Mendonca, 2014, p. 239). Compared to determining the LET for monoenergetic protons, which can be obtained from tables, calculating the mean local LET for realistic proton spectra like, for instance, a spread-out Bragg peak, is more complicated. Monte Carlo (MC)[9] simulations enable those calculations (Wilkens, 2003).

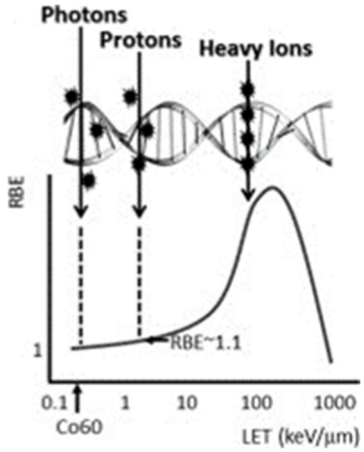

Fig. 4: *Relative Biological Effectiveness (RBE) of different ionizing radiation qualities. Illustration of how protons induce DNA damage that is slightly more clustered than photons (or Co60 γ-rays), which in DNA repair-proficient cells yields a RBE of 1.1. (Willers, et al., 2018)*

[9] A *Monte Carlo calculation* is a dose calculation method based on nuclear physics interactions of particles, in which millions or billions of particle histories are tracked to estimate the behavior of a real radiation beam (definition according to (IAEA, International Atomic Energy Agency, 2004, p. 274)).

1.2 Proton beam therapy physics

1.2.1 Physics of proton interactions in matter

In the following the four predominant types of interactions of protons in matter are presented, discussed and pictured in *Fig. 5*. Possible interactions of a proton with an atom or nucleus are Coulombic interactions with atomic electrons (*stopping*), Coulombic interactions with the atomic nucleus (*scattering*), nuclear reactions (*nuclear interactions*) and Bremsstrahlung. The interactions cause a *slowing down*, since protons collide with atomic electrons many times, a *deflection*, since protons collide with atomic nuclei many times, or they set secondary particles in motion after protons *collide* head-on *with a nucleus*.

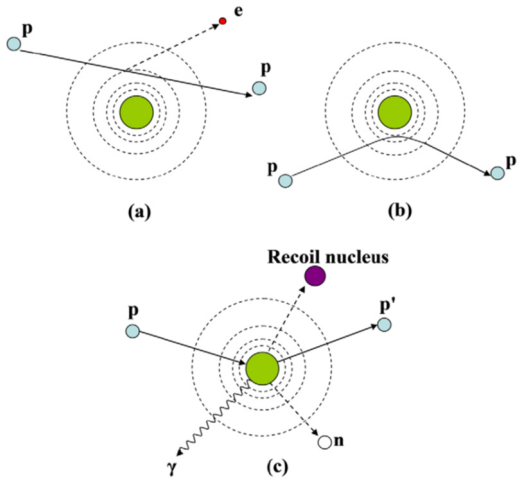

Fig. 5: *Schematic illustration of proton interaction mechanisms:*
(a) energy loss via inelastic Coulombic interactions,
(b) deflection of proton trajectory by repulsive Coulomb elastic scattering with nucleus,
(c) removal of primary proton and creation of secondary particles via non-elastic nuclear interaction
(p: proton, e: electron, n: neutron, γ: gamma rays)
(Newhauser & Zhang, 2015)

Stopping

The slowing down of protons in matter is chiefly a consequence of multiple collisions with electrons. The amount of energy loss is proportional to the interaction time at a given distance. Consequently, an increase of the rate of energy loss and therefore a rise towards the Bragg peak close to the end-of-range is noticeable during the proton´s slowing down process (Paganetti, Proton Therapy Physics Series in Medical Physics and Biomedical Engineering, 2012, p. 22).

Scattering

If you multiply the rest mass of an electron by 1836.2, you get the rest mass of a proton. Nearly all proton trajectories are therefore almost straight lines. Some of them, however, are deflected from their original straight-line paths due to a repulsive elastic Coulombic interaction as they pass in the proximity of the atomic nucleus, whose mass is quite high (Newhauser & Zhang, 2015). The probability of a proton to be deflected by a single atomic nucleus is, with just a few exceptions, very low. As a consequence the angular spread of a proton beam after it passed piece of matter is the result of many combined deflections. For this reason the common term for this kind of interaction is *multiple Coulomb scattering* (MCS). After the multiple scattering processes the spatial distributions of the protons is almost perfect Gaussian. The scattering is more pronounced for high Z materials (Paganetti, Proton Therapy Physics Series in Medical Physics and Biomedical Engineering, 2012, p. 37).

Nuclear interactions

Even though the occurrence of non-elastic nuclear reactions between protons and the atomic nucleus is rare, its effect, in the case one individual proton, is profoundly. A nuclear reaction can be described as follows: The proton´s entry into the nucleus is followed by an emission of a proton, deuteron, triton, or heaver ion, respectively, one or more neutrons (Newhauser & Zhang, 2015). The energies of these secondary particles (including the original proton, because its identification is not possible anymore) have a tendency to be much lower, their angles with the beam much larger than those of the primary protons. Due to their large deflection not many secondaries will enter the patient because of scatters and absorbers positioned in the beam line. (Paganetti, Proton Therapy Physics Series in Medical Physics and Biomedical Engineering, 2012, p. 48).

Bremsstrahlung

Eventually, there is a possibility for proton Bremsstrahlung, which occurs during every deceleration of a charged particle, though in terms of therapeutic proton beam energies it can be neglected (ICRU, 1993, p. 2).

Bragg peak

All three predominant interactions together form the so-called Bragg peak. In order to reach a covering of the target and sparing of the healthy tissue as best as accessible the Bragg peak is clever manipulated (e.g. spread out) in proton radiotherapy (Paganetti, Proton Therapy Physics Series in Medical Physics and Biomedical Engineering, 2012, p. 24).

1.2.2 Dose

The protons´ travel through tissue is accompanied by a kinetic energy loss. The amount of energy deposition in a small volume with mass *dm* is called dose

$$D = \frac{d\bar{\varepsilon}}{dm}$$

Equation 1

where $d\varepsilon$ is the mean energy imparted to matter of mass *dm*. Its SI unity is J kg^{-1} also named Gray (Gy) (ICRU, International Commission on Radiation Units and Measurements, 1998). In clinical practice reports usually use the water-equivalent dose, or dose to water (D_w). This is based on the fact that in analytical dose calculation engines, like those integrated in commercial planning systems, the human body is modeled as a composition of voxels of water which vary in their mass density, electron density or stopping power since the cells´ nuclei are the targets of ionization and a similarity of these to water is assumed (Paganetti, Dose to water versus dose to medium in proton beam, 2009).

1.2.3 Stopping power and linear energy transfer

The introduction of the *linear stopping power S*, which is defined as the energy *dE* lost by a charged particle per unit length *dl*, enables the description of the energy losses of a particle during passing through a medium.

$$S = -\frac{dE}{dl}$$

Equation 2

The result of the division of this quantity by the material´s *density* ρ is the *mass stopping power* S/ρ of a material.

$$\frac{S}{\rho} = -\frac{1}{\rho}\frac{dE}{dl}$$

Equation 3

It is expressed in the SI unit J m^2 kg^{-1} or, more commonly, in MeV cm^2 g^{-1}. An expression of the *total mass stopping power* S/ρ as a sum of the individual components *mass electronic stopping power* $(S/\rho)_{el}$ also referred to as *collision stopping power* $(S/\rho)_{col}$, energy loss due to collisions with electrons, *mass nuclear stopping power* $(S/\rho)_{nuc}$, energy loss due to elastic Coulomb collisions in which recoil energy is imparted to atoms, and *mass radiative stopping power* $(S/\rho)_{rad}$, energy loss due to emission of bremsstrahlung in the electric fields of atomic nuclei or atomic electrons is possible:

$$\frac{S}{\rho} = \frac{1}{\rho}\left(\frac{dE}{dl}\right)_{el} + \frac{1}{\rho}\left(\frac{dE}{dl}\right)_{rad} + \frac{1}{\rho}\left(\frac{dE}{dl}\right)_{nuc}$$

Equation 4

Additionally, the energy losses due to inelastic nuclear processes can be considered (ICRU, International Commission on Radiation Units and Measurements, 1998, pp. 10-11). In the case of protons and alpha particles the *electronic stopping power* is what contributes most to the total stopping power. The contribution of the nuclear stopping power must not be neglected just at very low energies. The inverse proportionality to the square of the mass of the charged particle causes the radiative stopping power, which is of importance for electrons, to make just an insignificant contribution when considering protons (ICRU, 1993, p. 2).

As an indication for the radiation quality the *linear energy transfer (LET)* or *restricted linear electronic stopping power*, L_Δ, of a material, for charged particles is introduced as the energy lost by a charged particle due to electronic collisions in traversing a distance *dl*, minus the sum of the kinetic energies of all the electrons released with kinetic energies above Δ:

$$L_\Delta = \frac{dE_\Delta}{dl}$$

Equation 5

Its SI unit is J m^{-1}. Other common expressions are eV m^{-1} or keV μm^{-1}. Even though an energy cutoff, Δ, and not a range cutoff is included in its definition, L_Δ is often described as *locally transferred* energy. If there is no energy cutoff, one gets the *unrestricted linear energy transfer* L_∞, an equivalent of S_{el} (ICRU, International Commission on Radiation Units and Measurements, 1998).

Only if a charged particle equilibrium[10] is ensured, the use of unrestricted LET is justified. While homogeneous regions show this equilibrium, its validity at interfaces and in the field penumbra is not strictly guaranteed. A mitigation of this effect might be achieved by choosing a relatively small voxel[11] size.
The application of the definitions given above is only possible for a single particle or a monoenergetic beam. If experiments are made, however, mostly a range of LET values needs to

[10] If the sum of the kinetic energies carried out of a volume element by secondary charged particles that arise within it is equal to the energy imparted to the element by charged particles that originate outside, a condition of *charged particle equilibrium* is said to exist (definition according to (ICRU, International Commission on Radiation Units and Measurements, 1979, p. 22)).
[11] A *voxel* is a *volume element*. The basic building block of a volumetric description of an object (definition according to (IAEA, International Atomic Energy Agency, 2004, p. 278)).

be considered. For a complete characterization of a radiation field, either the knowledge of the whole LET distribution or the mean value of such a distribution at every point is essential. From the point of view of practicability the second strategy is the more appropriate one. Commonly, two averages are used: dose averaged (LET_d) and track averaged (LET_t); the second is sometimes also called more intuitively fluence averaged LET_f (Grassberger & Paganetti, 2011).

The LET_t can be computed as follows:

$$LET_t(z) = LET_f(z) = \frac{\int_0^\infty S_{el}(E)\phi(E,z)dE}{\int_0^\infty \phi(E,z)dE}$$

Equation 6

where $S_{el}(E)$ is the *electronic stopping power* of primary charged particles with *kinetic energy E* and $\Phi(E,z)$ is the *fluence* of primary charged particles with *kinetic Energy E* at *location z*. It is also called fluence-averaged LET because of the use of the relative fluence as the weighting factor for its calculation. The use of the electronic stopping power implies unrestricted LET is calculated without considering the production of delta rays.

The dose-averaged LET can be calculated by the following formula:

$$LET_d(z) = \frac{\int_0^\infty S_{el}(E)D(E,z)dE}{\int_0^\infty D(E,z)dE}$$

Equation 7

where $S_{el}(E)$ is the *electronic stopping power* of primary charged particles with *kinetic energy E* and $D(E,z)$ is the *absorbed dose* contributed by primary charged particles with *kinetic Energy E* at *location z*. The relative dose is used as a weighting factor to compute LET_d. To estimate the absorbed dose the electronic stopping power and the fluence can be used. The basis of this estimation is the continuous-slowing-down approximation (CSDA)[12] assumption of energy loss. This estimation neglects the nuclear stopping power and the escape of delta rays and is given as

$$D(E,z) = \frac{S_{el}(E)\phi(E,z)}{\rho(z)}$$

Equation 8

where $\rho(z)$ is the *mass density* of the current medium where energy is deposited.

After the substitution of $D(E,z)$ with Equation 8, Equation 7 can be rewritten as

$$LET_d(z) = \frac{\int_0^\infty {S_{el}}^2(E)\phi(E,z)dE}{\int_0^\infty S_{el}(E)\phi(E,z)dE}$$

Equation 9

(Guan & Peeler, 2015).

[12] In the *continuous-slowing-down approximation* (CSDA), energy-loss fluctuations are neglected, and charged particles are assumed to lose their energy continuously along their tracks at a rate given by the stopping power. The *CSDA range*, calculated by integrating the reciprocal of the total stopping power with respect to energy, is a very close approximation to the average path length traveled by a charged particle in the course of slowing down to rest (definition according to (ICRU, 1993, p. 5)).

The consideration of unrestricted LET is essential in voxelized geometries for being able to obtain LET distributions without a dependence on the voxel size (Cortés-Giraldo & Carabe, 2015).

For all statements made in the course of this master thesis the dose-averaged LET was chosen to get an average value of LET. *Dose averaged* refers to the weighting of each particle according to the dose it deposits.

For dose levels applied clinically a sub-cellular structure is in general crossed by a rather large number of particle tracks. For high-LET ion beams, on the other hand, there are substantially fewer tracks per sub-subcellular target. An inhomogeneous local dose distribution might be a consequence. If this is the case, preference to LET_t should be given over LET_d. The limitations of the LET concept become here clearly visible. The lower the energy (and consequently the lower the fluence for a given dose) the higher the importance of the track structure.

The concept of LET was chosen as a base of all analysis made in course of this master thesis due to the fact that measurements on the radiobiological effect and biological modeling of radiation effects usually refer to LET values. Nevertheless, one has to keep in mind that for a correct handling of energy depositions a dealing with microdosimetric quantities is required. The observation of the energy deposition in a small volume characterizes the microdosimetric lineal energy concept.

Lineal energy y and *dose mean lineal energy* y_D are the microdosimetric quantities which correspond to LET and LET_d. The concept of LET, on the other hand, includes a definition per track length which results in the demand of defining unrestricted or restricted LET values. The still more frequent implementation of the LET concept is based on its easier way to apply (Grassberger & Paganetti, 2011).

Radiations can either sparsely ionize, those are called low LET radiations or densely ionize, so-called high LET radiations. While among the former are X rays and γ rays, the latter includes energetic neutrons, protons and heavy charged particles. Commonly used energies and particles for radiations lead to the following characteristic LET values: 2 keV/µm for 250 kVp X rays, 0.3 keV/µm for Cobalt-60 γ rays, 0.3 keV/µm for 3 MeV X rays and 0.25 keV/µm for 1 MeV electrons (IAEA, Radiation Oncology Physics: A Handbook for Teachers and Students, 2005, pp. 486-487).

Bethe-Bloch equation

The mass collision stopping power for heavy charged particles due to their Coulombic interaction with atomic electrons in matter can be described via the Bethe-Bloch equation

$$\frac{S}{\rho} = -\left(\frac{1}{\rho}\right)\left(\frac{dE}{dl}\right)_{el} = \frac{4\pi {r_e}^2 mc^2}{\beta^2}\,\frac{1}{u}\,\frac{Z}{A}\; z^2 L(\beta)$$

Equation 10

where $r_e = e^2/mc^2$ is the classical electron radius, mc^2 is the electron rest energy, u is the atomic mass unit, β is the particle velocity in units of the velocity of light ($\beta = v/c$ where v is the velocity of the projectile and c the speed of light), Z and A are the atomic number and relative atomic mass of the target atom, z is the charge number of the projectile and L is called stopping number. The fine description of the energy-loss process is included in the quantity L, whereas the other factors consider the gross features. The stopping number can be obtained by summing up three terms:

$$L(\beta) = L_0(\beta) + zL_1(\beta) + z^2 L_2(\beta)$$

Equation 11

The first term can be written as

$$L_0(\beta) = \frac{1}{2}\ln\left(\frac{2mc^2\beta^2 W_m}{1-\beta^2}\right) - \beta^2 - \ln I - \frac{C}{Z} - \frac{\delta}{2}$$

Equation 12

Where I is the mean excitation energy of the medium, C/Z is the shell correction, and $\delta/2$ the density-effect correction. W_m expresses the largest possible energy loss in a single collision with a free electron. When using restricted collision stopping powers, which is sometimes the case in track structure calculations in radiobiology, the cut-off value, W_c, which describes the biggest energy transfer from inelastic collisions, that is taken into account, replaces W_m in *Equation 12*. The Bethe-Bloch equation (*Equation 10*) without a shell correction is a correct description of the stopping-power if the particle´s velocity exceeds the velocities of the target´s bound atomic electrons. For higher projectile velocities the interactions with electrons in the K shell, respectively, in L or higher shells for even higher velocities, contribute less to the stopping power.

A polarization of the medium takes place when the projectile particle passes the medium. This effect causes a decrease of the stopping power and is taken into account by the density-effect correction. Just for kinetic energies similar as or even higher than the rest energy of the particle this modification is large.

The first-order Born approximation served as a basis for the derivation of Bethe´s theory. The second (Barkas correction) and the third term (Bloch correction) in *Equation 11* can be neglected except for low projectile velocities compared to the velocities of the atomic electrons (ICRU, 1993, pp. 4-6).

Equation 10 expresses what impact the projectile´s characteristics have on its energy loss rate. It depends inverse quadratically on its velocity and quadratically on the ion charge, but does not depend on the projectile mass. Furthermore, *Equation 10* shows the potential high impact of the absorber material on the energy loss rate. More particularly there is a direct proportionality of the linear stopping power on the mass density. In investigating proton therapy tissue can be substituted with water due to a similar density, effective Z/A and other properties. What is more, for the expression of proton energy loss and residual range in a variety of materials often water-equivalent values are used (Newhauser & Zhang, 2015).

1.2.4 Range

The depth at which 50 percent of particles in the medium have come to a standstill is defined as range. The individual protons do not lose all the same amount of energy. This effect is named range straggling. As a result, the definition of the range never refers to individual particles but always to a beam and is therefore inherently averaged (Newhauser & Zhang, 2015).

1.2.5 Range straggling

The total energy loss is composed of lots of individual interactions. As a result this quantity has a statistical error. Consequently, a stopping of all protons at the same depth will never happen, including the case where all protons initially have the same energy. The terms range straggling or energy straggling describe the stopping at different depths (Paganetti, Proton Therapy Physics Series in Medical Physics and Biomedical Engineering, 2012, p. 37).

1.3 Radiobiology of proton irradiation

Biological effect is not related to dose in a simple way. Furthermore, the dose-response relationships vary depending on the used radiation modality. Nevertheless, dose is the quantity which is given in prescriptions for clinical treatments. This is based on the fact that we just poorly understand biological effects. Moreover, applications are based on clinical experience with particular dose levels. To get to know how radiation acts on living cells the complex interaction of physical, biochemical, and physiological events need to be studied (Paganetti, Proton Therapy Physics Series in Medical Physics and Biomedical Engineering, 2012, pp. 593-594).

1.3.1 Radiation interaction with human tissue

Energy deposition events and DNA Damage[13]

When radiation passes through biological matter it ionizes and excites the medium molecules. The consequence is an energy deposition. In case of a penetration through a medium, the patterns of the deposited energies vary depending on the particle´s mass and energy as well as on the stopping medium´s physical and chemical properties (Nikjoo & Lindborg, 2010). In the interaction process of radiation with the human body tissue atoms play a role. Cellular and subsequent molecular effects are caused by ionizations. Heat is produced by vibration since radiation stimulates molecules to move into excited states. Even though the largest amount of the radiation´s energy is converted into heat, the effects of ionizations are of more importance for radiation therapy.
The essential genetic information is stored in the cell nucleus, which has a diameter of around 10 µm, or more precisely, in the double-helical DNA macromolecules. One can describe the DNA, which has a diameter of around 2 nm and just contributes very little to the total mass of the nucleus, as the radiation target, since mutation induction, carcinogenic transformation, and killing of most cell types is evidently crucially connected to damaged DNA molecules. There is a direct relation between DNA damage and cell death. All cellular functions are fundamentally connected with DNA (Paganetti, Proton Therapy Physics Series in Medical Physics and Biomedical Engineering, 2012, p. 594). Potential consequences of deposited energy on cells when looking at nucleic acids are single-strand breaks (SSB)[14], double-strand breaks (DSB)[15], DNA crosslinks[16], base damages[17] and bulky lesion[18].

A strand break is frequently the first damage a proton produces. Double-strand breaks (DSBs) can be the result of DNA strand breaks close together. Just a minor part of the initial biochemical damage results subsequently in a cellular effect. The other part is either insignificantly damaged or its repair is possible.

DNA damages activate various repair mechanisms. If DSBs are not repaired dysfunction and loss of genetic material are possible consequences. Cell death can occur due to chromosomal aberrations arising from the joining of pieces of DNA. In general, cell death is understood to mean the cell lost its reproductive capacity (Paganetti, Proton Therapy Physics Series in Medical

[13] DNA is under constant siege from a variety of damaging agents. *Damage to DNA* and the ability of cells to repair that damage have broad health implications, from aging and heritable diseases to cancer (definition according to (Brady & Yaeger, 2013, p. 158)).
[14] A *Single-Strand Break* (SSB) is an interruption of one single DNA strand due to a broken phosphoester bond or a chemical modified desoxyribose (definition according to (Reiser, Kuhn, & Debus, 2004, p. 30)).
[15] *A Double-Strand Break* (DSB) is an interruption of both DNA strands due to two SSBs very close together or if a particle penetrates the DNA transversely (definition according to (Reiser, Kuhn, & Debus, 2004, p. 30)).
[16] In case of high radiation doses *crosslinks* between the two DNA-strands or between one DNA strand and a protein are formed (Reiser, Kuhn, & Debus, 2004, p. 30)).
[17] *Base damages* are chemical modifications or loss of a purine or pyrimidine base, e.g. formation of pyrimidine dimers after UV-radiation (definition according to (Reiser, Kuhn, & Debus, 2004, p. 30)).
[18] If the above mentioned forms of DNA damage occur in combination and close together this is called *bulky lesion*. Bulky lesions are often irreparable damages (definition according to (Reiser, Kuhn, & Debus, 2004, p. 31)).

Physics and Biomedical Engineering, 2012, p. 594). Those cells which survive might suffer chromosome damage, genomic deletions or base changes (Nikjoo & Lindborg, 2010).

Sometimes the energy of an electron, which has its origination in an ionization process, is sufficiently high to be a trigger for further ionization processes. Such electrons are called δ – electrons. Their energies differ greatly. A consequence is a complex spatial pattern of energy deposition. Track-ends of low-energy δ – electrons may, for instance, result in clusters of ionizations and excitations. These are countered by ionizations and excitations for which an independent consideration is possible.

If water is ionized damages due to reactive radicals which may chemically react with the DNA may occur. These damages are called indirect effects. Direct effects, on the other hand, are lethal damages caused by the direct energy deposition in the DNA. In the case of low-LET (linear energy transfer) radiation the creation of free radicals by δ–electrons has the greatest impact. The higher the LET the more effect have direct hits (Paganetti, Proton Therapy Physics Series in Medical Physics and Biomedical Engineering, 2012, p. 595).

Ionization event distribution and lesion complexity

There is no direct proportionality between initial DSBs and cellular damage. A linear increase of the number of DSBs per cells with dose can frequently be established. The same number of DNA DSBs per unit dose produced by different modalities, for instance, photons and protons, can be appreciably differently distributed. Decisive for the radiation impacts is mainly how the DNA lesions are spatially distributed and not the type of DSBs. A study of the spatial distribution of energy deposition events, resulting complex lesions as well as repair mechanisms is essential for a comprehension of radiation effects. The lesions caused by low-LET radiation are predicted to be more randomly spatially distributed than those created by high-LET radiation. The higher the LET the more DSBs might occur in close proximity. This might be a reason for the effectiveness of high-LET radiation. Lesions caused by protons can be quite complex, they can include, for instance, single-strand breaks, double-strand breaks and more than two strand breaks. Commonly, the complexity of lesions caused by protons is higher than that of damages from photons. The higher the LET the more energy is delivered in direct hits which results in a further rise of complexity. Moreover, a higher concentration of damages in space is assumed to make their repair less likely. Chromosome aberrations caused by mis-joining, on the other hand, might appear more often. Part of the explanation of the varying radiation sensitivity of different cell lines could be the diverse spatial orientation of the DNA (Paganetti, Proton Therapy Physics Series in Medical Physics and Biomedical Engineering, 2012, pp. 596-597).

1.3.2 Dose-response relationships

If you plot a biological effect observed against the dose you obtain a dose response curve[19] (IAEA, Radiation Oncology Physics: A Handbook for Teachers and Students, 2005, p. 494). Dose-response curves, which, for instance, show cell survival, tumor induction or tissue response, as a function of dose, are used to visualize the response of a biological system to dose. The determining factor in the display of the cell survival curves is if the cells are able to proliferate unlimitedly or if they have lost this capability. Nearly all survival curves can be sufficiently accurately approximated by a linear-quadratic parameterization, the linear quadratic model (LQ, α/β-model, *Fig. 6*)

$$S(D) = \frac{N}{N_0}(D) = \exp\left(-\propto D - \beta D^2\right)$$

Equation 13

[19] A *dose-response curve* is a curve describing how a particular organ or tumor responds to radiation (i.e. relative response versus dose) (definition according to (IAEA, International Atomic Energy Agency, 2004, p. 273)).

where S is the survival fraction, N_0 is the initial number of cells, N the number of unaffected cells, D the absorbed dose and α and β are the LQ model tissue specific radiation sensitivity parameters. In the beginning the survival curve decreases linear (α term) (Paganetti, Proton Therapy Physics Series in Medical Physics and Biomedical Engineering, 2012, pp. 598-599). This linear term is a consequence of the lack of or defectively repaired DSBs which lead to the cell´s death. It describes, in other words, a small to missing repair capacity for radiation damages (Reiser, Kuhn, & Debus, 2004, p. 37).

After the linear increase a shoulder follows. Its expressiveness is determined by the ratio α/β, which can be an expression of the lesion repair capacity or of lesion induction mechanisms. The bigger the value of α/β the less pronounced is the shoulder of the curve (Paganetti, Proton Therapy Physics Series in Medical Physics and Biomedical Engineering, 2012, pp. 598-599). The dose value (in Gray) at which the linear and the quadratic component are the same is called *α/β value.*

$-\beta D^2$ is the model´s quadratic component. It is the result of repairable DSBs and characterizes therefore a high repair capacity.

The LQ model takes the impact of the fractionation on the radiation effect into account but does not consider the time factor (viz. the time of exposure) (Reiser, Kuhn, & Debus, 2004, p. 37).

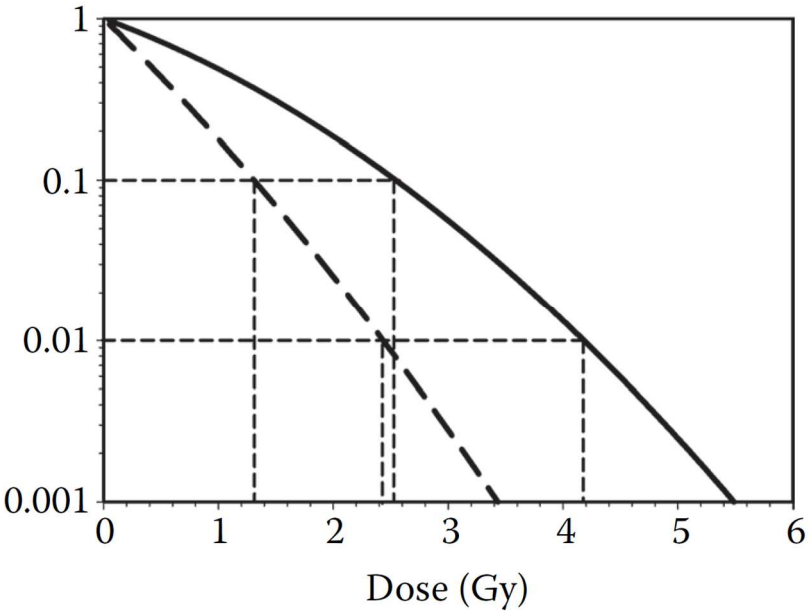

Fig. 6: *Example of two dose-response curves.*
The solid line might resemble the response after photon irradiation, and the long dashed line might be caused by low-energy proton irradiation. The relative biological effectiveness (RBE) at 10% survival would be ~2.55/1.3 = 1.96, whereas at 1% survival it would be ~4.15/2.4 = 1.73 (short dashed lines) (Paganetti, Proton Therapy Physics Series in Medical Physics and Biomedical Engineering, 2012, p. 599).

1.3.3 Relative biological effectiveness

The biological and clinical effects produced by radiations of diverse quality differ, even if the absorbed doses are the same. Factors which affect the radiation quality are the type of particles as well as their energy spectrum. The biological effectiveness of protons, for instance, is increased compared to photons. In other words the application of a lower proton dose achieves the same biological effect. The way in which energy is deposited on a subcellular scale determines the differences in effectivity.

In order to make an accurate estimation of the enhanced effectiveness of ions, the quantity *relative biological effectiveness* (*RBE*) is introduced. It is defined as the ratio of absorbed dose of a reference radiation D_γ of photons to the absorbed dose of any other radiation D_x to result in the same biological effect. The mainly used reference radiation quality are ^{60}Co γ-rays.

$$RBE(endpoint) = \frac{D_\gamma}{D_x}$$

Equation 14

The concept of RBE is characterized by its clarity, unambiguity and its well-definedness. There is uncertainty associated to the value for RBE because it is determined by experiments. The biological system as well the type and level of effect and many other factors influence the RBE. That is why it is important to give specifications on the dose and the experimental conditions which were applied for the determination of RBE. In general an increase of RBE is accompanied by a decrease of dose. In addition, in some cases, in particular at low doses, RBE is lower for early effects than for late effects[20] (IAEA, Relative Biological Effectiveness, 2008, pp. 5-6, 14).

RBE-weighted absorbed dose (D_{RBE}) is the name of the term you get by multiplying absorbed dose by RBE. Since RBE is dimensionless, RBE-weighted dose and absorbed dose are both measured in Gray (Gy). However, to prevent confusion, it is recommended to express RBE-weighted dose in Gy (RBE) (ICRU, International Commission on Radiation Units and Measurements, 2007, p. 28) .

For the treatment with protons a generic RBE is considered as clinically appropriate, hence recommended and consequently used, since one can interpret the disposable data in a sense that the value of RBE varies insignificantly with treatment parameters compared to the precision which is achievable for the determination of the RBE (Paganetti, et al., 2002). Generic, in this case, means one value is applied for all tissue types, doses per fraction, total doses, proton energies, and positions on the physical depth-dose curve. The RBE chosen for an application should be in good agreement with the RBE values determined on the basis of *in vivo*[21] studies and might, for instance, be 1.1. Even though a universal value of 1.1 for the conversion of absorbed dose into RBE-weighted absorbed dose in proton therapy is recommended, suggestions based on experiments are made for a potential increase of the RBE by 5-10 percent in the deepest areas of the SOBP in comparison to the middle of the SOBP. A substantial increase of the RBE can also be observed in the first few millimeters of the declining edge of the SOBP compared to the RBE at the distal Bragg peak. As a consequence the range of the RBE-weighted absorbed dose is elevated by 1 to 2 mm. A consideration of these effects might be appropriate in treatment planning and might become even more important in the event of single-field treatments or when organs at risk are in close proximity to the regions where the target is located (ICRU, International Commission on Radiation Units and Measurements, 2007, pp. 26-27).

1.3.4 RBE Models

As already mentioned many factors like ion type, energy, cell and tissue radiosensitivity, physical dose and biological endpoint influence in a complex manner the value of RBE. In order to personalize and optimize treatment plans, biophysical models that reflect these dependencies are

[20] *Late reactions* are reactions of the healthy tissue more than 90 days after end of radiotherapy treatment. The type and severity of late reaction is related to the body region treated, the applied radiation dose, the radiation technique (e.g., IMRT with sparing of organs at risk), and the individual predisposition of the patient. Late side effects can be long term or permanent (definition according to (Brady & Yaeger, 2013, p. 424)).
Side effect is an undesirable effect of a therapy which can lead to a change or a break-off in therapy (definition according to (Reuter, 2007, p. 1260).

[21] *In vivo* means *in life* whereas with *in vitro* is meant *in glass*, commonly involving cells in an artificial container (definition according to (IAEA, Technical Reports NO. 430 - Commissioning and Quality Assurance of Computerized Planning Systems for Radiation Treatment of Cancer, 2004, p. 274)).

needed. Those should enable to translate results of *in vitro* and *in vivo* experiments to the clinical setting. Due to the large number, complexity and poor understanding of quantification of mechanisms and pathways which are included in the transition of energy deposition into the observed biological effect these models always represent an approximation of the underlying processes. The finding of the right balance between accuracy and model complexity is challenging (Stewart, et al., 2018). Several models have been developed. One of them is presented below.

Wedenberg et al. model

The Wedenberg et al. model was developed for introducing a proton RBE dependent on the linear energy transfer (LET), the dose, and the tissue specific parameter α/β (see section *1.3.2 Dose-response relationships*) instead of assuming a constant RBE of 1.1 that is commonly applied in proton radiotherapy. Its goal was to use just a minimum number of assumptions necessary for enabling a capture of all basic features of the RBE. Furthermore, experimental data should support the model.

The LQ model, which provides a description of the survival fraction depending on the dose and the radiosensitivity parameters α and β, plus the RBE´s definition (see *Equation 14*) may serve as basis for a first expression of the RBE.

According to the LQ model the following expression of the survival fraction S is proposed

$$S = e^{-\propto D-\beta D^2}$$

Equation 15

where α and β are the radiosensitivity parameters of the model. The RBE is defined as the ratio of the dose of a reference radiation and the corresponding particle dose which leads to the identical biological response.

On the basis of the LQ model, one can equate the expressions for biological response as

$$S = S_{phot}$$

$$\propto D + \beta D^2 = \propto_{phot} D_{phot} + \beta_{phot} D_{phot}^2$$

Equation 16

where all quantities without the subscript *phot* refer to proton radiation, all others to photon radiation, to eventually get the RBE of protons.

After solving the quadratic equation for D_{phot} for the positive root, the following expression can be obtained

$$D_{phot} = -\frac{1}{2}\left(\frac{\propto}{\beta}\right)_{phot} + \sqrt{\frac{1}{4}\left(\frac{\alpha}{\beta}\right)_{phot}^2 + \frac{\alpha}{\beta_{phot}} D + \frac{\beta}{\beta_{phot}} D^2}.$$

Equation 17

By dividing D_{phot} by the dose D the RBE at that certain proton dose can be obtained

$$RBE = \frac{D_{phot}}{D} = -\frac{1}{2D}\left(\frac{\propto}{\beta}\right)_{phot} + \frac{1}{D}\sqrt{\frac{1}{4}\left(\frac{\alpha}{\beta}\right)_{phot}^2 + \frac{\alpha}{\propto_{phot}}\left(\frac{\propto}{\beta}\right)_{phot} D + \frac{\beta}{\beta_{phot}} D^2}$$

Equation 18

The ratio of LQ parameters from photon exposure $(\alpha/\beta)_{phot}$ is frequently in use to characterize the radiosensitivity of a cell type or tissue. It is suggested to describe the other two ratios´ dependence on the LET using analytical expressions and afterwards evaluate them by the use of statistical methods.

In the case of protons a rise of the ratio α/α_{phot} with rising LET up to about 30 keV/µm followed by a decrease can be observed. It is not fully ascertained how the ratio exactly increases with LET. Since the number of experimental data sets is limited the assumption of a simple linear dependence on the LET, L, is made:

$$\frac{\propto}{\propto_{phot}} = 1 + kL$$

Equation 19

The falling of α/α_{phot} at high LETs is not taken into account by *Equation 19*. Therefore, its validity is limited to LETs lower than 30 keV/µm. A non-consideration of that high values in this master thesis is appropriate, since they are not sufficiently relevant for energies which are in use in clinical proton therapy.

Even in cases where LET values are almost the same dissimilar α/α_{phot} are reported by different studies. A possible reason for this could be a variability between different cell lines. An influence of the slope k by the cell type is assumed. It is proposed that the slope and the tissue response related parameter $(\alpha/\beta)_{phot}$ are inversely related to one another.

Consequently α/α_{phot} can be expressed as follows

$$\frac{\propto}{\alpha_{phot}} = 1 + \frac{qL}{(\propto/\beta)_{phot}}$$

Equation 20

where q denotes a free parameter of the expression and a fit to cell survival experiments enables its determination. There is a lack of clarity in experimental data regarding the correlation between β/β_{phot} and LET. Since the dependence of this ratio on LET appears to be less pronounced β/β_{phot} is supposed to be a constant, for example 1.

The final expression for the RBE varying with proton dose, LET, and $(\alpha/\beta)_{phot}$ can be received by substituting *Equation 20* into *Equation* 18 and assuming that β/β_{phot} equals 1

$$RBE\left(D, L, \left(\frac{\alpha}{\beta}\right)_{phot}\right) = -\frac{1}{2D}\left(\frac{\propto}{\beta}\right)_{phot} + \frac{1}{D}\sqrt{\frac{1}{4}\left(\frac{\alpha}{\beta}\right)^2_{phot} + \left(qL + \left(\frac{\propto}{\beta}\right)_{phot}\right)D + D^2}$$

Equation 21

This expression is valid for single doses or doses per fraction.

Wedenberg et al. reported that a q of 0.434 Gy µm/keV fitted best their experimental data obtained in cell survival experiments (Wedenberg, Lind, & Hårdemark, 2013). This q value was also used for calculations done in the course of this master thesis.

1.4 Technological equipment of proton therapy

Every proton therapy facility comprises an accelerator with its associated systems, a beam transport system into at least one treatment room, a shielding, beam-shaping devices, a patient-positioning system and a control system.

1.4.1 Accelerators for proton beam therapy

For producing proton beams for medical use a circular accelerator is the tool of choice. It enables to attain the desired energies, and beam intensities. Different types of circular accelerators are applied. Those are the cyclotron, synchrocyclotron and the synchrotron.

The cyclotron

For this type protons are injected into the center of the machine by the ion source. An alternating high voltage is applied to two hollow semicircular electrodes, so-called *Dees*. Every time the proton passes through the space between the two electrodes it is accelerated by a sector of negative polarity which exerts a force of attraction. A magnetic field perpendicular to the particle´s trajectory is created by a magnetic circuit and a set of coils. No electric force acts on the proton when it emerges into the electrodes´ cavity again. According to Lorentz force the magnetic field bends the moving proton into a circle. Due to the electric field´s change of direction the proton is accelerated again when it re-enters the area between the Dees. The radius of its circular trajectory is larger now. By equating the centrifugal force on a particle of mass M at a distance r to the Lorentz force

$$qvB = \frac{Mv^2}{r}$$

Equation 22

one obtains an expression for the particle´s angular velocity ω

$$\omega = \frac{v}{r} = \frac{qB}{M}.$$

Equation 23

Since the accelerating electric field between the *Dees* stays in phase with the passage of the particles its frequency remains constant, more precisely, constant at the frequency expressed by *Equation 23*.

The synchrocyclotron

As soon as relativistic effects cause due to the enhanced particle energy a not negligible increase of the accelerated particle´s mass there is no possibility of keeping the frequency of the electric field between the Dees of a cyclotron constant anymore (*Equation 23*). Since it is essential to maintain the synchronicity between the electric field and the passage of the particles the frequency has to be modulated: The increase of the proton´s mass with energy causes the particle to need more time for moving through the Dee. Therefore, the frequency is reduced. The synchrocyclotron is producing a pulsed beam instead of a continuous one what is considered to be seen as a drawback of this accelerator type.

The synchrotron

Besides increasing the radius of the particle´s trajectory for a particle with an elevated speed it is also possible to enhance the magnetic field B for fulfilling *Equation 22*. The synchrotron operates according to this principle. Before their injection into a ring the particles are accelerated up to several MeV. In the ring they are accelerated synchronized with the angular frequency of the

particles by a high-frequency cavity at each revolution. A modification of the magnetic field is caused by the deflecting dipoles for maintaining the diameter of the protons´ trajectory at a constant value until the desired energy is reached. An advantage of this type is the possibility of producing a beam with variable energy, a negative aspect, on the other hand, is the obtainment of a pulsed beam of low pulse-repetition frequency. The typical duration of one acceleration cycle varies between one and three seconds. Depending on their design synchrotrons can be used not only for the generation of beams applied in proton but also in carbon-ion therapy (Mayles, Nahum, & Rosenwald, 2007, pp. 1010-1016).

1.4.2 Beam delivery systems

After the acceleration process the particles need to be transported to the target area. This is done by the beam delivery system. It ensures that the dose distribution delivered to the target is accurate, homogenous and as desired. After being extracted from the accelerator the proton beam has in general a narrow Gaussian profile. To obtain the required homogeneity in the dose distribution two different strategies are in use: The Passive Scattering and the Pencil-beam scanning (PBS). The former one is a technique which solely uses passive nonvariable field shaping elements to adapt the particle beam. Passive scatters increase the lateral spread of the narrow beam. The second one is an active beam scanning system. Here, a fine proton pencil-beam is swept in position with the help of magnets. In this way a precise three-dimensional dose deposition can be achieved. A variation of the protons´ intensity as well as of their energy is simultaneously possible.

Of course there is also the possibility to combine active and passive beam delivery systems. A combination of both strategies can, for instance, be helpful when treating tumors that are located at shallow depths. The particle accelerator might not allow to accelerate the particles to arbitrarily small energies. If it is not possible to achieve arbitrarily small energies, arbitrarily small particle ranges cannot be achieved either. To still be able to treat superficial tumors a so-called *range shifter* is used. Range shifters are absorber plates, which allow to shift the whole spread-out Bragg peak in depth (Schardt, Elsässer, & Schulz-Ertner, 2010).

1.5 Treatment implementation

1.5.1 Treatment planning and treatment planning systems (TPS)[22] for ion beam therapy

A Treatment Planning Systems is a computer based system used to simulate, calculate and optimize the radiotherapy treatment of patients. The main tasks are lesion localization, radiation plan generation according to safety and health constraints and geometric feasibility plan optimization (definition according to (Exarchos, Papadopoulos, & Fotiadis, 2009, p. 212)).

The term *Radiotherapy treatment planning* refers to the process which determines the machine instructions for the treatment delivery (like, for instance, beam energy, beam shape, spot positions and number of protons to be delivered in each spot) and the expected dose distribution in the patient based on radiation beam and patient´s anatomy models. The latter enables a quantification of the likelihood of controlling the tumor as well as of complications to the normal tissues. There are similarities of treatment planning for different radiation types (e.g. photons vs. heavy charged particles). However, in the design and optimization of treatment parameters one encounters

[22] A *radiation treatment planning system* is a device, usually a programmable electronic system that is used to simulate the application of radiation to a patient for a proposed radiotherapy treatment. In this context, usually a *treatment planning system (TPS)* includes: hardware, the computer operating system and TPS software (definition according to (IAEA, International Atomic Energy Agency, 2004, p. 276)).

specific implications when using protons. The same properties which make protons an excellent tool for radiotherapy (i.e. the finite range and the steep fall-off in dose deposition after the dose maximum) lead also to the necessity of taking particular care that the planned and the delivered dose correspond well. Invariance of the dose distribution due to small misalignments between beam and patient anatomy because of positioning errors or small anatomy changes can be assumed in the case of photon radiotherapy (XRT) with sufficient safety. This changes when applying protons. If the relative position of beam and patient model is different to what has been set during planning, the planned dose might differ significantly from the delivered dose.

1.5.1.1 Treatment planning and dose verification

At the beginning of treatment planning always the definition and delineation of the target volume has to be done. Commonly, all different forms of radiotherapy use the same kind of images for creating a patient model in the treatment planning process. The basis is always a computed tomography (CT)[23] dataset of the anatomical region to be treated. A 3D map of patient´s electron density is created. It is always made under the same conditions and with the same fixation aids (e.g., head mask) the treatment is accomplished with afterwards and is used to compute the beam attenuation, and consequently the dose distribution within the patient (Schwarz, 2011). To facilitate the definition of the target volume and organs at risk additional images with complementary image information e.g. from magnetic resonance imaging (MRI)[24] and positron emission tomography (PET)[25] are frequently combined with CT. A registration of all available image series to the planning CT series as well as delineation of target volume and critical structures in different slices on the basis of these images follows. A 3D model of the treatment geometry can be constructed from these contours. With the use of this model the finding of suitable beam entrance ports is possible. At this stage the avoidance of traversing or stopping towards critical structures should be ensured. Treatment with protons and heaver ions is typically performed with a few entrance ports due to their advantageous depth-dose characteristics. In doing so a maximum sparing of radiosensitive organs can be achieved. The integral dose delivered to a patient´s body can substantially be decreased for protons compared to photons.

When the definition of the target is done an adaption of the dose distribution to the planning target volume follows. In the ideal case, the planning target volume is covered entirely by 100% of the prescribed dose. At the same time dose for organs at risk should be a minimized. Commonly, proton plans are optimized for the absorbed dose applying a constant RBE value of 1.1. If other ions are used for treatment an optimization of the biological effective dose might be a more difficult task because of the diverse dependencies of RBE and the complex radiation field. Medical physicists have great interest in developing dose calculation models. Several algorithms[26] have been generated and are in use (Schwarz, 2011).

In order to make a calculation of the dose deposition as well as the accurate location of the Bragg peak in heterogeneous tissue possible, an establishment of the relationship between CT numbers and stopping power is required. For obtaining the relationship between the traversal of an ion

[23] *Computed tomography* (CT) is a radiographic method which produces sliced images of the patient´s body. Tissues and organs can so be displayed two-dimensional and free of superimposition. By summing up one gets information of the third dimension. It is part of the sectional imaging techniques (definition according to (Reiser, Kuhn, & Debus, 2004, p. 73)).

[24] *Magnetic resonance imaging* (MRI) is a procedure for generating sectional images in a freely selectable room level without the use of X-radiation (definition according to (Reiser, Kuhn, & Debus, 2004, p. 79)).

[25] *Positron emission tomography* (PET) is a type of nuclear medicine imaging based on the four-dimensional (spatial and time) distribution of a given radiotracer within human body and can reveal the metabolic function such as glucose metabolism. Therefore, it is often referred to as a functional imaging modality. Positron emission tomography (PET) scan is a nuclear medicine test that creates three-dimensional images according to metabolic uptake in cells. It is very useful in cancer staging, as malignant cells are PET avid (definition according to (Brady & Yaeger, 2013, p. 636)).

[26] An *algorithm* is a method used for a calculation, respectively, the specific steps involved in the calculation (definition according to (IAEA, Technical Reports NO. 430 - Commissioning and Quality Assurance of Computerized Planning Systems for Radiation Treatment of Cancer, 2004, p. 271)).

through a CT voxel to the corresponding path length the concept of water-equivalent path length (WEPL)[27] is in use. The definition of CT numbers which are given in Hounsfield units (HU)[28] is as follows

$$CT\ number(\vec{x}) = 1000 \cdot \frac{\mu(\vec{x}) - \mu_W}{\mu_W}$$

Equation 24

where $\mu(\vec{x})$ and μ_w are the *x-ray absorption coefficients* in tissue at *location* $\vec{x}$ respectively in water as reference medium. The relationship between CT number and stopping power or WEPL is not a simple functional one. However, one can start with an approximation by linear sections. A systematic investigation of methods to obtain the calibration of CT numbers for protons was done. According to the conducted studies one may assume range uncertainties of 1-2 mm for soft tissues in typical patient treatments in the head and neck region (Schardt, Elsässer, & Schulz-Ertner, 2010).

The physical quantity which is in use in clinical radiation therapy prescription is the absorbed dose. It is defined as the energy imparted by ionizing radiation per unit mass of medium. An essential aspect in radiation therapy treatment planning is the calculation of this absorbed dose. The aim of dose calculation algorithms is to simplify this procedure.

1.5.1.2 Dose calculation algorithms

One can divide the dose calculation algorithms which are in common use into three categories: correction-based algorithms (e.g. raytracing), model-based algorithms (e.g. Pencil beam algorithm) and Monte Carlo simulations. In the first category a semi empirical approach accounts for tissue heterogeneity and surface curvature on the basis of measured dose distributions in water (Brady & Yaeger, 2013, p. 158). A straight line between the source and each calculation point is traced. This enables to calculate radiological depths[29] in the body and takes heterogeneities into account. By using these depths an estimation of the dose from *Bragg curves* stored in a beam library or represented by analytical expressions can be given. However, here the effect of multiple scattering is not explicitly modelled (Mayles, Nahum, & Rosenwald, 2007, p. 1020). In the second category a prediction of patient dose distributions based on primary particle fluence and a dose kernel is made (Brady & Yaeger, 2013, p. 158). By the modelling on the basis of narrow beams with Gaussian profiles an approximation of multiple scattering of protons can be obtained. The dose distribution for beams of greater cross-sectional area and irregular shape is yielded by superpositing (or convoluting) these elementary beams. In comparison with the ray-tracing approach improved results can be gained using the pencil-beam method. Furthermore, those frequently bear resemblance to values computed with Monte-Carlo simulation (Mayles, Nahum, & Rosenwald, 2007, p. 1020). In the third category computer simulations of particle transport and energy deposition in patient geometry are used as a basis for dose distribution calculations (Brady & Yaeger, 2013, p. 158). The Monte-Carlo technique provides the possibility to compute dose distributions in the presence of heterogeneities more accurately. This is due to the modeling of elementary interactions and the following combination of the *histories* of a large number of particles. However, for achieving full accuracy some requirements have to be met: powerful computational capabilities, a good knowledge of the proton interactions and some means of

[27] The *water-equivalent path length* (WEPL) or just *equivalent path length* is the distance that is equivalent to that measured in water. It is usually calculated as the product of the distance in the considered materials and the ratio of electron density of the materials to that of water (Brady & Yaeger, 2013, p. 224).

[28] The *Hounsfield unit* (HU) is calculated from the linear absorption coefficient μ and measure of density. It is a relative absorption coefficient. The reference value is water (0 HU) (definition according to (Reiser, Kuhn, & Debus, 2004, p. 78)).

[29] The *effective* or *radiological depth* to a calculation point *P* is the thickness of water-equivalent tissue that would attenuate the radiation by the same amount as the actual tissue along a fan line between the surface and point *P* (definition according to (Mayles, Nahum, & Rosenwald, 2007, p. 564).

assigning tissue-composition data to the patient images acquired from the usual methods (e.g. CT scanning) (Mayles, Nahum, & Rosenwald, 2007, p. 1020).

Monte Carlo simulations

As Monte Carlo simulations were used to calculate all dose distributions presented in this work a closer description of this dose calculation algorithm follows.
The simulation of the radiation transport and energy deposition of individual particles which follow the fundamental laws of physics makes this dose calculation method theoretically to the most complete and rigorous one. As a matter of fact, electronic disequilibrium at medium interfaces and in tissue heterogeneities plus particle backscattering from dense materials like teeth, bones and metal prostheses in a patient are only taken into consideration by this method.

When calculating dose with Monte Carlo a computer program is used for the simulation of transport and interaction of individual particles in a patient. It samples randomly from probability distribution functions which govern the underlying physical processes. A reconstruction of the patient´s geometry is done on the basis of CT data with different biological media and mass densities. Tallying the ionization events that rise the energy deposition in individual calculation voxels enables the calculation of the dose distribution. For the obtainment of statistically meaningful dose distributions, the simulation needs to include a huge number ($>10^8$) of particles for a radiation treatment. This goes hand in hand with long CPU times.

The phase-space information (i.e., the angle, position, and energy) of the radiation particles has to be known precisely in order to compute dose accurately with Monte Carlo. One can either directly simulate the radiation beams from the clinical accelerator or use source models with parameter derived from measurements or Monte Carlo simulated phase space data to accomplish this. It is possible to directly simulate patient-specific beam modifiers like wedges, blocks, and multileaf collimators in the patient dose computation. By doing so their attenuation and scattering effects are accounted for (Brady & Yaeger, 2013, p. 164).

1.5.1.3 Dose optimization and biological modelling

TPSs provide optimization routines which vary in their degree of complexity. They often make use of *inverse planning*, a type of planning often used for IMPT[30], in which the dosimetric goals of the planning are stated initially and the planning system then automatically generates the plan that *best* (or at least adequately) satisfies the stated goals (definition according to (IAEA, Technical Reports NO. 430 - Commissioning and Quality Assurance of Computerized Planning Systems for Radiation Treatment of Cancer, 2004, p. 274)). A modification of beam weights[31] and geometry can be done by algorithms as well as a modulation of beam intensity in order to reach satisfaction of the user criteria. It is possible to specify these criteria as minimum, respectively, maximum doses to targets, respectively, critical structures or base them on a number of discrete points. The use of DVHs in optimization routines enables a specification of the required dose criteria for a variety of volumes. An incorporation of total prescription dose as well as fractionation information is feasible.
Commonly, two different optimization methods for treatment planning are used in proton therapy – *single-field optimization* (SFO) and *multifield optimization* (MFO). In SFO, spots from all proton fields are optimized individually. The created dose distribution from each beam has a greater uniformity than in the case of MFO. MFO optimizes the spots of all proton fields together.

[30] *Intensity-Modulated Proton Therapy (IMPT)* is a technique that allows for three-dimensional dose conformity to a target volume using protons through pencil-beam scanning with dynamic control and optimization of the beam energy and intensity throughout the scan (definition according to (Brady & Yaeger, 2013, p. 384)).
[31] The *beam weight* is the dose (relative or absolute) defined at each individual beam's normalization point under given conditions. (Note that in some TPSs, *beam weight* is only a relative strength and is not defined as precisely as this definition.) (definition according to (IAEA, Technical Reports NO. 430 - Commissioning and Quality Assurance of Computerized Planning Systems for Radiation Treatment of Cancer, 2004, p. 271)).

As a consequence in the dose from each individual field a high inhomogeneity, with large gradients outside as well as inside the targets, can occur (definition according to (Quan, et al., 2013)).

The modelling of distributions on the basis of not just dose but also on biological effects is of greater relevance for clinical use. Distributions of that kind assist to predict the *tumor control probability* (TCP) and also of the *normal tissue complication probability* (NTCP). An allowance of specific organ dose response is achievable using these algorithms. They can also help to assess dose fractionation and volume effects. The incorporation of patient specific data in the biological model can be an aid in predicting individual dose response (IAEA, Radiation Oncology Physics: A Handbook for Teachers and Students, 2005, p. 396).

1.5.1.4 Target volume definition

A description and visualization (*Fig. 1*) of anatomic volumes relating to the tumor which are of interest follows.

The g*ross tumor volume* (GTV) is the volume that includes palpable, visible, or demonstrable extent of a tumor. It may consist of the primary tumor, metastatic disease, or lymphadenopathy. The GTV usually represents the part of the malignant growth where the tumor cell density is the largest (definition according to (Brady & Yaeger, 2013, p. 304)).

The *clinical target volume* (CTV) includes the GTV as well as the regions of direct, local subclinical spread of disease that must be treated. The CTV often has a high tumor cell density nearest the GTV with decreasing density toward the periphery. The CTV volumes may not contain demonstrable tumor but are considered at risk, such as regional lymph nodes and their volumes, for subclinical spread (definition according to (Brady & Yaeger, 2013, p. 125)).

The *internal target volume* (ITV) consists of an internal margin added to the CTV to compensate for internal physiologic movement and variations in size, shape, and position of the CTV (Brady & Yaeger, 2013, p. 385)).

The *planning target volume* (PTV) includes the GTV, the CTV, and a margin to account for setup error, movement, and any possible geometric variations.

The PTV is the volume that includes the CTV with any ITV (if present) as well as a setup margin to account for patient movement and daily setup uncertainties (definition according to (Brady & Yaeger, 2013, p. 625)).

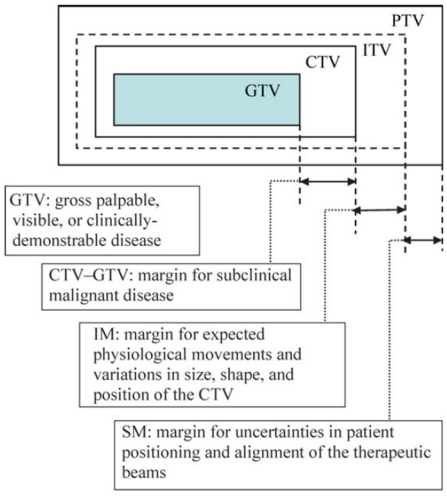

***Fig.** 7: Illustration of the volumes and margins relating to the definition of the target volume. (ICRU, International Commission on Radiation Units and Measurements, 2007, p. 84)*

1.5.1.5 Dose evaluation of treatment plans – Dose volume analysis

A *dose-volume histogram* (DVH) [respectively a *LET_d-volume histogram* (LET_dVH)] is a histogram showing the number of voxels (i.e. volume or relative volume) of a structure that receives a given dose [respectively LET_d] (definition according to (IAEA, Technical Reports NO. 430 - Commissioning and Quality Assurance of Computerized Planning Systems for Radiation Treatment of Cancer, 2004, p. 273)). There are three general types of DVHs, respectively, LET_dVHs, namely, *direct*, *cumulative* and *differential* DVHs, respectively, LET_dVHs (*Fig. 8*).
The *direct DVH* is the most basic DVH: a frequency plot of the number of voxels receiving the dose specified in each dose bin (definition according to (IAEA, Technical Reports NO. 430 - Commissioning and Quality Assurance of Computerized Planning Systems for Radiation Treatment of Cancer, 2004, p. 273)).

If one integrates the direct DVH one gets the *cumulative DVH*: each point on the cumulative DVH gives the volume of the structure that receives at least the specified dose (definition according to (IAEA, Technical Reports NO. 430 - Commissioning and Quality Assurance of Computerized Planning Systems for Radiation Treatment of Cancer, 2004, p. 273)). When starting at the highest dose bin, there is an accumulation of the volume towards zero dose. At last 100% of the total volume is reached. Even tough in general, the expression of volumes as a percentage of the total volume is common, in some cases the absolute volume might be more applicable. (Brady & Yaeger, 2013, p. 166)

The differential DVH is like the direct DVH, but the y axis (volume) values are divided by the dose bin size, in order to make the differential DVH independent of the dose bin size used for the histogram (definition according to (IAEA, Technical Reports NO. 430 - Commissioning and Quality Assurance of Computerized Planning Systems for Radiation Treatment of Cancer, 2004, p. 273)).

The use of DVHs in course of the treatment planning process helps to verify the dose´s adequacy and uniformity throughout the target volume, and the extent. Moreover, one can check the value of any hot spots in neighboring normal tissue. If structures and target volumes are specifically identified, it is possible to use them as a method to compare different treatment plans on a single graph (Mayles, Nahum, & Rosenwald, 2007, p. 722).

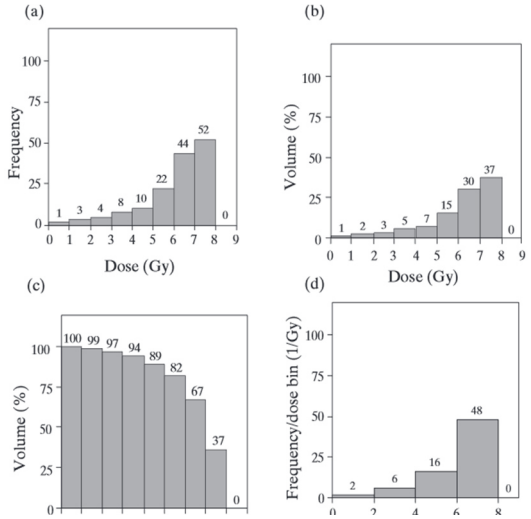

Fig. 8: *Four different DVH displays for the same dose distribution and structure.*
(a) Direct DVH (number of voxels versus dose).
(b) Direct DVH (per cent volume of structures).
(c) Cumulative DVH.
(d) Differential DVH (frequency/dose bin)
(IAEA, Technical Reports NO. 430 - Commissioning and Quality Assurance of Computerized Planning Systems for Radiation Treatment of Cancer, 2004, p. 39)

1.5.2 Patient setup

In proton beam therapy a precision and reproducibility of the patient set-up in the order of millimeters or less has to be ensured. The consideration of at least four issues is inevitable for achieving this:

Firstly, it has to be guaranteed that the patient is set up according to the treatment plan. Therefore the specification of position has to be provided by the *treatment planning system*. In practice anatomical reference marks, external fiducials which have a fixed link with the target volume, into internal structures inserted markers or implanted steel or gold marker seeds find application.

Secondly, the aim of the patient immobilization is to guarantee a nearly perfect reproducibility between the acquisition of the CT scan and each treatment session. Intrafraction movements are supposed to be minimized. Masks, foam molds, carbon fiber supports and orthopedic devices provide the basis for current systems.

Thirdly, the identification of the reference fiducials at each treatment session has to be ensured by the *system of verification of patient positioning*. Anatomical structures or reference marks are fast and reliably identified by radiological systems in the treatment room. By comparing their established position in space with the planned positions it is feasible to calculate corrections required for patient repositioning.

Fourthly, there should be a possibility to execute corrections to the position of the patient with high precision. This must be enabled by the *patient positioning system* which sometimes uses robotic concepts. (Mayles, Nahum, & Rosenwald, 2007, p. 1022)

1.6 Study outline

The linear energy transfer (LET) of monoenergetic proton beams used in therapy is relatively low and nearly constant. Just near the end of the beam´s range a significantly increase occurs. The maximum value is reached in proximity to the proton track-ends. In vitro cell survival experiments report an increase of relative biological effectiveness (RBE) towards the end of range. Assumptions are made that the rise of RBE might be caused by the risen LET. The variation of available cell survival data is substantial. However, in general one suggests an elevated proton RBE with an elevated LET, decreasing fractionation dose, and decreasing α/β of the tissue. Different RBE models predict the same correlations. Without taking this into consideration, clinical proton therapy still weights the physical dose with the generic RBE value of 1.1 to obtain the RBE-weighted dose used for treatment planning and delivery. Ignoring the increased RBE with increasing LET goes hand in hand with overlooking the extended biological range of about 0.8% of the proton range in current clinical operation. An increase of the risk of harmful effects to normal tissue might be a negative outcome of underestimating the RBE. The scientific and clinical proton community debates whether an incorporation in treatment planning and evaluation is necessary, and how the increased RBE can be incorporated, at present. At that point it takes a closer look at intensity modulated proton therapy (IMPT). Highly inhomogeneous dose and LET distributions may occur in this case. Undesired LET hot-spots in critical structures might be unwanted results. These hotspots might cause an increase of the normal tissue complication probability (NTCP)[32] due to the enhanced RBE. Without any doubt, every effort should be made to avoid or reduce such LET hotspots. At the same time the desired tumor control probability

[32] The *Normal Tissue Complication Probability* (NTCP) is defined as the probability that a given dose of radiation will cause an organ or structure to experience complications considering the specific biological cells of the organ or structure. The NTCP is used in treatment planning as a tool to differentiate among treatment plans.
It can also be defined as a dose-dependent mathematical model to gauge the probability of dose-induced complications in noncancerous tissue (definition according to (Brady & Yaeger, 2013, p. 560).

(TCP)[33] should be maintained. Consequently, a compromise of the physical target dose should be avoided, also considering RBE uncertainties and discrepancies between RBE models. The emerging difficult optimization problem might only be solvable by introducing additional objective functions to traditional dose objectives and selecting appropriate beam angles. Using just one single model for a direct optimization of the RBE-weighted dose (D_{RBE}) brings with it insecurity accounted for by the shortage of in vivo RBE data and RBE uncertainties. Therefore, a physical dose reoptimization on the basis of LET distribution and an implementation of different LET optimization strategies is suggested to allow a reduction of LET in critical structures. In order to reduce LET in critical structures those optimization strategies aim to shift stopping protons from regions of the target margins which are neighbored by critical structures toward areas in the center of the target or target margins which do not have critical structures in their proximity. The goal is a lowering of LET and RBE in critical structures, whereby the target coverage shall stay the same. In the event of mixed particle fields, it is suggested to look at the dose-averaged LET (LET_d) over the entire particle spectrum (Traneus & Ödén, 2018).
Before introducing LET_d optimization strategies an investigation of various LET_d-distributions to water based on different planning parameters and tumor localizations may be appropriate. As a first step a benchmark has to be done to gain a validated treatment planning system for further investigations. For this purpose LET_d distributions calculated with GATE8.0/Geant4.10.3 were used as a benchmark data[34] to compare with simulations done by a research version of the TPS RayStation (RS v5.99.50). Longitudinal LET_d profiles for two boxes centered at different depths and for a pencil beam were analyzed. Afterwards, the now validated treatment planning system RS v5.99.50 was used to first have a look at the dependency on the dose grid´s voxel size (results where again benchmarked against GATE8.0/Geant4.10.3) and then evaluate LET_d distributions resulting from three different target depths, three different target sizes, nineteen different angles (angles from 0° to 180°) separating two SFO[35] beams as well as beam numbers of one to ten with Monte Carlo (MC) simulations. The angular dependence of LET_d distributions was additionally determined for one clinical case – a pediatric head tumor. Finally, one- and two-field plans were generated for five clinical cases (two pediatric head tumors, one superficial tumor, one pediatric Ewing tumor and one pediatric ependymoma) and for the spherical phantom in RayStation using different optimization strategies. The effect of using two beams instead of one, varying the number of distal energy layers, limiting of maximum spot weights and the combination of both strategies in single field plans was tested. In the case of two-field plans SFO was compared with MFO for two (almost) orthogonally arranged beams. The different optimization settings were also applied to a spherical phantom. To gain an impression of the impact the difference in LET_d might have on the RBE the Wedenberg et al. model (see section *1.3.4 RBE Models*) was used.

1.7 MedAustron light ion beam therapy facility

MedAustron is a particle therapy center in Wiener Neustadt located in the country of Lower Austria (Austria). Since proton as well as carbon ion beams can be used for treatment as well as for clinical and non-clinical research it is a dual-particle facility. Its clinical operation using protons started in December 2016. In summer 2019 carbon ions were applied for the first time. At full operation up to 1000 patients are planned to be treated per year (Stock, Georg, Mayer, Böhlen, & Vatnitsky, 2015). At MedAustron three irradiation rooms, which are equipped with one horizontal beam line (H), one horizontal and one vertical beam line (H+V) and with a proton Gantry, which makes an irradiation from various angles possible, are available for patient treatment. In a separate room a horizontal beam line (H) can be used for non-clinical research. A

[33] The *Tumor Control Probability* (TCP) is defined as the probability that a given dose of radiation will provide tumor control or eradication considering the specific biological cells of the tumor. The "TCP" is used in treatment planning as a tool to differentiate among treatment plans (definition according to (Brady & Yaeger, 2013, p. 922)).
[34] A *benchmark data* is a standard data, carefully measured or carefully calculated, which can be used for testing a dose calculation algorithm (definition according to (IAEA, International Atomic Energy Agency, 2004, p. 271)).
[35] *SFO* stands for single-field optimization. A more detailed description will follow in section *1.5.1.4* .

synchrotron is used for the particles´ acceleration. Proton energies ranging from 62 to 252 MeV as well as carbon energies between 120 and 402 MeV/u are deployable. Non-clinically, proton energies up to 800 MeV are possible.

For the delivering of the particle beams the so-called active pencil-beam scanning method (PBS)[36] is used. Fast scanning magnets enable the scanning of the beam over the tumor volume orthogonal to the direction of the incident beam. The maximum area covered by the scanning field has a size of 200 x 200 mm^2 or 120 x 200 m^2 depending on the beam line. Irradiation of large size tumors is realized by field matching[37]. An adaption of the penetration depth from spill to spill is obtained by a change of the synchrotron´s extraction energy. Depth´s with protons from about 3 to 38 cm in human tissue are achievable. To date, beam´s diameters of 4 mm and 6 mm (size in vacuum) can be chosen for protons and carbons, respectively. It is possible to position the beam with an accuracy of ±0.5 mm.
The amount of applied dose must conform to the prescription. For this reason an online monitoring and controlling of beam parameters, like beam intensity, position and size, during the whole treatment procedure is indispensable. If these parameters deviate from their nominal values the beam is switched off. This action lasts less than 1 ms and ensures the patient´s security (Koschik, Osmić, Urschütz, & Benedikt, 2014).

Fig. 9: *3D model of the MedAustron facility. The ion sources, the linear accelerator, the synchrotron as well as the irradiation rooms are shown. On the left side additional building parts for the medical, technical and research areas are located.*
(Stock, et al., 2018)

[36] *Pencil-beam scanning* (PBS) is a technique that uses magnets to sweep a narrow proton pencil-beam and allows precise three-dimensional dose deposition. Both the intensity and energy of the protons can be modified throughout the scan (definition according to (Brady & Yaeger, 2013, p. 612)).
[37] *Match fields* are two or more fields in which their lateral edges abut to make a uniform dose profile across the junction (definition according to (Moyers & Vatnitsky, 2012, p. 505)).

2 MATERIALS AND METHODS

2.1 Research TPS – RS v5.99.50

At MedAustron the treatment planning system RayStation is in use. Computations in the course of this master thesis were done with version RS v5.99.50. This version is an evaluation version of the software where additional non-clinical features are available, like LET_t and LET_d scoring amongst many others, e.g. computation of detector sensitivity for alanine and TLDs.

RayStation enables to create treatment plans for Pencil Beam Scanning (PBS). For calculating the dose distributions the user can choose between a Pencil Beam[38] and a Monte Carlo algorithm. A positive aspect of the Pencil Beam dose calculation is its shorter calculation time when compared with Monte Carlo, nevertheless, its accuracy is reduced (RAYSTATION 6 - Reference Manual, 2016, p. 121). For all calculations presented in this master thesis the Monte Carlo dose engine was used.

2.1.1 Machine model parameters

Geometrical respectively material properties of the machine, so-called machine parameters, as well as beam model parameters are part of the machine model parameters in RayStation. Before being able to compute doses, an adjustment of different beam model[39] parameters to the specific treatment machine in use at the clinic is necessary. The beam model parameters include effective energy spectrum, spatial-angular distribution moments at the isocenter, dose monitor detector sensitivity and the effective focal points of the scanning magnets [40] (RAYSTATION 6 - Reference Manual, 2016, p. 125).

In RayStation an application is provided called RayPhysics. It enables to view and edit the machine parameters for all machines used for the computations. There is also the possibility for importing and exporting measurements, performing auto-modeling of the machine as well as for computing dose and comparing to measurements. For commissioning of proton machine models, however, the uncommissioned machine with all measurements and relevant machine parameters always needs to be sent to RaySearch Laboratories where the final commissioning is performed (RAYSTATION 6 - RayPhysics Manual, 2016, S. 11).

RaySearch Laboratories performs the beam modeling process for carbon ion treatment beams and provides the machine models to the customer (RAYSTATION 6 - Reference Manual, 2016, p. 179).

2.1.2 Scoring of dose

For each voxel, a calculation of the dose is performed in its center. The dose in the whole voxel is equated with the computed value. RayStation gives dose as dose-to-water (RAYSTATION 6 - Reference Manual, 2016, p. 135).For all calculated doses as well as LET_d values shown in this master thesis found the Monte Carlo dose engine v4.0 of the TPS RayStation v5.99.50.10 application.

[38] The *pencil beam dose algorithm* is based on a decomposition of the proton fluence into a large number of mini-beams, so-called *pencil-beams, laying close to each other* (RAYSTATION 6 - Reference Manual, 2016, p. 128).

[39] The *beam model* is the conceptual model used to create the dose distribution for a beam. The beam model is the basis for the algorithm that is coded into the software used for dose calculations (definition according (IAEA, Technical Reports NO. 430 - Commissioning and Quality Assurance of Computerized Planning Systems for Radiation Treatment of Cancer, 2004, p. 271)).

[40] For a more detailed description see (RAYSTATION 6 - Reference Manual, 2016, pp. 123-124).

2.1.3 Plan design – planning parameters

The planning system enables the user to decide on the dose grid in which the dose distribution is calculated. An editing of both the *Resolution* (dedicated in cm/voxel) and the *Grid* size is allowed (RAYSTATION 6 - User Manual, 2016, p. 302).

In order to create a proton treatment plan some **plan** and **beam computation settings** have to be specified by the user. Those are used as input for the plan computation. A description of the parameters which are relevant for this master thesis follows.

The *Air gap* is the prescribed minimum distance (*Gap*) between the most downstream object in the beam line and the patient outline. (RAYSTATION 6 - User Manual, 2016, p. 477)

The *Energy layer spacing* determines the longitudinal distance between the Bragg peaks. The user can set this parameter either to a *Constant* value displayed in cm water or use the *Automatic with scale* option. If the latter setting is selected a variable distance depending on the Bragg peak width is employed. In this case the energy separation between two adjacent energy layers it is equivalent to the energy loss over the width (80% dose level) of the most distal Bragg peak in the pair. A scaling factor of 1 implies that each Bragg peak intersects the following Bragg peak at about 80% of the dose maximum. A smaller scaling factor is accompanied by a decrease of distance.

The *Spot spacing* defines the lateral distance between two neighboring spots at the same energy layer. It is again possible to set this parameter to a *Constant* value (in cm) or to *Automatic with scale*. Choosing the second option means that the distance varies according to the radial spread in the Bragg peak for a specific energy. The user chooses a scaling factor which is multiplied by 1.06 times the projected sigma to get the spot distance. A variation of the spot distance between different energy layers is possible, within an energy layer impossible. The larger the scaling factor value the larger the spot distance.

There is the possibility of setting target margins during spot selection: One can select a number of *Proximal* and *Distal* energy layers which are added as a proximal respectively distal target

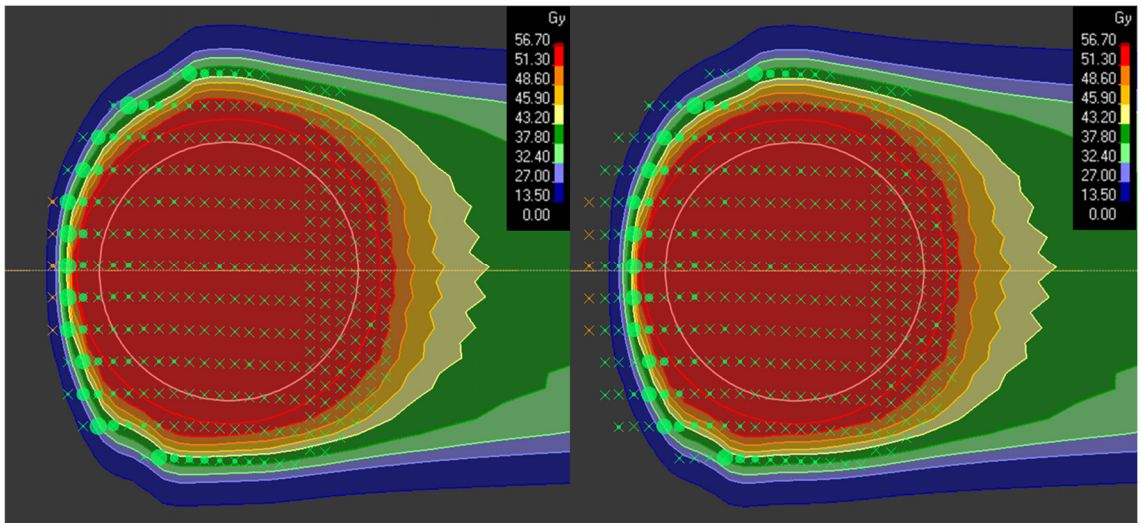

Fig. 10: *Visualization of one (picture on the left) versus three (picture on the right) distal energy layers. The positions of the individual Bragg peaks are displayed as crosses. The larger the dot on the cross, the higher the spot weight. Either one or three energy layers are placed after the energy layer with the highest spot weights at the distal edge of the target.*

margin (*Fig. 10*). The *Lateral* target margin can be either specified by selecting the *Automatic with scale* or the *Constant* option. Choosing the first one results in the determination of the lateral target margin as a function of the average spot size at the Bragg peak maximum for the highest energy. If the second one is applied a specification of the lateral margin in cm is feasible.

The user cannot only define the just described beam computation settings but also **optimization settings**.

Three different options for computing the dose are available: *Approximate PB*, if this is checked an approximate dose with the pencil beam dose engine is computed, *Clinical PB*, its selection results in the computation of a clinical dose with the pencil beam dose engine and *Monte Carlo*, in this option a dose is computed with the Monte Carlo dose engine. Selection of the option *Monte Carlo* allows to set the mean number of ions (number of Monte Carlo histories) per spot (*Ions/Spot*) or the statistical uncertainty in % (*uncert [%]*). Whenever it is set to compute to a certain statistical uncertainty, the dose computation proceeds until the required statistical uncertainty is achieved. The Monte Carlo dose engine is used for optimization, the result is always an approximate dose. It is considered *clinical* after final dose computation with the statistical uncertainty per beam lower than the threshold for clinical dose set in *Clinic Settings*.

Another parameter in the optimization settings which can be edited is the *Optimization tolerance*. When the change in objective value is less than this tolerance level the software stops the optimization. Its value should be about $1 \cdot 10^{-5}$ or $1 \cdot 10^{-6}$.

In the usual case an optimal solution is found by the optimization algorithm in 25 to 100 iterations. If the result is already satisfying prior to this or whenever there is the belief that the objectives will not be met it is possible to set a *Maximal number of iterations*.

After the optimization is finished it is possible to calculate a final dose.

It is feasible to specify a number of *Iterations before spot filtering*. A filtering of all spots with a weight below the minimum spot weight limit takes place after the defined number of iterations. When setting this value to 0 no removing of any spots is performed.

The parameters *Min spot weight* and *Max spot weight* (specified in MU/fx[41]) indicate the limits used when filtering out low respectively high weight spots. Adding a *Spot weight limit margin* (specified in %) allows to do not make the plan undeliverable despite the occurrence of some smaller modification of spot weights after optimization. Thus, it can be avoided to generate plans that violate the minimum spot weight constraints of the dose delivery system after normalization of the dose resulting from the optimization to the prescribed dose (RAYSTATION 6 - User Manual, 2016, pp. 555-560).

2.1.4 LET calculation

RS 5.99 calculates LET_d distributions according to *Equation 25*.

$$LET_d(z) = \frac{\int_0^\infty {S_{el}}^2(E)\phi(E,z)dE}{\int_0^\infty S_{el}(E)\phi(E,z)dE}$$

Equation 25

Whereby the stopping power S is calculated according to the Bethe-Bloch formula omitting the shell and density correction terms. Those two terms are important only for energies obviously higher or lower than those of interest for therapeutic protons.

[41] *MU* is the abbreviation for *monitor unit*. It is a measure of radiation *beam-on time* used for medical accelerators. One monitor unit is by convention equivalent to 1 cGy of absorbed dose in water under specific calibration conditions for the medical accelerators (definition according to (Brady & Yaeger, 2013, p. 515)).
Fx stands for fraction.

The used Bethe-Bloch formula for computation of the stopping power is then as follows:

$$S = \rho \frac{a_1}{\beta^2}\left[a_2 - ln\left(\frac{1}{\beta^2} - 1\right) - \beta^2\right]$$

$$\beta^2 = 1 - \left(1 + \frac{E}{m_p c^2}\right)^{-2}$$

Equation 26

with

$$a_1 = \frac{\kappa}{u}\sum_i w_i \frac{Z_i}{A_i}$$

$$a_2 = ln\frac{2m_e c^2}{I}$$

$$\kappa = \frac{4\pi e^4}{m_e c^2}$$

Equation 27

Where E is the *kinetic energy* of the protons, Z_i, w_i, and A_i the elemental composition, in atomic number, weight and mass, respectively, ρ and I the mass density, and mean ionization energy of the medium, u the atomic mass unit, c the speed of light, m_e and m_p the electron and proton masses, and e the elementary charge (RAYSTATION 6 - Reference Manual, 2016, p. 124).

2.1.5 Plan optimization

RayStation enables the generation of optimized proton plans for the Pencil Beam Scanning (PBS) treatment technique with respect to treatment objectives and constraints defined by the user. A hexagonal spot pattern with optimized spot weights is the outcome for a PBS plan (RAYSTATION 6 - User Manual, 2016, p. 544).

An objective function that is to be minimized and optionally a number of constraints are the components of the optimization problem. In cases where the fulfillment of a requirement is mandatory a constraint can be used. In the optimal solution the best value of the objective function is given and at the same time no constraints are violated.

The specification of optimization functions as either part of the objective function or used as individual constraints is done by the user. Weights are assigned to the optimization functions included in the objective function based on their relative importance. Typically an objective function or constraint affects the total dose of the beam set (RAYSTATION 6 - User Manual, 2016, pp. 503-506).

2.2 Validation of RS v5.99.50

In order to ensure the correctness of the algorithm performance, LET_d to water distributions computed using the Monte Carlo (MC) method in the TPS RayStation (RS v5.99.50) were benchmarked against GATE8.0/Geant4.10.3 MC simulations. Two plans with a target of 5x5x5 cm^3 centered at a depth of 6 and 30 cm in water and one 160 MeV pencil beam (range in water: 17.4 cm) were optimized in RS v5.99.50 and recalculated with GATE8.0/Geant4.10.3.

Different dose grids ((0.1x0.1x0.1) cm^3, (0.2x0.2x0.2) cm^3 and (0.3x0.3x0.3) cm^3) were used to investigate the voxel size dependence. LET_d distributions were extracted directly from the RS v5.99.50 software.

2.3 Analysis of LET_d distributions

2.3.1 Voxel size dependence

For the definition of the patient, respectively, phantom and problem geometry RayStation uses a dose grid (*Fig. 11*). There is a boundedness of the whole computation problem to this dose grid. The transport of radiation as well as the computation of dose is just performed inside this dose grid. One can choose a voxel grid resolution between 1 to 5 mm (RAYSTATION 6 - Reference Manual, 2016, p. 14).

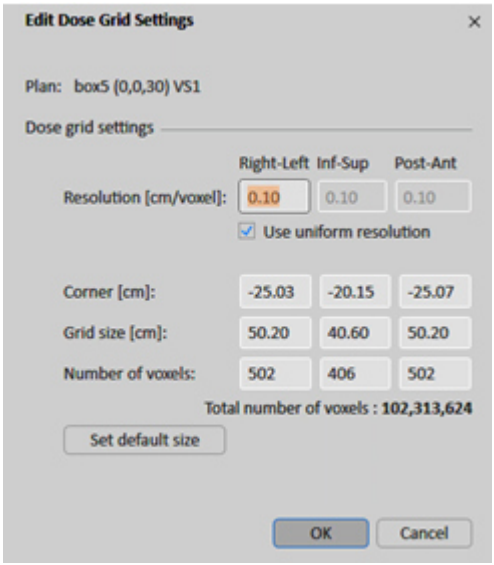

Fig. 11: *Adjusting the dose grid settings in RayStation v5.99.50*

For clinical purposes grid resolutions between 1 to 3 mm are used to avoid excessive averaging over small structures, e.g. nerves or vessels. In order to investigate the dependence on the dose grid´s voxel size a (5x5x5) cm^3 water target was centered at 6 and 30 cm depths in a water phantom (*Fig. 11*). The LET_d distributions were calculated with variable resolution of the dose grid including (0.1x0.1x0.1) cm^3, (0.2x0.2x0.2) cm^3 and (0.3x0.3x0.3) cm^3 (*Fig. 12*)[42] using two different dose calculation softwares: RS v5.99.50 and GATE8.0/Geant4.10. Afterwards lateral LET_d profiles along the central beam axis were analyzed.

For calculating LET_d gradients the following formula was used:

$$\nabla LET_d(x) \approx \frac{LET_d(x+h) - LET_d(x-h)}{2h}$$

Equation 28

where *f(x)* is the LET_d value at the actual position *x* and *h* is the step length.

[42] In the following in all figures showing dose or LET_d distributions not just the PTV but also a CTV which was created by contracting the PTV by 0.3 cm uniformly in all directions is displayed.

Relative deviations were calculated as follows:

$$Relative\ deviation[\%] = \frac{LET_d(x,y) - LET_d(x,y_0)}{LET_d(x,y_0)} \cdot 100$$

Equation 29

Where $LET_d(x,y)$ is the LET_d value at position x calculated with voxel size y. y_0 refers to the reference voxel size, in this case to the voxel size (0.1x0.1x0.1) cm^3.

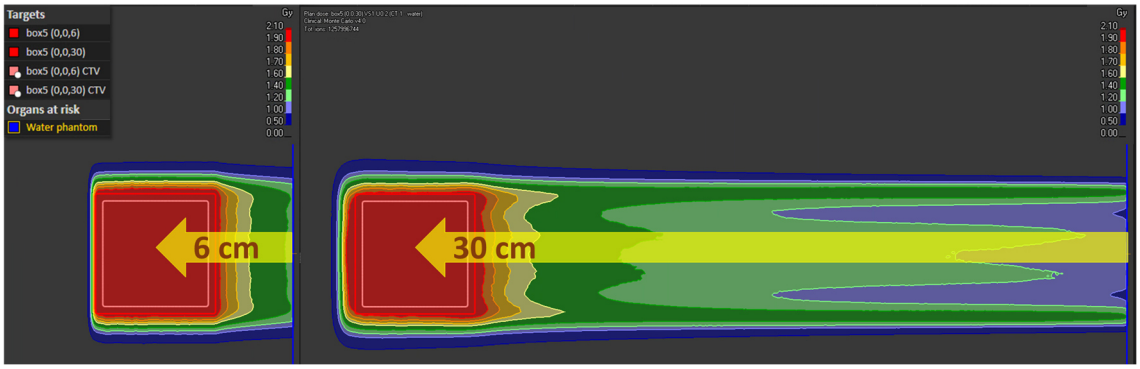

Fig. 12: *Plan design and resulting RBE-weighted dose distributions for investigating the voxel size dependence.*
A (5x5x5) cm^3 water target was centered at a depth of 6 cm (center of the target is located at a depth of 6 cm; left image) and 30 cm (center of the target is located at a depth of 30 cm, right image) in a water phantom. The beam direction is from right to left.

For all plans created with a view to investigate the voxel size dependence the prescribed dose was 2 Gy and the number of fractions was 1. Moreover, the following values for the planning parameters (for a definition see section *2.1.3 Plan design – planning parameters*) were selected: The *Gap* was *64.8 cm*, the *Energy layer spacing* was set to *Automatic with scale 1*, the *Spot Spacing* to *Automatic with scale 0.7*, the number of *Proximal* energy layers to *1*, the number of *Distal* energy layers to *1*, the *Lateral* target margin to *Constant, 0.5 cm*. For computing the doses the option *Monte Carlo* was chosen and a statistical *uncertainty* of *0.2%* respectively *0.1%*. The *Optimization tolerance* was $1.000 \cdot 10^{-5}$, the *Maximal number of iterations 40*, the *Iterations before spot filtering 20*, the *Min spot weight* $0.9000 \cdot 10^6$ *Np/fx*, the *Max spot weight* $1000.0000 \cdot 10^6$ *Np/fx* and the *Spot weight limit margin 5.0%*.

2.3.2 Angular dependence

Phantom case

Two SFO fields separated by 0° to 180° in steps of 10° for a spherical target with 4 cm diameter in the center of a cylindrical water phantom and subsequent analysis of Dose Volume Histograms (DVHs) and LET_d Volume Histograms (LET_d-VHs) in concentric rings[43] around the target enabled to study the angular dependence (*Fig. 13* and *Fig. 14*).

Calculations done in the interest of looking at the angular dependence were based on a prescribed dose of 54 Gy and a number of fractions of 30.

[43] Whenever *ring* is used in the following it denotes the geometrical structure of a shell.

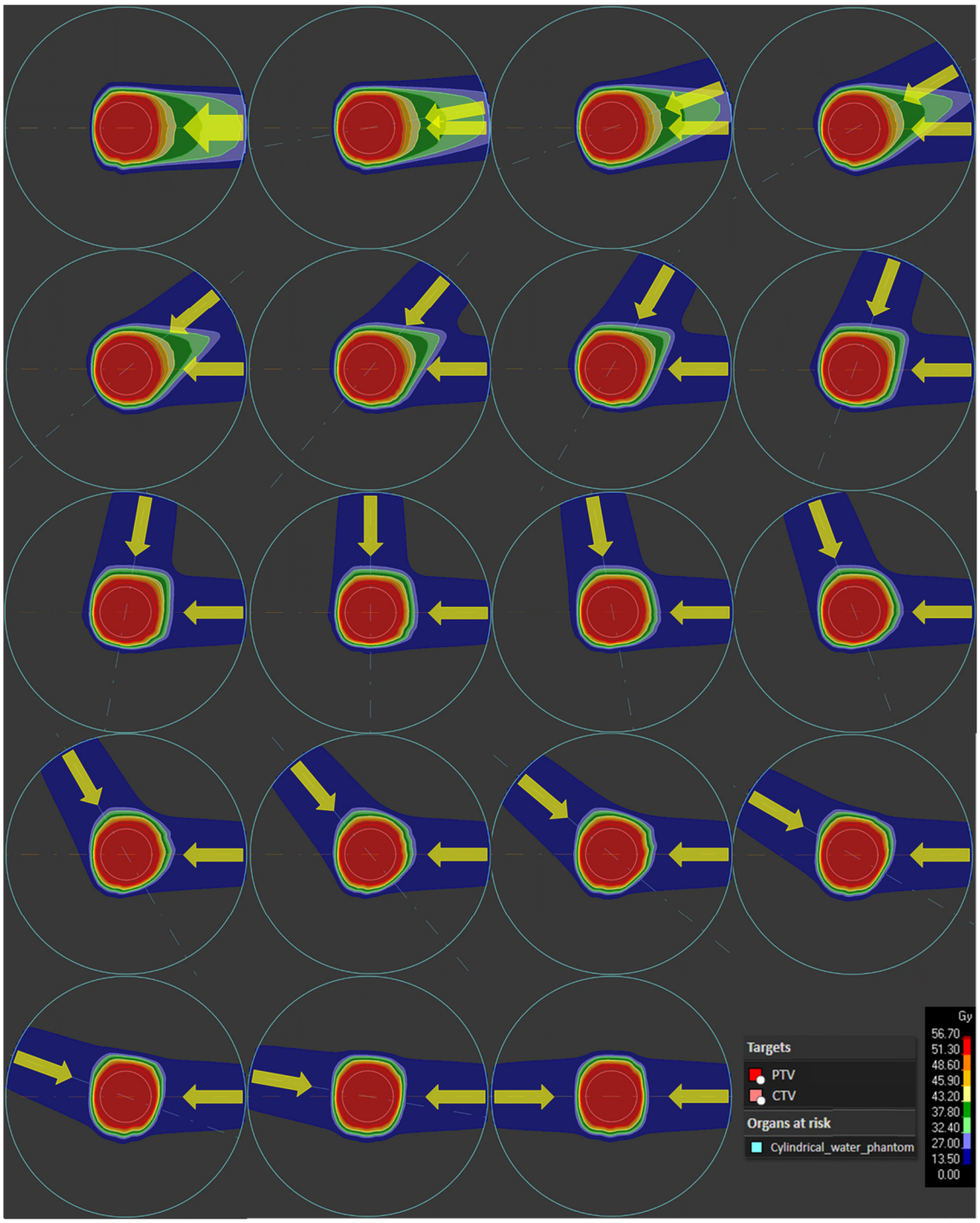

Fig. 13: *Plan design and resulting RBE-weighted dose distributions for investigating the angular dependence.*

Two SFO fields separated by an increasing angle for a spherical target with 4 cm diameter centered in a cylindrical water phantom.

The planning parameters used for investigating the angular dependence were as follows: The *Dose Grid Resolution* was *0.20 cm/voxel*, the *Gap* was *20.0 cm* The *Energy layer spacing* was *Automatic with scale 1*, the *Spot spacing* was *Automatic with scale 0.95*, the number of *Proximal* energy layers was *1*, the number of *Distal* energy layers was *1*, the *Lateral* target margin was *Constant, 0.5 cm*, the dose was computed with the *Monte Carlo* option with a statistical *uncertainty* of *0.5%*, the *Optimization tolerance* was $1.000 \cdot 10^{-5}$, the *Maximal number of iterations*

40, the *Iterations before spot filtering 20*, the *Min spot weight 0.8800·10⁶ Np/fx*, the *Max spot weight 100.0000·10⁶ Np/fx* and the *Spot weight limit margin 5.0%*.

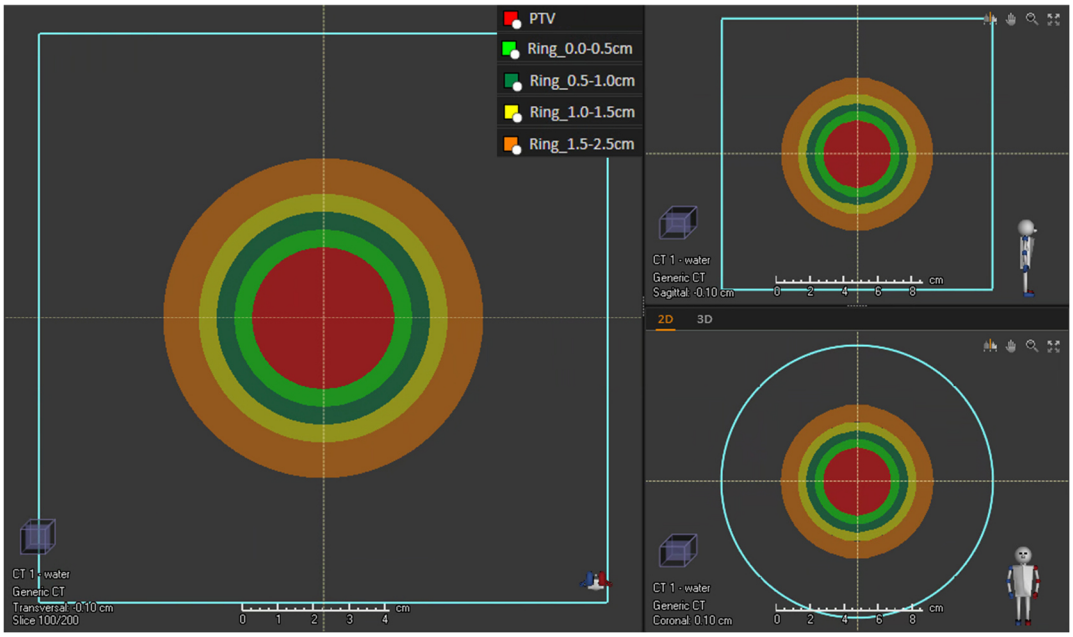

Fig. 14: *Patient, respectively, phantom modeling for investigating the angular dependence.*

The image on the left side shows the transversal, the upper image on the right side the sagittal and the lower image on the right side the coronal plane. The innermost red circle margins the PTV. In the rings around the PTV the DVHs and LET_dVHs were computed and investigated. The blue cylinder symbolizes the water phantom.

Clinical case

The impact a change of the angle separating two SFO beams has on the LET_d distributions was additionally inspected for one clinical case – a pediatric head tumor (*Fig. 15*). This patient was

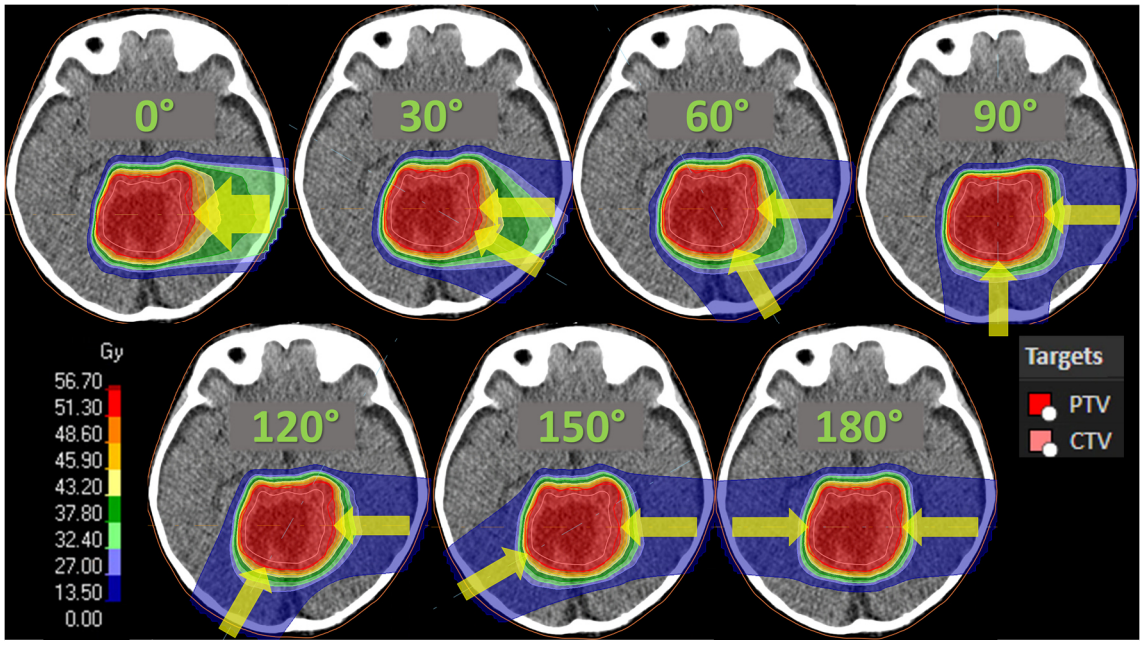

Fig. 15*: Plan design and resulting RBE-weighted dose distributions for investigating the angular dependence of a clinical case.*
Two SFO fields separated by an increasing angle for a pediatric head tumor exemplary for seven different angles.

also described in section *2.4.2 Clinical cases.* A list of the planning parameters which were used for this case can be found there.

2.3.3 Depth and field size dependence

A (2x2x2) cm^3, a (5x5x5) cm^3 and a (10x10x10) cm^3 water target were centered at 8 cm, 18 cm and 28 cm depths in a water phantom to assess depth dependence (*Fig. 16*).

In the interest of being able to make statements about the field size dependence the same settings as just stated were used. The prescribed dose for exploring the depth and field size dependence was 2 Gy and the number of fractions was 1.

For all plans which were created for examining the depth and field size dependence the planning parameters were kept constant. The *Dose Grid Resolution* was *0.20 cm/voxel*, the *Gap* was *20.0 cm*, the *Energy layer spacing* was *Automatic with scale 1*, the *Spot spacing* was *Automatic with scale 1*, the number of *Proximal* energy layers was *1*, the number of *Distal* energy layers was *1*, the *Lateral* target margin was *Automatic with scale 1*, the dose was computed with the *Monte Carlo* option with a statistical *uncertainty* of *0.5%*, the *Optimization tolerance* was $1.000 \cdot 10^{-5}$, the *Maximal number of iterations 40*, the *Iterations before spot filtering 20*, the *Min spot weight* $0.9000 \cdot 10^{6}$ *Np/fx*, the *Max spot weight* $1000.0000 \cdot 10^{6}$ *Np/fx* and the *Spot weight limit margin 5.0%*.

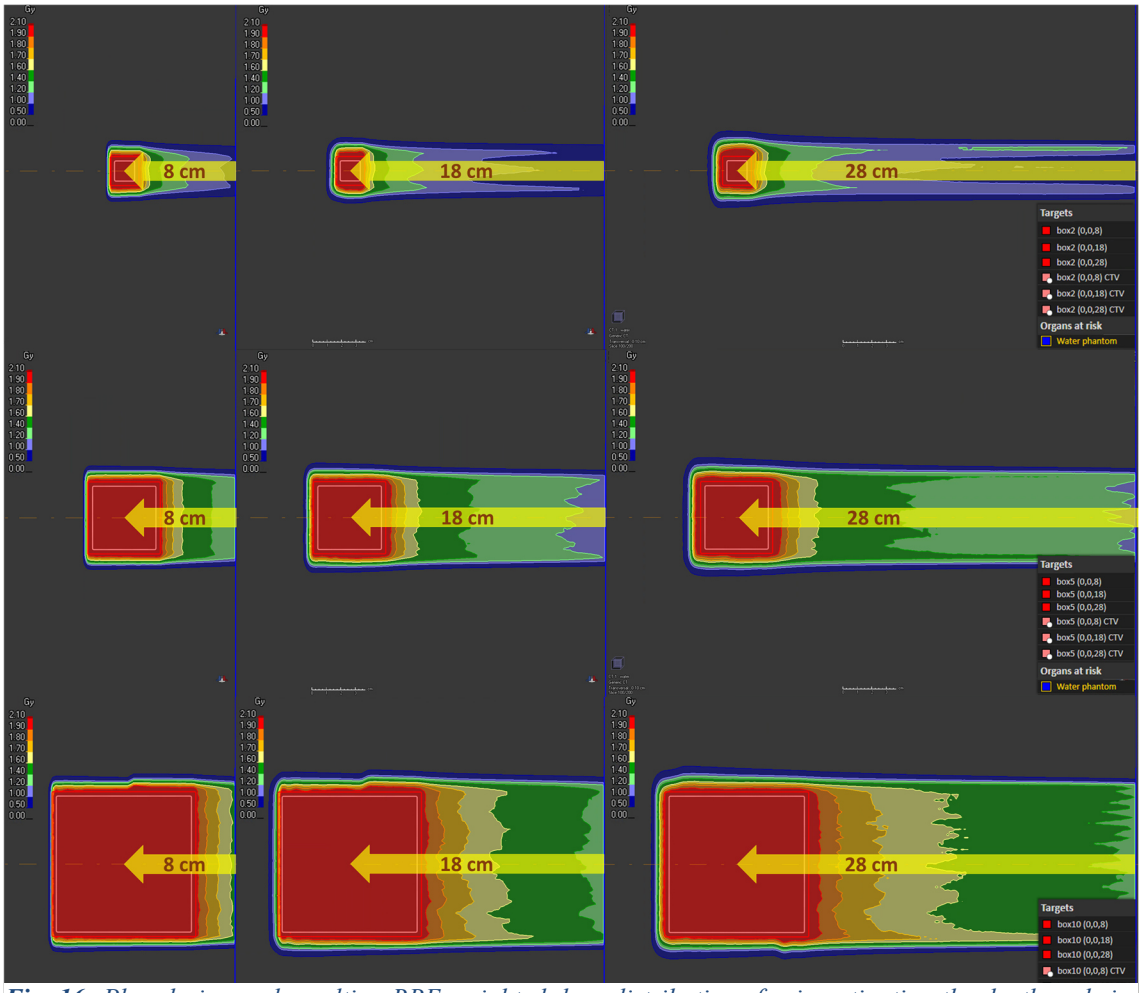

Fig. 16: *Plan design and resulting RBE-weighted dose distributions for investigating the depth and size dependence.*

A (2x2x2) cm^3 (images on the top), a (5x5x5) cm^3 (images in the middle) and a (10x10x10) cm^3 (images on the bottom) water target were centered at a depth of 8 cm (images on the left), 18 cm (images in the middle) and 28 cm (images on the right) in a water phantom. The beam direction is always from right to left.

2.3.4 Number of beams dependence

SFO plans with one to ten beams for the same target as used in section *3.2.2 Angular dependence* (a spherical target with 4 cm diameter in the center of a cylindrical water phantom) were created (*Fig. 17*). Dose Volume Histograms (DVHs) and LET_d Volume Histograms (LET_d-VHs) in concentric rings around the target were analyzed and their dependence on the number of beams was studied.

The following settings were applied: The prescribed dose was 270 Gy[44] and the number of fractions 30. The *Dose Grid Resolution* was *0.20 cm/voxel*, the *Gap* was *20.0 cm*, the *Energy layer spacing* was *Automatic with scale 1*, the *Spot spacing* was *Automatic with scale 0.95*, the number of *Proximal* energy layers was *1*, the number of *Distal* energy layers was *1*, the *Lateral* target margin was *Constant, 0,5 cm*, the dose was computed with the *Monte Carlo* option with a statistical *uncertainty* of *0.5%*, the *Optimization tolerance* was $1.000 \cdot 10^{-5}$, the *Maximal number of iterations 40*, the *Iterations before spot filtering 20*, the *Min spot weight* $0.9200 \cdot 10^{6}$ *Np/fx*, the *Max spot weight* $100.0000 \cdot 10^{6}$ *Np/fx* and the *Spot weight limit margin 5.0%*.

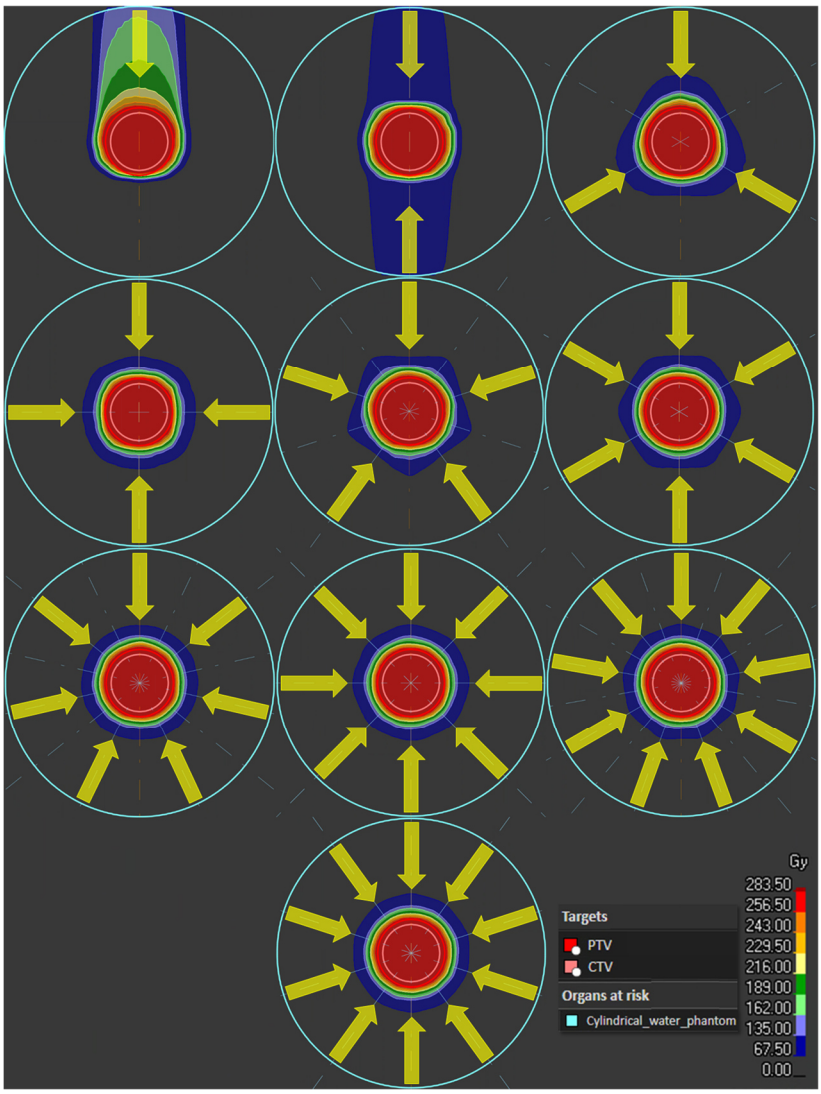

Fig. 17: *Plan design and resulting RBE-weighted dose distributions for investigating the dependence on the number of beams. The number of SFO beams for a spherical target with 4 cm diameter centered in a cylindrical water phantom was increased from one to ten. The arrows indicate the incidence angles.*

[44] An unusually high prescribed dose was used here. This had the following reason: If a lower prescribed dose had been used, the particle number per spot and beam would have come lower than the minimum particle number defined by the used machine for many spots. Those spots would have been filtered out. Consequently, it would not have been possible to achieve a homogenous dose distribution per beam inside the target.

2.4 Investigation of the influence of different optimization settings on LET_d distributions

As mentioned previously in section *2.1.3 Plan design – planning parameters* the user of the treatment planning system is able to adjust a series of planning parameters. One aim of the present master thesis was to modify some of those parameters while keeping the others constant and investigating the resulting change in the LET_d distributions in the target as well as in the areas around it. Not just the phantom case, but also five clinical patients were examined.

Plans with one and three distal energy layers, with and without maximum spot weight limitation, with one and two beams and using either SFO or MFO were generated. In *Table 1* all different combinations as well as the respective abbreviations used in this master thesis are listed.

***Table 1**: Specifications and abbreviations of plans generated for investigating the influence of different optimization settings.*

Abbreviation	Optimization method	Maximum spot weight limitation	Number of beams	Number of distal energy layers
SFO_1_1	SFO	No	1	1
SFO_L_1_1	SFO	Yes	1	1
SFO_1_3	SFO	No	1	3
SFO_L_1_3	SFO	Yes	1	3
SFO_2_1	SFO	No	2	1
SFO_L_2_1	SFO	Yes	2	1
SFO_2_3	SFO	No	2	3
SFO_L_2_3	SFO	Yes	2	3
MFO_1	MFO	No	2	1
MFO_L_1	MFO	Yes	2	1
MFO_3	MFO	No	2	3
MFO_L_3	MFO	Yes	2	3

The approach for investigating the different optimization settings was always as follows: First the SFO_1_1, the SFO_2_1 and the MFO_1 plan were created in a way that their PTV and brain DVHs looked as similar as possible. To obtain the SFO_1_3, SFO_2_3 and MFO_3 plans just the number of distal energy layers for each beam was changed from one to three. For all plans with a maximum spot weight limitation the respective plan without a maximum spot weight limitation functioned as initial plan. The parameter *Max spot weight* was reduced as far as possible to not loose coverage of the PTV. It was ensured that neither the PTV DVH nor the dose to 98% of the PTV changed visibly. For the phantom case not only the impact of maximum but also of minimum spot weight limitation was analyzed. The abbreviations used for the corresponding plans include *_MaxL_MinL_* (e.g. *SFO_MaxL_MinL_1_1* stands for a *SFO_1_1* plan with maximum and minimum spot weight limitation). *Fig. 18* shows the values obtained for *Max* respectively *Min spot weight* for all clinical and phantom plans.

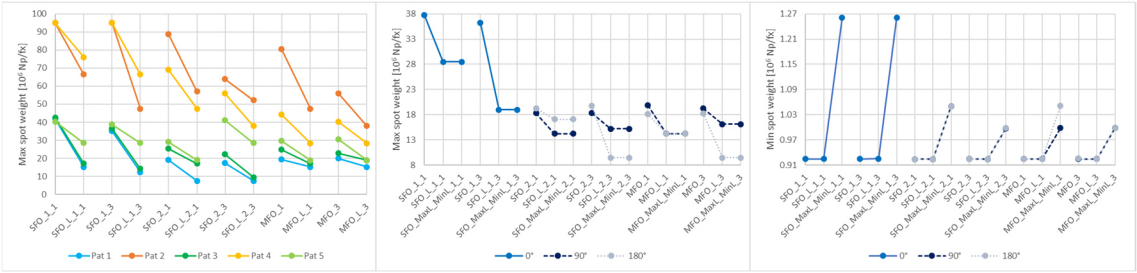

***Fig. 18**: Investigation of different optimization settings. Maximum spot weight for all clinical (image on the left) and phantom plans (image in the middle) as well as minimum spot weight for all phantom plans (image on the right) in 10^6 Np/fx.*

2.4.1 Phantom case

Some planning parameters did not change when investigating the different optimization settings. Those were as follows: The *Dose Grid Resolution* was *0.20 cm/voxel*, the *Gap* was *20.0 cm*, the *Energy layer spacing* was *Automatic with scale 1*, the *Spot spacing* was *Automatic with scale 0.95*, the number of *Proximal* energy layers was *1*, the number of *Distal* energy layers was *1*, the *Lateral* target margin was *Automatic with scale 0.5*, the dose was computed with the *Monte Carlo* option with a statistical *uncertainty* of *0.5%*, the *Optimization tolerance* was $1.000 \cdot 10^{-5}$, the *Maximal number of iterations 40*, the *Iterations before spot filtering 20*, the *Min spot weight* $0.8800 \cdot 10^{6}$ *Np/fx*, the *Max spot weight* $100.0000 \cdot 10^{6}$ *Np/fx* and the *Spot weight limit margin 5.0%*. The prescribed dose was always *54 Gy* and the number of fractions *30*.

The phantom was the same as used for examining the *angular dependence (see section 3.2.2 Angular dependence)*. A spherical target with 4 cm diameter was centered in a cylindrical water phantom. Single as well as two field plans separated by an angles of 90° and 180° were created. DVHs and LET_d-VHs in concentric rings around the target were subsequently analyzed.

2.4.2 Clinical cases

The examined optimization strategies were applied to five clinical cases: two pediatric head tumors (in the following *Patient 1* and *Patient 3*), one superficial tumor (*Patient 2*), one pediatric Ewing tumor (*Patient 4*) and one pediatric ependymoma (*Patient 5*). All plans were calculated using the following settings: the dose was computed with the *Monte Carlo* option with a statistical *uncertainty* of *0.5%*, the *Optimization tolerance* was $1.000 \cdot 10^{-5}$, the *Maximal number of iterations 40*, the *Iterations before spot filtering 20*, and the *Spot weight limit margin 5.0%*.

Due to different planning conditions some planning parameters were adapted to each case: The *Dose Grid Resolution* was *0.20 cm/voxel* or *0.30 cm/voxel*, the *Gap* was *16.0 cm*, *18.0 cm*, *20.0 cm*, *20.5 cm*, *20.6 cm* or *25.0 cm*, the *Energy layer spacing* was *Automatic with* different *scales* (*0.95, 1 and 1.1.*), the *Min spot weight* was either $0.8800 \cdot 10^{6}$ *Np/fx* or $0.9200 \cdot 10^{6}$ *Np/fx*, the *Max spot weight* was either $1000.0000 \cdot 10^{6}$ *Np/fx* or $100.0000 \cdot 10^{6}$ *Np/fx*[45]. The number of *Proximal* layers was either *0* or *1*. For cases that used a range shifter the *Lateral* target margin was *Constant, 0.5cm*, the *Spot spacing* was *Constant, 0.5 cm*, for cases without a range shifter the *Lateral* target margin was *Constant, 0.4cm* and the *Spot spacing* was *Automatic with* different *scales* (*0.8, 0.85 and 0.9*). The prescribed dose was always *54 Gy*, the number of fractions either *30* or *27*.

Table 3 and *Table 4* summarize the planning parameters applied for the clinical as well as the phantom cases. They make clear that results presented in this paper were obtained with different planning parameters. This should be kept in mind when comparing obtained findings. In the column *Machine* respectively *Range Shifter* the names of different machines as they were used in the treatment planning system are listed. If no range shifter was applied *None* is written in the corresponding column.

The patient geometry (PTV and CTV as well as the following organs at risk: brainstem, right and left bulbus, chiasm, right and left hippocampus, right and left tempolobe), the evaluation structures (PTV, ring 0.0 to 0.5 cm around the PTV, ring 0.5 to 1.0 cm around the PTV, ring 1.0 to 1.5 cm around the PTV and ring 1.5 to 2.5 cm around the PTV) and the RBE-weighted dose distributions for the planning strategy: two field, SFO, one distal energy layer, no maximum spot weight limitation are shown in *Fig. 19 - Fig. 23* for the five clinical cases. *Table 2* gives the sizes of the patients´ PTV, brain and $TNTV_B$ (Total normal tissue volume brain) which corresponds to the brain minus the PTV.

[45] The given values for the *Max spot weight* are rather high. Therefore, plans using these could justifiably be referred to as *without maximum spot weight limitation*. For plans denoted as *with maximum spot weight limitation* these values were significantly lower.

For the clinical cases not only LET_d and dose values were examined, but also the percentage of the $TNTV_B$´s volume receiving at least 5, 10, 20 and 30 Gy. These values can give some indication of the sparing of normal tissue.

Table 2: *Sizes of the PTV, the brain and the $TNTV_B$ for five investigated clinical cases in cm^3.*

Patient	Size of the PTV	Size of the brain	Size of the $TNTV_B$
Patient 1	58.7	1325.6	1267.1
Patient 2	122.2	1276.9	1200.6
Patient 3	77.4	1748.1	1670.5
Patient 4	317.8	1484.0	1311.6
Patient 5	52.5	1242.1	1193.1

***Table 3**: Used planning parameters for all different plans, first part. The first column shows whether the dependence on the voxelsize, the angle separating two SFO beams, the depth and size, the number of beams, different optimization settings for the phantom case or different optimization settings for the clinical cases was investigated.*

	Plan Design							Optimization settings	
	Machine	Dose Grid Resolution [cm/voxel]	Range Shifter	Gap [cm]	MC Uncert [%]	Prescribed dose [Gy]	Number of fractions	Optimization tolerance	Max number of iterations
Voxelsize									
box5 (0,0,6)	IR3HBL	0.1/0.2/0.3	None	64.8	0.2/0.1/0.1	2	1	1.00E-05	40
box5 (0,0,30)	IR3HBL	0.1/0.2/0.3	None	64.8	0.1	2	1	1.00E-05	40
Angle	IR2_4	0.2	None	20	0.5	54	30	1.00E-05	40
Depth and size	IR3HBL	0.2	None	20	0.5	2	1	1.00E-05	40
Number of beams	IR2VBL_gantry_1	0.2	None	20	0.5	270	30	1.00E-05	40
Optimization settings	IR2_4	0.2	None	20	0.5	54	30	1.00E-05	40
CLINICAL CASES									
Pat1	IR2_4	0.3	None	20.0/20.6	0.5	54	30	1.00E-05	40
Pat2	IR2_5	0.2	RS3cmR1	16	0.5	54	27	1.00E-05	40
Pat3	IR2_4	0.2	None	20.5/20.0	0.5	54	30	1.00E-05	40
Pat4	IR2VBL_gantry_1	0.2	RS3cmR1	18	0.5	54	30	1.00E-05	40
Pat5	IR2VBL_gantry_1	0.2	None	25	0.5	54	30	1.00E-05	40

***Table 4:** Used planning parameters for the different plans, second part. The first column shows whether the dependence on the voxelsize, the angle separating two SFO beams, the depth and size, the number of beams, different optimization settings for the phantom case or different optimization settings for the clinical cases was investigated.*

	Spot filtering settings				Beam Computation Settings				
					Spot pattern		Target margins		
	Iterations before spot filtering	Min spot weight [10^6 NP/fx]	Max spot weight [10^6 NP/fx]	Spot weight limit margin [%]	Energy layer spacing	Spot spacing	Proximal [Layers]	Distal [Layers]	Lateral
Voxelsize									
box5 (0,0,6)	20	0.9	1000	5	Automatic with scale 1	Automatic with scale 0.7	1	1	Constant, 0.5 cm
box5 (0,0,30)	20	0.9	1000	5	Automatic with scale 1	Constant, 0.3 cm	1	1	Constant, 0.5 cm
Angle	20	0.88	100	5	Automatic with scale 1	Automatic with scale 0.95	1	1	Constant, 0.5 cm
Depth and size	20	0.9	1000	5	Automatic with scale 1	Automatic with scale 1	1	1	Automatic with scale 1
Number of beams	20	0.92	100	5	Automatic with scale 1	Automatic with scale 0.95	1	1	Constant, 0.5 cm
Optimization settings	20	0.88	100	5	Automatic with scale 1	Automatic with scale 0.95	1	1/2/3	Constant, 0.5 cm
CLINICAL CASES									
Pat1	20	0.92	10000	5	Automatic with scale 1	Automatic with scale 0.8	0/1	1/2/3	Constant, 0.4 cm
Pat2	20	0.88	100/ -	5	Automatic with scale 1.1	Constant, 0.5 cm	1	1/2/3	Constant, 0.5 cm
Pat3	20	0.88	100	5	Automatic with scale 1	Automatic with scale 0.8/0.9	1	1/2/3	Constant, 0.4 cm
Pat4	20	0.92	100	5	Automatic with scale 1	Constant, 0.5 cm	1	1/2/3	Constant, 0.5 cm
Pat5	20	0.92	100	5	Automatic with scale 0.95	Automatic with scale 0.85	0	1/2/3	Constant, 0.4 cm

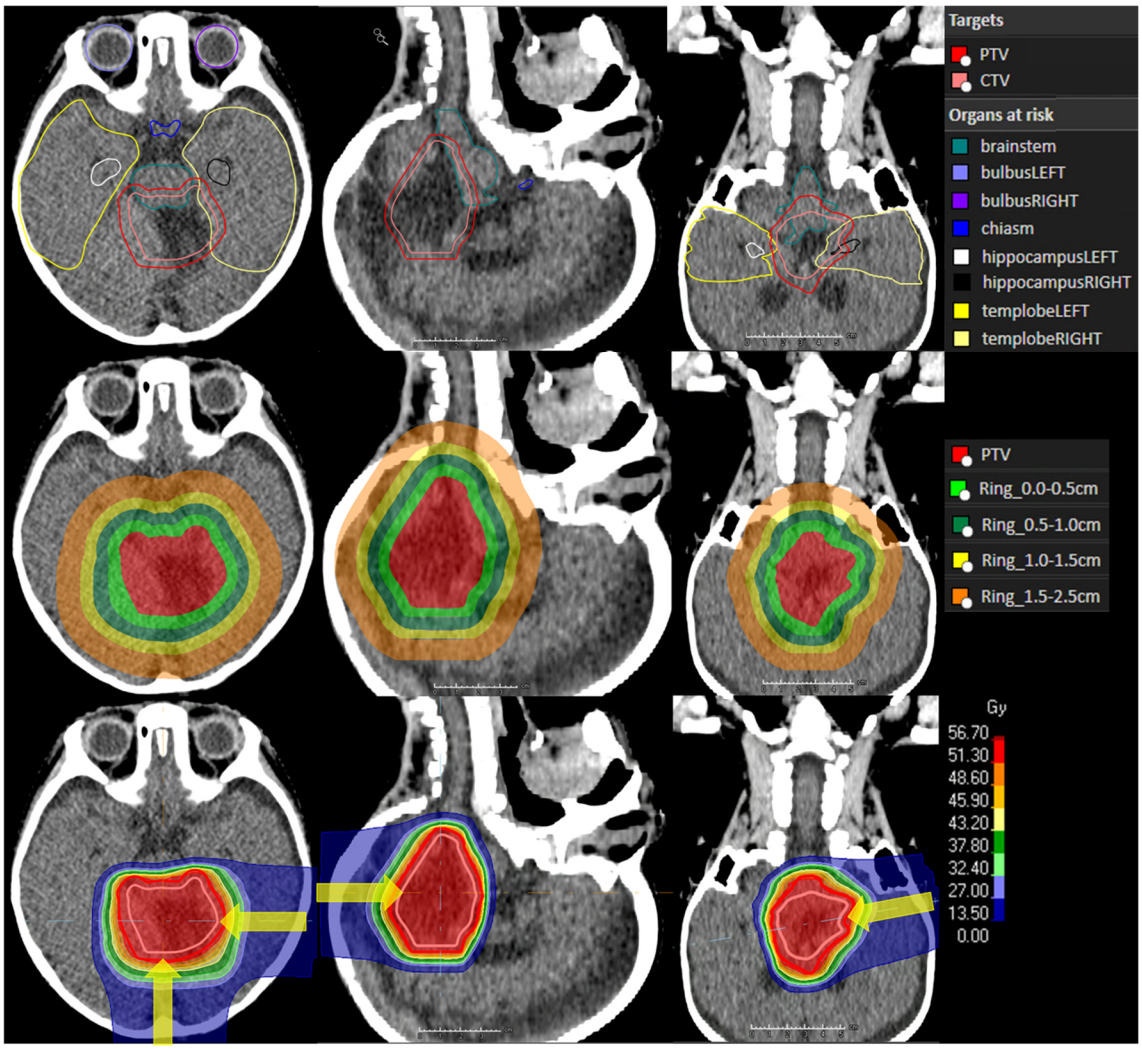

***Fig. 19**: Patient 1. Patient geometry (images on the top), evaluation structures (images in the middle) and RBE-weighted dose distributions (images on the bottom) for the planning strategy: two field, SFO, one distal energy layer, no maximum spot weight limitation. The pictures on the left show transversal, the pictures in the middle sagittal and the pictures on the right coronal planes. The arrows indicate the incidence angles.*

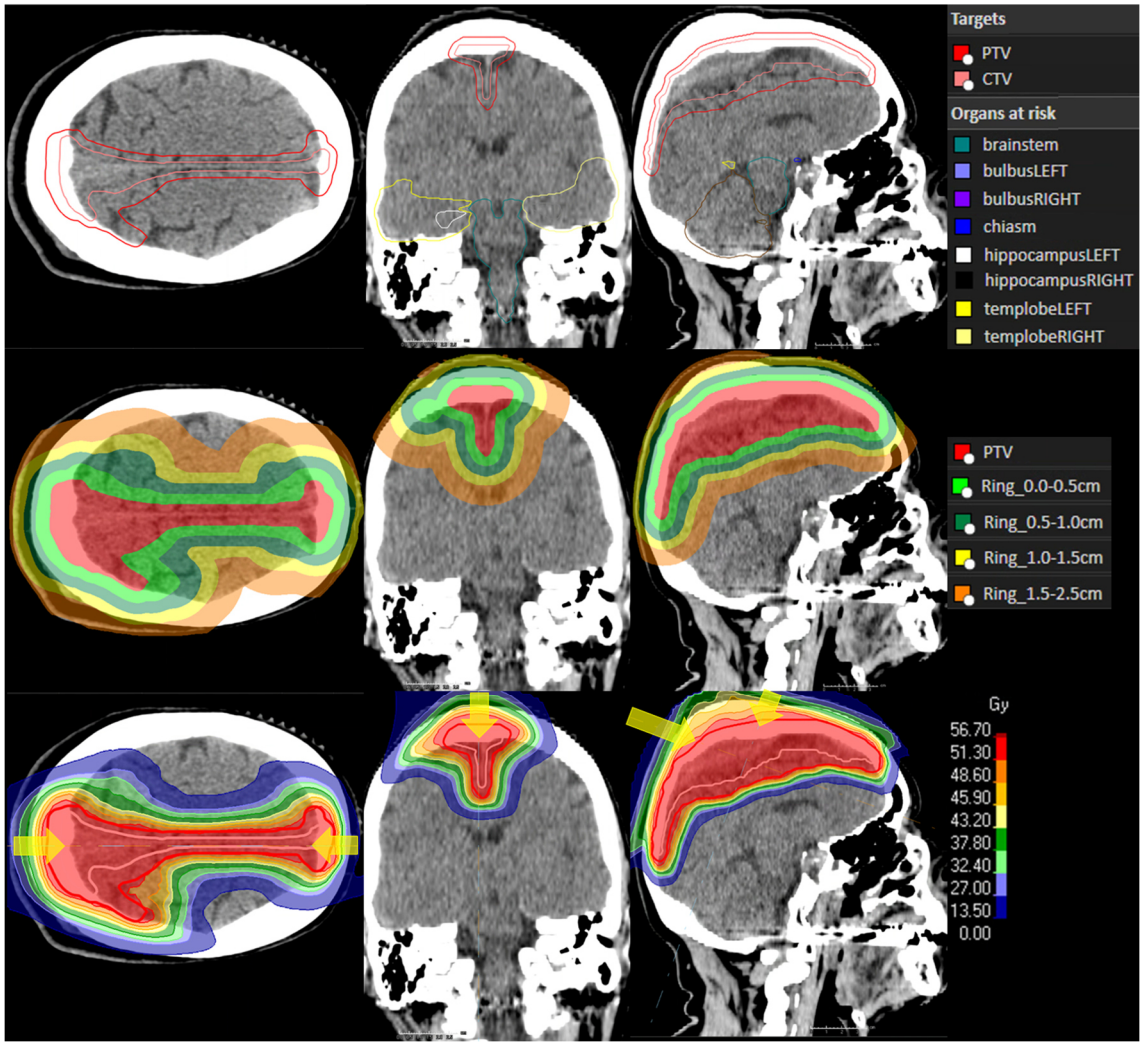

Fig. 20: *Patient 2. Patient geometry (images on the top), evaluation structures (images in the middle) and RBE-weighted dose distributions (images on the bottom) for the planning strategy: two field, SFO, one distal energy layer, no maximum spot weight limitation. The pictures on the left show transversal, the pictures in the middle sagittal and the pictures on the right coronal planes. The arrows indicate the incidence angles.*

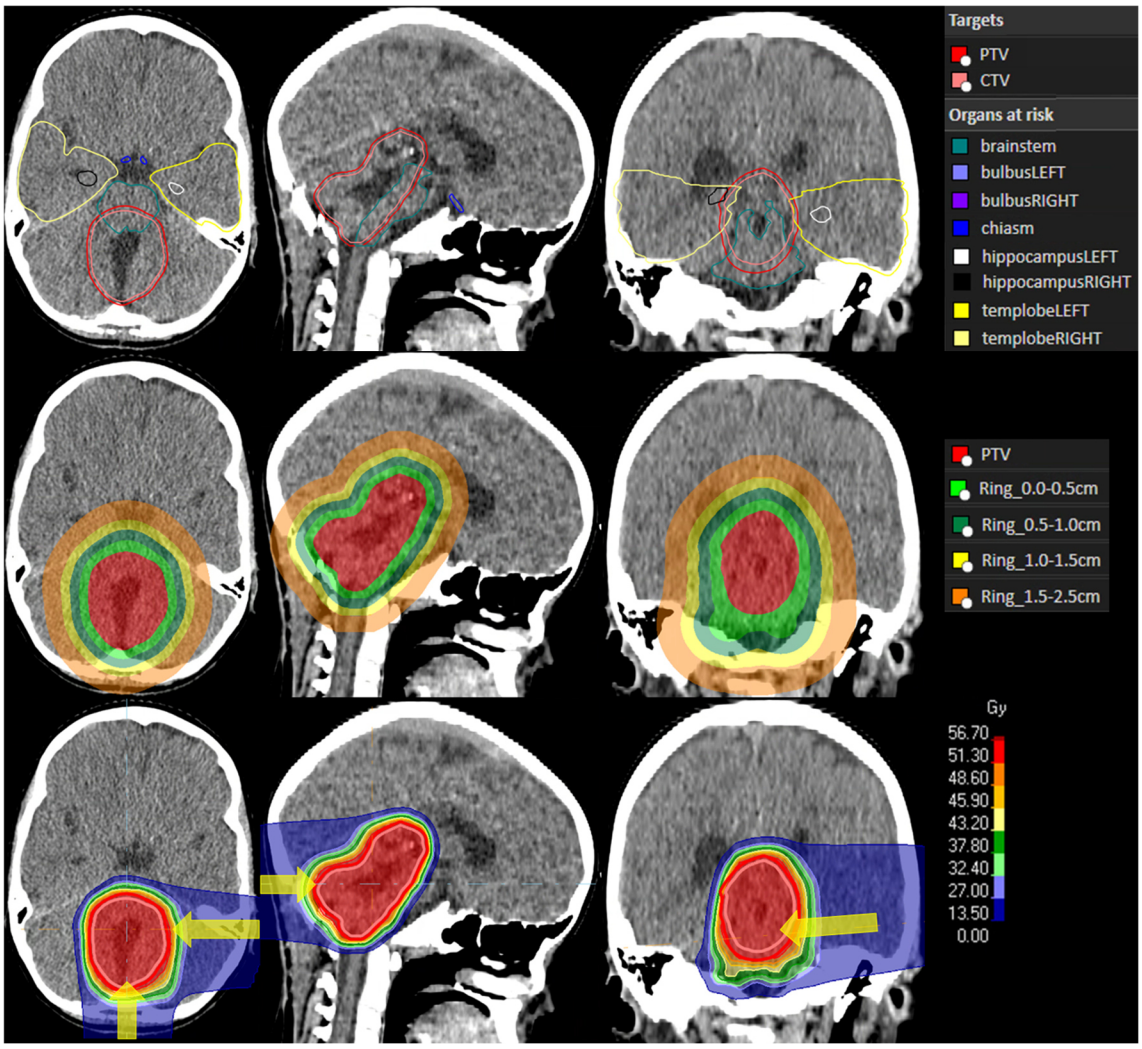

Fig. 21: *Patient 3. Patient geometry (images on the top), evaluation structures (images in the middle) and RBE-weighted dose distributions (images on the bottom) for the planning strategy: two field, SFO, one distal energy layer, no maximum spot weight limitation. The pictures on the left show transversal, the pictures in the middle sagittal and the pictures on the right coronal planes. The arrows indicate the incidence angles.*

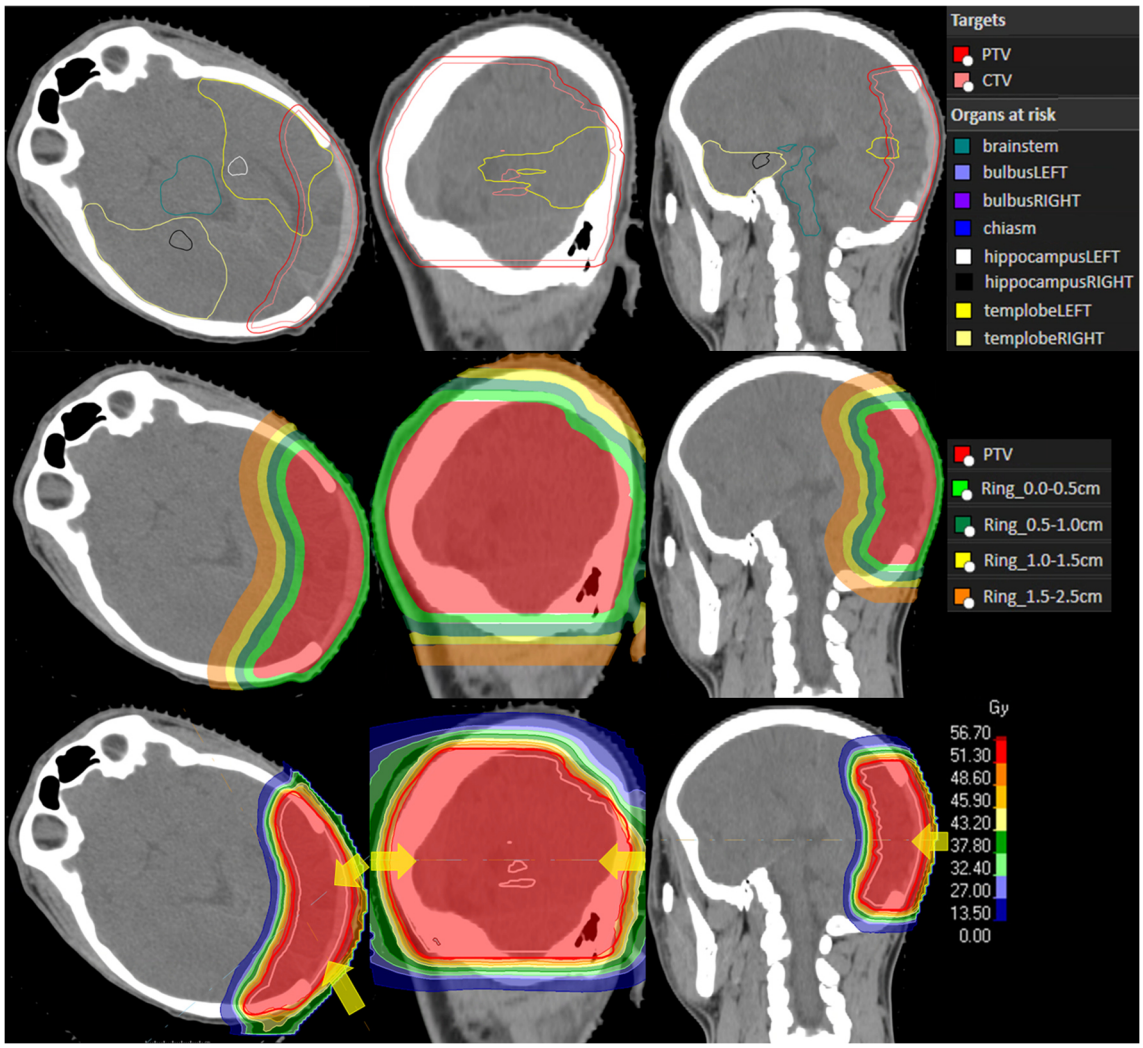

Fig. 22: *Patient 4. Patient geometry (images on the top), evaluation structures (images in the middle) and RBE-weighted dose distributions (images on the bottom) for the planning strategy: two field, SFO, one distal energy layer, no maximum spot weight limitation. The pictures on the left show transversal, the pictures in the middle sagittal and the pictures on the right coronal planes. The arrows indicate the incidence angles.*

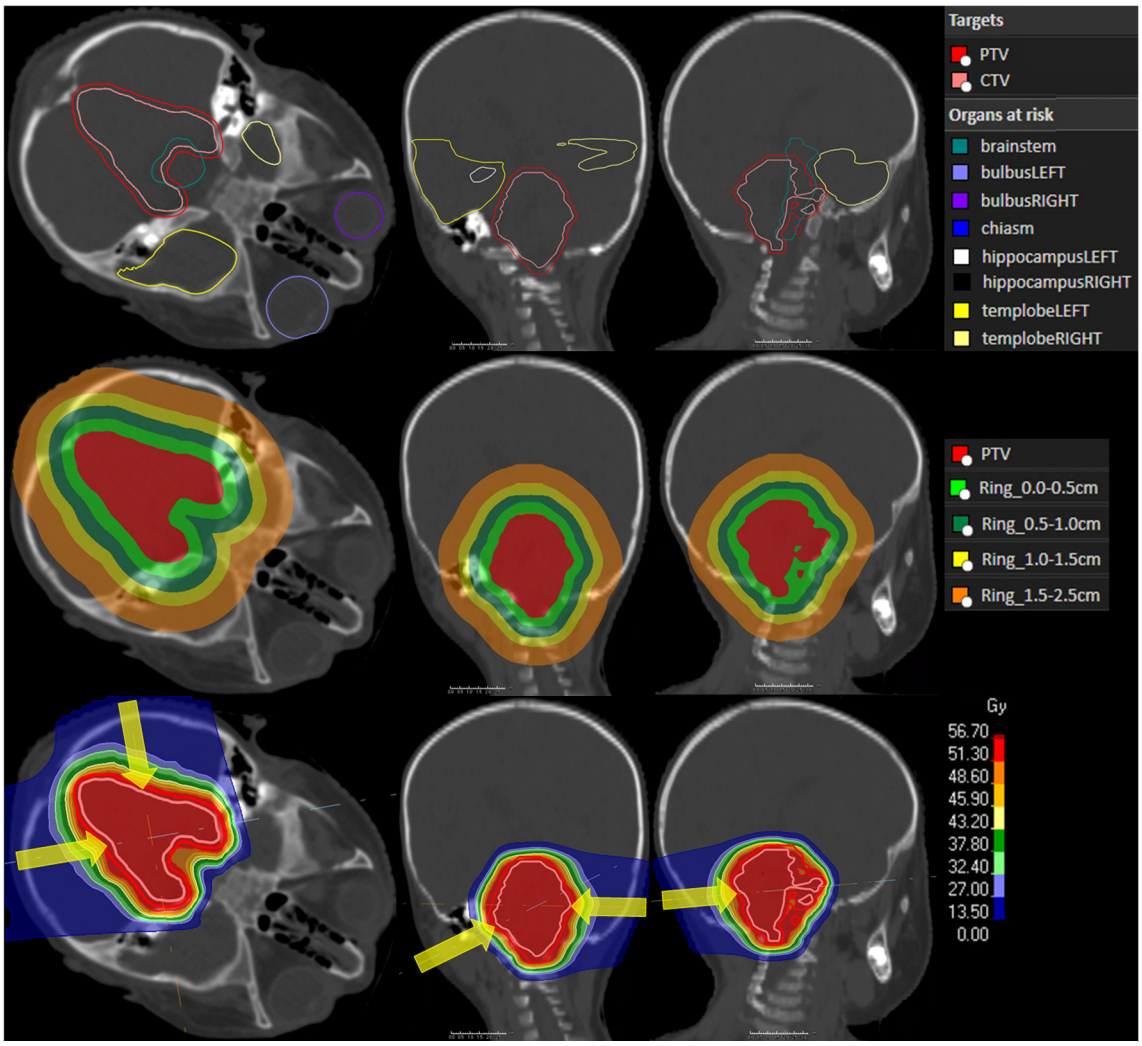

Fig. 23: *Patient 5. Patient geometry (images on the top), evaluation structures (images in the middle) and RBE-weighted dose distributions (images on the bottom) for the planning strategy: two field, SFO, one distal energy layer, no maximum spot weight limitation. The pictures on the left show transversal, the pictures in the middle sagittal and the pictures on the right coronal planes. The arrows indicate the incidence angles.*

3 RESULTS

3.1 Validation RS v5.99.50

LET_d values calculated with RS v5.99.50 agreed well with those computed with GATE8.0/Geant4.10.3. The average deviations where within ±5% for all examined profiles (*Fig. 24*).

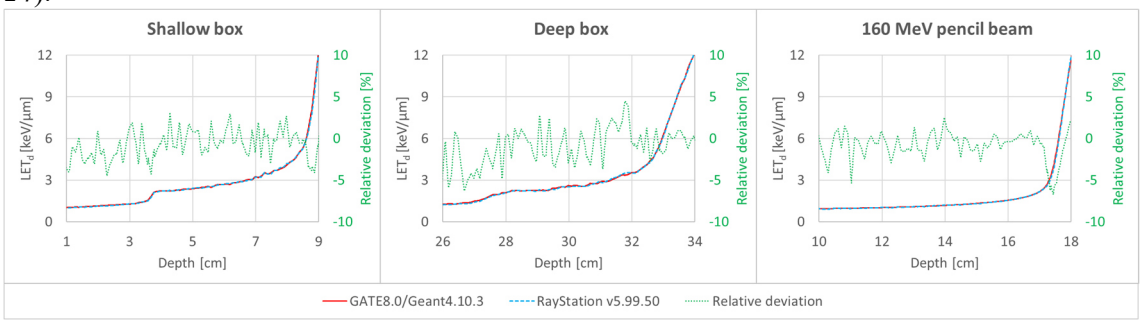

***Fig. 24**: Depth LET_d profile computed along the central beam axis with RayStation v5.99.50 (dashed blue line) and with GATE8.0/Geant4.10.3 (solid red line) as function of depth for a 5x5x5 cm^3 box centered at a depth of 6 (first picture) and 30 cm (second picture) as well as for a 160 MeV pencil beam (range in water: 17.4 cm; third picture). The relative deviations of the LET_d computed with RayStation v5.99.50 from the LET_d computed with GATE8.0/Geant4.10.3 are also shown (dotted green line).*

3.2. Analysis of LET_d distributions

3.2.1 Voxel size dependence

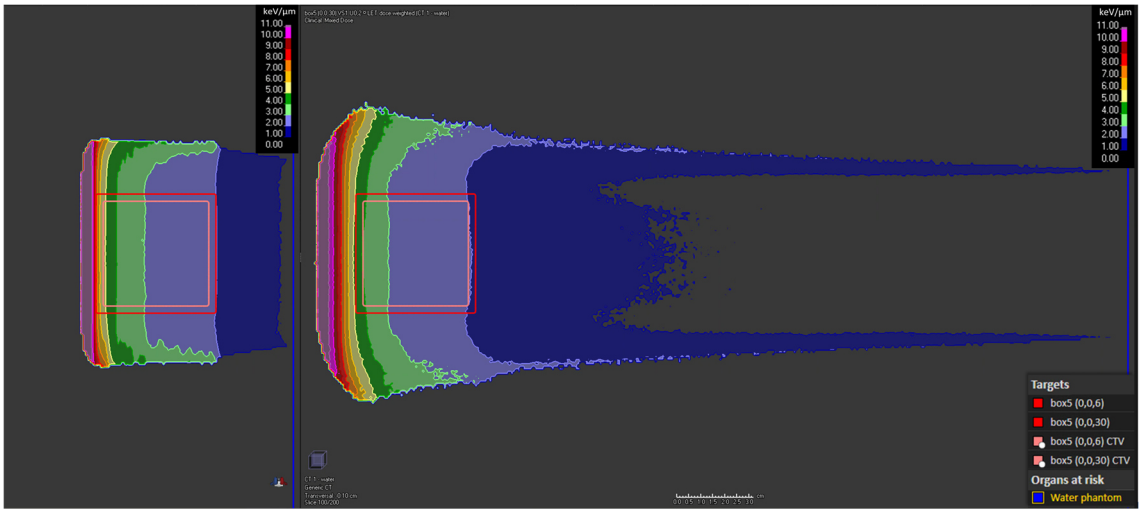

***Fig. 25:** Calculated LET_d distributions for investigating the voxel size dependence.*

A (5x5x5) cm^3 water target was centered at a depth of 6 cm (left image) and 30 cm (right image) in a water phantom. The shown distributions were calculated with a voxel size of (0.1x0.1x0.1) cm^3.

In *Fig. 25* LET_d distributions calculated for investigating the voxel size dependence are displayed. As shown in *Fig. 26* no systematic deviations of values computed with different voxel sizes were observed in the calculated longitudinal LET_d distributions. *Fig. 27* shows that high values of relative deviation only occurred when the gradient of the LET_d distribution was high. *Table 5* lists the mean values and standard deviations of the signed and unsigned relative deviations of the LET_d values computed with a (0.2x0.2x0.2) cm^3, respectively, with a (0.3x0.3x0.3) cm^3 from the LET_d values computed with a (0.1x0.1x0.1) cm^3. All mean values of the relative deviations were below ±0.2%. More figures which confirm the presented results can be found in the appendix (*A.1 Voxel size dependence*).

Table 5: *Voxel size dependence: The mean values and standard deviations of the signed and unsigned relative deviations of the LET_d computed with a (0.2x0.2x0.2) cm^3, respectively, with a (0.3x0.3x0.3) cm^3 from the LET_d computed with a (0.1x0.1x0.1) cm^3 are shown.*

	Voxel side length [mm]	Mean value (Sign. rel. dev.)[%]	Standard dev. (Sign. rel. dev.)[%]	Mean value (Unsign. rel. dev.)[%]	Standard dev. (Unsign. rel. dev.)[%]
Shallow Box	2	-0.17	5.46	2.50	4.86
Shallow Box	3	-0.16	7.53	3.58	6.62
Deep Box	2	0.03	2.87	0.88	2.73
Deep Box	3	0.09	3.92	1.14	3.76

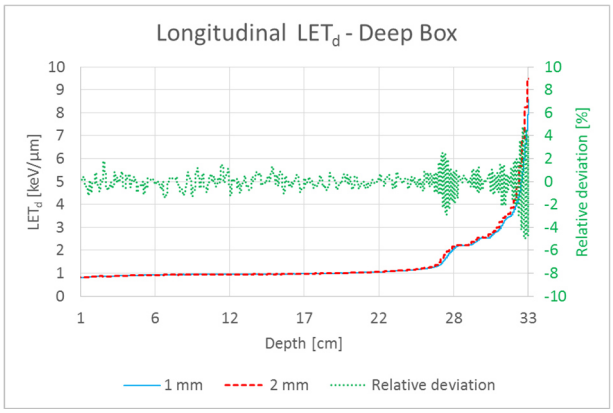

Fig. 26*: Voxel size dependence. Depth LET_d profile along the central beam axis computed with varying dose grid ((0.1x0.1x0.1) cm^3 (solid blue line) and (0.2x0.2x0.2) cm^3 (dashed red line)) as function of depth for the deep box (30 cm in water) using the TPS RS v5.99.50. The relative deviation of the LET_d computed with a (0.2x0.2x0.2) cm^3 from the LET_d computed with a (0.1x0.1x0.1) cm^3 is also shown (dotted green line).*

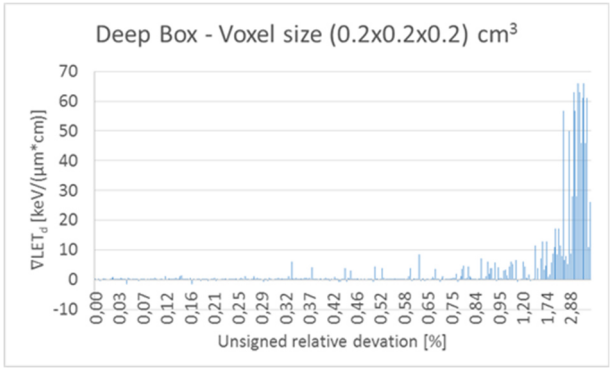

Fig. 27: *Voxel size dependence. LET_d gradient depending on the unsigned relative deviation of the LET_d computed with a (0.2x0.2x0.2) cm^3 from the LET_d computed with a (0.1x0.1x0.1) cm^3 for the deep box (30 cm in water) using the TPS RS v5.99.50.*

3.2.2 Angular dependence

Phantom case

Increasing the angle separating two SFO beams led to a decrease of maximum LET_d around the PTV as depicted in the calculated LET_d distributions (*Fig. 28*) as well as LET_dVHs (*Fig. 29)*, whereas the RBE-weighted dose stayed almost the same for all different angles (*Fig. 29*). *Fig. 30* and *Fig. 31* as well as *Table 6* - *Table 11* summarize the maximum LET_d and dose values[46] to the

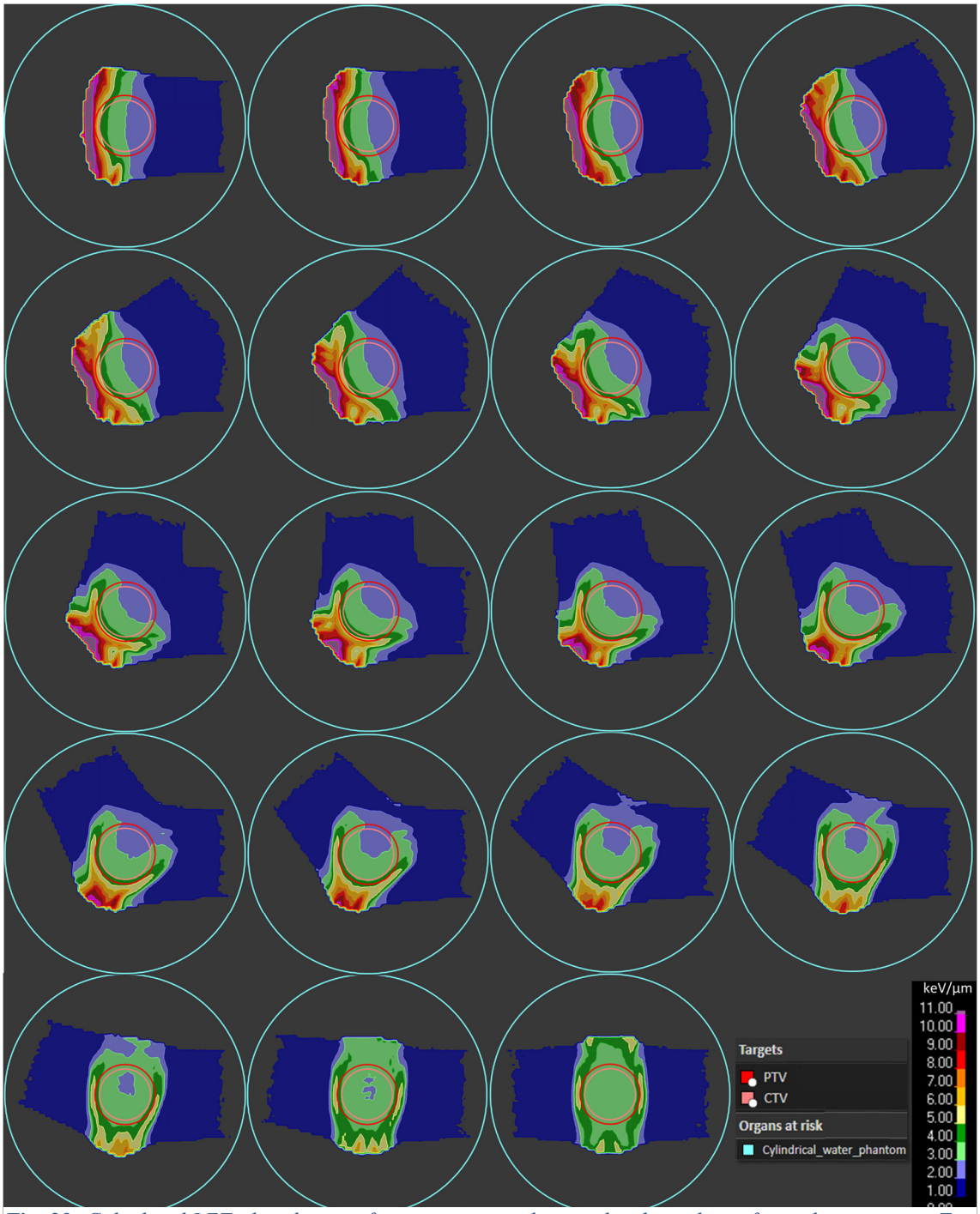

***Fig. 28**: Calculated LET_d distributions for investigating the angular dependence for a phantom case. Two SFO fields separated by an increasing in steps of 10° from 0° to 180° for a spherical target with 4 cm diameter centered in a cylindrical water phantom.*

[46] All dose values shown in this master thesis are biological-weighted dose values obtained by applying an RBE of 1.1.

PTV and to four rings around the PTV as well as the maximum LET_d and dose values to 2% of the PTV respectively of these four rings. The ratios of those values to the values resulting from the plans with a separation angle of 0° are also illustrated (*Fig. 32* and *Fig. 33*) and listed (*Table 6 - Table 11*).

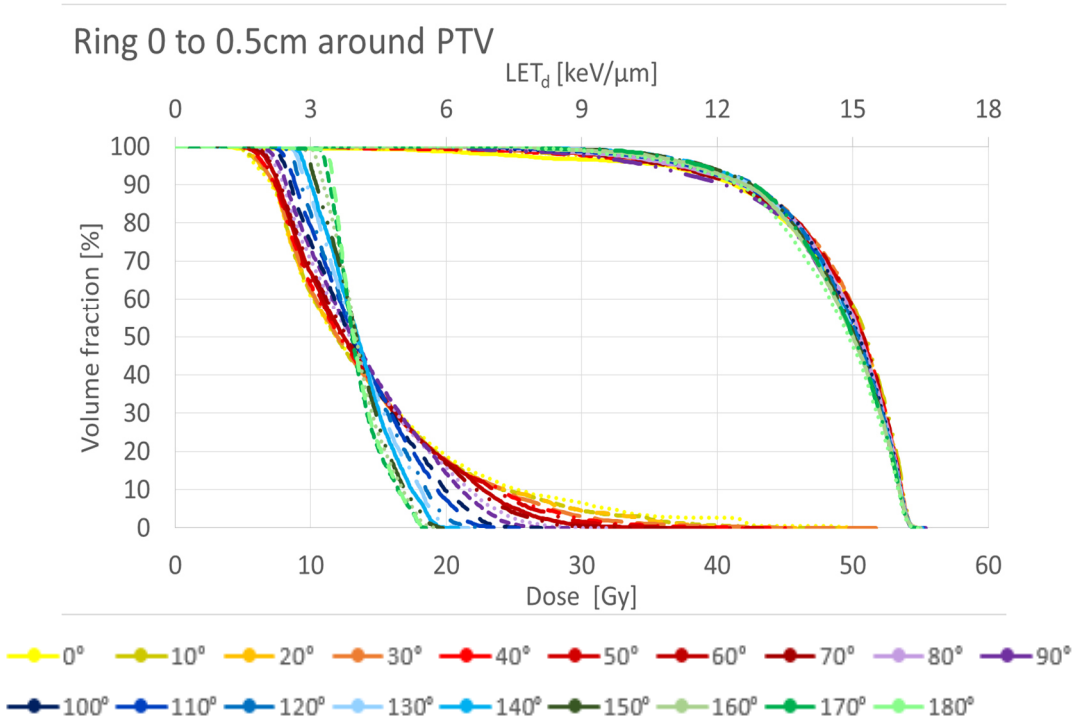

Fig. 29: *Angular dependence. DVHs (upper lines) and LET_dVHs (lower lines) with varying angle separating two SFO beams (angle varies from 0° to 180° in steps of 10°) represented exemplarily in a ring from 0.0 to 0.5 cm around the PTV for a spherical target with 4 cm diameter centered in a cylindrical water phantom.*

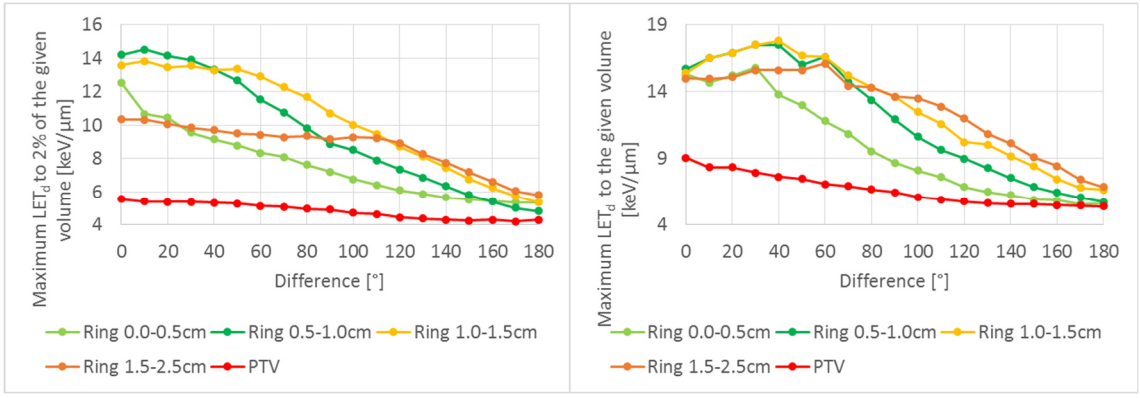

***Fig. 30**: Angular dependence. Maximum LET_d to 2% of (left picture) respectively maximum LET_d to (right picture) four different rings (0.0 to 0.5 cm, 0.5 to 1.0 cm, 1.0 to 1.5 cm, 1.5 to 2.5 cm) around the PTV as well as maximum LET_d to 2% of respectively maximum LET_d to the PTV as a function of the angle separating two SFO beams for a spherical target with 4 cm diameter centered in a cylindrical water phantom.*

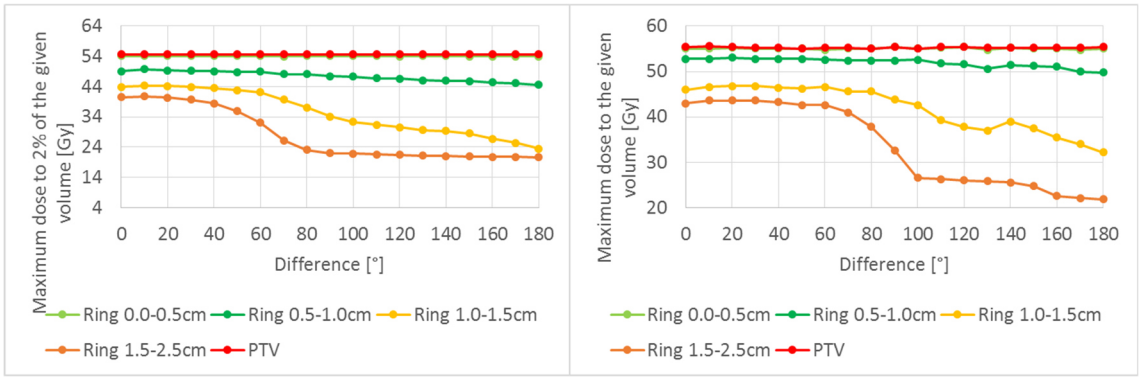

***Fig. 31:** Angular dependence. Maximum dose to 2% of (left picture) respectively maximum dose to (right picture) four different rings (0.0 to 0.5 cm, 0.5 to 1.0 cm, 1.0 to 1.5 cm, 1.5 to 2.5 cm) around the PTV as well as maximum dose to 2% of respectively maximum dose to the PTV as a function of the angle separating two SFO beams in Gy for a spherical target with 4 cm diameter centered in a cylindrical water phantom.*

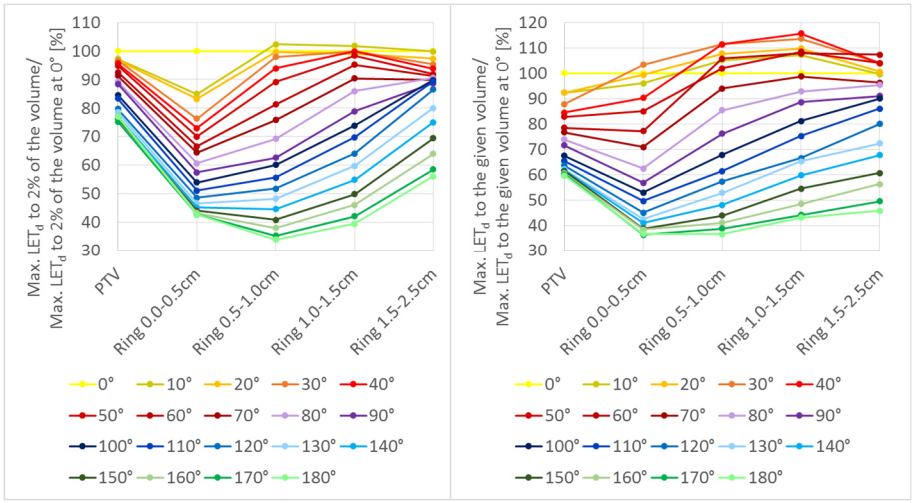

Fig. 32: Angular dependence. Maximum LET_d to 2% of (left picture) respectively maximum LET_d to (right picture) four different rings (0.0 to 0.5 cm, 0.5 to 1.0 cm, 1.0 to 1.5 cm, 1.5 to 2.5 cm) around the PTV as well as maximum LET_d to 2% of respectively maximum LET_d to the PTV divided by the maximum LET_d to 2% of respectively maximum LET_d to the given volume. Plan setup: two SFO beams separated by 0° to 180° in steps of 10° for a spherical target with 4 cm diameter centered in a cylindrical water phantom.

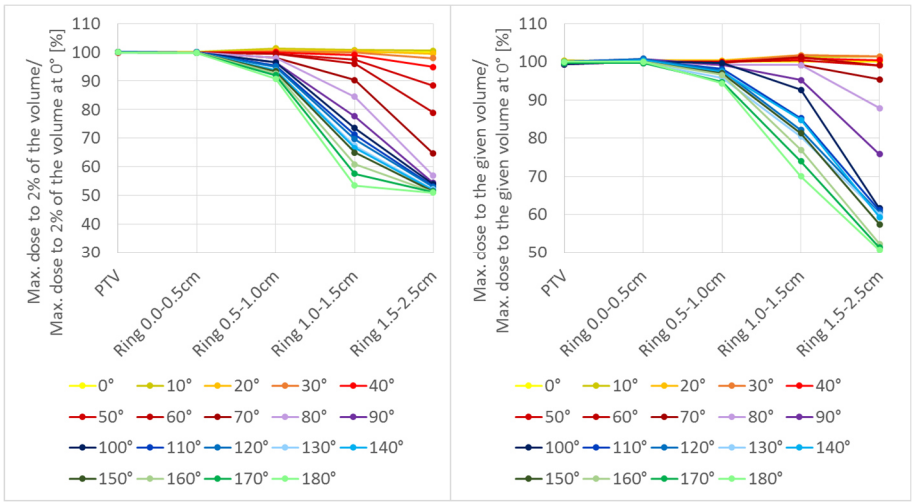

Fig. 33: Angular dependence. Maximum dose to 2% of (left picture) respectively maximum dose to (right picture) four different rings (0.0 to 0.5 cm, 0.5 to 1.0 cm, 1.0 to 1.5 cm, 1.5 to 2.5 cm) around the PTV as well as maximum dose to 2% of respectively maximum dose to the PTV divided by the maximum dose to 2% of respectively maximum dose to the given volume. Plan setup: two SFO beams separated by 0° to 180° in steps of 10° for a spherical target with 4 cm diameter centered in a cylindrical water phantom.

Table 6: *Angular dependence. Maximum LET_d to 2% of four different rings (0.0 to 0.5 cm, 0.5 to 1.0 cm, 1.0 to 1.5 cm, 1.5 to 2.5 cm) around the PTV as well as maximum LET_d to 2% of the PTV for a spherical target with 4 cm diameter centered in a cylindrical water phantom. The first column gives the angle separating the two SFO fields. The other columns give the maximum LET_d to 2% of the respective volumes in keV/µm and the proportions of maximum LET_d to 2% of the respective volume at 0° in %.*

Diff	Max. LET_d to 2% of PTV	Max. LET_d to 2% of PTV/Max. LET_d to 2% of PTV at 0°	Max. LET_d to 2% of ring 0.0-0.5cm	Max. LET_d to 2% of ring 0.0-0.5cm/ Max. LET_d to 2% of ring 0-0.5cm at 0°	Max. LET_d to 2% of ring 0.5-1.0cm	Max. LET_d to 2% of ring 0.5-1.0cm/ Max. LET_d to 2% of ring 0.5-1.0cm at 0°	Max. LET_d to 2% of ring 1.0-1.5cm	Max. LET_d to 2% of ring 1.0-1.5cm/ Max. LET_d to 2% of ring 1.0-1.5cm at 0°	Max. LET_d to 2% of ring 1.5-2.5cm	Max. LET_d to 2% of ring 1.5-2.5cm/ Max. LET_d to 2% of ring 1.5-2.5cm at 0°
[°]	[keV/µm]	[%]	[keV/µm]	[%]	[keV/µm]	[%]	[keV/µm]	[%]	[keV/µm]	[%]
0	5.6	100.0	12.6	100.0	14.2	100.0	13.6	100.0	10.3	100.0
10	5.4	97.3	10.7	85.0	14.5	102.3	13.8	101.8	10.3	99.8
20	5.4	96.7	10.4	83.2	14.1	99.6	13.5	99.1	10.1	97.4
30	5.4	96.7	9.6	76.2	13.9	98.0	13.6	99.8	9.9	95.3
40	5.3	95.7	9.2	73.0	13.3	93.9	13.3	97.8	9.7	93.8
50	5.3	94.9	8.8	70.0	12.7	89.2	13.4	98.4	9.5	91.9
60	5.1	92.5	8.4	66.5	11.5	81.2	12.9	95.1	9.4	91.2
70	5.1	91.3	8.1	64.5	10.8	75.9	12.3	90.4	9.3	89.8
80	5.0	89.2	7.6	60.7	9.8	69.2	11.7	86.0	9.4	90.6
90	4.9	88.4	7.2	57.4	8.9	62.6	10.7	78.9	9.2	88.7
100	4.7	84.6	6.8	54.0	8.5	60.1	10.0	73.9	9.3	89.9
110	4.6	83.3	6.4	51.1	7.9	55.7	9.5	69.8	9.2	89.4
120	4.4	79.7	6.1	48.6	7.4	51.8	8.7	64.1	8.9	86.5
130	4.4	78.6	5.9	46.7	6.9	48.3	8.1	59.7	8.3	80.0
140	4.3	77.2	5.7	45.1	6.3	44.6	7.5	54.9	7.8	75.1
150	4.2	76.4	5.5	44.0	5.8	40.8	6.8	49.8	7.2	69.4
160	4.3	77.1	5.4	43.2	5.4	38.0	6.3	46.0	6.6	64.0
170	4.2	75.2	5.4	42.6	5.0	35.2	5.7	42.1	6.1	58.6
180	4.3	77.1	5.4	42.7	4.8	33.9	5.4	39.5	5.8	56.1

Table 7*: Angular dependence. Maximum LET_d to four different rings (0.0 to 0.5 cm, 0.5 to 1.0 cm, 1.0 to 1.5 cm, 1.5 to 2.5 cm) around the PTV as well as maximum LET_d to the PTV for a spherical target with 4 cm diameter centered in a cylindrical water phantom. The first column gives the angle separating the two SFO fields. The other columns give the maximum LET_d of the respective volumes in keV/µm and the proportions of maximum LET_d of the respective volume at 0° in %.*

Diff	Max. LET_d to PTV	Max. LET_d to PTV/Max. LET_d to PTV at 0°	Max. LET_d to ring 0.0-0.5cm	Max. LET_d to ring 0.0-0.5cm/ Max. LET_d to ring 0-0.5cm at 0°	Max. LET_d to ring 0.5-1.0cm	Max. LET_d to ring 0.5-1.0cm/ Max. LET_d to ring 0.5-1.0cm at 0°	Max. LET_d to ring 1.0-1.5cm	Max. LET_d to ring 1.0-1.5cm/ Max. LET_d to ring 1.0-1.5cm at 0°	Max. LET_d to ring 1.5-2.5cm	Max. LET_d to ring 1.5-2.5cm/ Max. LET_d to ring 1.5-2.5cm at 0°
[°]	[keV/µm]	[%]	[keV/µm]	[%]	[keV/µm]	[%]	[keV/µm]	[%]	[keV/µm]	[%]
0	9.1	100.0	15.3	100.0	15.7	100.0	15.4	100.0	15.0	100.0
10	8.4	92.3	14.7	96.1	16.5	105.1	16.5	107.1	15.0	99.7
20	8.4	92.3	15.2	99.3	16.9	107.6	16.9	109.7	15.1	100.7
30	8.0	87.8	15.8	103.3	17.5	111.5	17.5	113.6	15.6	104.0
40	7.7	84.5	13.8	90.2	17.5	111.5	17.8	115.6	15.6	104.0
50	7.5	82.9	13.0	85.0	16.0	101.9	16.7	108.4	15.6	104.0
60	7.1	78.5	11.8	77.1	16.6	105.7	16.6	107.8	16.1	107.3
70	6.9	76.7	10.9	70.9	14.8	93.9	15.2	98.7	14.5	96.3
80	6.7	73.8	9.6	62.4	13.4	85.4	14.3	92.9	14.3	95.3
90	6.5	71.6	8.7	56.9	12.0	76.1	13.7	88.6	13.7	91.0
100	6.1	67.4	8.1	52.9	10.7	67.8	12.5	81.2	13.5	90.0
110	5.9	65.4	7.6	49.7	9.7	61.5	11.6	75.3	12.9	86.0
120	5.8	63.6	6.9	45.0	9.0	57.3	10.3	66.6	12.0	80.0
130	5.6	62.1	6.5	42.5	8.3	52.9	10.1	65.3	10.9	72.3
140	5.6	61.7	6.3	40.9	7.6	48.1	9.2	59.7	10.2	67.7
150	5.6	61.4	5.9	38.7	6.9	43.8	8.4	54.5	9.1	60.7
160	5.5	60.6	5.9	38.3	6.4	41.0	7.5	48.4	8.5	56.3
170	5.4	60.1	5.6	36.3	6.1	38.7	6.8	44.2	7.4	49.5
180	5.4	59.7	5.6	36.7	5.7	36.6	6.6	43.1	6.9	45.7

Table 8: *Angular dependence. Maximum dose to 2% of four different rings (0.0 to 0.5 cm, 0.5 to 1.0 cm, 1.0 to 1.5 cm, 1.5 to 2.5 cm) around the PTV as well as maximum dose to 2% of the PTV for a spherical target with 4 cm diameter centered in a cylindrical water phantom. The first column gives the angle separating the two SFO fields. The other columns give the maximum dose to 2% of the respective volumes in Gy and the proportions of maximum dose of the respective volume at 0° in %.*

Diff	Max. dose to 2% of PTV	Max. dose to 2% of PTV/Max. dose to 2% of PTV at 0°	Max. dose to 2% of ring 0-0.5cm	Max. dose to 2% of ring 0.0-0.5cm/ Max. dose to 2% of ring 0-0.5cm at 0°	Max. dose to 2% of ring 0.5-1.0cm	Max. dose to 2% of ring 0.5-1.0cm/ Max. dose to 2% of ring 0.5-1.0cm at 0°	Max. dose to 2% of ring 1.0-1.5cm	Max. dose to 2% of ring 1.0-1.5cm/ Max. dose to 2% of ring 1.0-1.5cm at 0°	Max. dose to 2% of ring 1.5-2.5cm	Max. dose to 2% of ring 1.5-2.5cm/ Max. dose to 2% of ring 1.5-2.5cm at 0°
[°]	[Gy]	[%]	[Gy]	[%]	[Gy]	[%]	[Gy]	[%]	[Gy]	[%]
0	54.6	100.0	54.1	100.0	49.1	100.0	44.0	100.0	40.5	100.0
10	54.6	100.0	54.2	100.1	49.8	101.4	44.3	100.8	40.7	100.5
20	54.6	100.0	54.1	100.0	49.4	100.6	44.1	100.3	40.3	99.5
30	54.6	99.9	54.1	100.0	49.2	100.3	43.9	99.9	39.7	97.9
40	54.6	99.9	54.1	100.0	49.1	100.0	43.5	99.1	38.4	94.9
50	54.6	99.9	54.1	99.9	48.8	99.3	42.8	97.4	35.8	88.4
60	54.6	100.0	54.1	100.0	48.9	99.6	42.2	95.9	32.0	78.9
70	54.6	100.0	54.0	99.9	48.2	98.2	39.7	90.3	26.2	64.7
80	54.6	100.0	54.1	100.0	48.1	98.0	37.2	84.5	23.1	56.9
90	54.7	100.1	54.1	100.0	47.4	96.5	34.1	77.7	22.0	54.4
100	54.6	99.9	54.1	100.0	47.4	96.5	32.3	73.6	21.8	53.9
110	54.6	99.9	54.0	99.9	46.8	95.3	31.3	71.3	21.5	53.1
120	54.7	100.0	54.0	99.9	46.6	95.0	30.6	69.6	21.4	52.9
130	54.6	99.9	54.1	99.9	46.0	93.7	29.6	67.3	21.1	52.2
140	54.6	100.0	54.1	100.0	46.0	93.7	29.3	66.6	21.0	51.7
150	54.6	100.0	54.0	99.9	45.8	93.4	28.6	65.0	20.9	51.5
160	54.6	100.0	54.0	99.9	45.4	92.5	26.8	60.9	20.8	51.2
170	54.6	99.9	54.0	99.8	45.2	92.0	25.3	57.6	20.7	51.2
180	54.6	100.0	53.9	99.7	44.5	90.7	23.5	53.5	20.7	51.0

Table 9: *Angular dependence. Maximum dose to four different rings (0.0 to 0.5 cm, 0.5 to 1.0 cm, 1.0 to 1.5 cm, 1.5 to 2.5 cm) around the PTV as well as maximum dose to the PTV for a spherical target with 4 cm diameter centered in a cylindrical water phantom. The first column gives the angle separating the two SFO fields. The other columns give the maximum dose of the respective volumes in Gy and the proportions of maximum dose of the respective volume at 0° in % for a spherical target with 4 cm diameter centered in a cylindrical water phantom.*

Diff	Max. dose to PTV	Max. dose to PTV/Max. dose to PTV at 0°	Max. dose to ring 0-0.5cm	Max. dose to ring 0.0-0.5cm/ Max. dose to ring 0-0.5cm at 0°	Max. dose to ring 0.5-1.0cm	Max. dose to ring 0.5-1.0cm/ Max. dose to ring 0.5-1.0cm at 0°	Max. dose to ring 1.0-1.5cm	Max. dose to ring 1.0-1.5cm/ Max. dose to ring 1.0-1.5cm at 0°	Max. dose to ring 1.5-2.5cm	Max. dose to ring 1.5-2.5cm/ Max. dose to ring 1.5-2.5cm at 0°
[°]	[Gy]	[%]	[Gy]	[%]	[Gy]	[%]	[Gy]	[%]	[Gy]	[%]
0	55.4	100.0	55.0	100.0	52.8	100.0	46.0	100.0	43.0	100.0
10	55.6	100.4	55.0	100.0	52.8	100.0	46.6	101.3	43.6	101.4
20	55.4	100.0	55.2	100.4	53.0	100.4	46.8	101.7	43.6	101.4
30	55.2	99.6	55.0	100.0	52.8	100.0	46.8	101.7	43.6	101.4
40	55.2	99.6	55.0	100.0	52.8	100.0	46.4	100.9	43.2	100.5
50	55.0	99.3	55.0	100.0	52.8	100.0	46.2	100.4	42.6	99.1
60	55.2	99.6	54.8	99.6	52.6	99.6	46.6	101.3	42.6	99.1
70	55.2	99.6	55.0	100.0	52.4	99.2	45.6	99.1	41.0	95.3
80	55.0	99.3	55.0	100.0	52.4	99.2	45.6	99.1	37.8	87.9
90	55.4	100.0	55.4	100.7	52.4	99.2	43.8	95.2	32.6	75.8
100	55.0	99.3	55.0	100.0	52.6	99.6	42.6	92.6	26.5	61.6
110	55.4	100.0	55.2	100.4	51.8	98.1	39.2	85.2	26.3	61.2
120	55.4	100.0	55.4	100.7	51.6	97.7	37.8	82.2	26.0	60.5
130	55.2	99.6	54.8	99.6	50.6	95.8	37.0	80.4	25.8	60.0
140	55.2	99.6	55.2	100.4	51.4	97.3	39.0	84.8	25.5	59.3
150	55.2	99.6	55.0	100.0	51.2	97.0	37.4	81.3	24.7	57.4
160	55.2	99.6	55.0	100.0	51.0	96.6	35.4	77.0	22.5	52.3
170	55.2	99.6	54.8	99.6	50.0	94.7	34.0	73.9	22.1	51.4
180	55.4	100.0	55.0	100.0	49.8	94.3	32.2	70.0	21.8	50.7

Clinical case

Fig. 34 - *Fig. 36* show the results for the LET_d distributions and the maximum LET_d values. These values were similar to those obtained for the phantom case. Of course the values were not exactly the same. However, for the sphere as well as for the patient the maximum LET_d and dose values to the PTV decreased just slightly with increasing separation angle, whereas the maximum dose values to the two rings which are furthest away from the target did not change much till an separation angle of about 40°, then they fell about 30 to 50%. If one wants to adduce a difference between the clinical and the phantom case most obvious might be that for the clinical one the structure where the highest maximum LET_d values occurred was always the ring 1.5 to 2.5 cm around the PTV for the phantom case until an separation angle of 80° the highest LET_d values were obtained in rings closer to the PTV.

The percentage of the $TNTV_B$´s total volume receiving at least 5 or 10 Gy increased, receiving at least 20 or 30 Gy decreased with growing angle between the two beams (*Fig. 37* and *Table 14)*.

Fig. 40 depicts similarities and differences between the clinical and phantom situation by displaying for both cases the change in maximum LET_d to the PTV as well as to the rings around the PTV when modifying the angle between two fields.

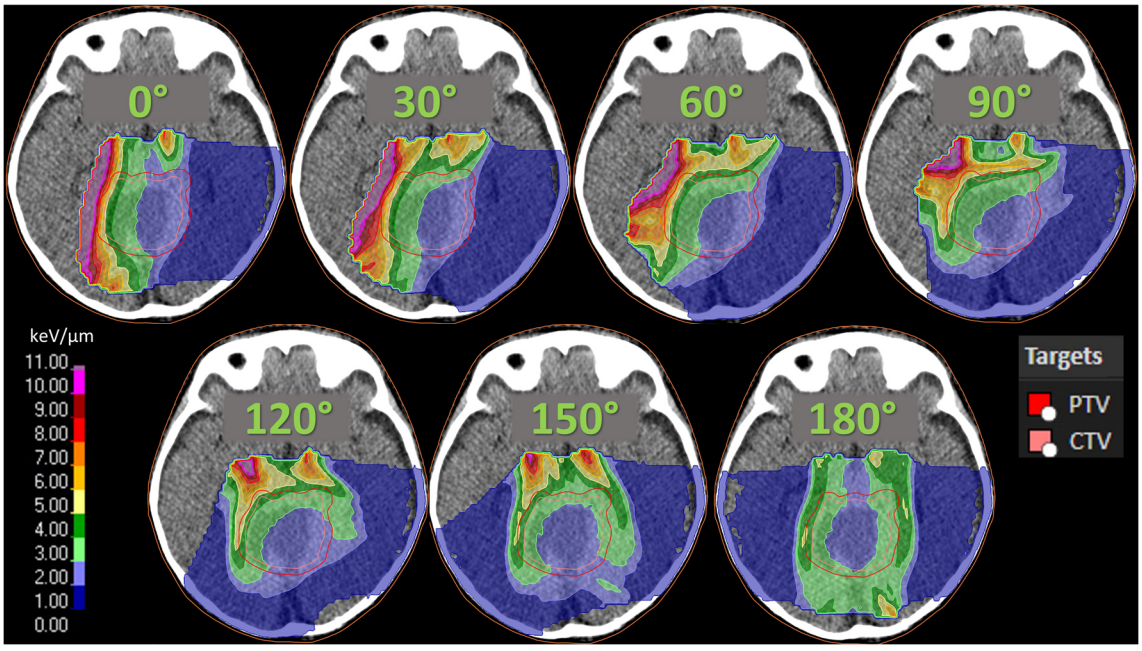

Fig. 34: *Calculated LET_d distributions for investigating the angular dependence for a clinical case – a pediatric head tumor.*

Two SFO fields separated by an increasing angle exemplary for seven different angles.

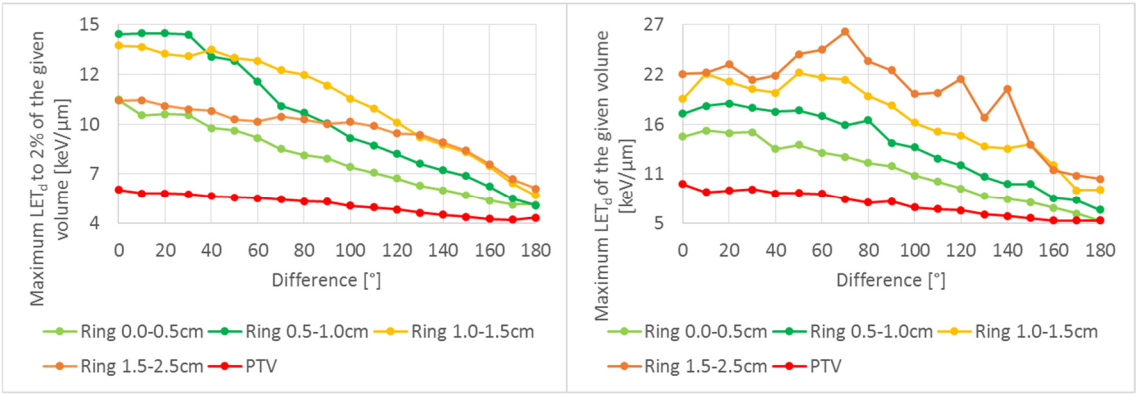

Fig. 35: *Angular dependence. Maximum LET$_d$ to 2% of (left picture) respectively maximum LET$_d$ to (right picture) four different rings (0.0 to 0.5 cm, 0.5 to 1.0 cm, 1.0 to 1.5 cm, 1.5 to 2.5 cm) around the PTV as well as maximum LET$_d$ to 2% of respectively maximum LET$_d$ to the PTV as a function of the angle separating two SFO beams in keV/µm for a clinical case – a pediatric head tumor.*

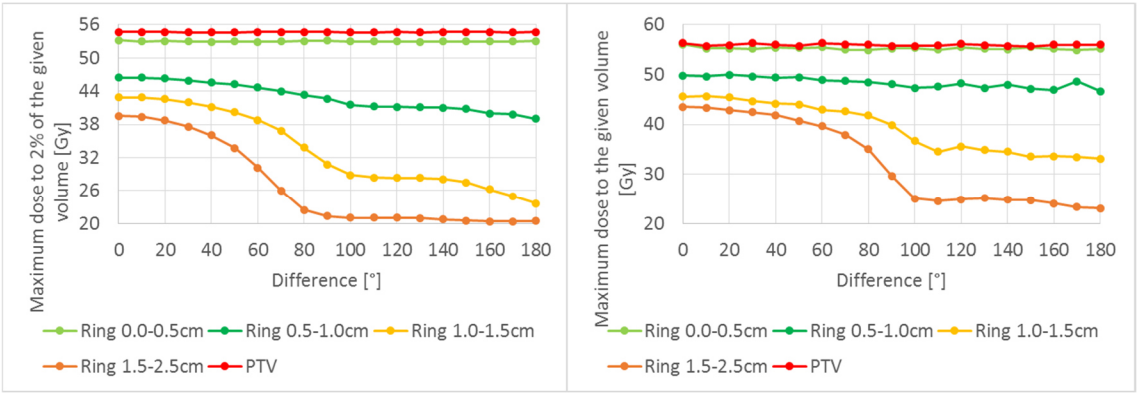

Fig. 36: *Angular dependence. Maximum dose to 2% of (left picture) respectively maximum dose to four different rings (0.0 to 0.5 cm, 0.5 to 1.0 cm, 1.0 to 1.5 cm, 1.5 to 2.5 cm) around the PTV as well as maximum dose to 2% of respectively maximum dose to the PTV as a function of the angle separating two SFO beams in Gy for a clinical case – a pediatric head tumor.*

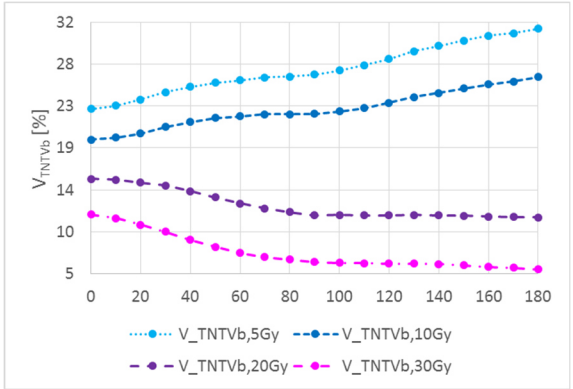

Fig. 37*: Percentage of the TNTV$_B$ receiving at least 5, 10, 20 and 30 Gy (RBE) as a function of the angle separating two SFO beams for a clinical case – a pediatric head tumor.*

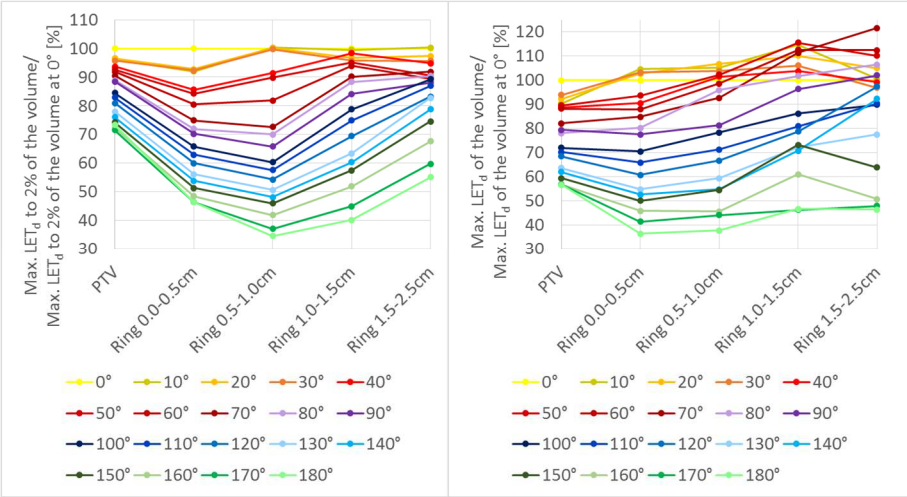

Fig. 38: *Angular dependence. Maximum LET$_d$ to 2% of (left picture) respectively maximum LET$_d$ to (right picture) four different rings (0.0 to 0.5 cm, 0.5 to 1.0 cm, 1.0 to 1.5 cm, 1.5 to 2.5 cm) around the PTV as well as maximum LET$_d$ to 2% of respectively maximum LET$_d$ to the PTV divided by the maximum LET$_d$ to 2% of respectively maximum LET$_d$ to the given volume using two beams separated by an angle of 0° of eighteen different angles separating two SFO beams in [%] for a clinical case – a pediatric head tumor.*

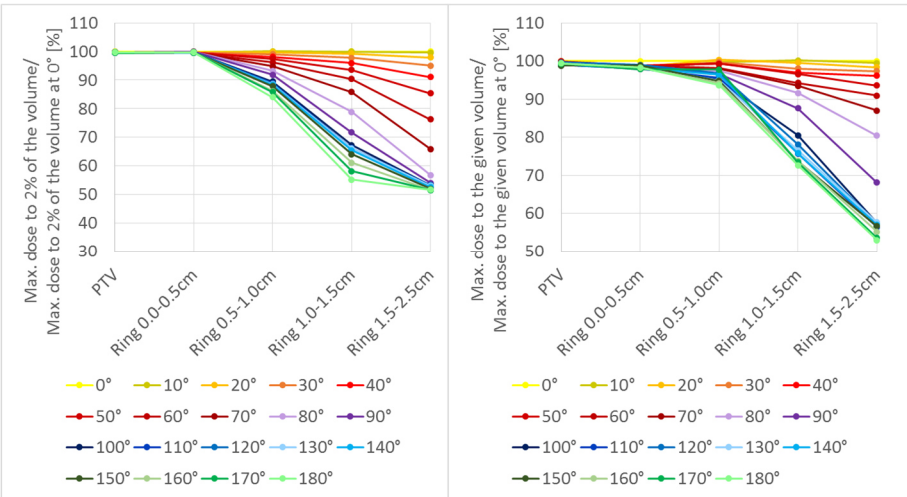

Fig. 39: *Angular dependence. Maximum dose to 2 % of (left picture) respectively maximum dose to (right picture) four different rings (0.0 to 0.5 cm, 0.5 to 1.0 cm, 1.0 to 1.5 cm, 1.5 to 2.5 cm) around the PTV as well as maximum dose to 2% of respectively maximum dose to the PTV divided by the maximum dose to 2% of respectively maximum dose to the given volume using two beams separated by an angle of 0° of eighteen different angles separating two SFO beams in [%] for a clinical case – a pediatric head tumor.*

Table 10: *Angular dependence. Maximum LET_d to 2% of four different rings (0.0 to 0.5 cm, 0.5 to 1.0 cm, 1.0 to 1.5 cm, 1.5 to 2.5 cm) around the PTV as well as maximum LET_d to 2% of the PTV for a clinical case – a pediatric head tumor. The first column gives the angle separating the two SFO fields. The other columns give the maximum LET_d of the respective volumes in keV/µm and the proportions of maximum LET_d of the respective volume at 0° in %.*

Diff	Max. LET_d to 2% of PTV	Max. LET_d to 2% of PTV/Max. LET_d to 2% of PTV at 0°	Max. LET_d to 2% of ring 0-0.5cm	Max. LET_d to 2% of ring 0.0-0.5cm/ Max. LET_d to 2% of ring 0-0.5cm at 0°	Max. LET_d to 2% of ring 0.5-1.0cm	Max. LET_d to 2% of ring 0.5-1.0cm/ Max. LET_d to 2% of ring 0.5-1.0cm at 0°	Max. LET_d to 2% of ring 1.0-1.5cm	Max. LET_d to 2% of ring 1.0-1.5cm/ Max. LET_d to 2% of ring 1.0-1.5cm at 0°	Max. LET_d to 2% of ring 1.5-2.5cm	Max. LET_d to 2% of ring 1.5-2.5cm/ Max. LET_d to 2% of ring 1.5-2.5cm at 0°
[°]	[keV/µm]	[%]	[keV/µm]	[%]	[keV/µm]	[%]	[keV/µm]	[%]	[keV/µm]	[%]
0	5.9	100.0	10.9	100.0	14.5	100.0	13.9	100.0	10.8	100.0
10	5.7	96.3	10.0	92.0	14.5	100.3	13.8	99.5	10.8	100.3
20	5.7	96.6	10.1	92.7	14.5	100.2	13.4	96.7	10.5	97.3
30	5.6	95.7	10.0	92.3	14.5	99.8	13.3	95.7	10.3	95.7
40	5.5	93.7	9.3	85.7	13.2	91.4	13.6	98.3	10.2	94.8
50	5.5	92.7	9.2	84.3	13.0	89.8	13.2	95.1	9.8	90.5
60	5.4	91.9	8.7	80.5	11.9	81.8	13.0	93.9	9.7	89.5
70	5.3	90.5	8.1	74.9	10.5	72.6	12.5	90.2	9.9	91.9
80	5.2	88.9	7.8	71.9	10.1	70.0	12.2	88.3	9.8	90.5
90	5.2	88.4	7.6	70.2	9.5	65.8	11.7	84.1	9.5	88.1
100	5.0	84.4	7.1	65.7	8.7	60.4	10.9	78.8	9.6	89.2
110	4.9	82.9	6.8	62.9	8.3	57.6	10.4	74.9	9.4	87.0
120	4.8	81.0	6.5	60.0	7.9	54.3	9.6	69.4	9.0	83.3
130	4.6	78.0	6.1	56.1	7.3	50.6	8.8	63.4	8.9	82.7
140	4.5	76.1	5.8	53.8	7.0	48.1	8.4	60.3	8.5	78.8
150	4.4	74.3	5.6	51.3	6.7	45.9	8.0	57.5	8.1	74.6
160	4.3	72.2	5.3	48.5	6.1	41.9	7.2	51.9	7.3	67.7
170	4.2	71.4	5.0	46.4	5.4	37.1	6.2	45.0	6.5	59.8
180	4.3	73.4	5.0	46.4	5.0	34.5	5.6	40.2	5.9	55.0

Table 11*: Angular dependence. Maximum LET_d to four different rings (0.0 to 0.5 cm, 0.5 to 1.0 cm, 1.0 to 1.5 cm, 1.5 to 2.5 cm) around the PTV as well as maximum LET_d to the PTV for a clinical case – a pediatric head tumor. The first column gives the angle separating the two SFO fields. The other columns give the maximum LET_d of the respective volumes in keV/µm and the proportions of maximum LET_d of the respective volume at 0° in %.*

Diff	Max. LET^d to PTV	Max. LET^d to PTV/Max. LET^d to PTV at 0°	Max. LET^d to ring 0.0-0.5cm	Max. LET^d to ring 0.0-0.5cm/ Max. LET^d to ring 0-0.5cm at 0°	Max. LET^d to ring 0.5-1.0cm	Max. LET^d to ring 0.5-1.0cm/ Max. LET^d to ring 0.5-1.0cm at 0°	Max. LET^d to ring 1.0-1.5cm	Max. LET^d to ring 1.0-1.5cm/ Max. LET^d to ring 1.0-1.5cm at 0°	Max. LET^d to ring 1.5-2.5cm	Max. LET^d to ring 1.5-2.5cm/ Max. LET^d to ring 1.5-2.5cm at 0°
[°]	[keV/µm]	[%]	[keV/µm]	[%]	[keV/µm]	[%]	[keV/µm]	[%]	[keV/µm]	[%]
0	9.39	100.00	14.67	100.00	17.18	100.00	18.80	100.00	21.58	100.00
10	8.48	90.35	15.33	104.56	18.05	105.09	21.56	114.70	21.70	100.55
20	8.66	92.22	15.06	102.66	18.33	106.72	20.70	110.10	22.64	104.91
30	8.82	93.91	15.13	103.15	17.82	103.72	19.92	105.99	20.90	96.84
40	8.33	88.74	13.28	90.56	17.42	101.43	19.51	103.78	21.39	99.13
50	8.41	89.61	13.73	93.60	17.56	102.21	21.71	115.52	23.77	110.16
60	8.29	88.23	12.90	87.96	16.93	98.56	21.16	112.56	24.24	112.35
70	7.71	82.11	12.44	84.79	15.93	92.71	20.93	111.36	26.23	121.56
80	7.33	78.01	11.75	80.15	16.47	95.89	19.12	101.69	22.98	106.52
90	7.46	79.39	11.37	77.55	13.95	81.23	18.10	96.29	22.00	101.95
100	6.75	71.93	10.33	70.45	13.46	78.36	16.19	86.13	19.37	89.79
110	6.59	70.18	9.65	65.82	12.26	71.34	15.20	80.87	19.50	90.36
120	6.43	68.45	8.91	60.72	11.46	66.70	14.79	78.67	21.02	97.42
130	5.98	63.63	8.04	54.81	10.20	59.40	13.55	72.06	16.72	77.48
140	5.81	61.88	7.71	52.57	9.40	54.74	13.31	70.81	19.90	92.22
150	5.57	59.34	7.34	50.08	9.37	54.56	13.77	73.24	13.77	63.80
160	5.32	56.66	6.73	45.88	7.82	45.53	11.47	61.00	10.94	50.71
170	5.33	56.75	6.06	41.34	7.58	44.11	8.70	46.27	10.33	47.88
180	5.32	56.69	5.33	36.36	6.48	37.72	8.78	46.69	10.00	46.34

Table 12: *Angular dependence. Maximum dose to 2% of four different rings (0.0 to 0.5 cm, 0.5 to 1.0 cm, 1.0 to 1.5 cm, 1.5 to 2.5 cm) around the PTV as well as maximum dose to 2% of the PTV for a clinical case – a pediatric head tumor. The first column gives the angle separating the two SFO fields. The other columns give the maximum dose of the respective volumes in Gy and the proportions of maximum dose of the respective volume at 0° in %.*

Diff	Max. dose to 2% of PTV	Max. dose to 2% of PTV/Max. dose to 2% of PTV at 0°	Max. dose to 2% of ring 0-0.5cm	Max. dose to 2% of ring 0.0-0.5cm/ Max. dose to 2% of ring 0-0.5cm at 0°	Max. dose to 2% of ring 0.5-1.0cm	Max. dose to 2% of ring 0.5-1.0cm/ Max. dose to 2% of ring 0.5-1.0cm at 0°	Max. dose to 2% of ring 1.0-1.5cm	Max. dose to 2% of ring 1.0-1.5cm/ Max. dose to 2% of ring 1.0-1.5cm at 0°	Max. dose to 2% of ring 1.5-2.5cm	Max. dose to 2% of ring 1.5-2.5cm/ Max. dose to 2% of ring 1.5-2.5cm at 0°
[°]	[Gy]	[%]	[Gy]	[%]	[Gy]	[%]	[Gy]	[%]	[Gy]	[%]
0	55.2	100.0	53.1	100.0	46.4	100.0	42.9	100.0	39.5	100.0
10	55.1	99.8	52.9	99.6	46.4	100.1	42.9	100.0	39.4	99.6
20	55.0	99.7	53.0	99.7	46.3	99.7	42.6	99.3	38.7	97.9
30	55.0	99.7	53.0	99.7	45.9	99.0	41.9	97.8	37.6	95.1
40	55.0	99.7	52.9	99.5	45.6	98.2	41.2	95.9	36.0	91.1
50	55.0	99.6	52.9	99.6	45.2	97.4	40.2	93.6	33.8	85.4
60	55.0	99.7	52.9	99.6	44.6	96.2	38.8	90.4	30.2	76.3
70	55.1	99.8	53.0	99.7	44.0	94.8	36.8	85.9	26.0	65.9
80	55.0	99.6	53.1	99.8	43.3	93.3	33.8	78.9	22.5	56.8
90	55.0	99.7	53.1	99.9	42.7	91.9	30.8	71.7	21.4	54.1
100	55.0	99.6	52.9	99.6	41.5	89.5	28.9	67.3	21.1	53.2
110	55.0	99.7	53.0	99.6	41.3	88.9	28.4	66.2	21.1	53.3
120	55.1	99.8	53.0	99.7	41.1	88.7	28.3	66.0	21.0	53.2
130	55.0	99.7	52.9	99.5	41.1	88.6	28.4	66.1	21.0	53.1
140	55.0	99.7	52.9	99.6	41.0	88.3	28.1	65.5	20.8	52.5
150	55.0	99.7	53.0	99.7	40.8	87.8	27.5	64.1	20.6	52.0
160	55.0	99.7	53.0	99.6	40.0	86.2	26.2	61.1	20.4	51.6
170	55.0	99.6	53.0	99.6	39.8	85.8	25.0	58.2	20.4	51.5
180	55.0	99.7	53.0	99.8	39.0	84.0	23.7	55.2	20.5	51.7

Table 13*: Angular dependence. Maximum dose to four different rings (0.0 to 0.5 cm, 0.5 to 1.0 cm, 1.0 to 1.5 cm, 1.5 to 2.5 cm) around the PTV as well as maximum dose to the PTV for clinical case – a pediatric head tumor. The first column gives the angle separating the two SFO fields. The other columns give the maximum dose of the respective volumes in Gy and the proportions of maximum dose of the respective volume at 0° in % for a spherical target with 4 cm diameter centered in a cylindrical water phantom.*

Diff	Max. dose to PTV	Max. dose to PTV/Max. dose to PTV at 0°	Max. dose to ring 0-0.5cm	Max. dose to ring 0.0-0.5cm/ Max. dose to ring 0-0.5cm at 0°	Max. dose to ring 0.5-1.0cm	Max. dose to ring 0.5-1.0cm/ Max. dose to ring 0.5-1.0cm at 0°	Max. dose to ring 1.0-1.5cm	Max. dose to ring 1.0-1.5cm/ Max. dose to ring 1.0-1.5cm at 0°	Max. dose to ring 1.5-2.5cm	Max. dose to ring 1.5-2.5cm/ Max. dose to ring 1.5-2.5cm at 0°
[°]	[Gy]	[%]	[Gy]	[%]	[Gy]	[%]	[Gy]	[%]	[Gy]	[%]
0	56.3	100.0	56.1	100.0	49.8	100.0	45.6	100.0	43.6	100.0
10	55.7	99.0	55.2	98.4	49.6	99.7	45.6	100.1	43.3	99.5
20	55.9	99.2	55.2	98.5	49.9	100.3	45.4	99.6	42.8	98.4
30	56.2	99.9	55.1	98.3	49.6	99.7	44.7	98.0	42.4	97.4
40	56.0	99.4	55.4	98.8	49.4	99.3	44.2	97.0	41.9	96.1
50	55.7	99.0	55.3	98.6	49.4	99.4	44.0	96.6	40.7	93.5
60	56.3	99.9	55.4	98.9	48.8	98.2	43.0	94.3	39.6	91.0
70	56.0	99.4	55.0	98.0	48.7	97.9	42.6	93.5	37.9	87.0
80	56.0	99.4	54.9	97.9	48.5	97.4	41.7	91.6	35.0	80.5
90	55.7	99.0	55.2	98.5	48.0	96.6	39.9	87.6	29.7	68.2
100	55.7	99.0	55.3	98.6	47.3	95.1	36.7	80.5	25.0	57.5
110	55.8	99.1	55.0	98.1	47.6	95.6	34.5	75.8	24.6	56.5
120	56.1	99.7	55.5	99.0	48.2	96.9	35.6	78.1	24.9	57.2
130	55.9	99.3	55.1	98.3	47.3	95.0	34.9	76.6	25.1	57.7
140	55.7	99.0	55.1	98.2	48.0	96.4	34.6	75.8	24.8	57.0
150	55.6	98.8	55.4	98.8	47.2	94.8	33.6	73.6	24.7	56.7
160	56.0	99.4	55.1	98.3	46.9	94.2	33.6	73.8	24.0	55.2
170	55.9	99.3	54.9	97.8	48.6	97.7	33.5	73.4	23.3	53.6
180	56.0	99.4	55.1	98.3	46.6	93.7	33.1	72.7	23.1	53.0

Table 14: *Angular dependence. Percentage of the TNTVB´s total volume receiving at least 5, 10, 20 and 30 Gy for a clinical case – a pediatric head tumor. The first column gives the angle separating the two SFO fields.*

Diff [°]	$V_{TNTVb,5Gy}$ [%]	$V_{TNTVb,10Gy}$ [%]	$V_{TNTVb,20Gy}$ [%]	$V_{TNTVb,30Gy}$ [%]
0	22.70	19.37	15.19	11.36
10	23.04	19.59	15.10	10.97
20	23.68	20.04	14.78	10.23
30	24.47	20.73	14.47	9.50
40	25.07	21.29	13.85	8.62
50	25.49	21.72	13.21	7.87
60	25.77	21.91	12.53	7.21
70	26.07	22.12	12.01	6.79
80	26.14	22.12	11.60	6.51
90	26.37	22.16	11.28	6.27
100	26.83	22.41	11.29	6.15
110	27.38	22.77	11.28	6.10
120	28.06	23.34	11.24	6.07
130	28.86	23.97	11.31	6.09
140	29.47	24.39	11.27	6.02
150	30.00	24.86	11.21	5.89
160	30.55	25.33	11.15	5.73
170	30.79	25.63	11.07	5.64
180	31.28	26.09	11.03	5.44

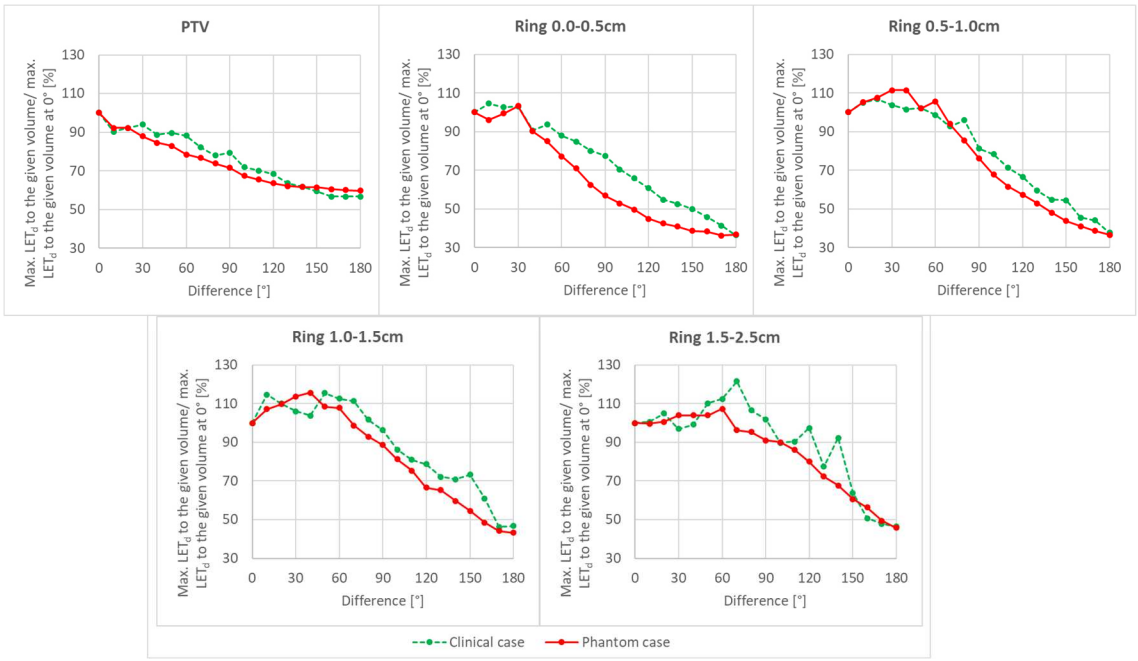

Fig. 40: *Angular dependence. Comparison between the clinical case and the phantom case. Maximum LET_d to four different rings (0.0 to 0.5 cm, 0.5 to 1.0 cm, 1.0 to 1.5 cm, 1.5 to 2.5 cm) around the PTV as well as maximum LET_d to the PTV divided by the maximum LET_d to the given volumes for the clinical case (green dashed line) and for the phantom case (red solid line) are shown.*

3.2.3 Depth and field size dependence

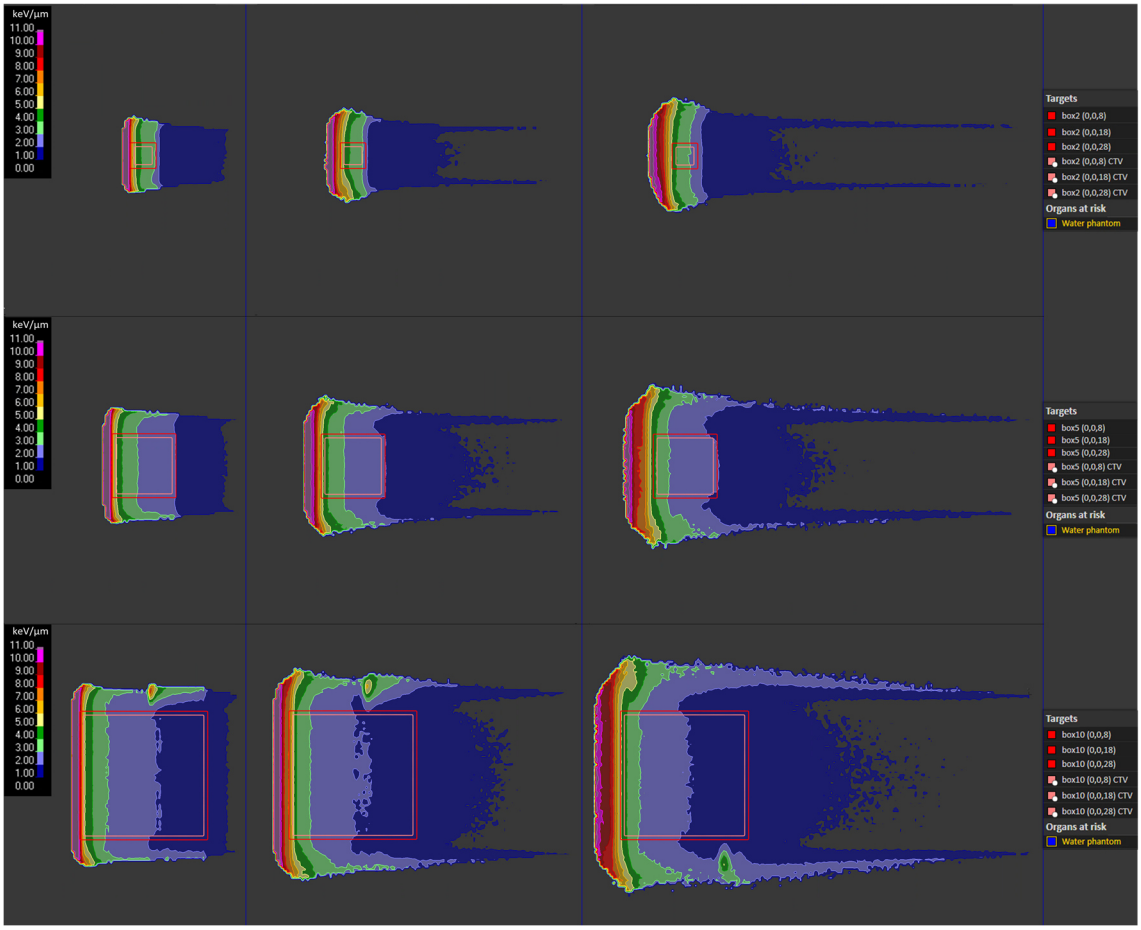

Fig. 41: *Calculated LET_d distributions for investigating the depth and field size dependence. A (2x2x2) cm^3 (images on the top), a (5x5x5) cm^3 (images in the middle) and a (10x10x10) cm^3 (images on the bottom) water target were centered at a depth of 8 cm (images on the left), 18 cm (images in the middle) and 28 cm (images on the right) in a water phantom. The beam direction is always from right to left.*

Analysis of the depth found the highest maximum LET_d for superficial targets (*Fig. 41*). LET_d profiles along the central beam axis of the targets obtained when investigating the depth and field size dependence are presented in *Fig. 43*. Evaluating the field size dependence revealed: the smaller the target, the higher the maximum LET_d. *Fig. 42* illustrates the values of maximum LET_d to respectively to 2% of the target for the three different target sizes as a function of the target´s depth respectively for the three different target depths as a function of target size. *Table 15* lists the abbreviations for the different cubical targets used in this master thesis.

The Wedenberg et al. model (see section *1.3.4 RBE Models*) was used to calculate RBE and RBE-weighted dose profiles (*Fig. 44*). A figure as well as a table showing the relative and absolute deviations of those values from the corresponding calculations applying a constant RBE of 1.1 can be found in the appendix (*A.2 Depth and field size dependence - Results: Fig. 100* and *Table 24*). Two different parameters for the tissue radiosensitivity were investigated: an α/β of 2 Gy and of 10 Gy. As already mentioned in section *Wedenberg et al. model*, Wedenberg et al. reported that 0.434 Gy µm/keV was the value of the parameter *q* of their model which fitted best their experimental data (Wedenberg, Lind, & Hårdemark, 2013). This q value was also used for calculations presented in the following.

A summary of the maximum LET_ds, RBEs and RBE weighted doses as well as the depths at which those maxima occurred can be found in *Table 16* and *Table 17*. They show a similar dependence on depth and size for the maximum RBE as for the maximum LET_d values. For each

box the depths of the RBE and LET_d were identical. The corresponding RBE-weighted dose maxima were located less deep. The RBE-weighted dose maxima were typically found in a position deeper than the distal edge of the target. *Fig. 45* shows the calculated maximum RBEs and maximum RBE-weighted doses.

***Table 15**: Depth and field size dependence. Target nomenclature.*
The first column gives the labels of the targets, the second column gives the depth of the targets centers in a water phantom and the third the side lengths of the cubical targets.

Target label	Depth [cm]	Side length of the cubical target [cm]
box2 (0,0,8)	8	2
box5 (0,0,8)	8	5
box10 (0,0,8)	8	10
box2 (0,0,18)	18	2
box5 (0,0,18)	18	5
box10 (0,0,18)	18	10
box2 (0,0,28)	28	2
box5 (0,0,28)	28	5
box10 (0,0,28)	28	10

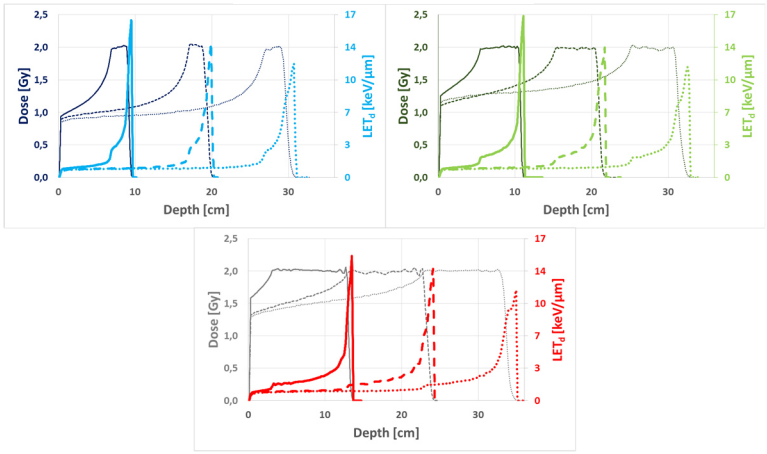

***Fig. 43**: Depth and field size dependence. RBE-weighted dose profiles (dark blue, dark green respective grey lines) and LET_d profiles (light blue, light green respective. red lines) along the central beam axis of water targets with three different sizes ((2x2x2) cm^3 (upper left image), (5x5x5) cm^3 (upper right image) and (10x10x10) cm^3 (lower image)) at a depth of 8 cm (solid lines), 18 cm (dashed lines) and 28 cm (dotted lines).*

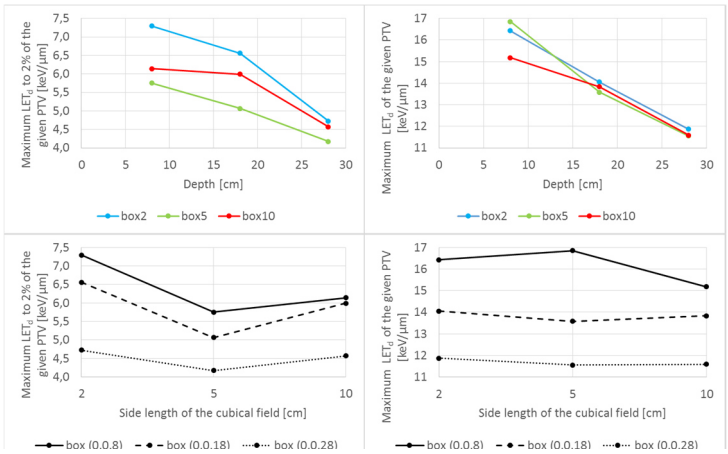

***Fig. 42:** Depth and field size dependence. Maximum LET_d along the central axis of water targets to 2% of the given PTV (pictures on the left) respectively to the given PTV (pictures on the right) in keV/µm as a function of the targets' depths (upper pictures) respectively side lengths of the cubical targets (lower pictures).*

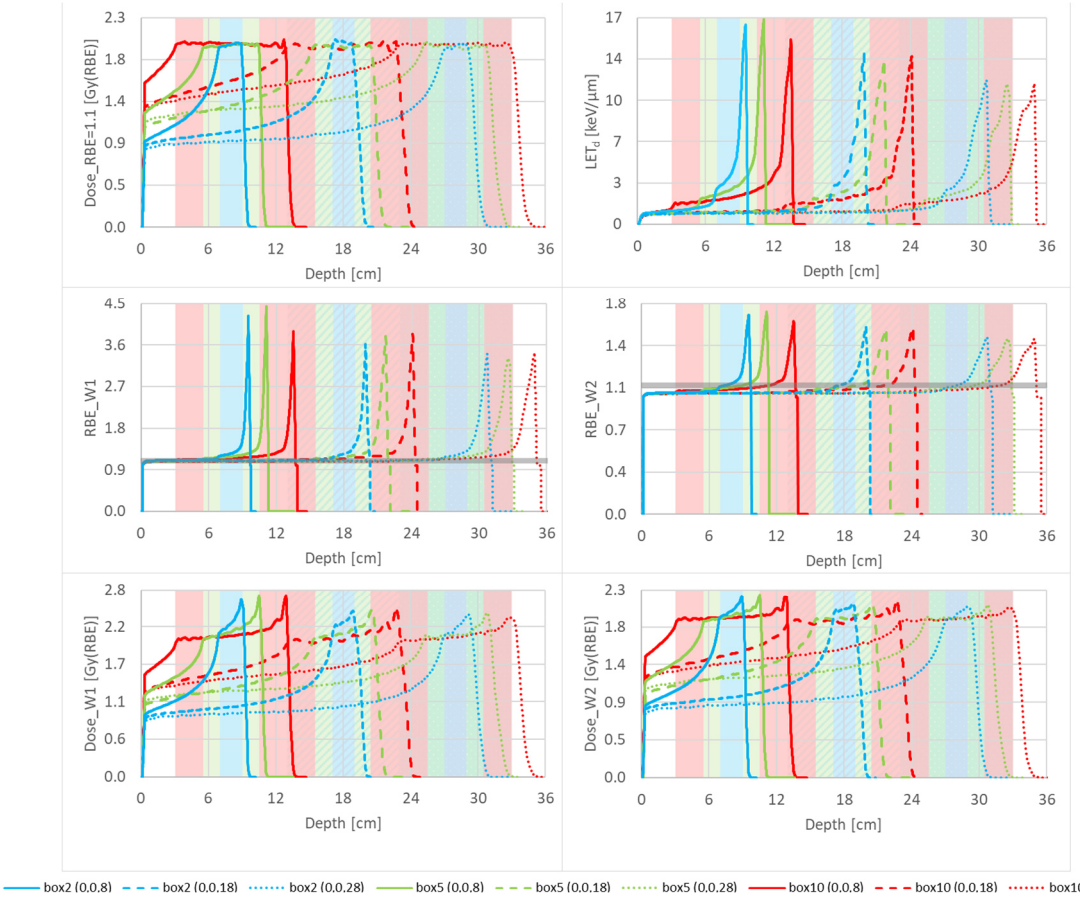

***Fig. 44**: Depth and field size dependence. RBE-weighted dose (calculated using a constant RBE of 1.1; picture on the top, left side), LET$_d$ (picture on the top, right sight), RBE (pictures in the second row, the straight horizontal orange line depicts the constant RBE of 1.1) and RBE-weighted dose (pictures in the third row) profiles along a line through the center of a (2x2x2) cm^3 (blue lines), a (5x5x5) cm^3 (green lines) and a (10x10x10) cm^3 (red lines) box at a depth of 8 cm (solid lines), 18 cm (dashed lines) and 28 cm (dotted lines) calculated using the Wedenberg et al. model and an α/β value of 2 Gy (pictures on the left) respectively 10 Gy (pictures on the right). The colors in the background depict the locations of the different boxes.*

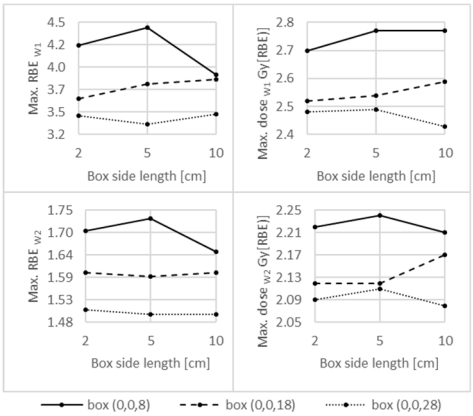

***Fig. 45:** Depth and field size dependence. Maximum RBE (pictures in the first column) and maximum RBE-weighted dose (pictures in the second column) occurring along a line through the center of a (2x2x2) cm^3), a (5x5x5) cm^3 respectively a (10x10x10) cm^3 box at a depth of 8 cm (solid lines), 18 cm (dashed lines) and 28 cm as a function of the box side length calculated using the Wedenberg et al. and α/β value of 2 Gy (pictures on the top) respectively 10 Gy (pictures on the bottom).*

Table 16: *Depth and field size dependence. Investigation of the RBE-weighted dose calculated with the Wedenberg et al. model using an α/β value of 2 Gy.*
The first column gives the labels of the targets, the second column gives the calculated maximum LET_ds, the third the depths at which the maximum LET_ds occurred, the fourth the calculated maximum RBEs, the fifth the depths at which the maximum RBEs occurred, the sixth the calculated maximum RBE-weighted doses and the seventh the depths at which the maximum RBE-weighted doses occurred.

Target label	Max. LET_d [keV/µm]	Depth of max. LET_d [cm]	Max. RBE_{W1}	Depth of max. RBE_{W1} [cm]	Max. $dose_{W1}$ [Gy(RBE)]	Depth of max. $dose_{W1}$ [cm]
box2 (0,0,8)	16.43	9.51	4.23	9.52	2.65	8.92
box5 (0,0,8)	16.86	11.12	4.44	11.13	2.72	10.52
box10 (0,0,8)	15.18	13.52	3.89	13.52	2.72	12.92
box2 (0,0,18)	14.05	19.92	3.62	19.92	2.47	18.91
box5 (0,0,18)	13.58	21.71	3.79	21.71	2.49	20.53
box10 (0,0,18)	13.83	24.12	3.84	24.12	2.54	22.72
box2 (0,0,28)	11.87	30.71	3.42	30.72	2.43	29.12
box5 (0,0,28)	11.56	32.52	3.32	32.52	2.44	30.73
box10 (0,0,28)	11.59	34.91	3.44	34.91	2.38	32.95

Table 17: *Depth and field size dependence. Investigation of the RBE-weighted dose calculated with the Wedenberg et al. model using an α/β value of 10 Gy.*
The first column gives the labels of the targets, the second column gives the calculated maximum LET_ds, the third the depths at which the maximum LET_ds occurred, the fourth the calculated maximum RBEs, the fifth the depths at which the maximum RBEs occurred, the sixth the calculated maximum RBE-weighted doses and the seventh the depths at which the maximum RBE-weighted doses occurred.

Target label	Max. LET_d [keV/µm]	Depth of max. LET_d [cm]	Max. RBE_{W2}	Depth of max. RBE_{W2} [cm]	Max. $dose_{W2}$ [Gy(RBE)]	Depth of max. $dose_{W2}$ [cm]
box2 (0,0,8)	16.43	9.51	1.70	9.51	2.22	8.91
box5 (0,0,8)	16.86	11.12	1.73	11.12	2.24	10.52
box10 (0,0,8)	15.18	13.52	1.65	13.52	2.21	12.74
box2 (0,0,18)	14.05	19.92	1.60	19.92	2.12	18.72
box5 (0,0,18)	13.58	21.71	1.59	21.71	2.12	20.52
box10 (0,0,18)	13.83	24.12	1.60	24.12	2.17	22.72
box2 (0,0,28)	11.87	30.71	1.51	30.71	2.09	29.11
box5 (0,0,28)	11.56	32.52	1.50	32.52	2.11	30.72
box10 (0,0,28)	11.59	34.91	1.50	34.91	2.08	32.73

3.2.4 Number of beams dependence

The LET_d distributions resulting from an increase of the number of beams are displayed in *Fig. 46*. Cleary visible at first glance is that adding a second beam has the highest impact on the LET_d distribution. When just one beam was used the highest LET_d values occurred in the distal-fall off. The areas where LET_d exceeded 7 keV/µm almost disappeared when using two beams, completely disappeared when using three or more beams. LET_d gradients inside and outside the PTV decreased. The henceforth highest LET_d values (of about 4 keV/µm) appeared in a ring bordering the PTV. In the center of the PTV an area with LET_d values lower than 3 keV/µm emerged. In the remaining parts of the PTV LET_d was about 3 keV/µm.

The values of maximum LET_d respectively to 2% of the PTV and to four rings around the PTV (*Fig. 47*) reflect what was just mentioned. Using two instead of one beam could decrease maximum LET_d to the rings around the PTV by 31 to 71% (*Fig. 50*). Maximum LET_d to the PTV was reduced by 36%. The further reduction of maximum LET_d when using three or more fields was less than 13% for the rings and the PTV. The maximum dose to respectively to 2% of the PTV and the two rings closest to the PTV (*Fig. 48*) stayed almost the same for all numbers of beams. The maximum dose to the two other rings decreased by 30 (ring 1.0 to 1.5 cm around the PTV) respectively 50% (ring 1.5 to 2.5 cm around the PTV) when using two beams instead of one (*Fig. 51*). Starting from six beams those values did not change considerably. The average LET_d to the PTV hardly varied for all numbers of beams (*Fig. 49*). The minimum LET_d first increased, the maximum LET_d first decreased, starting from a number of two beams, both values remained nearly unchanged. *Table 18* - *Table 21* give the computed LET_d and dose values.

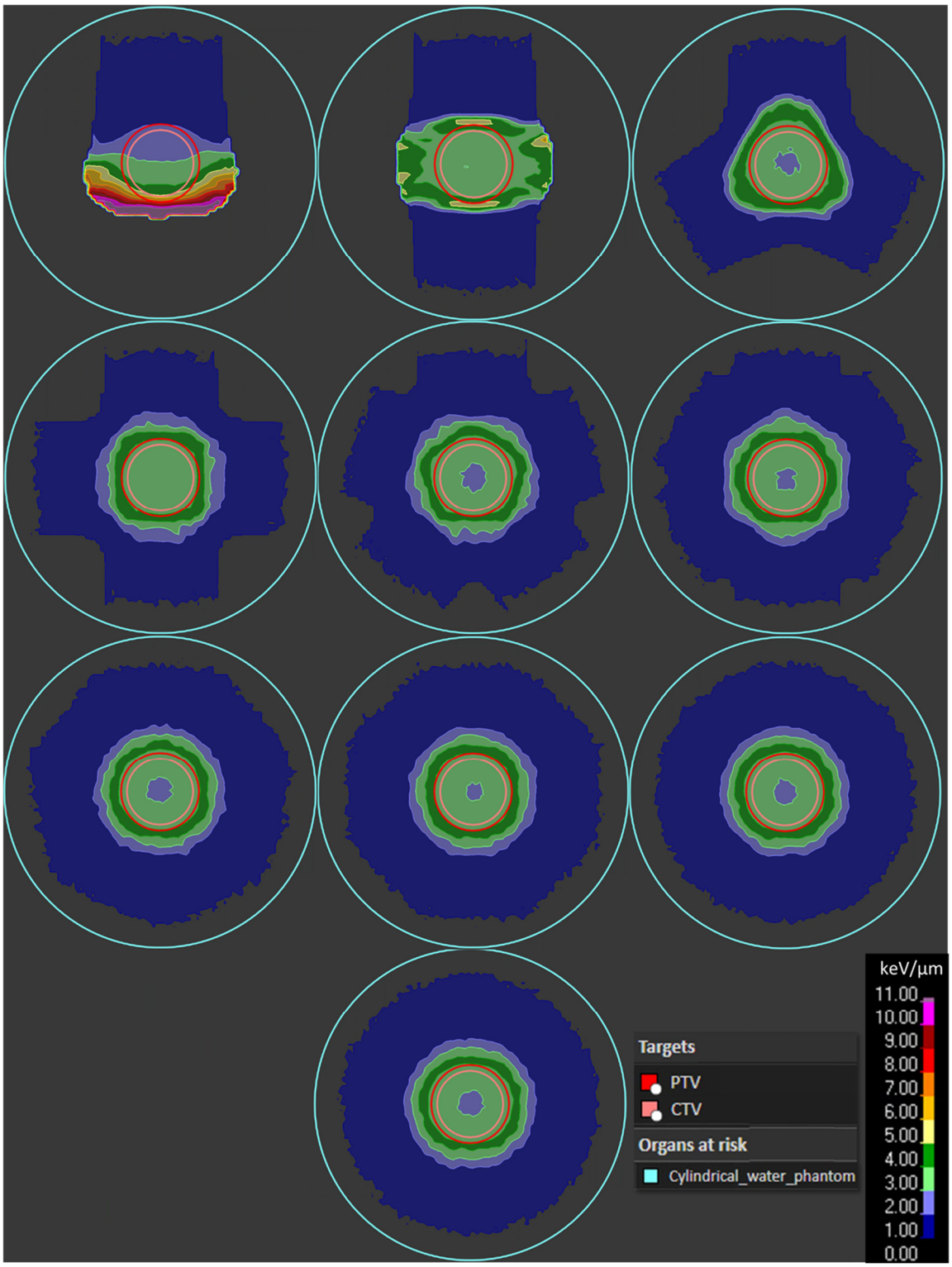

Fig. 46: *Calculated LET_d distributions for investigating the dependence on the number of beams.*

The number of SFO beams for a spherical target with 4 cm diameter centered in a cylindrical water phantom was increased from one to ten.

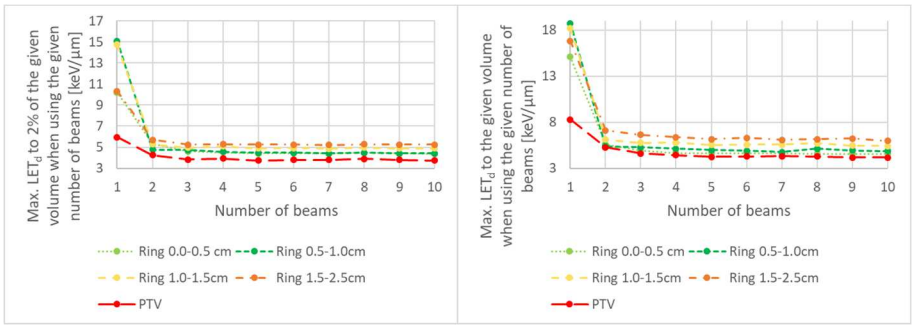

Fig. 47: *Dependence on the number of beams. Maximum LET$_d$ to 2% of (left picture) respectively maximum LET$_d$ to (right picture) four different rings (0.0 to 0.5 cm, 0.5 to 1.0 cm, 1.0 to 1.5 cm, 1.5 to 2.5 cm) around the PTV as well as maximum LET$_d$ to 2% of respectively maximum LET$_d$ to the PTV as a function of the number of SFO beams in keV/µm.*

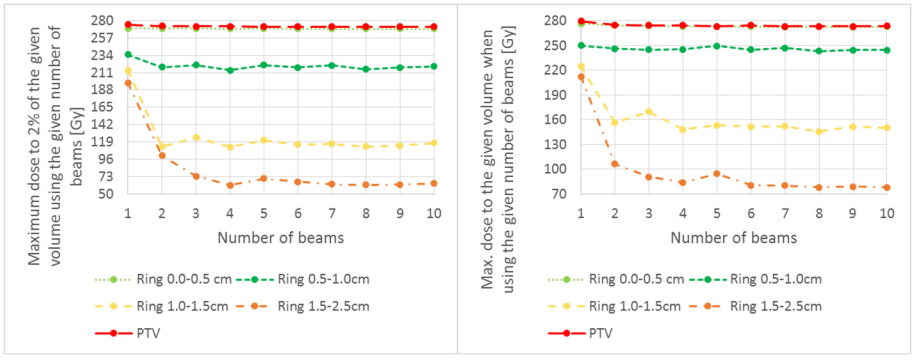

Fig. 48*: Dependence on the number of beams. Maximum dose to 2% of (left picture) respectively maximum dose to (right picture) four different rings (0.0 to 0.5 cm, 0.5 to 1.0 cm, 1.0 to 1.5 cm, 1.5 to 2.5 cm) around the PTV as well as maximum dose to 2% of respectively maximum LET$_d$ to the PTV as a function of the number of SFO beams in Gy.*

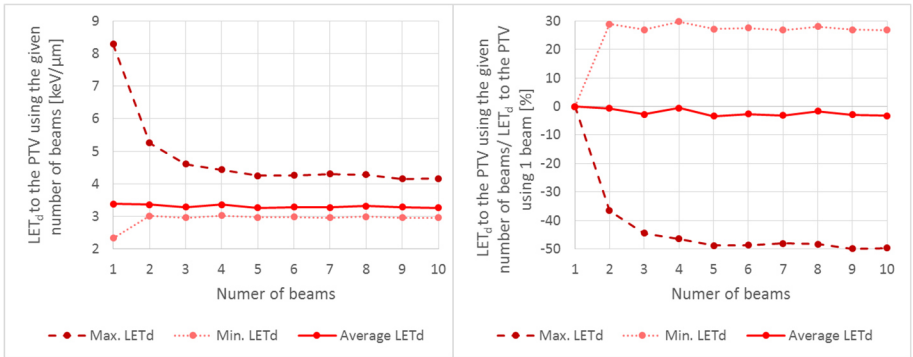

Fig. 49: *Dependence on the number of beams. Maximum, minimum and average LET$_d$ to the PTV as a function of the number of SFO beams in keV/µm (left picture) as well as relative deviations of those values from the corresponding values obtained when using one beam in % (right picture).*

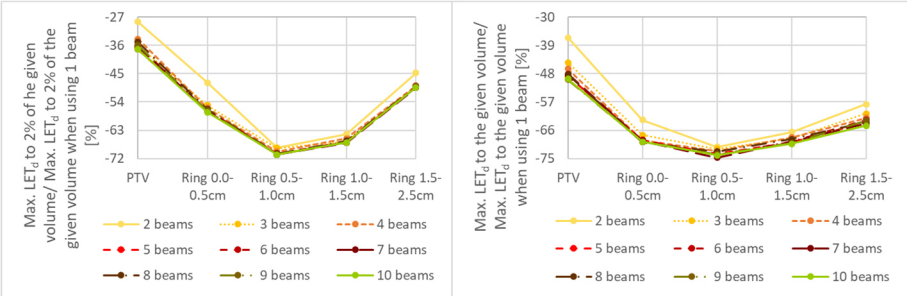

Fig. 50: *Dependence on the number of beams. Relative deviations of maximum LET_ds (right picture) to respectively to 2% of (left picture) the given volume when using two to ten SFO beams from the maximum LET_ds to respectively to 2% of the given volume obtained when using one beam in %.*

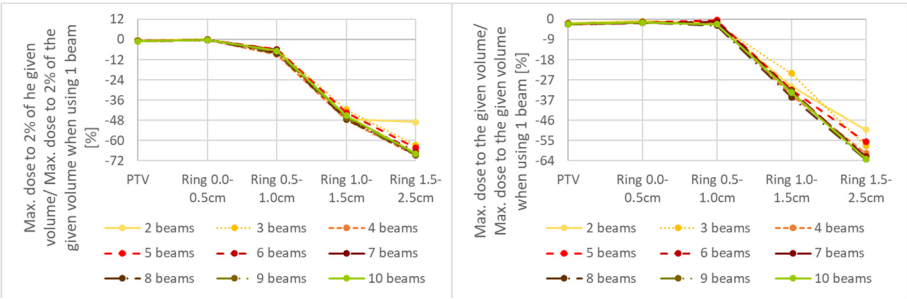

Fig. 51: *Dependence on the number of beams. Relative deviations of maximum doses (right picture) to respectively to 2% of (left picture) the given volume when using two to ten SFO beams from the maximum doses to respectively to 2% of the given volume obtained when using one beam in %.*

Table 18: *Number of beams dependence. Maximum LET_d to 2% of four different rings (0.0 to 0.5 cm, 0.5 to 1.0 cm, 1.0 to 1.5 cm, 1.5 to 2.5 cm) around the PTV as well as maximum LET_d to 2% of the PTV for a spherical target with 4 cm diameter centered in a cylindrical water phantom. The first column gives the number of used SFO fields. The other columns give the maximum LET_d to 2% of the respective volumes in keV/µm and the proportions of maximum LET_d to 2% of the respective volume obtained when using one beam in %.*

# of beams	Max. LET_d to 2% of PTV	Max. LET_d to 2% of PTV/Max. LET_d to 2% of PTV for 1 beam	Max. LET_d to 2% of ring 0.0-0.5cm	Max. LET_d to 2% of ring 0.0-0.5cm/ Max. LET_d to 2% of ring 0-0.5cm for 1 beam	Max. LET_d to 2% of ring 0.5-1.0cm	Max. LET_d to 2% of ring 0.5-1.0cm/ Max. LET_d to 2% of ring 0.5-1.0cm for 1 beam	Max. LET_d to 2% of ring 1.0-1.5cm	Max. LET_d to 2% of ring 1.0-1.5cm/ Max. LET_d to 2% of ring 1.0-1.5cm for 1 beam	Max. LET_d to 2% of ring 1.5-2.5cm	Max. LET_d to 2% of ring 1.5-2.5cm/ Max. LET_d to 2% of ring 1.5-2.5cm for 1 beam
	[keV/µm]	[%]	[keV/µm]	[%]	[keV/µm]	[%]	[keV/µm]	[%]	[keV/µm]	[%]
1	6.0	100.0	10.2	100.0	15.1	100.0	14.7	100.0	10.3	100.0
2	4.3	71.5	5.3	52.2	4.8	31.6	5.3	35.7	5.7	55.3
3	3.8	64.1	4.6	45.0	4.7	31.2	5.0	33.6	5.2	50.8
4	3.9	66.0	4.5	44.1	4.6	30.2	5.1	34.4	5.3	51.2
5	3.7	62.7	4.4	43.0	4.5	29.6	4.9	33.1	5.2	50.6
6	3.8	63.8	4.4	43.4	4.5	29.6	4.9	33.3	5.2	50.8
7	3.8	63.6	4.4	43.3	4.4	29.3	4.9	33.0	5.2	50.6
8	3.9	65.1	4.5	43.8	4.5	29.6	5.0	33.6	5.3	50.9
9	3.8	64.0	4.4	43.2	4.4	29.2	4.9	33.1	5.2	50.7
10	3.7	62.8	4.4	42.8	4.4	29.3	4.9	33.1	5.2	50.7

Table 19: *Number of beams dependence. Maximum LET_d to four different rings (0.0 to 0.5 cm, 0.5 to 1.0 cm, 1.0 to 1.5 cm, 1.5 to 2.5 cm) around the PTV as well as maximum LET_d to the PTV for a spherical target with 4 cm diameter centered in a cylindrical water phantom. The first column gives the number of used SFO fields. The other columns give the maximum LET_d of the respective volumes in keV/µm and the proportions of maximum LET_d of the respective volume obtained when using one beam in %.*

# of beams	Max. LET_d to PTV	Max. LET_d to PTV/Max. LET_d to PTV for 1 beam	Max. LET_d to ring 0.0-0.5cm	Max. LET_d to ring 0.0-0.5cm/ Max. LET_d to ring 0-0.5cm for 1 beam	Max. LET_d to ring 0.5-1.0cm	Max. LET_d to ring 0.5-1.0cm/ Max. LET_d to ring 0.5-1.0cm for 1 beam	Max. LET_d to ring 1.0-1.5cm	Max. LET_d to ring 1.0-1.5cm/ Max. LET_d to ring 1.0-1.5cm for 1 beam	Max. LET_d to ring 1.5-2.5cm	Max. LET_d to ring 1.5-2.5cm/ Max. LET_d to ring 1.5-2.5cm for 1 beam
	[keV/µm]	[%]	[keV/µm]	[%]	[keV/µm]	[%]	[keV/µm]	[%]	[keV/µm]	[%]
1	8.3	100.0	15.1	100.0	18.7	100.0	18.2	100.0	16.8	100.0
2	5.3	63.5	5.6	37.2	5.4	28.7	6.1	33.4	7.1	42.3
3	4.6	55.5	4.9	32.5	5.3	28.0	5.7	31.4	6.6	39.3
4	4.4	53.6	4.7	30.8	5.1	27.3	5.8	31.8	6.4	37.9
5	4.2	51.2	4.7	30.9	5.0	26.5	5.5	30.3	6.2	36.5
6	4.3	51.4	4.7	30.8	4.9	26.2	5.6	30.5	6.3	37.3
7	4.3	51.9	4.6	30.6	4.8	25.3	5.6	30.4	6.1	36.1
8	4.3	51.7	4.6	30.2	5.1	27.2	5.7	31.2	6.2	36.5
9	4.1	50.1	4.6	30.3	4.9	26.4	5.4	29.9	6.2	37.1
10	4.2	50.3	4.6	30.3	4.9	26.0	5.4	29.7	6.0	35.5

Table 20: *Number of beams dependence. Maximum dose to 2% of four different rings (0.0 to 0.5 cm, 0.5 to 1.0 cm, 1.0 to 1.5 cm, 1.5 to 2.5 cm) around the PTV as well as maximum dose to 2% of the PTV for a spherical target with 4 cm diameter centered in a cylindrical water phantom. The first column gives the angle separating the two SFO fields. The other columns give the maximum dose to 2% of the respective volumes in Gy and the proportions of maximum dose to 2% of the respective when using one beam in %.*

# of beams	Max. dose to 2% of PTV	Max. dose to 2% of PTV/Max. dose to 2% of PTV for 1 beam	Max. dose to 2% of ring 0.0-0.5cm	Max. dose to 2% of ring 0.0-0.5cm/ Max. dose to 2% of ring 0-0.5cm for 1 beam	Max. dose to 2% of ring 0.5-1.0cm	Max. dose to 2% of ring 0.5-1.0cm/ Max. dose to 2% of ring 0.5-1.0cm for 1 beam	Max. dose to 2% of ring 1.0-1.5cm	Max. dose to 2% of ring 1.0-1.5cm/ Max. dose to 2% of ring 1.0-1.5cm for 1 beam	Max. dose to 2% of ring 1.5-2.5cm	Max. dose to 2% of ring 1.5-2.5cm/ Max. dose to 2% of ring 1.5-2.5cm for 1 beam
	[Gy]	[%]	[Gy]	[%]	[Gy]	[%]	[Gy]	[%]	[Gy]	[%]
1	274.5	100.0	269.7	100.0	235.0	100.0	214.3	100.0	197.4	100.0
2	273.0	99.5	269.7	100.0	218.4	92.9	112.8	52.7	100.6	51.0
3	272.5	99.3	269.6	100.0	221.0	94.0	124.9	58.3	73.4	37.2
4	272.4	99.2	269.3	99.8	214.2	91.1	112.3	52.4	61.6	31.2
5	272.0	99.1	269.4	99.9	221.0	94.0	121.1	56.5	70.4	35.7
6	272.0	99.1	269.3	99.9	217.9	92.7	115.5	53.9	65.9	33.4
7	271.9	99.0	269.1	99.8	220.5	93.8	116.6	54.4	62.8	31.8
8	271.8	99.0	269.1	99.8	215.3	91.6	112.7	52.6	62.1	31.5
9	271.8	99.0	269.2	99.8	217.8	92.7	114.4	53.4	62.5	31.7
10	271.7	99.0	269.1	99.8	219.1	93.2	117.4	54.8	63.6	32.2

Table 21: *Number of beams dependence. Maximum dose to four different rings (0.0 to 0.5 cm, 0.5 to 1.0 cm, 1.0 to 1.5 cm, 1.5 to 2.5 cm) around the PTV as well as maximum dose to the PTV for a spherical target with 4 cm diameter centered in a cylindrical water phantom. The first column gives the angle separating the two SFO fields. The other columns give the maximum dose of the respective volumes in Gy and the proportions of maximum dose of the respective volume when using one beam in %.*

# of beams	Max. dose to PTV	Max. dose to PTV/Max. dose to PTV for 1 beam	Max. dose to ring 0.0-0.5cm	Max. dose to ring 0.0-0.5cm/ Max. dose to ring 0-0.5cm for 1 beam	Max. dose to ring 0.5-1.0cm	Max. dose to ring 0.5-1.0cm/ Max. dose to ring 0.5-1.0cm for 1 beam	Max. dose to ring 1.0-1.5cm	Max. dose to ring 1.0-1.5cm/ Max. dose to ring 1.0-1.5cm for 1 beam	Max. dose to ring 1.5-2.5cm	Max. dose to ring 1.5-2.5cm/ Max. dose to ring 1.5-2.5cm for 1 beam
	[Gy]	[%]	[Gy]	[%]	[Gy]	[%]	[Gy]	[%]	[Gy]	[%]
1	279.4	100.0	276.6	100.0	250.0	100.0	224.6	100.0	212.2	100.0
2	274.6	98.3	274.4	99.2	246.1	98.4	156.5	69.7	106.1	50.0
3	274.3	98.1	273.7	98.9	244.6	97.8	169.7	75.5	90.8	42.8
4	274.1	98.1	273.1	98.7	245.3	98.1	147.9	65.8	83.7	39.5
5	273.2	97.8	273.2	98.8	249.2	99.7	153.1	68.2	94.4	44.5
6	274.3	98.2	272.4	98.5	244.8	97.9	151.5	67.4	80.4	37.9
7	273.2	97.7	272.3	98.4	247.0	98.8	151.9	67.6	80.1	37.7
8	273.2	97.8	272.8	98.7	243.0	97.2	145.6	64.8	77.8	36.7
9	273.2	97.7	272.3	98.5	244.5	97.8	151.3	67.4	78.8	37.2
10	273.5	97.9	272.5	98.5	244.4	97.8	150.2	66.8	78.0	36.7

3.3 Investigation of the influence of different optimization settings on LET_d distributions

3.3.1 Phantom case

The dose and LET_d distributions as well as the location of pencil beams when using the Pencil Beam instead of the Monte Carlo algorithm (see section *2.1 Research TPS – RS v5.99.50*) which were calculated for the spherical phantoms using different optimization settings are shown in *Fig. 52 - Fig. 56.* They make the consequences the different optimization settings had on the location and weight of the individual Bragg peaks beams clear. Let us look at the phantom one field case first. As described in section *2.1.3 Plan design – planning parameters* in more detail the treatment planner can change the parameters *Min spot weight* and *Max spot weight*. Those indicate limits used when filtering out low respectively high weight spots. Let us look at the phantom one field case first. Without a limitation of maximum spot weight, the spot weight of the last energy layer (more precisely the last energy layer before the distal energy layer) had by far the highest spot weight. The spot weight of the other spots was clearly smaller. Introducing a maximum spot weight lowered the spot weight of spots with a higher weight than the limit. The relative reduction of the weights of those spots that exceed the limit the most was the highest. The difference between high and low weighted spot weights decreased. Therefore, in the depiction of spots the size of the points before the last high weighted energy layer increased. Setting also a minimum spot weight resulted in disappearance of the lowest weighted spots. Changing the number of distal energy layers from one two three added two more energy layers after the highest weighted energy layer in the distal area of the field. However, the added individual spots did not always exceed the default limit of minimum spot weight. Some of the spots were filtered out. Therefore not after every high weighted spot three crosses displaying the individual Bragg peaks were apparent. For the two field plans the position and weight of the individual spots for both fields are shown. The figure for each of the two SFO fields seemed not to differ from the one field figure. At a first glance the SFO and MFO pencil beam illustration looked very similar. On closer inspection of the case for which the angle between the two fields was 180° some differences could be recognized. When using single-field optimization all higher weighted spots were located in the distal areas and the whole PTV was covered uniformly with spots. Whereas in the MFO plans some higher weighted spots occurred in the proximal distal energy layers. Moreover, small areas without any spots inside the target could be identified.

When looking at the LET_d distributions calculated for two SFO fields separated by an angle of 180° (*Fig. 55*) a noticeable effect appeared: In the target cold spots of LET_d could be seen in the plans with three distal energy layers and maximum spot weight limitation respectively minimum and maximum spot weight limitation. The same characteristic occurred in the MFO field plan with three distal energy layers (*Fig. 56*).

Fig. 57 - Fig. 59 as well as *Table 22* and *Table 23* illustrate that neither maximum LET_d nor maximum dose to respectively to 2% of the PTV changed significantly when changing optimization settings. The highest absolute change in maximum LET_d values was noticed for the single field plans. Furthermore, the highest maximum LET_d values occurred not always in the same ring around the PTV depending on the used optimization settings, whereas the lowest maximum LET_d values were in the PTV for all different plans. A different behavior was found for the dose: The highest maximum dose values always occurred in the PTV. Moreover, the further away the evaluation structure from the target, the lower was its maximum dose value. When looking at the variations in minimum, average and maximum LET_d respectively dose to 50% and 98% of the PTV in *Fig. 59* one might notice that those were by tendency the highest for the maximum LET_d values.

Line doses (*Fig. 61*) of the different plans were exported along a line through the center of the spherical target (*Fig. 60*). With the use of the Wedenberg et al. model (see section *1.3.4 RBE Models*) RBE, RBE-weighted dose and the relative deviation of those values from the

corresponding calculations applying a constant RBE of 1.1 were determined (*Fig. 62* - *Fig. 64*). For the RBE-weighted doses the absolute deviations are also shown (*Fig. 65*). Three different scenarios were simulated to consider the tissue radiosensitivity: an α/β of 2 Gy, 10 Gy respectively of 10 Gy in the CTV and of 2 Gy around the CTV. The q value was always 0.434 Gy µm/keV. The almost linear relation between LET_d and RBE values computed with the Wedenberg et al. model values is displayed in *Fig. 66.*

Fig. 61 indicates that the highest of all maximum LET_d values appeared in ring 0.5 to 1.0 cm around the PTV as well as in ring 1.0 to 1.5 cm and ring 0.0 to 0.5 cm around the PTV. Since, however physical dose decreased abruptly outside the PTV, the enhanced LET_d values affected the biological dose computed using the Wedenberg et al. model significantly only in the PTV and the ring 0.0 to 0.5 cm around the PTV (*Fig. 63*). In other words, even though the relation between LET_d and RBE predicted by the Wedenberg et al. model was almost linear (*Fig. 66*), the highest biological-weighted dose values did not arise from the highest RBE values. The absolute difference between the RBE-weighted doses calculated taking account of the LET_d distributions and the RBE-weighted dose computed using a constant value was the highest in the areas located directly next to the target (*Fig. 65*).

Applying an α/β value of 2 Gy led to a calculated RBE of more than 1.2 in the whole PTV for all plans. RBE values close to 2.0 were computed in the distal regions of the fields. In areas more than 2 cm away from the target the computed RBE values were smaller than 1.1. Using an α/β value of 10 Gy caused an average RBE of approximately 1.1 in the target, a bit less in the proximal, a bit more (up to around 1.5) in the distal areas of the fields. The RBEs calculated using an α/β value of 10 Gy were smaller than those computed applying an α/β value of 2 Gy for all distances. Employing an α/β value of 10 Gy in the CTV and of 2 Gy around the CTV came along with an average RBE of about 1.1 in the target, of almost 2.0 in the rings 0.0 to 1.0 cm around the target.

The minimum LET_d values at which the RBE values calculated using the Wedenberg et al. model exceeded a value of 1.1 can be read out from *Fig. 66*. Those LET_d values were 1.41 keV/µm for an α/β value of 2 Gy, 3.25 keV/µm for an an α/β value of 10 Gy and 1.90 keV/µm for an α/β value of 10 Gy in the CTV and 2 Gy around the CTV.

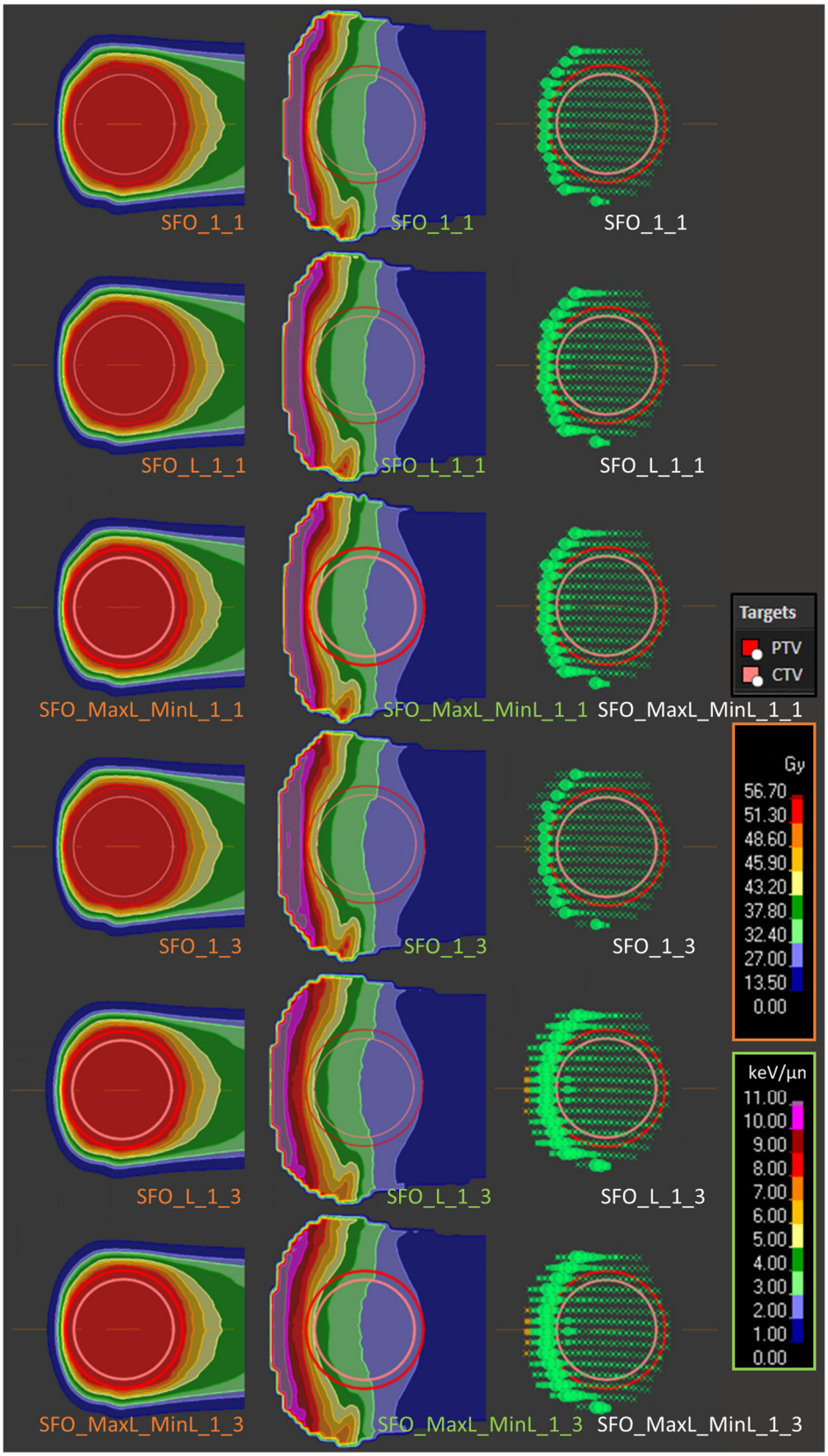

Fig. 52: *Calculated dose (pictures on the left) and LET_d distributions (pictures in the middle) as well as the positions of the individual Bragg peaks displayed as crosses (pictures on the right) for investigating the influence of different optimization settings. The larger the dots on the cross, the higher is the relative spot weight within a field. One field (coming from the right) irradiated a spherical target with 4 cm diameter centered in a cylindrical water phantom.*

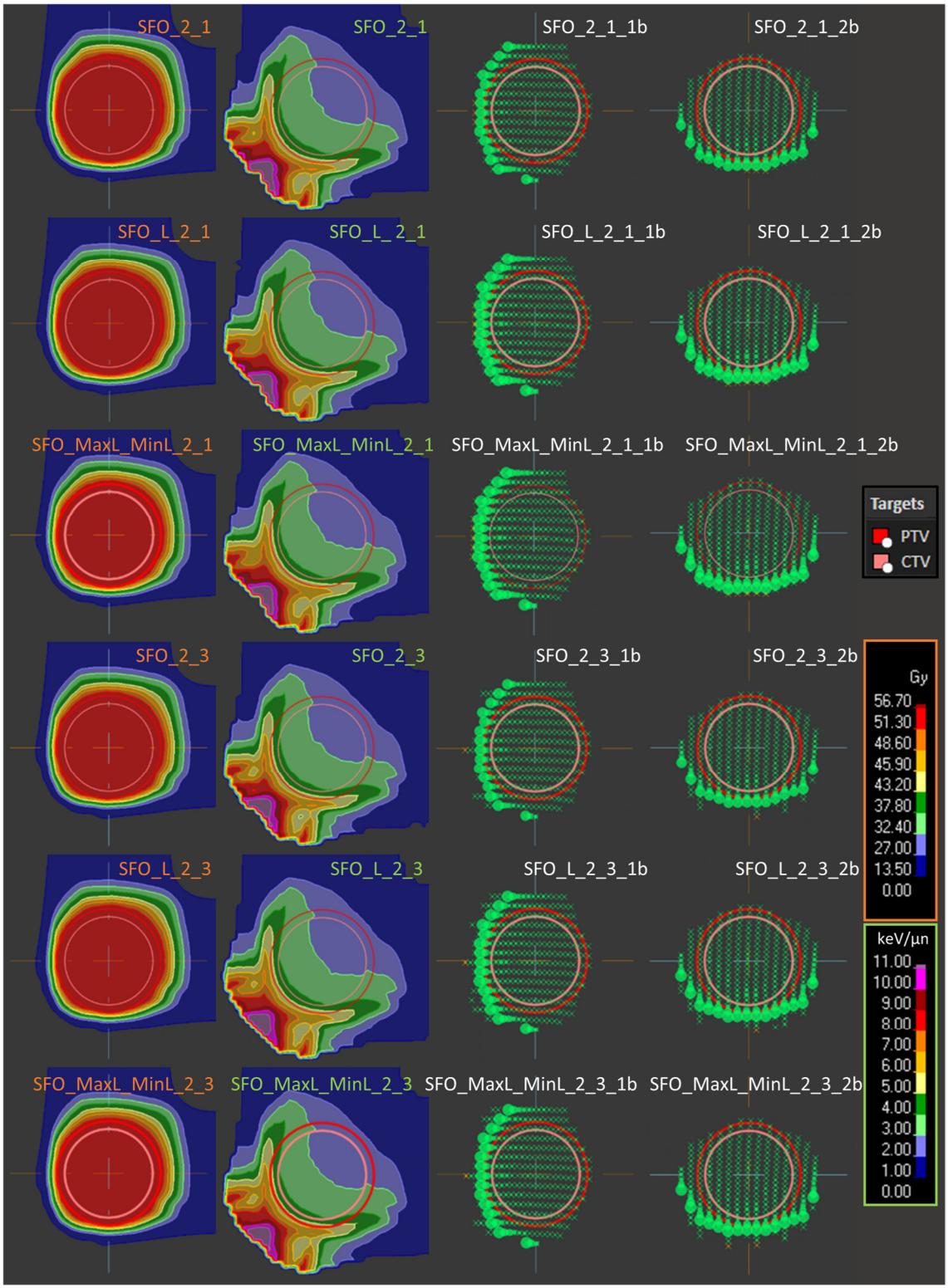

Fig. 53: *Calculated dose (pictures on the left) and LET_d distributions (pictures in the middle) as well as the positions of the individual Bragg peaks displayed as crosses (two pictures on the right) for investigating the influence of different optimization settings. The larger the dots on the cross, the higher is the relative spot weight within a field. Two SFO-fields separated by an angle of 90° (one coming from the right abbreviated with "1b" and one coming from above abbreviated with "2b") irradiated a spherical target with 4 cm diameter centered in a cylindrical water phantom.*

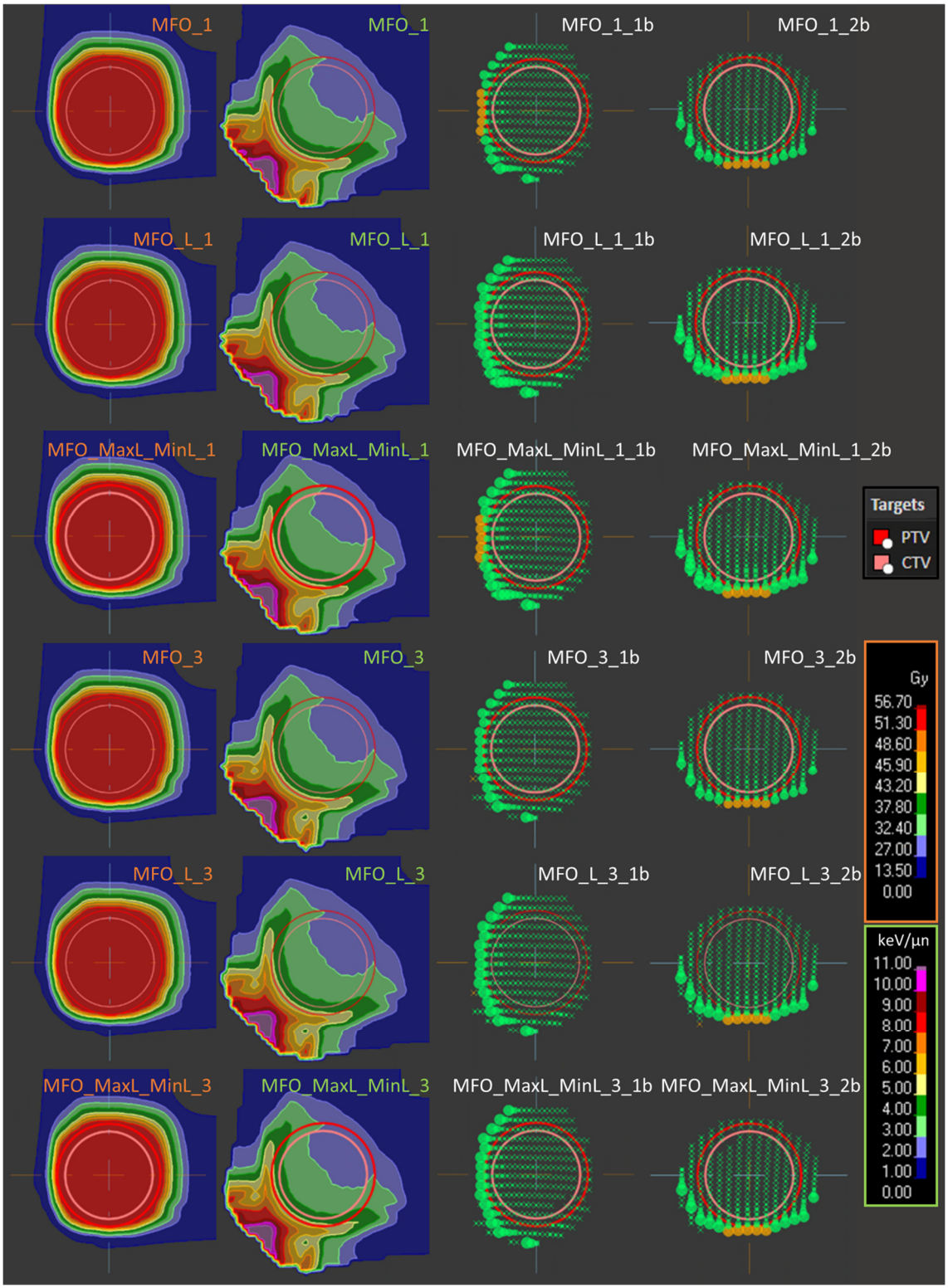

Fig. 54: *Calculated dose (pictures on the left) and LET_d distributions (pictures in the middle) as well as the positions of the individual Bragg peaks displayed as crosses (two pictures on the right) for investigating the influence of different optimization settings. The larger the dots on the cross, the higher is the relative spot weight within a field. Two MFO fields separated by an angle of 90° (one coming from the right abbreviated with "1b" and one coming from above abbreviated with "2b") irradiated a spherical target with 4 cm diameter centered in a cylindrical water phantom.*

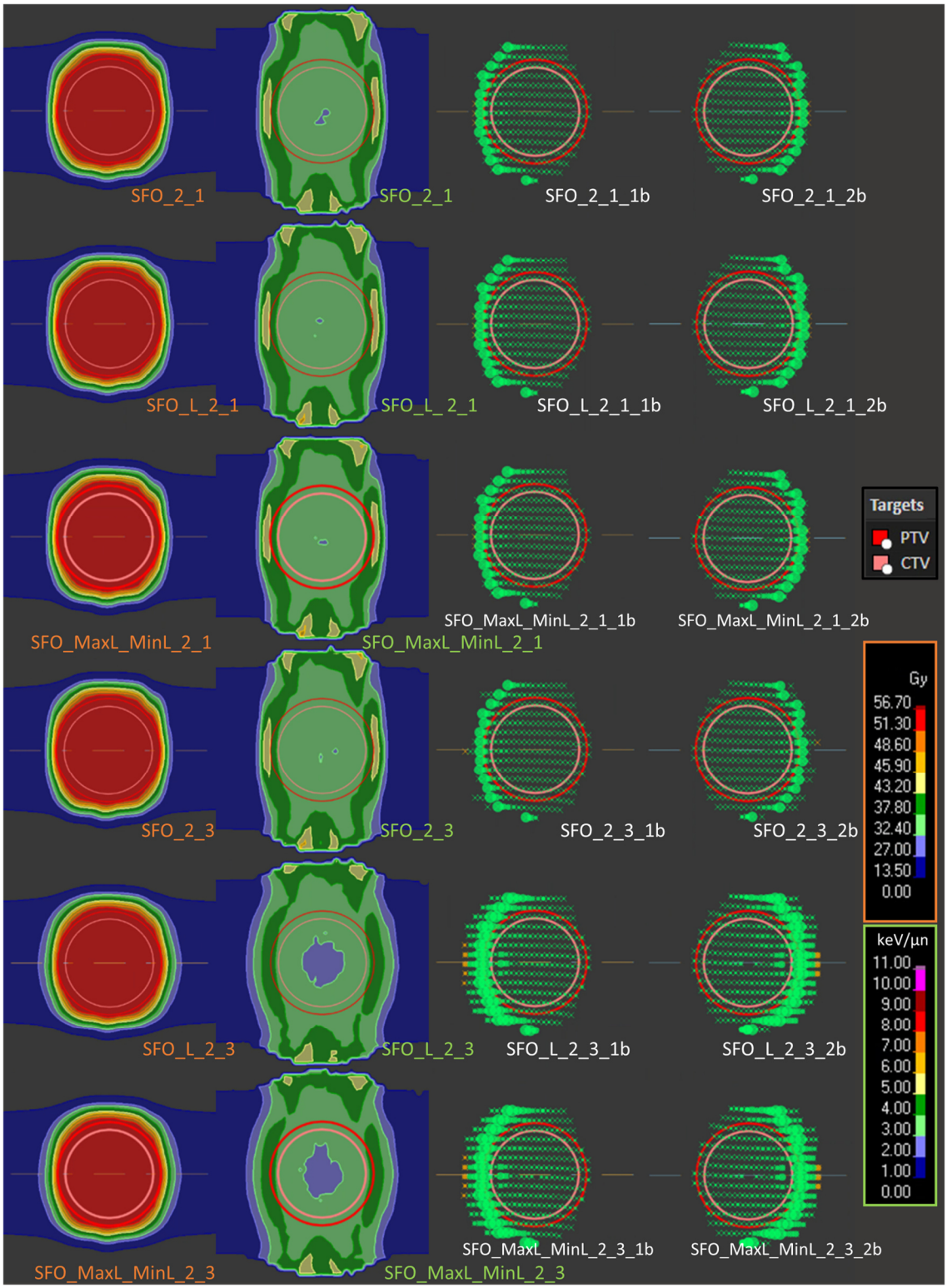

Fig. 55: *Calculated dose (pictures on the left) and LET_d distributions (pictures in the middle) as well as the positions of the individual Bragg peaks displayed as crosses (two pictures on the right) for investigating the influence of different optimization settings. The larger the dots on the cross, the higher is the relative spot weight within a field. Two SFO fields separated by an angle of 180° (one coming from the right abbreviated with "1b" and one coming from the left abbreviated with "2b") irradiated a spherical target with 4 cm diameter centered in a cylindrical water phantom.*

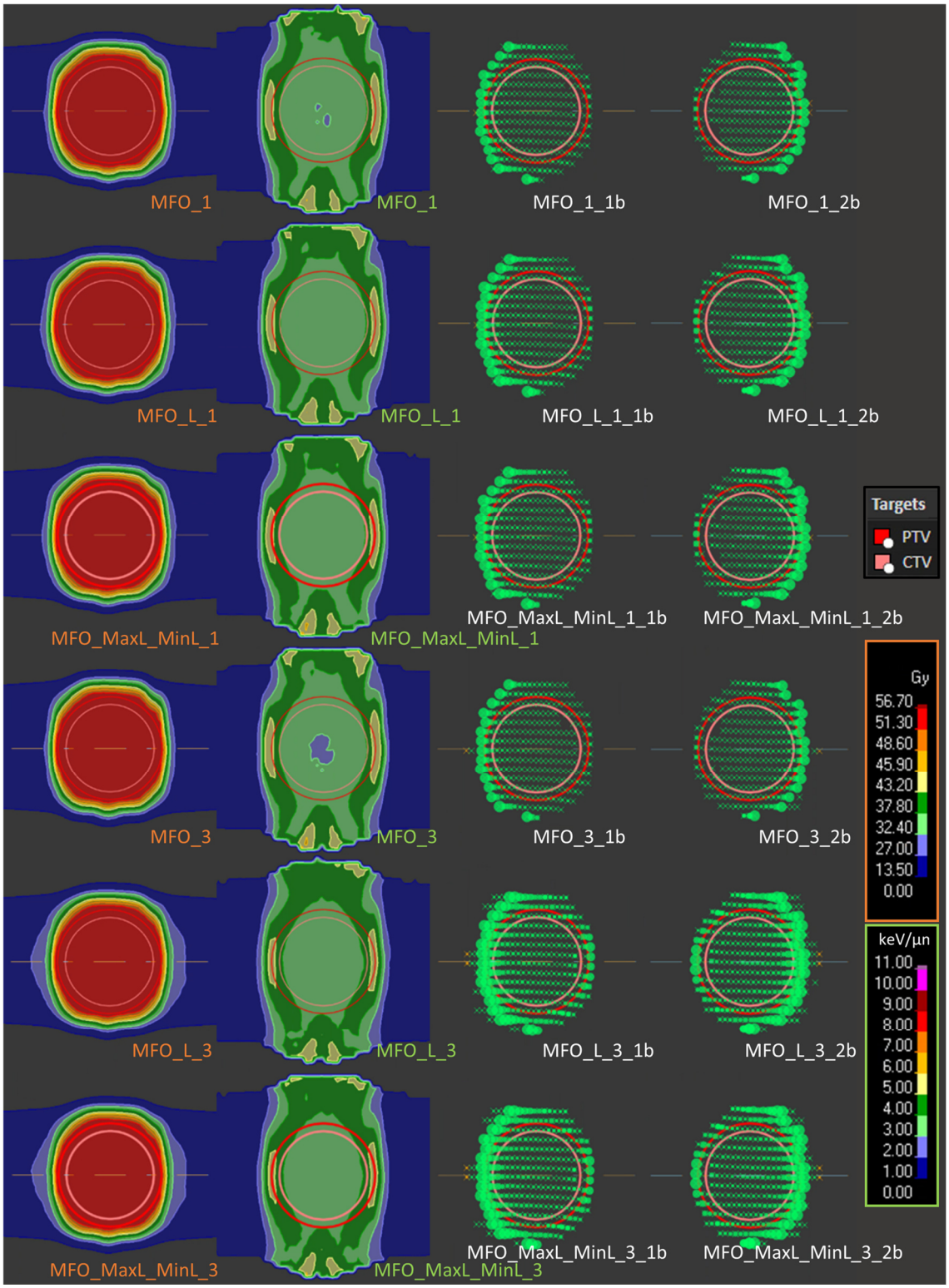

Fig. 56: *Calculated dose (pictures on the left) and LET_d distributions (pictures in the middle) as well as the positions of the individual Bragg peaks displayed as crosses (two pictures on the right) for investigating the influence of different optimization settings. The larger the dots on the cross, the higher is the relative spot weight within a field. Two MFO fields separated by an angle of 180° (one coming from the right abbreviated with "1b" and one coming from the left abbreviated with "2b") irradiated a spherical target with 4 cm diameter centered in a cylindrical water phantom.*

Fig. 57: *Influence of different optimization settings. Maximum LET$_d$ to 2% of (pictures on the left) respectively maximum LET$_d$ to (pictures on the right) four different rings (0.0 to 0.5 cm, 0.5 to 1.0 cm, 1.0 to 1.5 cm, 1.5 to 2.5 cm) around the PTV (a spherical target with 4 cm diameter centered in a cylindrical water phantom) as well as maximum LET$_d$ to 2% of respectively maximum LET$_d$ to the PTV as a function of different optimization settings. For calculating the values shown on the pictures on the top one beam was used, for those in the middle two beams separated by an angle of 90° and for those on the bottom two beams separated by an angle of 180°.*

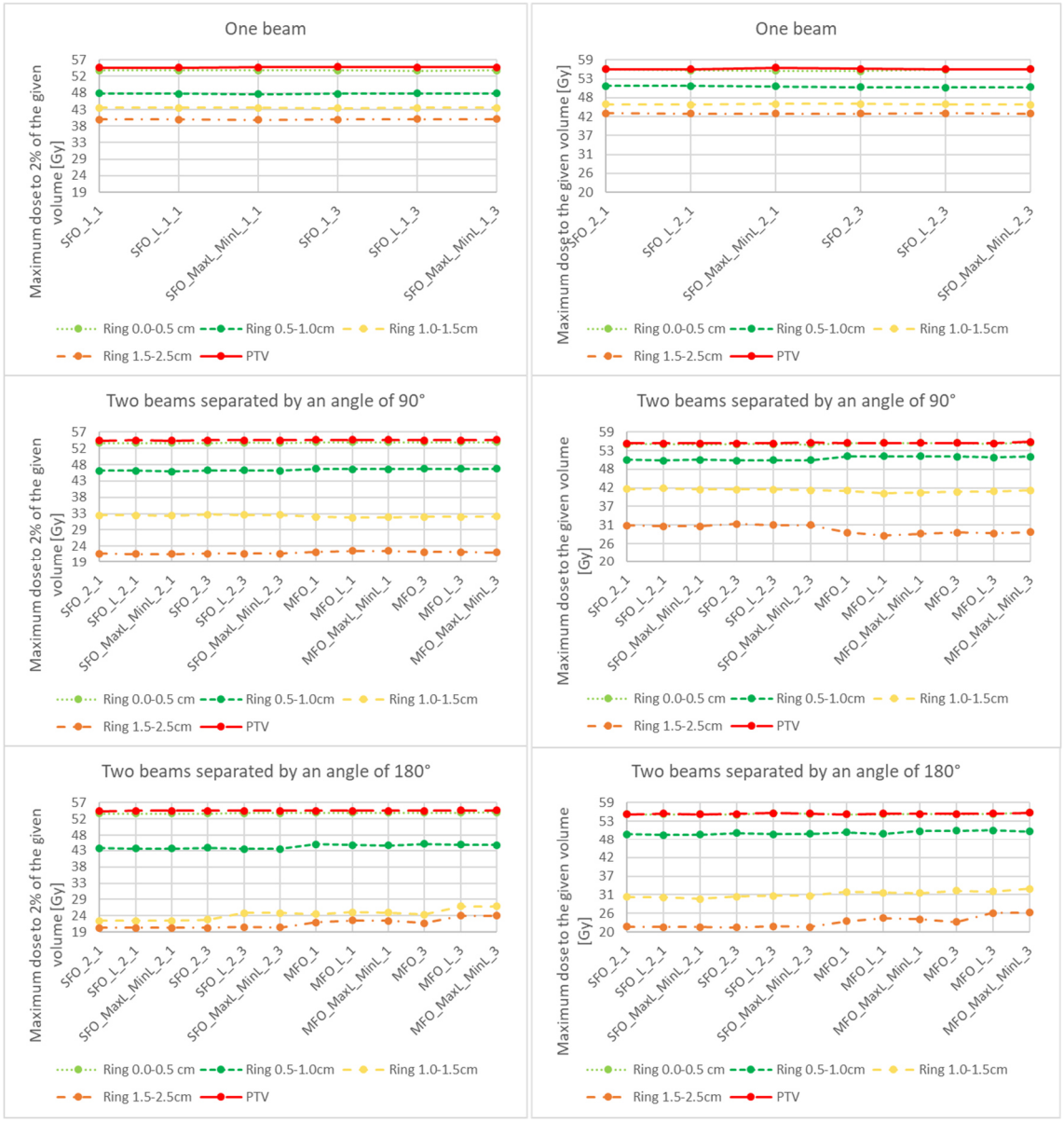

Fig. 58: *Influence of different optimization settings. Maximum dose to 2% of (pictures on the left) respectively maximum dose to (pictures on the right) four different rings (0.0 to 0.5 cm, 0.5 to 1.0 cm, 1.0 to 1.5 cm, 1.5 to 2.5 cm) around the PTV (a spherical target with 4 cm diameter centered in a cylindrical water phantom) as well as maximum dose to 2% of respectively maximum dose to the PTV as a function of different optimization settings. For calculating the values shown on the pictures on the top one beam was used, for those in the middle two beams separated by an angle of 90° and for those on the bottom two beams separated by an angle of 180°.*

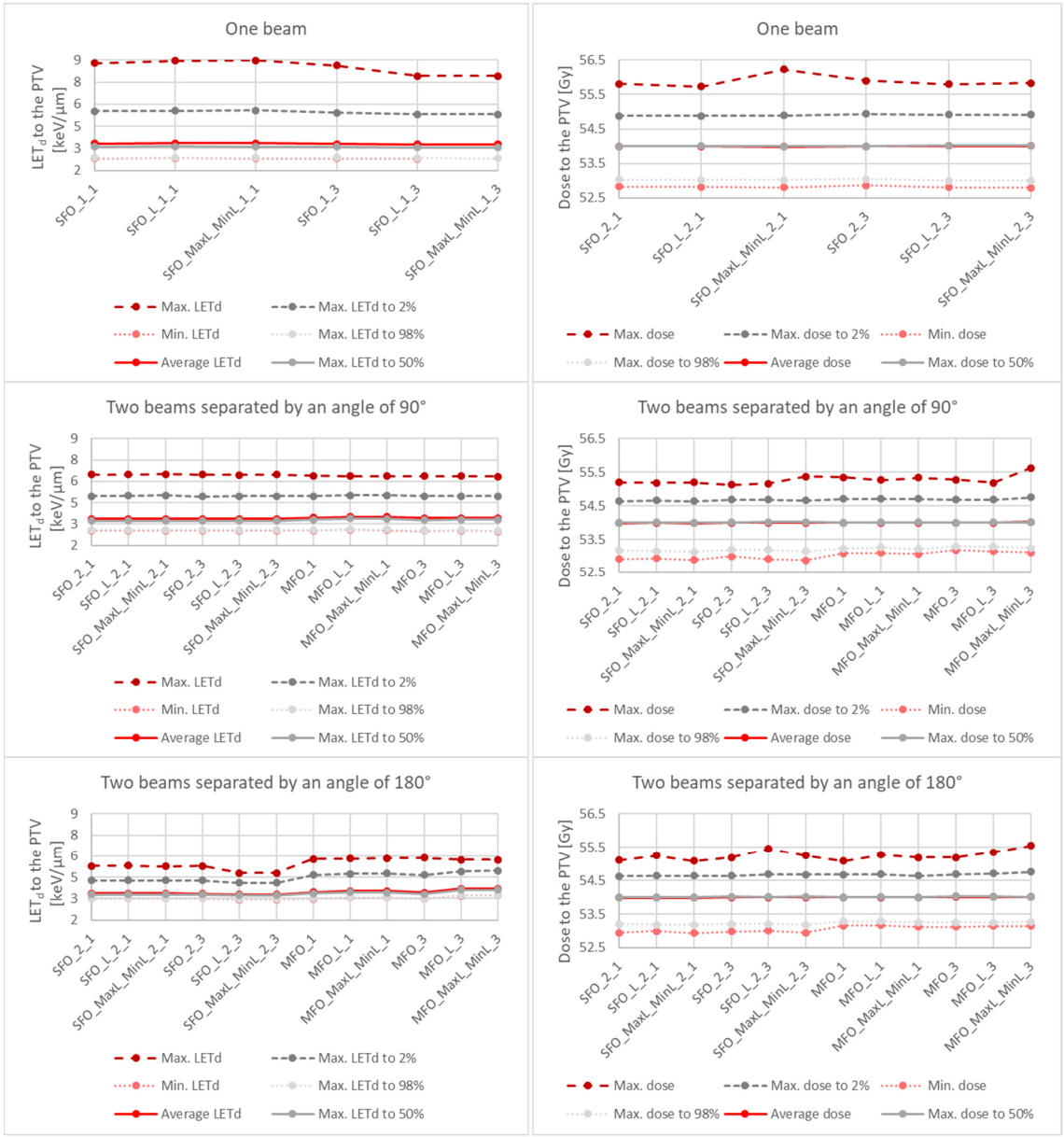

Fig. 59: *Influence of different optimization settings. Maximum, minimum and average LET_d to the PTV (a spherical target with 4 cm diameter centered in a cylindrical water phantom), maximum LET_d to 2%, 98% and 50% of the PTV (pictures on the left) respectively maximum, minimum and average dose to the PTV, maximum dose to 2%, 98% and 50% of the PTV as a function of different optimization settings. For calculating the values shown on the pictures on the top one beam was used, for those in the middle two beams separated by an angle of 90° and for those on the bottom two beams separated by an angle of 180°.*

Table 22: *Influence of different optimization settings. Maximum LET_d to 2% of and maximum LET_d to four different rings (0.0 to 0.5 cm, 0.5 to 1.0 cm, 1.0 to 1.5 cm, 1.5 to 2.5 cm) around the PTV as well as maximum LET_d to 2% of, maximum, minimum and average LET_d to the PTV for a spherical target with 4 cm diameter centered in a cylindrical water phantom in keV/µm. The first column gives the plan abbreviation.*

Plan	Min. LET_d to PTV	Avg. LET_d to PTV	Max. LET_d to PTV	Max. LET_d to 2% of PTV	Max. LET_d to ring 0.0-0.5cm	Max. LET_d to 2% of ring 0.0-0.5cm	Max. LET_d to ring 0.5-1.0cm	Max. LET_d to 2% of ring 0.5-1.0cm	Max. LET_d to ring 1.0-1.5cm	Max. LET_d to 2% of ring 1.0-1.5cm	Max. LET_d to ring 1.5-2.5cm	Max. LET_d to 2% of ring 1.5-2.5cm
SFO_1_1	2.33	3.34	8.80	5.52	15.25	12.25	17.86	15.23	17.56	14.52	15.83	10.39
SFO_L_1_1	2.34	3.35	8.93	5.55	14.68	11.89	17.58	15.49	17.58	14.30	15.98	10.31
SFO_MaxL_MinL_1_1	2.33	3.35	8.96	5.57	14.77	11.94	17.65	15.29	17.02	14.30	15.92	10.30
SFO_1_3	2.33	3.31	8.63	5.43	12.32	11.59	15.15	12.09	15.15	12.91	14.69	10.49
SFO_L_1_3	2.30	3.27	7.90	5.30	9.54	8.93	16.76	10.86	17.36	14.34	16.17	10.87
SFO_MaxL_MinL_1_3	2.30	3.27	7.92	5.31	9.53	8.94	16.77	10.86	17.39	14.31	16.04	10.88
90°_SFO_2_1	2.55	3.37	6.48	4.96	8.80	7.36	12.79	9.20	15.99	11.40	15.99	9.04
90°_SFO_L_2_1	2.55	3.37	6.48	4.99	8.67	7.31	12.65	9.19	15.06	11.26	15.06	9.01
90°_SFO_MaxL_MinL_2_1	2.54	3.38	6.50	5.00	8.71	7.34	12.87	9.20	14.93	11.27	14.92	8.99
90°_SFO_2_3	2.55	3.36	6.47	4.93	8.71	7.26	12.02	8.98	13.61	10.77	13.93	9.20
90°_SFO_L_2_3	2.55	3.36	6.43	4.95	8.63	7.19	11.55	8.84	13.44	10.52	13.44	9.23
90°_SFO_MaxL_MinL_2_3	2.55	3.36	6.46	4.96	8.62	7.20	11.71	8.86	13.02	10.64	13.29	9.19
90°_MFO_1	2.56	3.44	6.40	4.97	8.84	7.28	12.86	9.27	15.16	11.46	15.16	9.13
90°_MFO_L_1	2.60	3.50	6.36	5.02	8.91	7.28	12.71	9.26	15.31	11.36	15.31	9.14
90°_MFO_MaxL_MinL_1	2.59	3.50	6.35	5.03	8.86	7.28	12.71	9.28	15.40	11.36	15.40	9.14
90°_MFO_3	2.52	3.42	6.36	4.96	8.81	7.18	12.26	8.97	13.90	10.83	14.11	9.23
90°_MFO_L_3	2.53	3.42	6.35	4.96	8.55	7.17	12.04	8.90	14.52	10.63	14.52	9.21
90°_MFO_MaxL_MinL_3	2.49	3.42	6.32	4.97	8.62	7.20	12.13	8.92	14.55	10.72	14.55	9.27
180°_SFO_2_1	3.01	3.36	5.30	4.28	5.63	5.30	5.77	4.83	6.59	5.40	7.32	5.85
180°_SFO_L_2_1	3.01	3.36	5.32	4.28	5.62	5.30	5.79	4.83	6.69	5.40	7.01	5.83
180°_SFO_MaxL_MinL_2_1	3.01	3.36	5.27	4.29	5.64	5.28	5.77	4.83	6.52	5.41	6.96	5.85
180°_SFO_2_3	3.00	3.35	5.30	4.27	5.58	5.29	5.71	4.80	6.54	5.37	6.94	5.83
180°_SFO_L_2_3	2.94	3.28	4.79	4.12	4.79	4.65	5.53	4.57	6.17	5.22	6.92	5.68
180°_SFO_MaxL_MinL_2_3	2.93	3.29	4.79	4.12	4.79	4.64	5.51	4.57	6.18	5.23	6.92	5.65
180°_MFO_1	2.99	3.45	5.80	4.67	5.80	5.53	5.83	4.92	6.77	5.49	7.18	5.83
180°_MFO_L_1	3.07	3.53	5.81	4.75	5.81	5.48	5.85	4.93	6.68	5.50	7.07	5.80
180°_MFO_MaxL_MinL_1	3.06	3.52	5.85	4.77	5.85	5.49	5.82	4.92	6.57	5.52	7.08	5.80
180°_MFO_3	2.97	3.42	5.86	4.66	5.86	5.56	5.89	4.88	6.55	5.44	7.47	5.79
180°_MFO_L_3	3.21	3.69	5.72	4.92	5.72	5.29	5.79	4.88	6.31	5.42	7.34	5.72
180°_MFO_MaxL_MinL_3	3.22	3.70	5.73	4.95	5.73	5.32	5.75	4.90	6.26	5.43	7.28	5.72

Table 23: *Influence of different optimization settings. Maximum dose to 2% of and maximum dose to four different rings (0.0 to 0.5 cm, 0.5 to 1.0 cm, 1.0 to 1.5 cm, 1.5 to 2.5 cm) around the PTV as well as maximum dose to 2% of, maximum, minimum and average dose to the PTV for a spherical target with 4 cm diameter centered in a cylindrical water phantom in keV/µm. The first column gives the plan abbreviation.*

Plan	Min. dose to PTV	Avg. dose to PTV	Max. dose to PTV	Max. dose to 2% of PTV	Max. dose to ring 0.0-0.5cm	Max. dose to 2% of ring 0.0-0.5cm	Max. dose to ring 0.5-1.0cm	Max. dose to 2% of ring 0.5-1.0cm	Max. dose to ring 1.0-1.5cm	Max. dose to 2% of ring 1.0-1.5cm	Max. dose to ring 1.5-2.5cm	Max. dose to 2% of ring 1.5-2.5cm
SFO_1_1	52.83	54.00	55.81	54.88	55.81	54.02	50.86	47.33	45.54	43.22	42.97	39.88
SFO_L_1_1	52.82	54.00	55.73	54.88	55.44	54.01	50.93	47.31	45.49	43.23	42.91	39.88
SFO_MaxL_MinL_1_1	52.81	53.99	56.23	54.89	55.29	53.97	50.75	47.24	45.68	43.22	42.85	39.84
SFO_1_3	52.87	54.00	55.90	54.94	55.24	54.01	50.59	47.26	45.72	43.20	42.83	39.88
SFO_L_1_3	52.81	54.01	55.80	54.91	55.70	53.96	50.46	47.34	45.62	43.27	43.00	39.97
SFO_MaxL_MinL_1_3	52.80	54.01	55.83	54.92	55.83	53.99	50.62	47.36	45.49	43.28	42.83	39.98
90°_SFO_2_1	52.91	53.98	55.20	54.63	54.93	53.88	50.35	45.70	41.60	32.78	30.93	21.55
90°_SFO_L_2_1	52.93	53.99	55.18	54.66	54.93	53.88	50.08	45.70	41.92	32.75	30.71	21.53
90°_SFO_MaxL_MinL_2_1	52.89	53.98	55.19	54.63	54.82	53.89	50.31	45.48	41.56	32.62	30.69	21.50
90°_SFO_2_3	52.99	53.99	55.12	54.68	54.98	53.88	50.05	45.83	41.50	32.93	31.29	21.61
90°_SFO_L_2_3	52.91	54.00	55.16	54.68	54.96	53.90	50.25	45.87	41.57	32.91	31.02	21.60
90°_SFO_MaxL_MinL_2_3	52.88	53.99	55.37	54.66	54.86	53.87	50.20	45.76	41.30	32.82	30.99	21.58
90°_MFO_1	53.09	53.99	55.34	54.71	55.16	54.10	51.39	46.31	41.13	32.34	28.75	22.09
90°_MFO_L_1	53.10	54.00	55.26	54.70	55.26	54.12	51.37	46.19	40.41	32.12	27.86	22.41
90°_MFO_MaxL_MinL_1	53.06	54.00	55.33	54.71	55.33	54.06	51.31	46.17	40.65	32.14	28.49	22.35
90°_MFO_3	53.18	54.00	55.28	54.68	55.27	54.12	51.23	46.36	40.78	32.33	28.79	22.02
90°_MFO_L_3	53.14	54.00	55.18	54.68	55.06	54.12	51.00	46.31	40.98	32.27	28.60	22.03
90°_MFO_MaxL_MinL_3	53.11	54.02	55.63	54.75	55.44	54.07	51.24	46.34	41.35	32.36	28.88	21.97
180°_SFO_2_1	52.95	53.98	55.10	54.62	55.10	53.86	49.12	43.46	30.31	22.29	21.54	20.28
180°_SFO_L_2_1	52.99	53.98	55.24	54.63	55.01	53.86	48.89	43.38	30.20	22.26	21.47	20.27
180°_SFO_MaxL_MinL_2_1	52.94	53.98	55.08	54.63	55.04	53.84	49.01	43.40	29.80	22.24	21.49	20.25
180°_SFO_2_3	52.98	54.00	55.18	54.63	54.92	53.88	49.53	43.56	30.49	22.66	21.38	20.27
180°_SFO_L_2_3	53.01	54.00	55.45	54.68	55.45	53.90	49.20	43.29	30.76	24.56	21.72	20.40
180°_SFO_MaxL_MinL_2_3	52.95	54.00	55.24	54.67	55.21	53.90	49.34	43.27	30.70	24.52	21.52	20.37
180°_MFO_1	53.16	54.00	55.08	54.67	55.08	54.06	49.81	44.63	31.87	24.19	23.18	21.80
180°_MFO_L_1	53.17	53.99	55.26	54.68	55.08	54.10	49.32	44.34	31.59	24.74	24.10	22.40
180°_MFO_MaxL_MinL_1	53.12	53.99	55.18	54.64	55.18	54.07	50.07	44.30	31.55	24.65	23.82	22.32
180°_MFO_3	53.12	54.01	55.18	54.68	55.12	54.12	50.23	44.67	32.15	24.11	23.01	21.62
180°_MFO_L_3	53.15	54.01	55.34	54.71	55.13	54.12	50.30	44.44	31.92	26.51	25.66	23.76
180°_MFO_MaxL_MinL_3	53.14	54.01	55.54	54.75	55.54	54.16	50.00	44.40	32.76	26.50	25.70	23.81

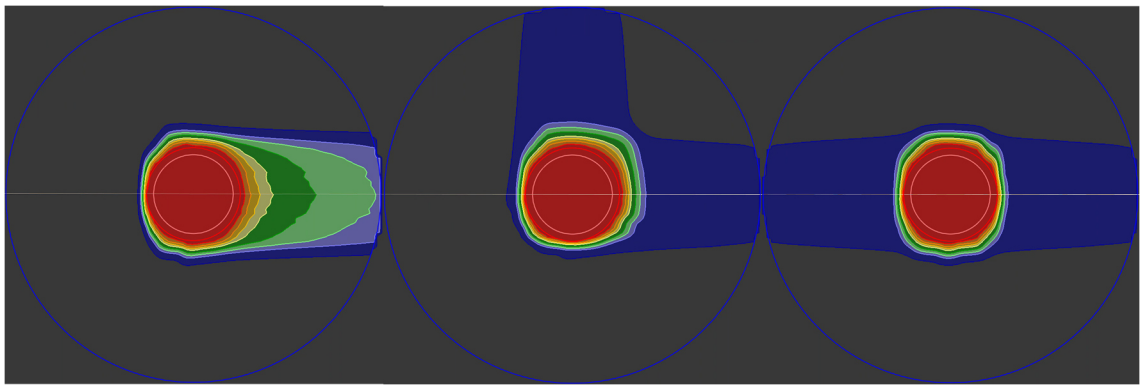

Fig. 60: *Location of a line through the center of a spherical target with 4 cm diameter centered in a cylindrical water phantom along which LET_d and dose values which in the following were used for the calculation of RBEs and RBE-weighted doses were exported. The line was drawn from the right to the left side.*

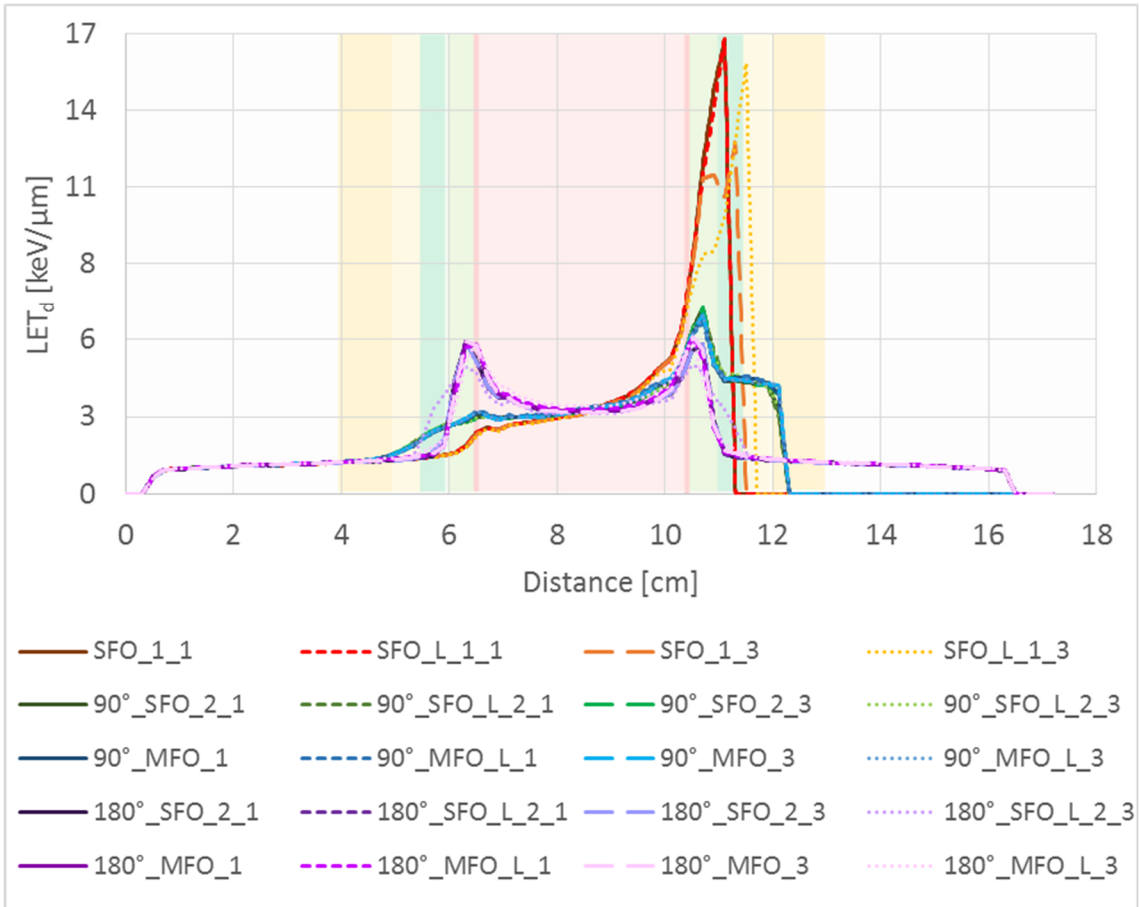

Fig. 61*: LET_d values along a line through the center of a spherical target with 4 cm diameter centered in a cylindrical water phantom calculated using different optimization settings. For the two field plans separation angles of 90° and 180° were investigated. The colors in the background depict the locations of the CTV, the PTV as well as of rings (0.0-0.5 cm, 0.5-1.0 cm, 1.0-1.5 cm and 1.5-2.5 cm) around the PTV.*

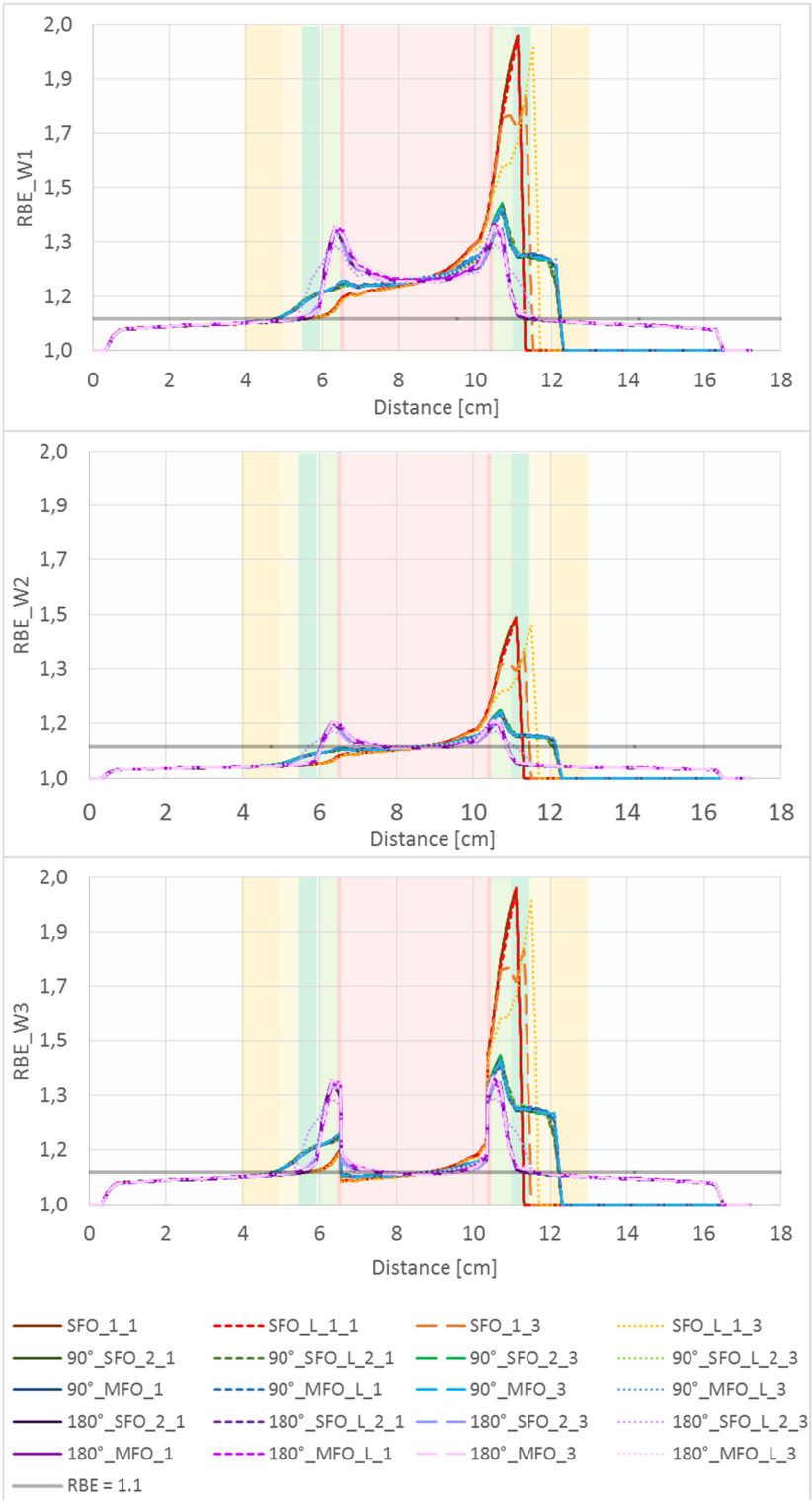

Fig. 62: *RBEs along a line through the center of a spherical target with 4 cm diameter centered in a cylindrical water phantom calculated for one fraction (prescribed dose per fraction: 1.8 Gy(RBE)) using the Wedenberg et al. model and an α/β value of 2 Gy (picture on the top), 10 Gy (picture in the middle) respectively of 10 Gy in the CTV and 2 Gy around the CTV for different optimization settings. For the two field plans separation angles of 90° and 180° were investigated. A straight horizontal line depicts the constant RBE of 1.1. The colors in the background depict the locations of the CTV, the PTV as well as of rings (0.0-0.5 cm, 0.5-1.0 cm, 1.0-1.5 cm and 1.5-2.5 cm) around the PTV.*

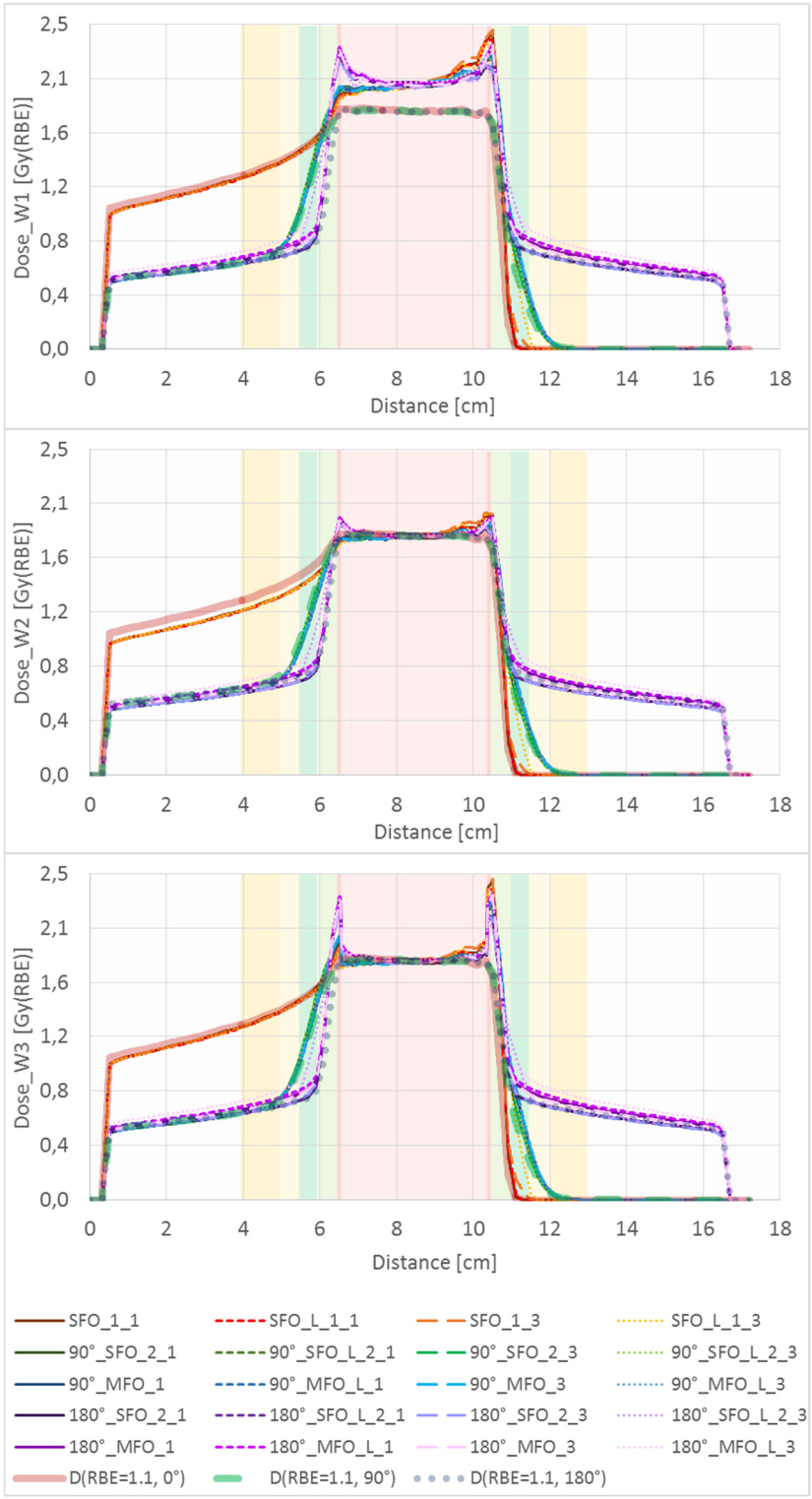

Fig. 63: *RBE-weighted doses along a line through the center of a spherical target with 4 cm diameter centered in a cylindrical water phantom calculated for one fraction (prescribed dose per fraction: 1.8 Gy(RBE)) using the Wedenberg et al. model and an α/β value of 2 Gy (picture on the top), 10 Gy (picture in the middle) respectively of 10 Gy in the CTV and 2 Gy around the CTV for different optimization settings. For the two field plans separation angles of 90° and 180° were investigated. The RBE-weighted dose calculated using a constant RBE of 1.1 for one beam and two beams separated by an angle of 90 ° respectively 180° for the optimization settings SFO, no maximum spot weight limitation and one distal energy layer are also shown. The colors in the background depict the locations of the CTV, the PTV as well as of rings (0.0-0.5 cm, 0.5-1.0 cm, 1.0-1.5 cm and 1.5-2.5 cm) around the PTV.*

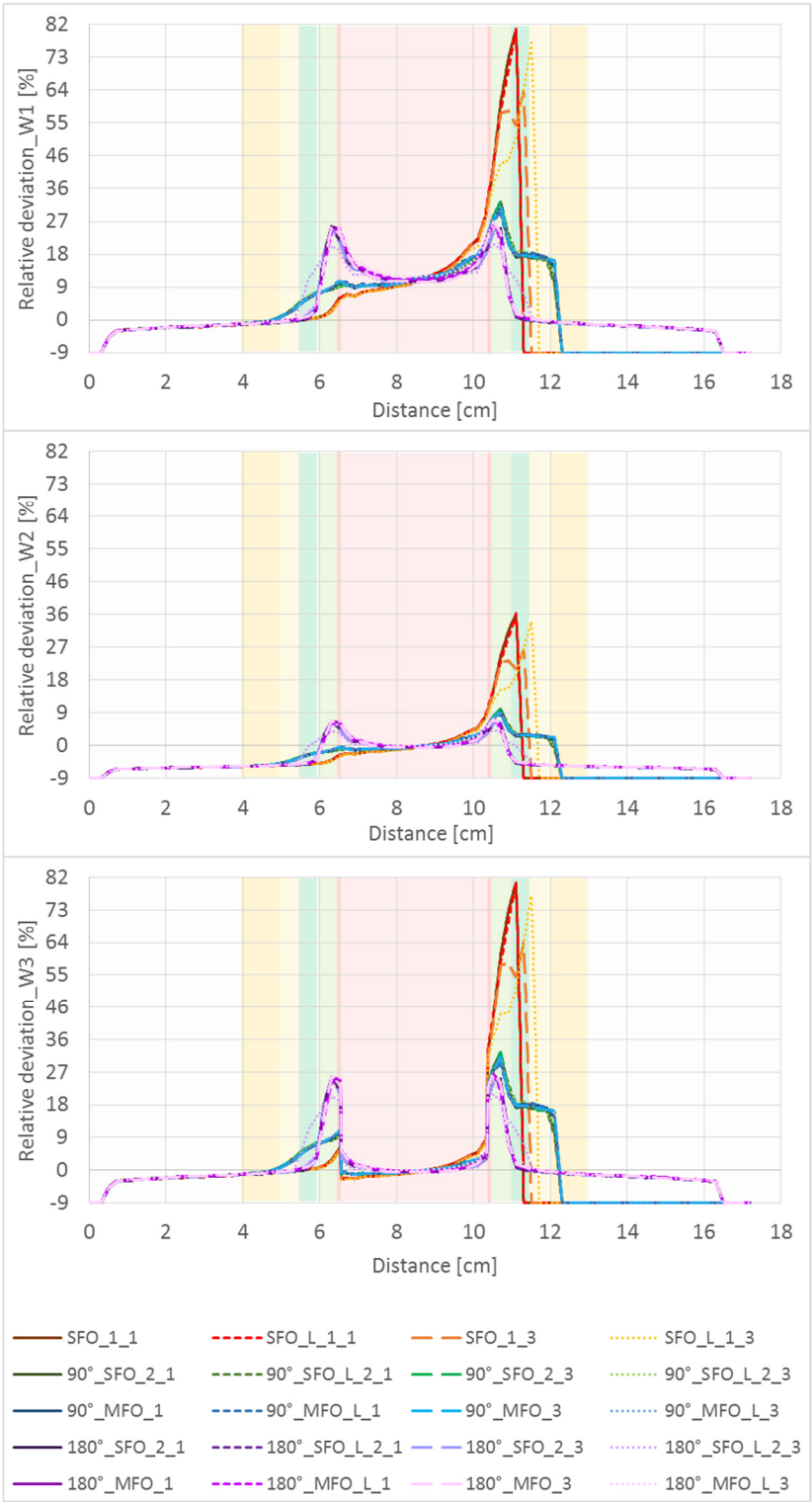

Fig. 64: *Relative deviations of RBEs calculated for one fraction (prescribed dose per fraction: 1.8 Gy(RBE)) using the Wedenberg et al. model and an α/β value of 2 Gy (picture on the top), 10 Gy (picture in the middle) respectively of 10 Gy in the CTV and 2 Gy around the CTV from the RBE of 1.1 along a line through the center of a spherical target with 4 cm diameter centered in a cylindrical water phantom for different optimization settings. For the two field plans separation angles of 90° and 180° were investigated. The colors in the background depict the locations of the CTV, the PTV as well as of rings (0.0-0.5 cm, 0.5-1.0 cm, 1.0-1.5 cm and 1.5-2.5 cm) around the PTV.*

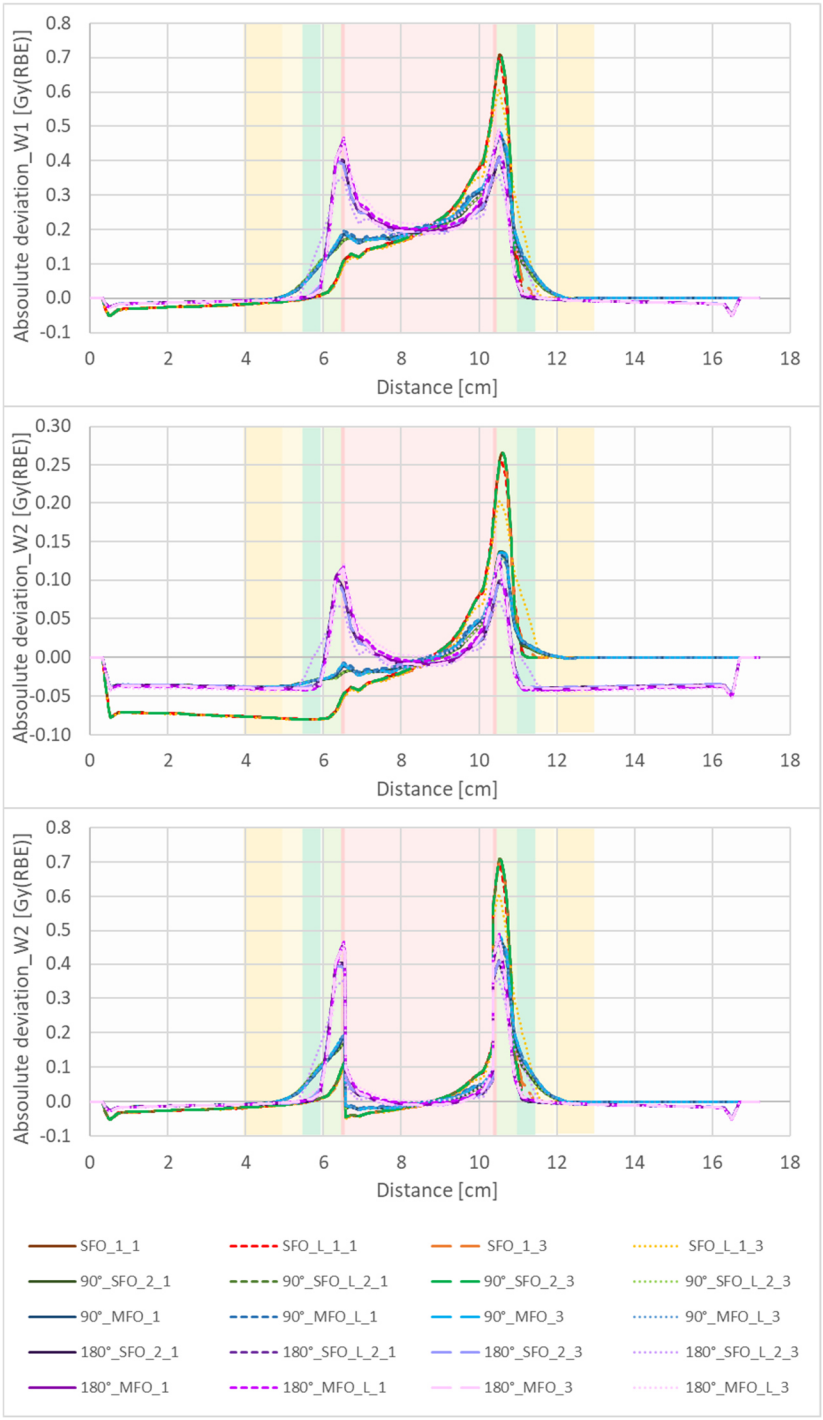

Fig. 65: *Absolute deviations of RBEs calculated for one fraction (prescribed dose per fraction: 1.8 Gy(RBE)) using the Wedenberg et al. model and an α/β value of 2 Gy (picture on the top), 10 Gy (picture in the middle) respectively of 10 Gy in the CTV and 2 Gy around the CTV from the RBE of 1.1 along a line through the center of a spherical target with 4 cm diameter centered in a cylindrical water phantom for different optimization settings. For the two field plans separation angles of 90 ° and 180 ° were investigated. The colors in the background depict the locations of the CTV, the PTV as well as of rings (0.0-0.5 cm, 0.5-1.0 cm, 1.0-1.5 cm and 1.5-2.5 cm) around the PTV.*

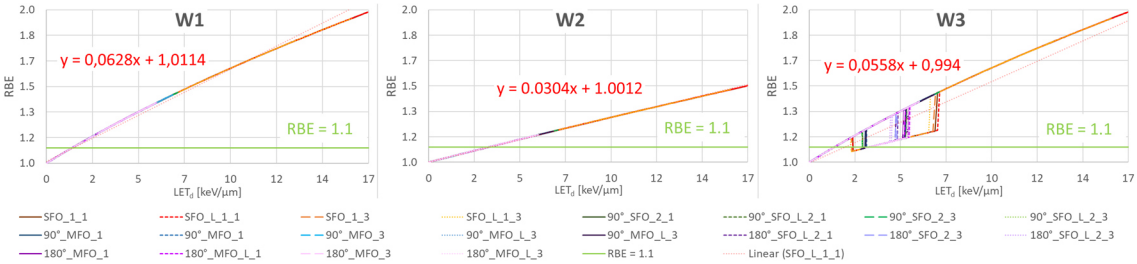

Fig. 66: *RBEs as a function of LET_d calculated with the Wedenberg et a. model using an α/β value of 2 Gy (picture on the left), of 10 Gy (picture in the middle) respectively of 10 Gy in the CTV and 2 Gy around the CTV (picture on the right), a prescribed dose of 1.8 Gy(RBE) and 0.434 Gy µm/keV q for different optimization settings. For the two field plans separation angles of 90° and 180° were investigated. A straight green horizontal line depicts the constant RBE of 1.1. The corresponding trend lines (red dotted lines) are also shown.*

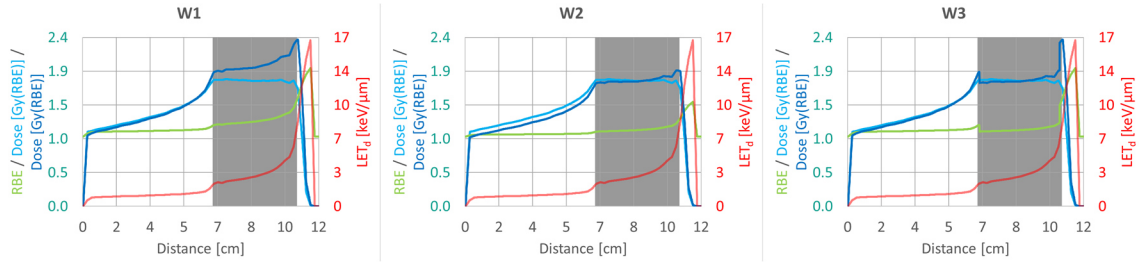

Fig. 67: *LET_d (red lines), biological-weighted dose (calculated using a RBE of 1.1, light blue lines), RBE (calculated using the Wedenberg et al. model and an α/β value of 2 Gy, picture on the left, of 10 Gy, picture in the middle, respectively of 10 Gy in the CTV and 2 Gy around the CTV, picture on the right) and corresponding biological-weighted dose (dark blue lines) profiles along the central axis of a spherical water target. The grey background depicts the location of the target.*

3.3.2 Clinical cases

Fig. 68 - *Fig. 72* summarize the results obtained for the five clinical cases applying different optimization settings. The dose and LET_d distributions as well as the locations of pencil beams[47] exemplary for one clinical case can be found there. Concerning the location of pencil beams, one might notice the greater divergence between SFO and MFO plans when comparing with the phantom case.

The influence the different optimization settings had on the DVH and LET_dVH of the PTV as well as of the ring from 0.0 to 0.5 cm around the PTV is depicted in *Fig. 73* and *Fig. 74*. The DVHs for the PTV just varied slightly with applied optimization settings. However, one can observe that the lines of all different plans gathered into three groups – one field, two field SFO and two field MFO plans. The differences within these groups were minor. Nevertheless, plans with three distal energy layers tended to be shifted to slightly lower LET_d values. The best coverage could be obtained using MFO, the worst for the single field plans. When looking at an LET_d to the PTV of about 3 keV/µm the following was found: The volume fraction which received at least 3 keV/µm was the lowest for the SFO and the highest for the single field plans. The same behavior was noticed at any LET_d value to the PTV above 1.4 keV/µm[48]. The DVHs of the ring from 0.0 to 0.5 cm around the PTV showed a similar behavior. The maximum dose values were also the highest for the MFO plans and the lowest for the single field plans. Nonetheless, when looking at the one field and the two field SFO plans, for those using three distal energy layers a little higher dose values were determined for volume fractions less than 80%. In the LET_dVHs the lines corresponding to one field plans applying a limitation of maximum spot weight separated from those without a limitation. The maximum LET_d calculated for the latter was about half of the maximum LET_d computed for the former. For the two field plans no substantial differences were observed.

Fig. 75 - *Fig. 89* show the maximum LET_d and dose values to respectively to 2% of the PTV and four rings around the PTV as well as the maximum LET_d and dose to 98%, 50% of the PTV for all investigated clinical patients. Differences and similarities between the individual cases could be determined. Section *3.3.3 Comparisons* gives details of the influence of the different optimization settings on the LET_d and dose values averaged over all clinical cases.

The percentages of the $TNTV_B$´s total volume receiving at least 5, 10, 20 and 30 Gy (in the following $V_{TNTb,5Gy}$, $V_{TNTb,10Gy}$, $V_{TNTb,20Gy}$, and $V_{TNTb,30y}$) depending on the used optimization settings are depicted in figure *Fig. 90* for all clinical cases. For *Patient 3* and *5* those values did not differ much for all plans using one beam. In comparison, the values for $V_{TNTb,5Gy}$ were a bit higher for $V_{TNTb,30y}$ slightly lower for the two field plans. This was also obtained for *Patient 1* with an additional decrease of all for values for MFO plans. For *Patient 4* just the increase of $V_{TNTb,5Gy}$ but not the decrease $V_{TNTb,30y}$ was determined. For *Patient 5* both neither increase nor decrease occurred but just a slight variation of all values depending on the applied settings.

[47] The locations of pencil beams shown in the figures were obtained using the Pencil Beam algorithm and not the Monte Carlo algorithm which was used for calculating the presented dose and LET_d distributions.
[48] The minimum LET_d to the PTV was for all plans shown in the described figure at least 1.4 keV/µm.

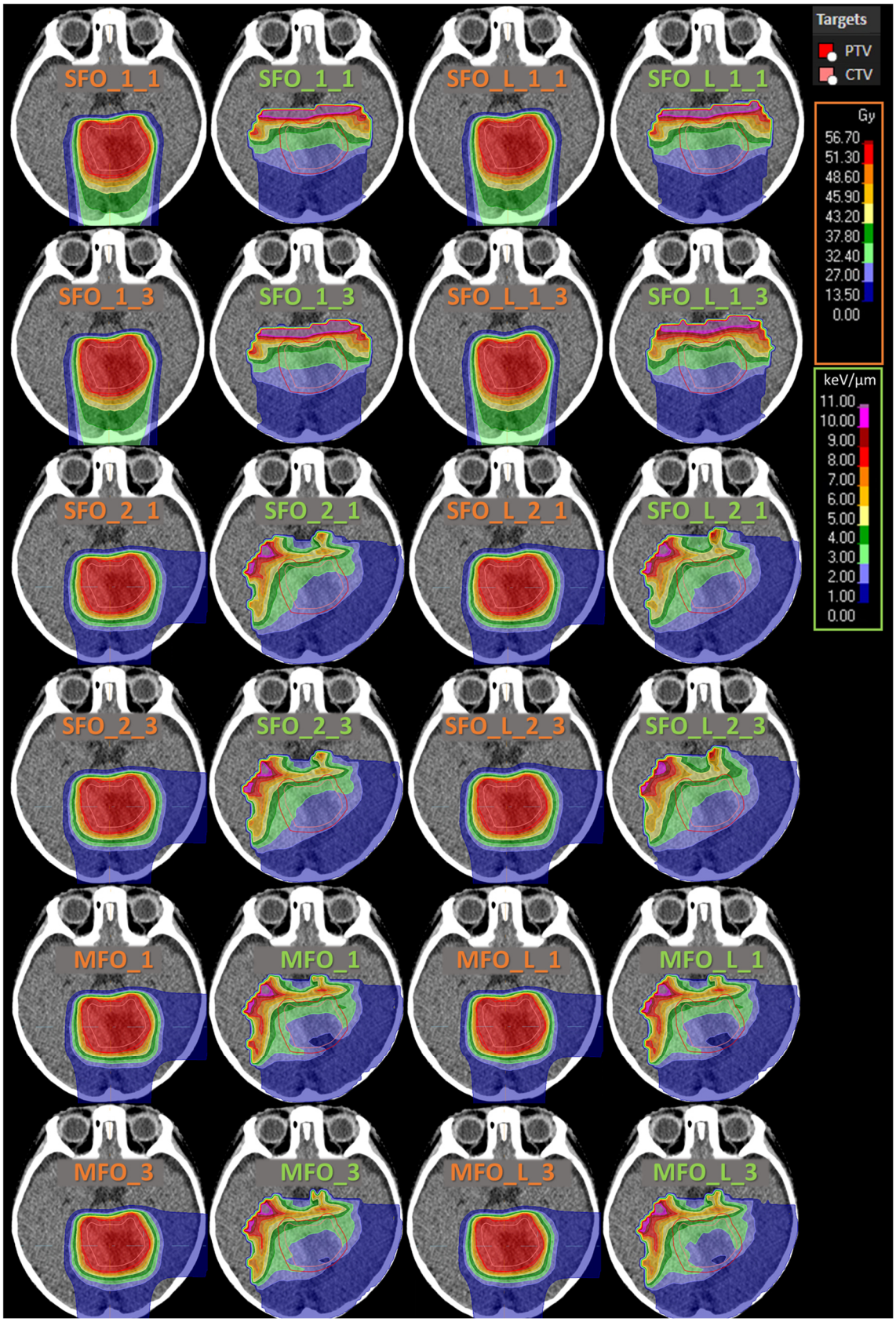

Fig. 68: *Calculated dose (first and third pictures in each row) and LET_d distributions (second and forth pictures in each row) for investigating the influence of different optimization settings for the first clinical case - a pediatric head tumor.*

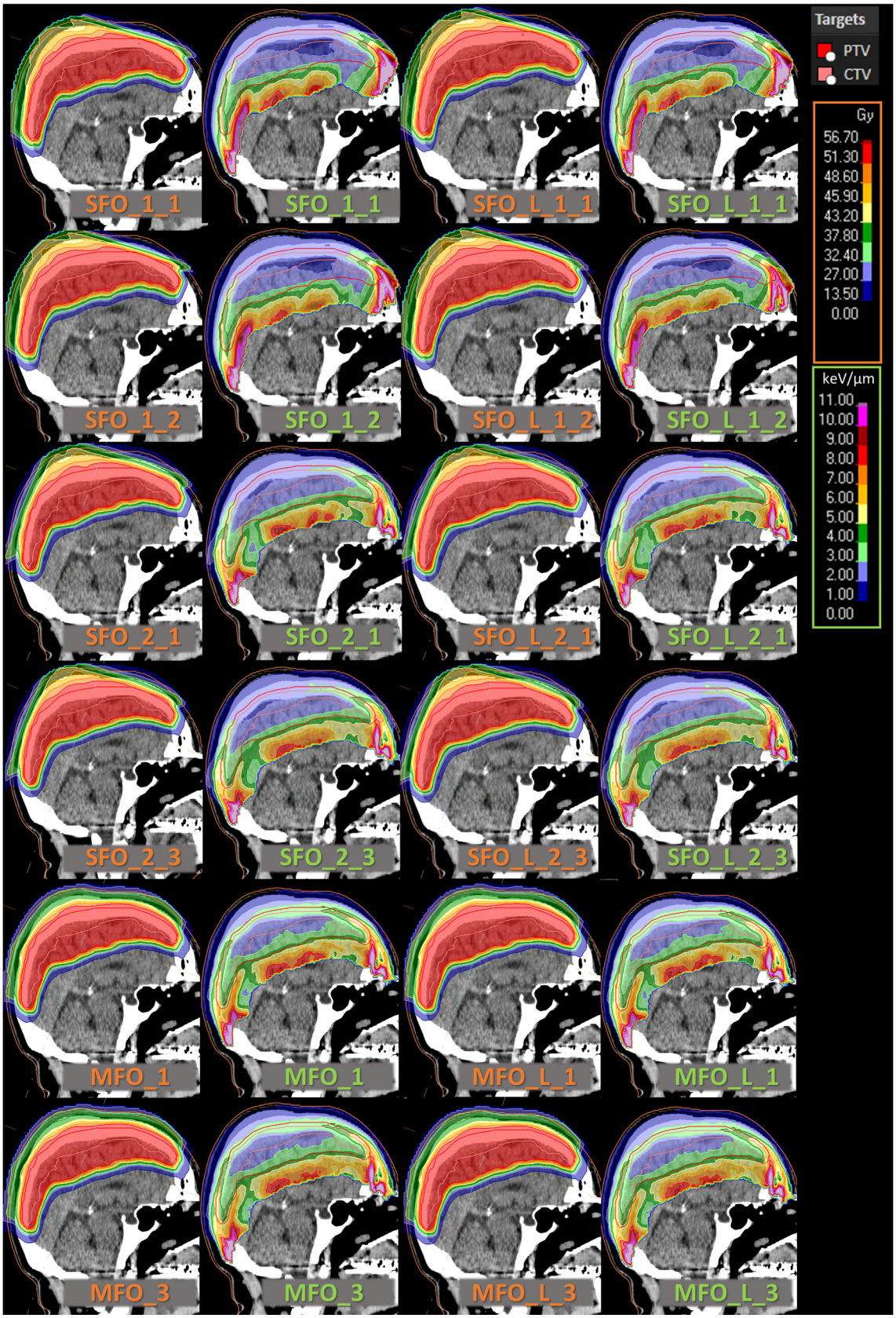

***Fig. 69**: Calculated dose (first and third pictures in each row) and LET_d distributions (second and forth pictures in each row) for investigating the influence of different optimization settings for the second clinical case - a superficial tumor.*

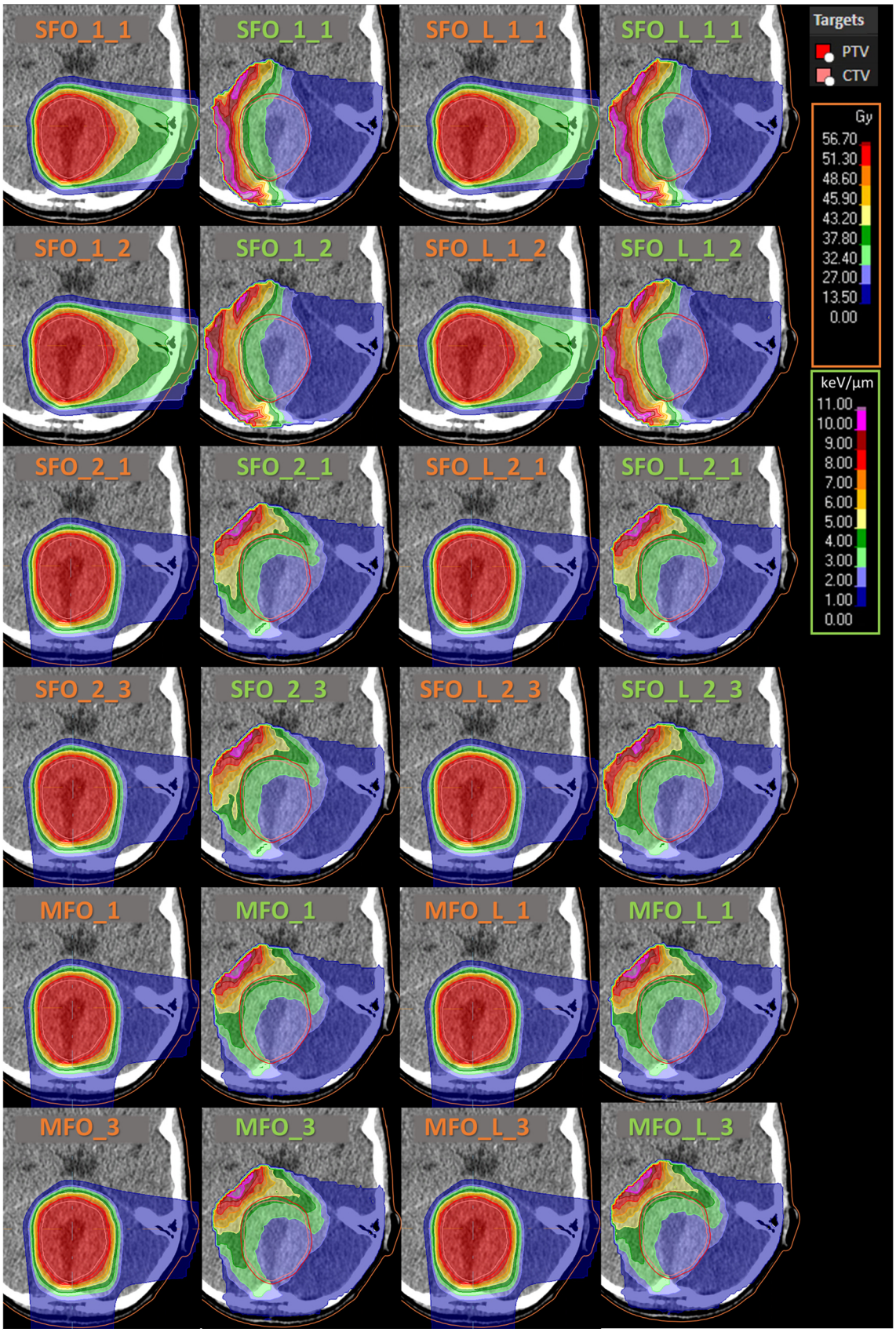

***Fig. 70**: Calculated dose (first and third pictures in each row) and LET_d distributions (second and forth pictures in each row) for investigating the influence of different optimization settings for the third clinical case - a pediatric head tumor.*

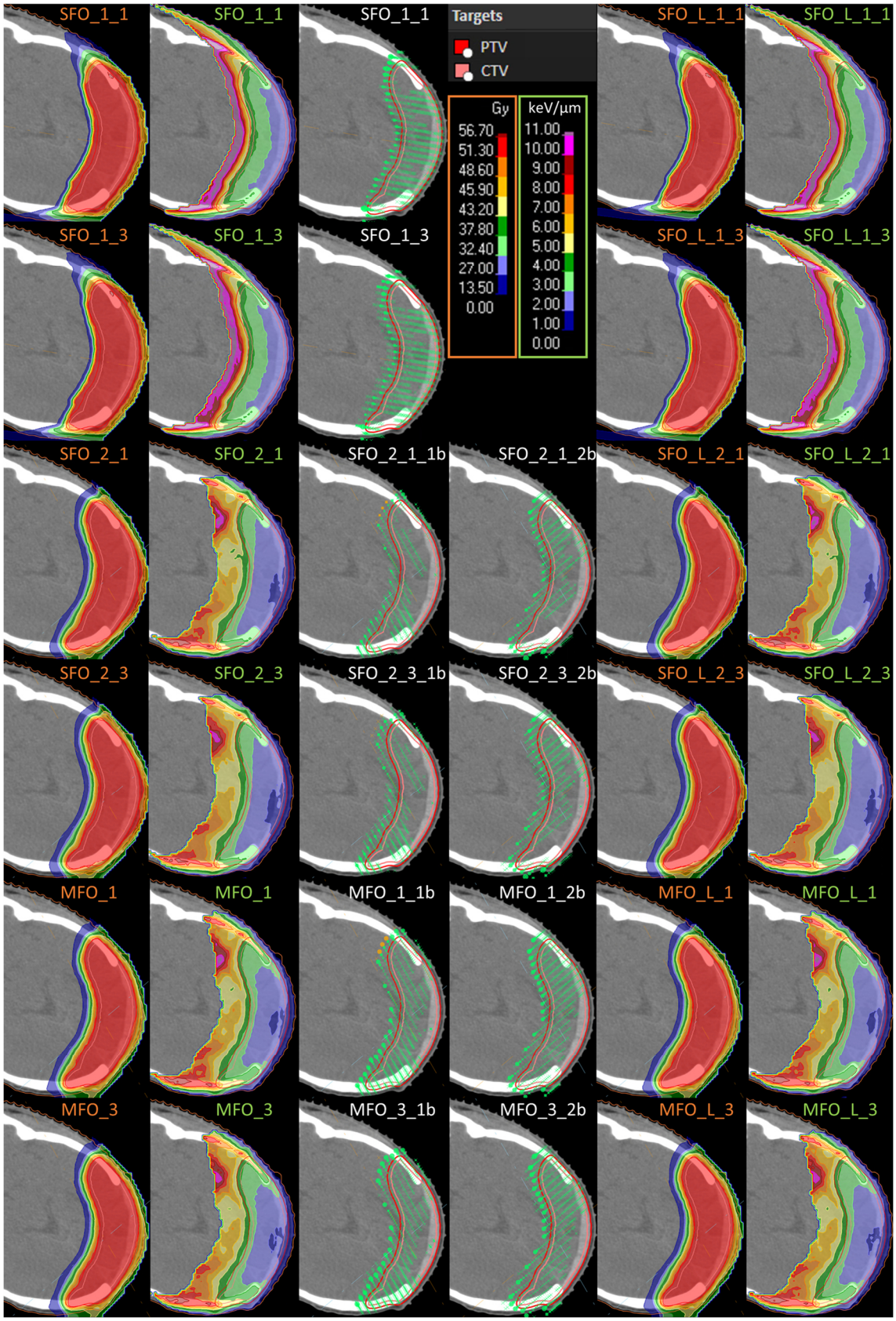

Fig. 71: *Calculated dose (first and forth/fifth pictures in each row) and LET_d distributions (second and fifth/sixth pictures in each row) as well as positions of the individual Bragg peaks displayed as crosses (one/two pictures in the middle, in cases where two fields were used "1b" stands for the first, "2b" for the second field) for investigating the influence of different optimization settings for the forth clinical case – a pediatric Ewing tumor. The lager the dot on the cross, the higher the spot weight.*

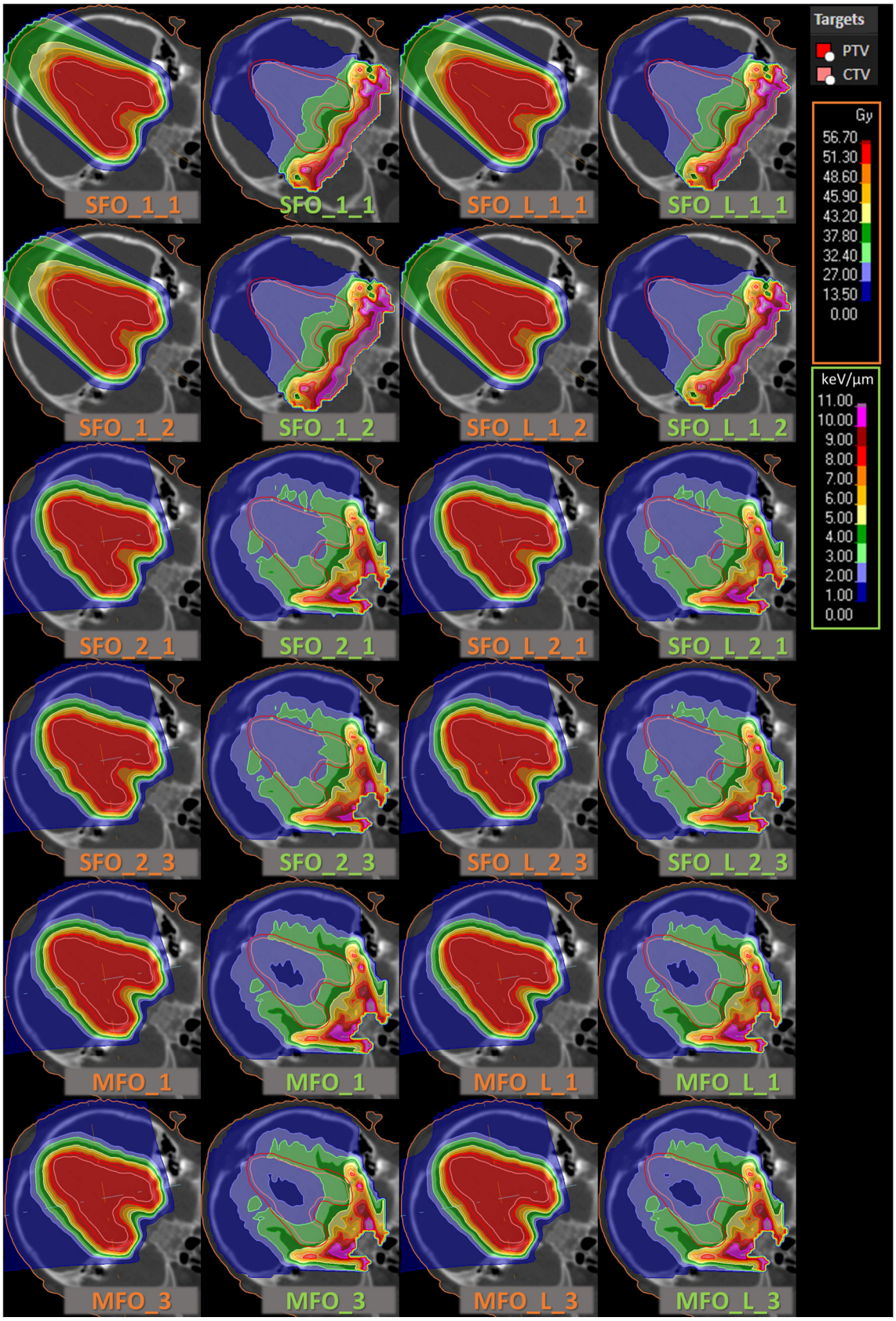

Fig. 72: *Calculated dose (first and third pictures in each row) and LET_d distributions (second and forth pictures in each row) for investigating the influence of different optimization settings for the fifth clinical case - an ependymoma.*

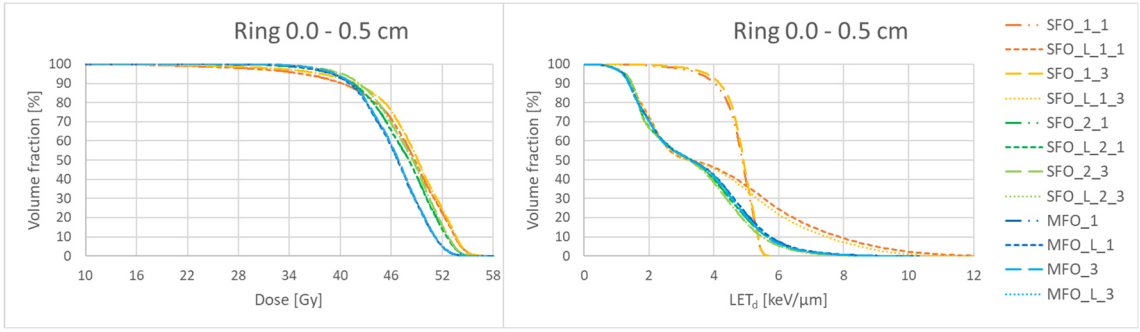

Fig. 73: *DVHs and LET_dVHs of plans resulting from different optimization settings for the ring 0.0 to 0.5 cm around the PTV and the forth clinical case.*

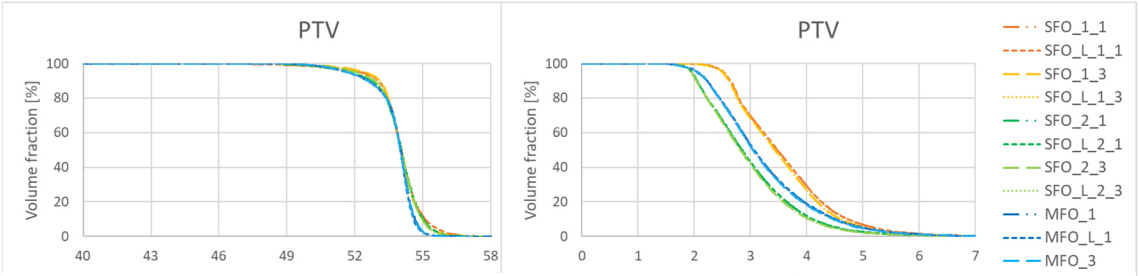

Fig. 74*: DVHs and LET_dVHs of plans resulting from different optimization settings for the PTV and the forth clinical case.*

1. Patient

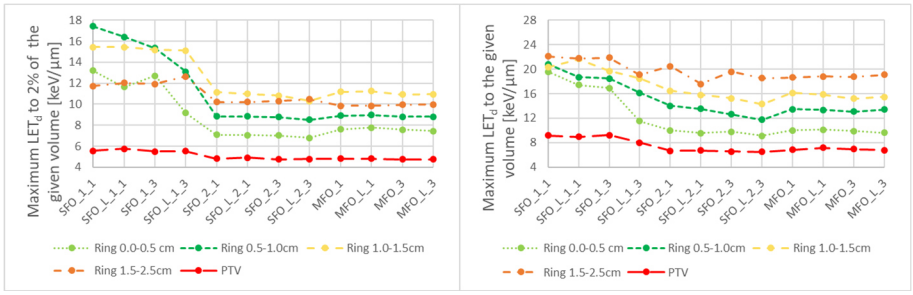

Fig. 75: Influence of different optimization settings. Maximum LET_d to 2% of (left picture) respectively maximum LET_d to (right picture) four different rings (0.0 to 0.5 cm, 0.5 to 1.0 cm, 1.0 to 1.5 cm, 1.5 to 2.5 cm) around the PTV as well as maximum LET_d to 2% of respectively maximum LET_d to the PTV as a function of different optimization settings for the first clinical patient.

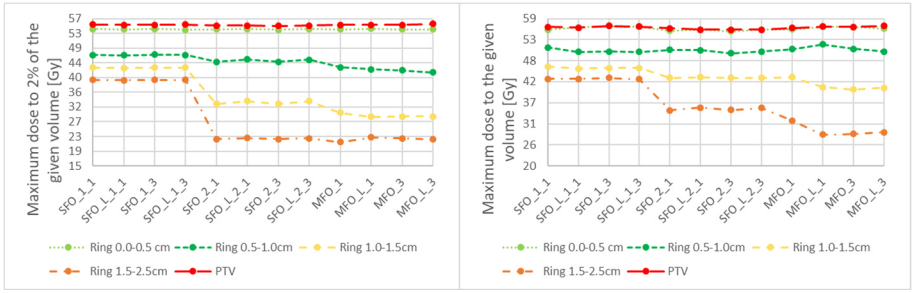

Fig. 76: Influence of different optimization settings. Maximum dose to 2% of (left picture) respectively maximum dose to (right picture) four different rings (0.0 to 0.5 cm, 0.5 to 1.0 cm, 1.0 to 1.5 cm, 1.5 to 2.5 cm) around the PTV as well as maximum dose to 2% of respectively maximum dose to the PTV as a function of different optimization settings for the first clinical patient.

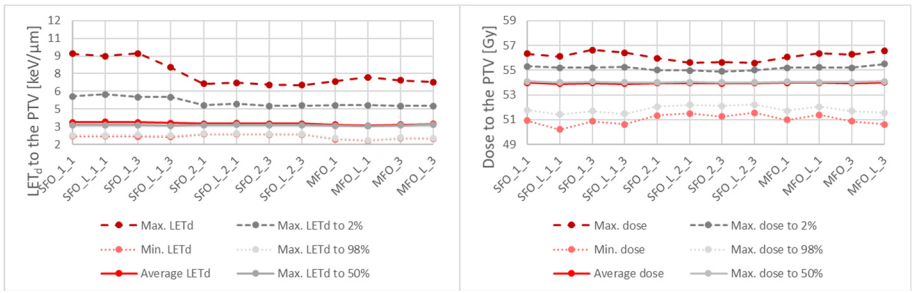

Fig. 77: Influence of different optimization settings. Maximum, minimum and average LET_d to the PTV, maximum LET_d to 2%, 98% and 50% of the PTV (left picture) respectively maximum, minimum and average dose to the PTV, maximum dose to 2%, 98% and 50% of the PTV (right picture) as a function of different optimization settings for the first clinical patient.

2. Patient

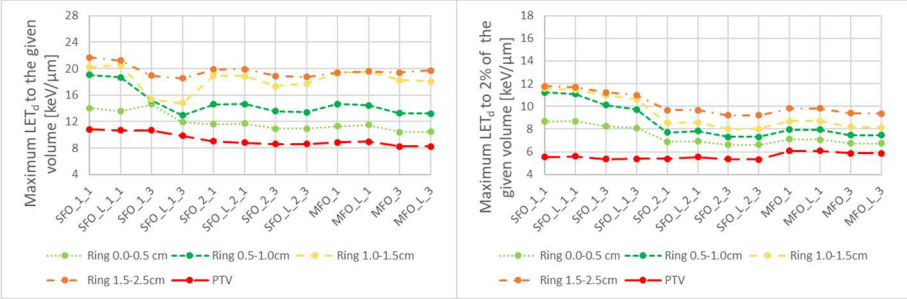

Fig. 78: Influence of different optimization settings. Maximum LET_d to 2% of (left picture) respectively maximum LET_d to (right picture) four different rings (0.0 to 0.5 cm, 0.5 to 1.0 cm, 1.0 to 1.5 cm, 1.5 to 2.5 cm) around the PTV as well as maximum LET_d to 2% of respectively maximum LET_d to the PTV as a function of different optimization settings for the second clinical patient.

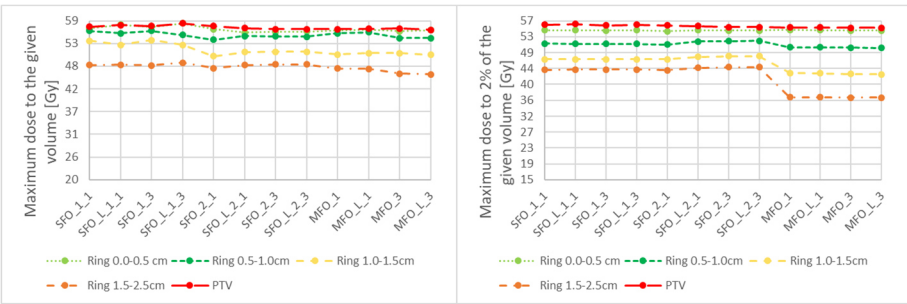

***Fig. 79:** Influence of different optimization settings. Maximum dose to 2% of (left picture) respectively maximum dose to (right picture) four different rings (0.0 to 0.5 cm, 0.5 to 1.0 cm, 1.0 to 1.5 cm, 1.5 to 2.5 cm) around the PTV as well as maximum dose to 2% of respectively maximum dose to the PTV as a function of different optimization settings for the second clinical patient.*

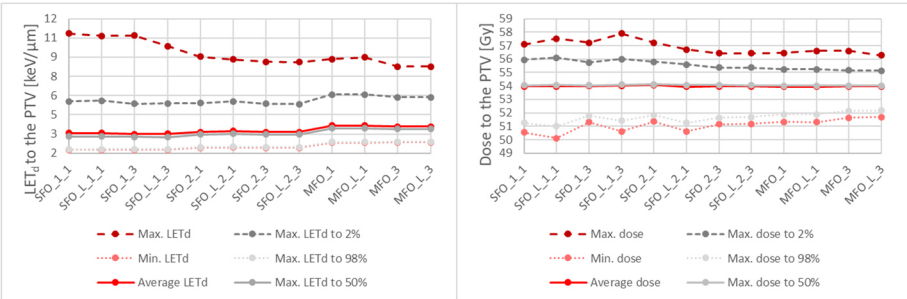

***Fig. 80:** Influence of different optimization settings. Maximum, minimum and average LET_d to the PTV, maximum LET_d to 2%, 98% and 50% of the PTV (left picture) respectively maximum, minimum and average dose to the PTV, maximum dose to 2%, 98% and 50% of the PTV (right picture) as a function of different optimization settings for the second clinical patient.*

3. Patient

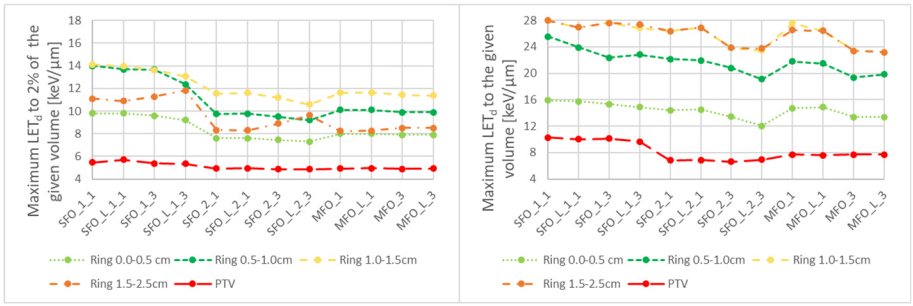

Fig. 81: Influence of different optimization settings. Maximum LET_d to 2% of (left picture) respectively maximum LET_d to (right picture) four different rings (0.0 to 0.5 cm, 0.5 to 1.0 cm, 1.0 to 1.5 cm, 1.5 to 2.5 cm) around the PTV as well as maximum LET_d to 2% of respectively maximum LET_d to the PTV as a function of different optimization settings for the third clinical patient.

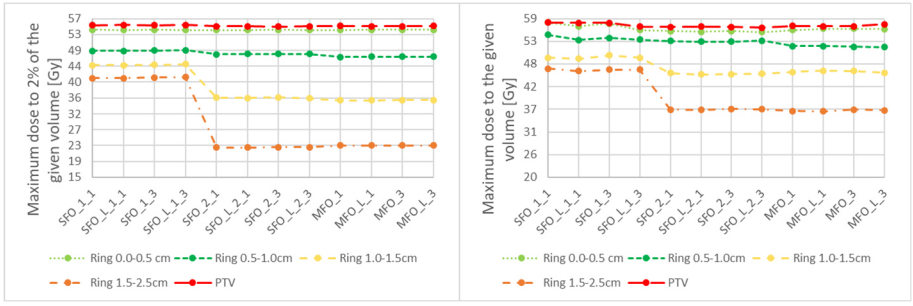

***Fig. 82:** Influence of different optimization settings. Maximum dose to 2% of (left picture) respectively maximum dose to (right picture) four different rings (0.0 to 0.5 cm, 0.5 to 1.0 cm, 1.0 to 1.5 cm, 1.5 to 2.5 cm) around the PTV as well as maximum dose to 2% of respectively maximum dose to the PTV as a function of different optimization settings for the third clinical patient.*

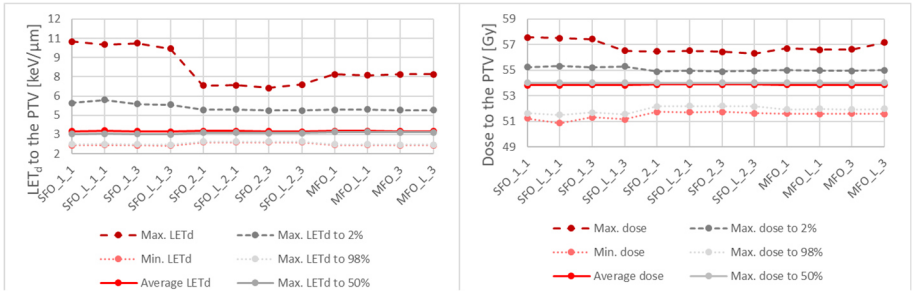

***Fig. 83:** Influence of different optimization settings. Maximum, minimum and average LET_d to the PTV, maximum LET_d to 2%, 98% and 50% of the PTV (left picture) respectively maximum, minimum and average dose to the PTV, maximum dose to 2%, 98% and 50% of the PTV (right picture) as a function of different optimization settings for the third clinical patient.*

4. Patient

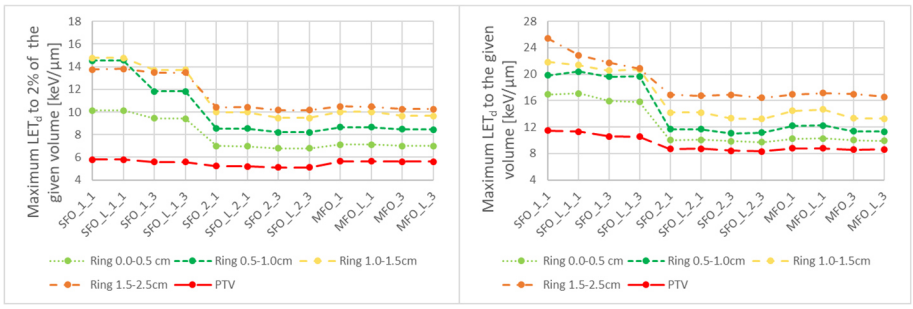

Fig. 84: Influence of different optimization settings. Maximum LET$_d$ to 2% of (left picture) respectively maximum LET$_d$ to (right picture) four different rings (0.0 to 0.5 cm, 0.5 to 1.0 cm, 1.0 to 1.5 cm, 1.5 to 2.5 cm) around the PTV as well as maximum LET$_d$ to 2% of respectively maximum LET$_d$ to the PTV as a function of different optimization settings for the forth clinical patient.

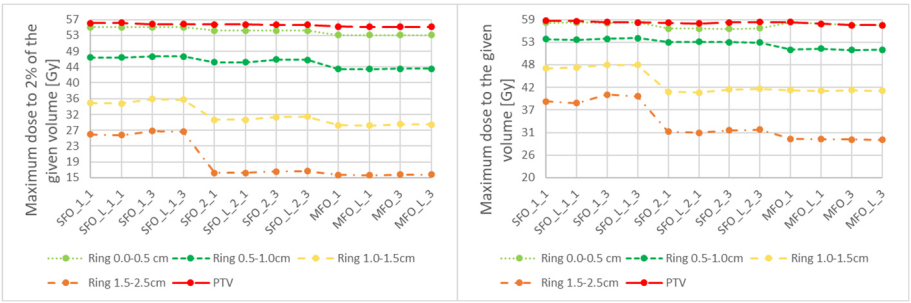

Fig. 85: Influence of different optimization settings. Maximum dose to 2% of (left picture) respectively maximum dose to (right picture) four different rings (0.0 to 0.5 cm, 0.5 to 1.0 cm, 1.0 to 1.5 cm, 1.5 to 2.5 cm) around the PTV as well as maximum dose to 2% of respectively maximum dose to the PTV as a function of different optimization settings for the forth clinical patient.

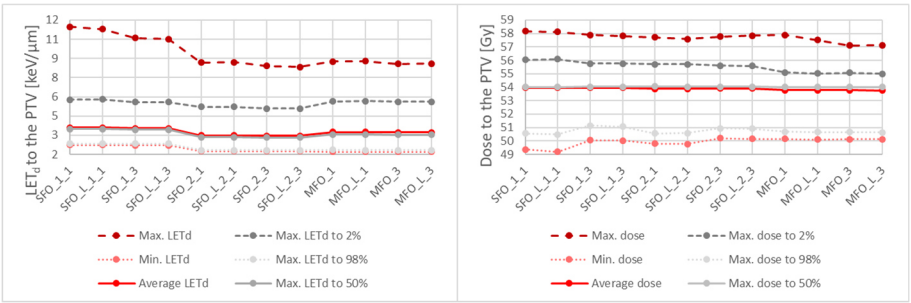

Fig. 86: Influence of different optimization settings. Maximum, minimum and average LET$_d$ to the PTV, maximum LET$_d$ to 2%, 98% and 50% of the PTV (left picture) respectively maximum, minimum and average dose to the PTV, maximum dose to 2%, 98% and 50% of the PTV (right picture) as a function of different optimization settings for the forth clinical patient.

5. Patient

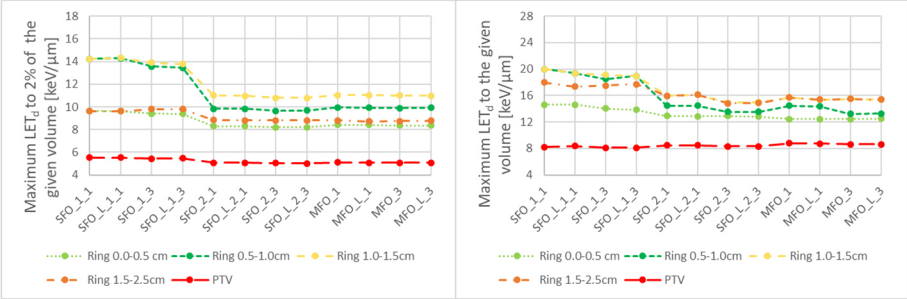

Fig. 87: Influence of different optimization settings. Maximum LET_d to 2% of (left picture) respectively maximum LET_d to (right picture) four different rings (0.0 to 0.5 cm, 0.5 to 1.0 cm, 1.0 to 1.5 cm, 1.5 to 2.5 cm) around the PTV as well as maximum LET_d to 2% of respectively maximum LET_d to the PTV as a function of different optimization settings for the fifth clinical patient.

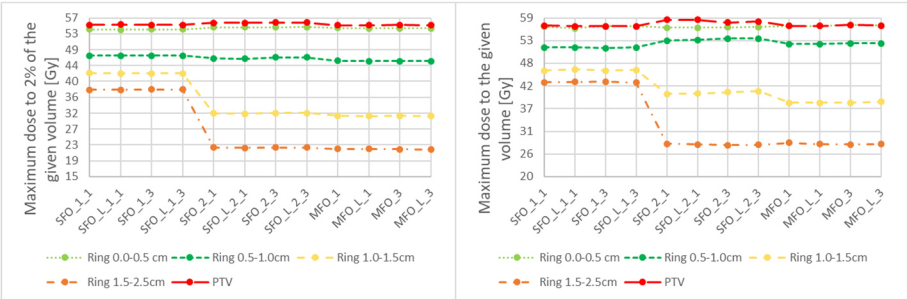

Fig. 88: Influence of different optimization settings. Maximum dose to 2% of (left picture) respectively maximum dose to (right picture) four different rings (0.0 to 0.5 cm, 0.5 to 1.0 cm, 1.0 to 1.5 cm, 1.5 to 2.5 cm) around the PTV as well as maximum dose to 2% of respectively maximum dose to the PTV as a function of different optimization settings for the fifth clinical patient.

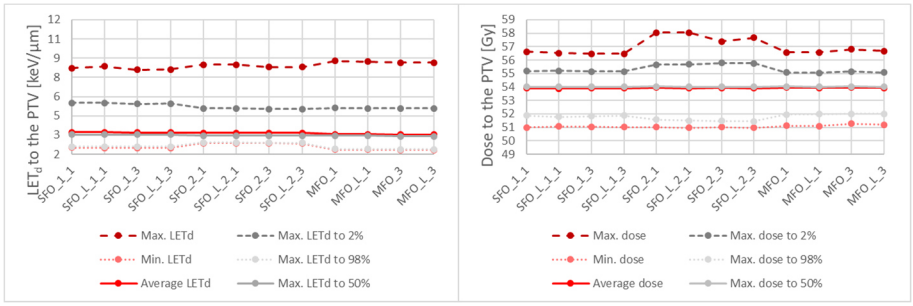

Fig. 89: Influence of different optimization settings. Maximum, minimum and average LET_d to the PTV, maximum LET_d to 2%, 98% and 50% of the PTV (left picture) respectively maximum, minimum and average dose to the PTV, maximum dose to 2%, 98% and 50% of the PTV (right picture) as a function of different optimization settings for the fifth clinical patient.

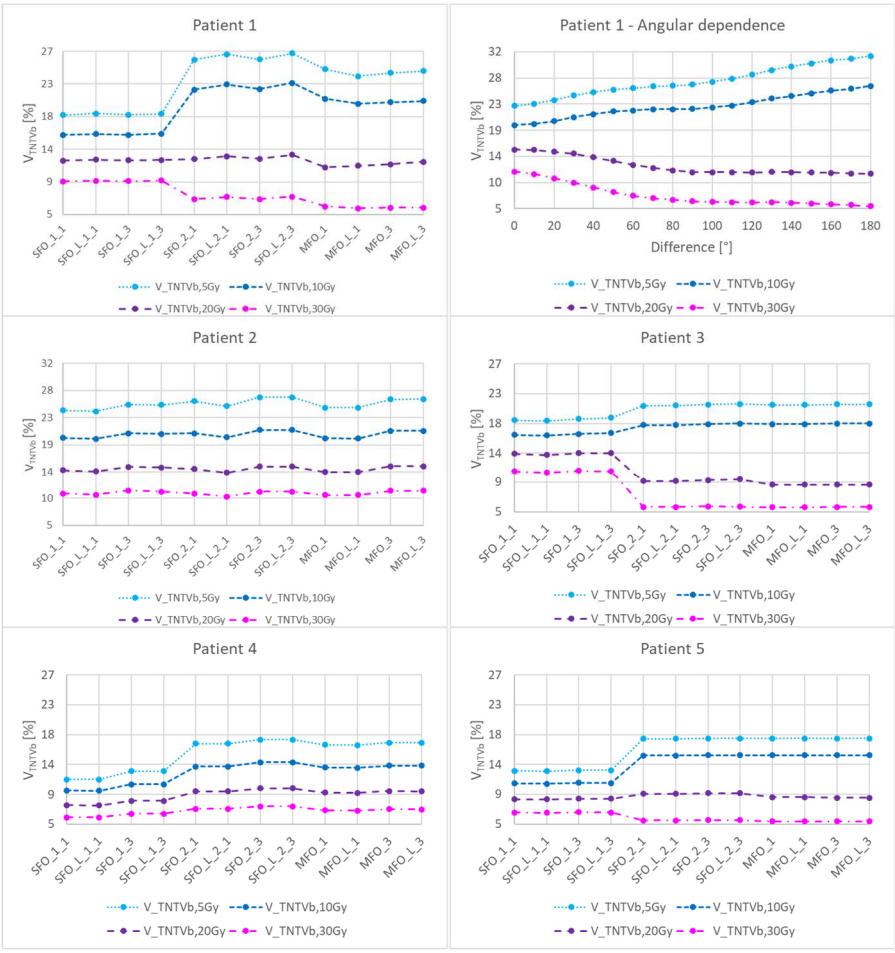

Fig. 90: *Influence of different optimization settings. Percentage of the $TNTV_B$'s total volume receiving at least 5, 10, 20 and 30 Gy as a function of different optimization settings respectively the angle separating two SFO beams for the first clinical patient (right picture on the top).*

3.3.3 Comparisons

In this chapter the effects of varying the investigated optimization parameters on the LET_d and dose distributions are summarized over all patient cases.

The influence of each optimization parameter was individually examined. One certain optimization parameter was altered (e.g. number of distal energy layers[49]). The relative deviations of the maximum LET_d values obtained after the alternations from those calculated before the alternation were computed. In the following, the evaluated relative deviations where averaged over all five patient cases. Average, maximum and minimum relative deviations as well as the corresponding standard deviations were calculated. The same was done for the maximum dose, the minimum and average LET_d and the percentage of the $TNTV_B$ receiving 5, 10, 20 and 30 Gy. All computed values are displayed in *Fig. 91* to *Fig. 96.* The x-axes in the figures show which plans were compared. Additionally, the respective deviations for the phantom cases were examined in dependence of the beam spacing (0°, 90° and 180°) and can be found in the appendix (*A.3 Comparisons - Results*). The results which were considered to be most crucial are summarized in the following.

[49] In concrete terms the following optimization parameters were altered: The number of distal energy layers was changed from one to three, a maximum spot weight limitation was introduced, the number of beams was changed from one to two and the optimization strategy was changed from SFO to MFO. Moreover, the influence of changing two of these parameters at once was studied: introducing a maximum spot weight limitation and simultaneously changing the number of distal energy layers from one two three.

Maximum LET_d around the PTV

For the **clinical cases maximum LET_d** to the ring from 0.0 to 0.5 cm **around the PTV** was reduced by an overall average[50] of

- **23.30%** (±14.26%) when using two **beams** compared to one
- **8.83%** (±9.72%) when using three **distal energy and maximum spot weight limitation** compared to one distal energy layer and no maximum spot weight limitation
- **6.10%** (±6.77%) when using three **distal energy layers** compared to one distal energy layer
- **3.02%** (±6.89%) when introducing a **maximum spot weight limitation**
- **0.45%** (±3.86%) when using **MFO** compared to **SFO**

For the **phantom one field plans maximum LET_d** to the ring from 0.0 to 0.5 cm **around the PTV** was reduced by an average of

- **37.42%** when using three **distal energy and maximum spot weight limitation** compared to one distal energy layer and no maximum spot weight limitation
- **27.09%** (±7.92%) when using three **distal energy layers** compared to one distal energy layer
- **13.14%** (±9.43%) when introducing a **maximum spot weight limitation**

For the **phantom two field plans separated by an angle of 90° maximum LET_d** to the ring from 0.0 to 0.5 cm **around the PTV** was reduced by an average of

- **30.30%** (±12.78%) when using two **beams** compared to one[51]
- **2.58%** (±0.66%) when using three **distal energy and maximum spot weight limitation** compared to one distal energy layer and no maximum spot weight limitation
- **1.44%** (±1.54%) when using three **distal energy layers** compared to one distal energy layer
- **1.14%** (±1.38%) when introducing a **maximum spot weight limitation**
- **0.90%** (±1.36%) when using **MFO** compared to **SFO**

For the **phantom two field plans separated by an angle of 180° maximum LET_d** to the ring from 0.0 to 0.5 cm **around the PTV** was reduced by an average of

- **55.54%** (±7.45%) when using two **beams** compared to one
- **8.09%** (±6.27%) when using three **distal energy and maximum spot weight limitation** compared to one distal energy layer and no maximum spot weight limitation
- **4.03%** (±6.24%) when using three **distal energy layers** compared to one distal energy layer
- **4.09%** (±5.84%) when introducing a **maximum spot weight limitation**
- **7.70%** (±6.77%) when using **MFO** compared to **SFO**

[50] The listed average values were obtained by averaging twice. A description of how these average values were calculated follows. For a better understanding it is described exemplarily for one optimization parameter – the number of distal energy layers. The average values for all other optimization parameters can be calculated analogously. In all single field plans with and without maximum spot weight limitation as well as in all SFO and MFO two field plans with and without maximum spot weight limitation the number of distal energy layers was changed from one to three. All other optimization parameters were kept constant. Consequently, for every plan with three distal energy layers a reference plan with one distal energy layer existed. The relative deviations of the plans with three distal energy layers from the corresponding reference plans with one distal energy layer were computed. Thus, in total, six relative deviation values were obtained. This was done for all five clinical cases. Each of the obtained relative deviations were averaged over all five clinical cases. The six average relative deviations were averaged again. This time the average over the six average relative deviations was taken. The obtained average was called overall average and the obtained standard deviation overall standard deviation σ. The values given in brackets are $\pm\sigma$. The average values for the phantom case were obtained by averaging just once, since naturally the averaging over all five clinical cases was absent here.

[51] Whenever using the expression *two beams compared to one*, it refers to the process of comparing the two field plans separated by an angle of 90° (180°) with the corresponding single field plans.

Maximum LET_d to the PTV

For the **clinical cases** the average relative deviation of **maximum LET_d to the PTV** was

- **-17.13%** (±11.76%) when using two **beams** compared to one
- **-3.99%** (±3.77%) when using three **distal energy and maximum spot weight limitation** compared to one distal energy layer and no maximum spot weight limitation
- **-3.09%** (±2.90%) when using three **distal energy layers** compared to one distal energy layer
- **-0.91%** (±3.20 when introducing a **maximum spot weight limitation**
- **-4.18%** (±5.20%) when using **MFO** compared to **SFO**

For the **phantom one field plans** the average relative deviation of **maximum LET_d to the PTV** was

- **-10.16%** when using three **distal energy and maximum spot weight limitation** compared to one distal energy layer and no maximum spot weight limitation
- **-6.74%** (±4.79%) when using three **distal energy layers** compared to one distal energy layer
- **-3.42%** (±4.96%) when introducing a **maximum spot weight limitation**

For the **phantom two field plans separated by an angle of 90°** the average relative deviation of **maximum LET_d to the PTV** was

- **-24.92%** (±3.52%) when using two **beams** compared to one
- **-0.68%** (±0.03%) when using three **distal energy and maximum spot weight limitation** compared to one distal energy layer and no maximum spot weight limitation
- **-0.37%** (±0.29%) when using three **distal energy layers** compared to one distal energy layer
- **-0.31%** (±0.29%) when introducing a **maximum spot weight limitation**
- **1.51%** (±0.29%) when using **MFO** compared to **SFO**

For the **phantom two field plans separated by an angle of 180°** the average relative deviation of **maximum LET_d to the PTV** was

- **-35.87%** (±4.21%) when using two **beams** compared to one
- **-5.48%** (±4.12%) when using three **distal energy and maximum spot weight limitation** compared to one distal energy layer and no maximum spot weight limitation
- **0.34%** (±2.57%) when using three **distal energy layers** compared to one distal energy layer
- **-2.87%** (±4.01%) when introducing a **maximum spot weight limitation**
- **-12.11%** (±4.20%) when using **MFO** compared to **SFO**

Minimum LET_d to the PTV

For the **clinical cases** the average relative deviation of **minimum LET_d to the PTV** was

- **1.69%** (±16.81%) when using two **beams** compared to one
- **-0.44%** (±1.23%) when using three **distal energy and maximum spot weight limitation** compared to one distal energy layer and no maximum spot weight limitation
- **-0.03%** (±2.30%) when using three **distal energy layers** compared to one distal energy layer
- **-0.38%** (±1.39%) when introducing a **maximum spot weight limitation**
- **6.29%** (±15.25%) when using **MFO** compared to **SFO**

For the **phantom one field plans** the average relative deviation of **minimum LET_d to the PTV** was

- **-1.59%** when using three **distal energy and maximum spot weight limitation** compared to one distal energy layer and no maximum spot weight limitation
- **-0.94%** (±0.81%) when using three **distal energy layers** compared to one distal energy layer
- **-0.64%** (±0.82%) when introducing a **maximum spot weight limitation**

For the **phantom two field plans separated by an angle of 90°** the average relative deviation of **minimum LET_d to the PTV** was

- **30.30%** (±12.78%) when using two **beams** compared to one
- **9.81%** (±0.95%) when using two **beams** compared to one
- **-0.68%** (±0.03%) when using three **distal energy and maximum spot weight limitation** compared to one distal energy layer and no maximum spot weight limitation
- **-1.04%** (±1.12%) when using three **distal energy layers** compared to one distal energy layer
- **0.45%** (±0.80%) when introducing a **maximum spot weight limitation**
- **-0.24%** (±1.23%) when using **MFO** compared to **SFO**

For the **phantom two field plans separated by an angle of 180°** the average relative deviation of **minimum LET_d to the PTV** was

- **30.23%** (±3.80%) when using two **beams** compared to one
- **2.48%** (±4.74%) when using three **distal energy and maximum spot weight limitation** compared to one distal energy layer and no maximum spot weight limitation
- **-2.60%** (±4.29%) when using three **distal energy layers** compared to one distal energy layer
- **2.12%** (±3.80%) when introducing a **maximum spot weight limitation**
- **-2.46%** (±4.09%) when using **MFO** compared to **SFO**

V_{TNTVb}

For the **clinical cases** the average relative deviation of $V_{TNTVb,5Gy}$ was

- **25.56%** (±15.24%) when using two **beams** compared to one
- **2.41%** (±2.71%) when using three **distal energy and maximum spot weight limitation** compared to one distal energy layer and no maximum spot weight limitation
- **2.34%** (±2.86%) when using three **distal energy layers** compared to one distal energy layer
- **0.08%** (±1.29%) when solely introducing a **maximum spot weight limitation**
- **2.28%** (±3.26%) when using **MFO** compared to **SFO**

For the **clinical cases** the average relative deviation of $V_{TNTVb,10Gy}$ was

- **22.76%** (±14.82%) when using two **beams** compared to one
- **2.44%** (±2.66%) when using three **distal energy and maximum spot weight limitation** compared to one distal energy layer and no maximum spot weight limitation
- **2.41%** (±2.79%) when using three **distal energy layers** compared to one distal energy layer
- **0.04%** (±1.31%) when solely introducing a **maximum spot weight limitation**
- **2.49%** (±3.65%) when using **MFO** compared to **SFO**

For the **clinical cases** the average relative deviation of $V_{TNTVb,20Gy}$ was

- **-0.90%** (±17.90%) when using two **beams** compared to one
- **2.89%** (±2.73%) when using three **distal energy and maximum spot weight limitation** compared to one distal energy layer and no maximum spot weight limitation
- **2.75%** (±2.76%) when using three **distal energy layers** compared to one distal energy layer
- **0.15%** (±1.45%) when solely introducing a **maximum spot weight limitation**
- **4.88%** (±3.02%) when using **MFO** compared to **SFO**

For the **clinical cases** the average relative deviation of $V_{TNTVb,30Gy}$ was

- **-16.42%** (±22.77%) when using two **beams** compared to one
- **2.34%** (±2.96%) when using three **distal energy and maximum spot weight limitation** compared to one distal energy layer and no maximum spot weight limitation
- **2.64%** (±3.00%) when using three **distal energy layers** compared to one distal energy layer
- **-0.28%** (±1.80%) when solely introducing a **maximum spot weight limitation**
- **5.01%** (±6.87%) when using **MFO** compared to **SFO**

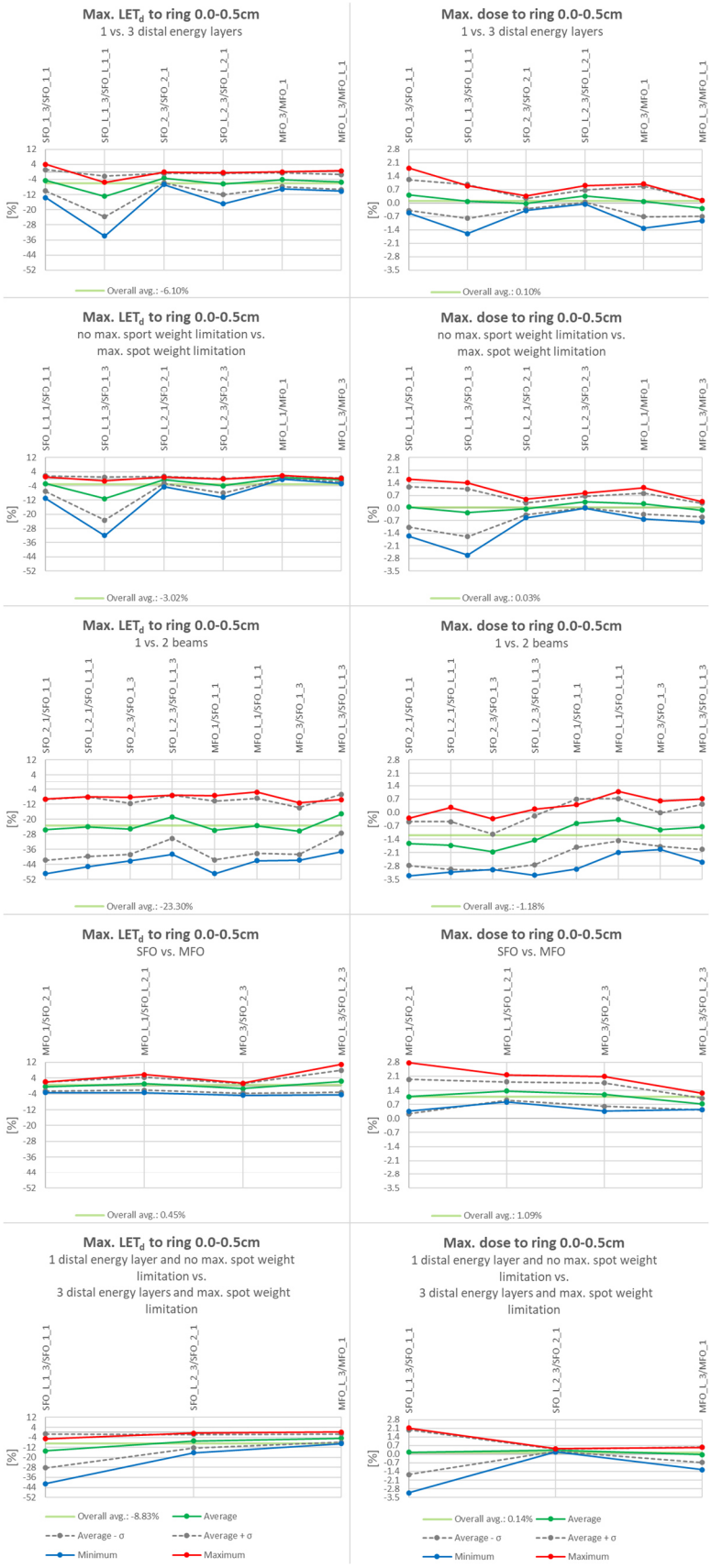

Fig. 91: *Change of maximum LET_d (images in the first column) and dose (images in the second column) to the ring from 0.0 to 0.5 cm around the PTV resulting from the change of one optimization setting averaged over all clinical cases in %. The x-axis shows which plans were compared.*

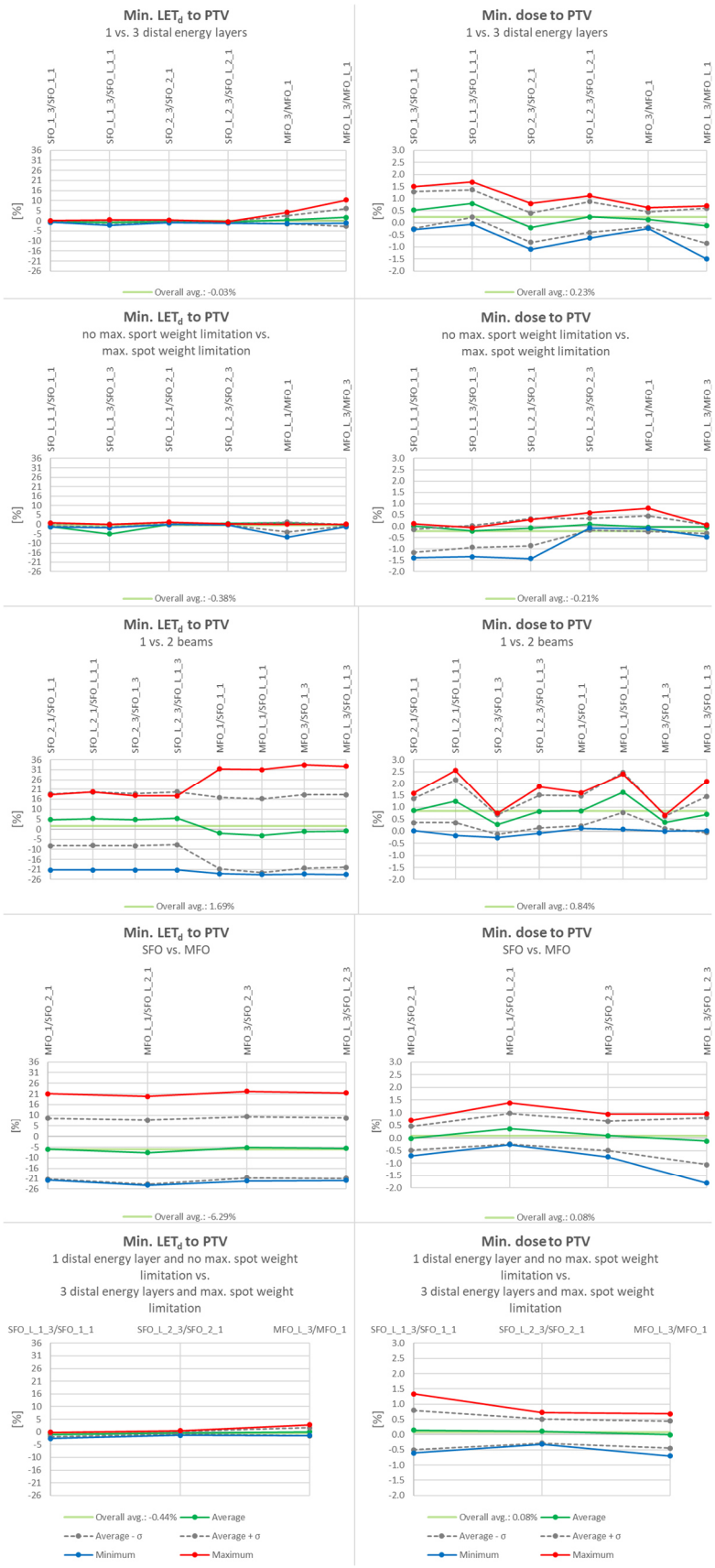

Fig. 92: *Change of minimum LET_d (images in the first column) and dose (images in the second column) to the PTV resulting from the change of one optimization setting averaged over all clinical cases in %. The x-axis shows which plans were compared.*

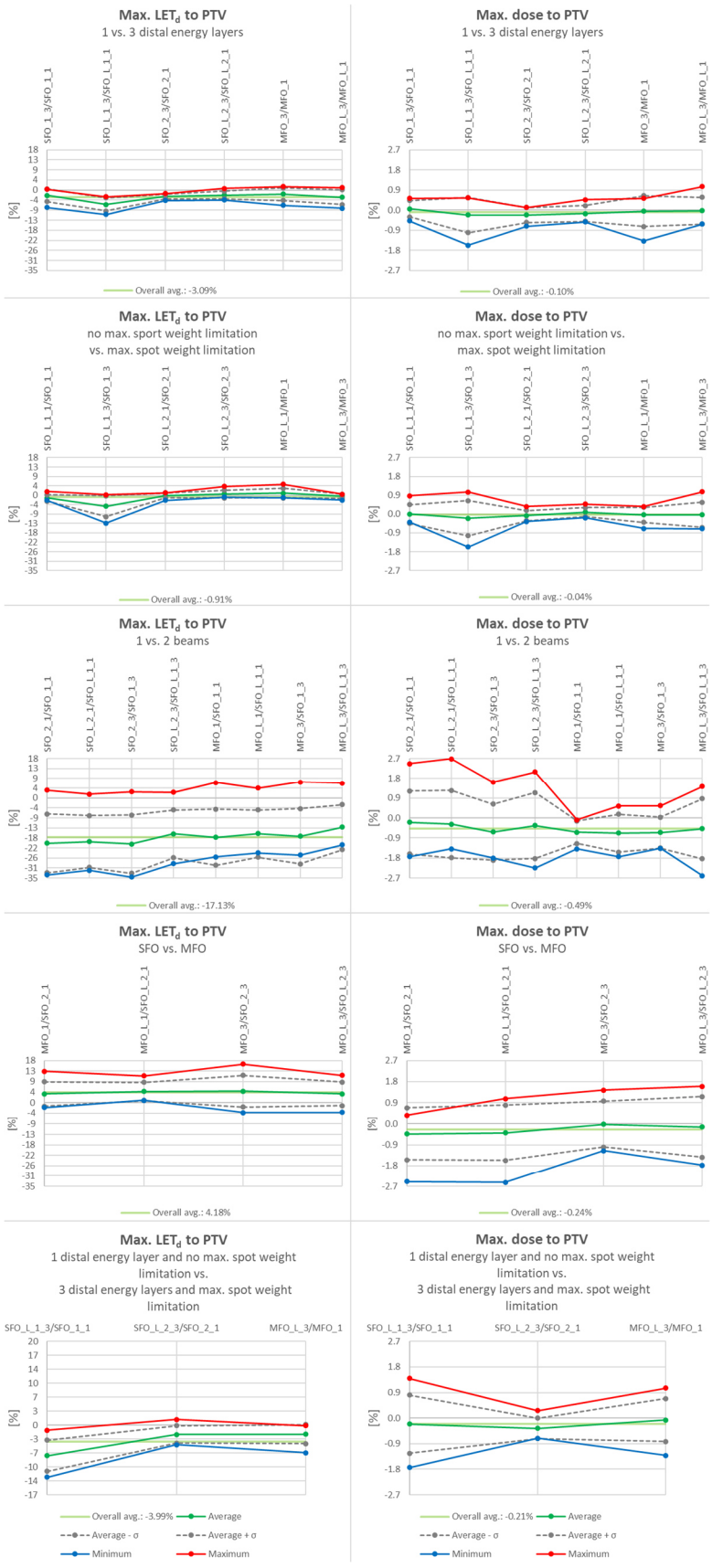

Fig. 93: *Change of maximum LET_d (images in the first column) and dose (images in the second column) to the PTV resulting from the change of one optimization setting averaged over all clinical cases in %. The x-axis shows which plans were compared.*

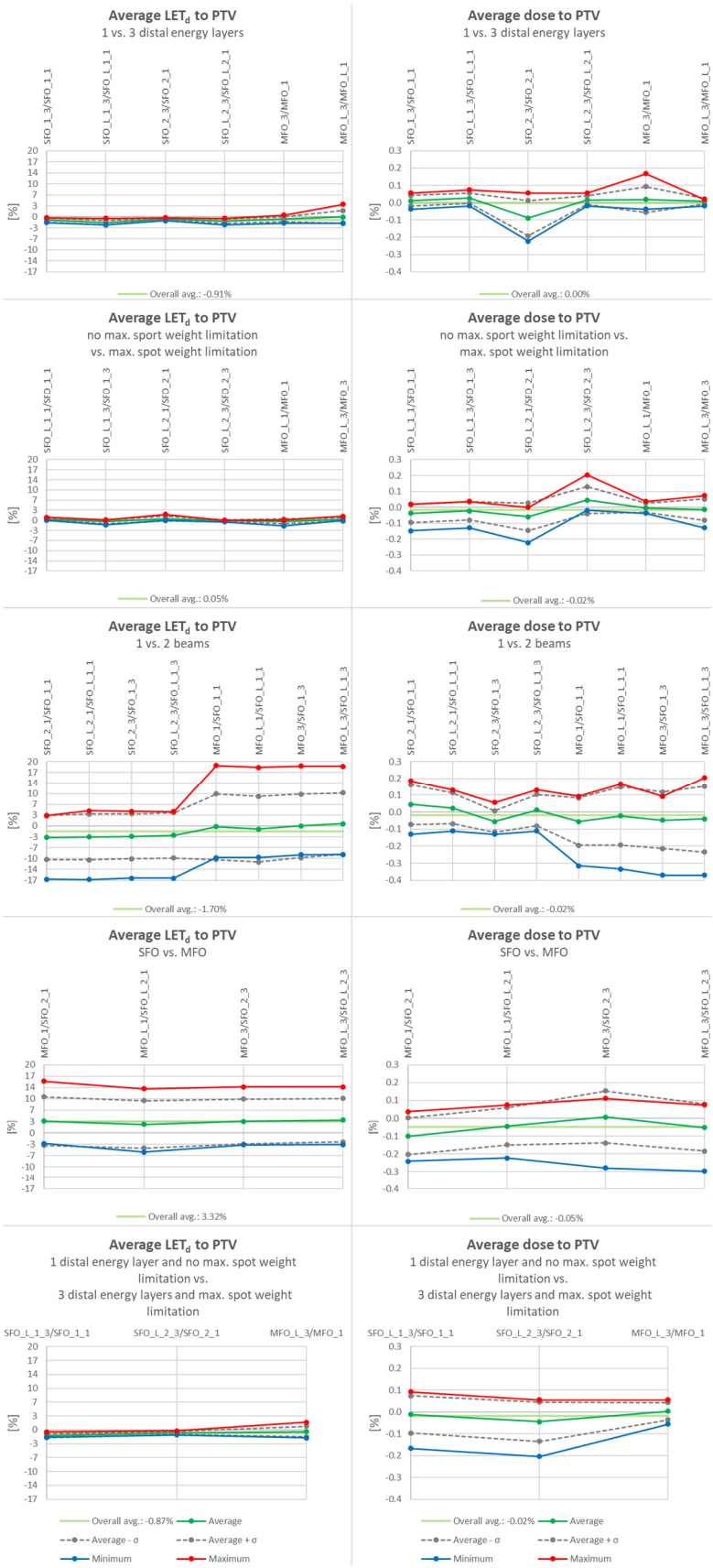

Fig. 94: *Change of average LET_d (images in the first column) and dose (images in the second column) to the PTV resulting from the change of one optimization setting averaged over all clinical cases in %. The x-axis shows which plans were compared.*

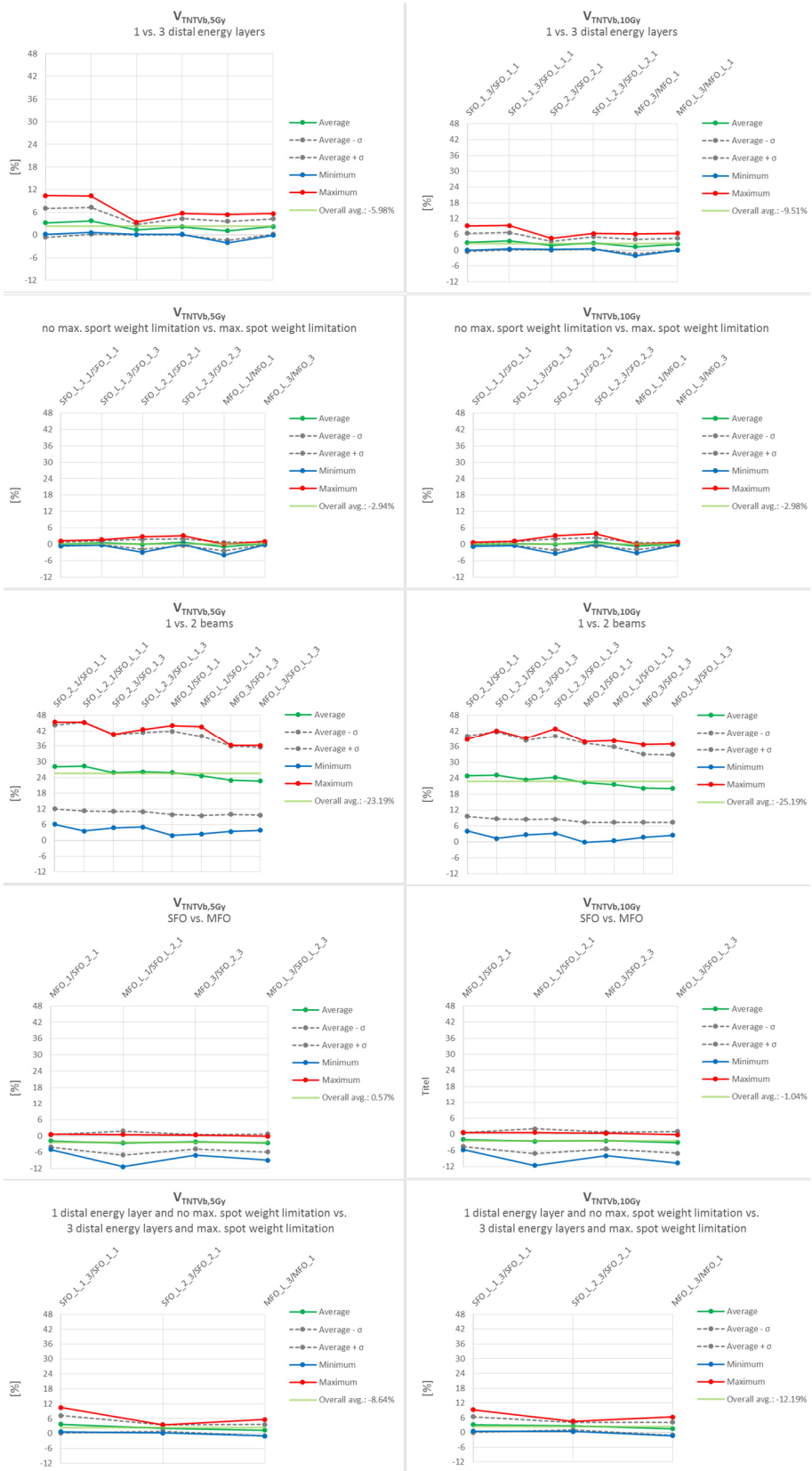

***Fig. 95**: Change of $V_{TNTVb,5Gy}$ (pictures on the left) respectively change of $V_{TNTVb,10Gy}$ (pictures on the right) resulting from the change of one optimization setting averaged over all clinical cases in %. The x-axis shows which plans were compared.*

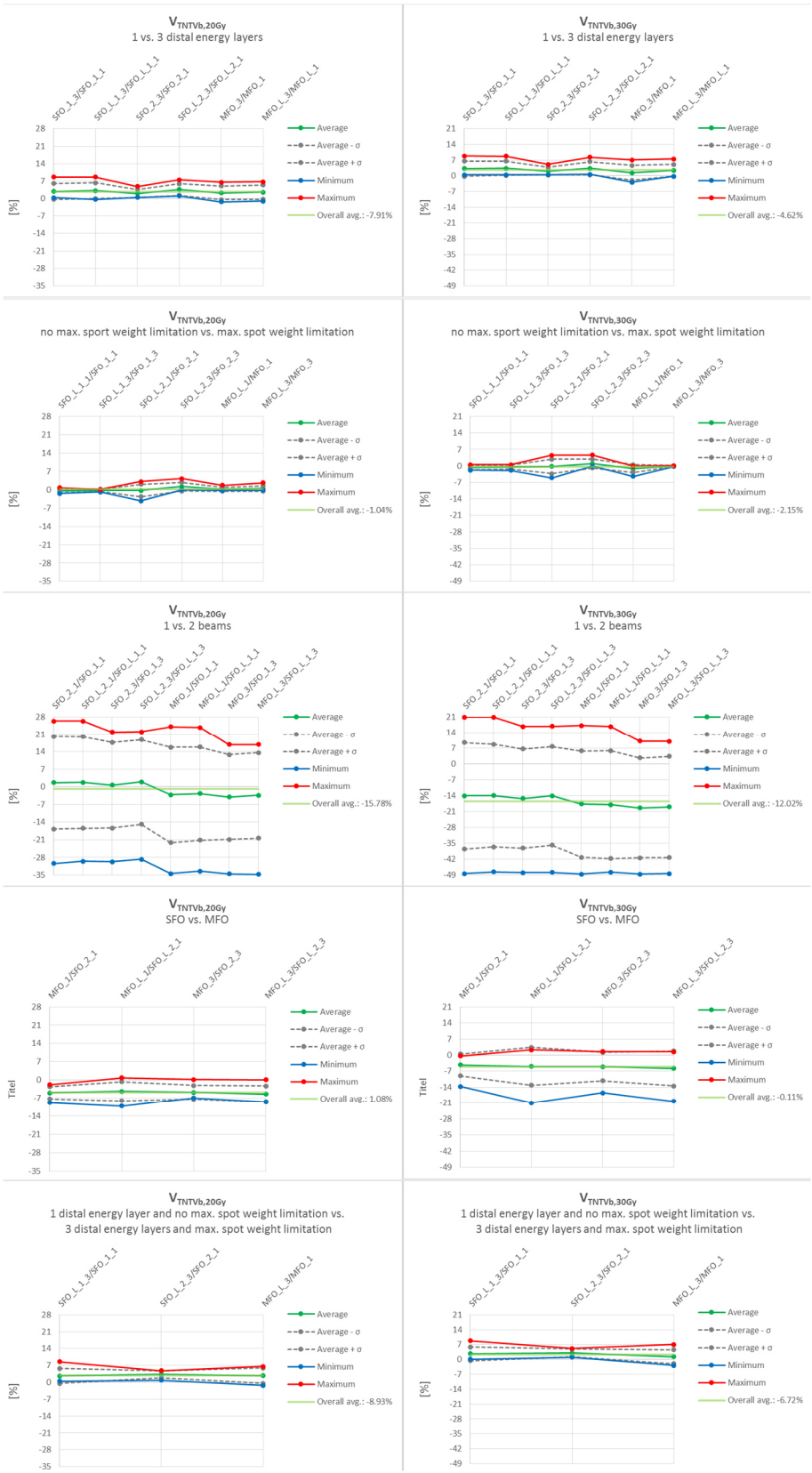

Fig. 96: *Change of $V_{TNTVb,20Gy}$ (pictures on the left) respectively change of $V_{TNTVb,30Gy}$ (pictures on the right) resulting from the change of one optimization setting averaged over all clinical cases in %. The x-axis shows which plans were compared.*

4 DISCUSSION AND CONCLUSION

4.1 Motivation for the use of dose-averaged LET

Since in the course of this work not just single particles or monoenergetic beams were examined but mixed particle fields an averaging of LET values was performed. In section *1.2.3 Stopping power and linear energy transfer* was already pointed out that two different ways of calculating this average are common – dose averaging and track averaging. As this study was based on clinical background and in the usual case for clinical dose levels a sufficiently large number of particle tracks crosses a sub-cellular structure the dose-averaged LET and not the track-averaged LET seemed to be the more meaningful quantity and was chosen for all calculations.

Generally, it is possible that the underlying LET distributions of two sorts of equivalent dose distributions are different, since dose is given as LET times particle fluence. Consequently a homogenous dose distribution is no guarantee for a homogeneous LET_d or RBE distribution.

A potential advantage of the use of LET_d as a surrogate for RBE is that it is a pure physical quantity. Its quite accurate determination on the basis of the treatment plan information is possible. LET_d alone will never provide actual proton RBE values. However, since RBE rises with LET_d for a given dose and α/β, LET_d is a correlated indicator for local increase or decrease of RBE. (Paganetti, et al., 2019).

Cell experiments showed that the local complexity of the individual DSBs tend to increase with increasing particle LET. It was observed that the production of more than one DSB by an individual electron while passing through a cell is seldom independent of its kinetic energy. Protons, on the contrary, are capable of producing multiple DSBs in close spatial proximity. Due to that the chance of an incorrect rejoining and consequently a chromosome aberration is enhanced. This might state a reason for the observed increased cell lethality with increasing LET up to a peak which is specific for the particle type. One cause for the variations in RBE observed in experiments seems to be the per track number of DSBs respectively proximity effects. The overall kinetics and accuracy of the DSB rejoining process in turn are influenced by the local DSB complexity. Considering the formation of unrepairable DSBs respectively the biological processing of repairable DSBs into lethal chromosome aberrations as a basis for tendencies in the RBE as a function of LET appears to be plausible (Stewart, et al., 2015).

4.2 Validation RS v5.99.50

The LET_d distributions calculated by RS v5.99.50 were in good agreement with those computed with GATE8.0/Geant4.10.3. Therefore, RS was successfully validated against an independent code and could be used as a reliable tool for LET_d distribution display for further investigations described in this master thesis.

4.3 Analysis of LET_d distributions

Voxel size dependence

As shown in *Figure 17* and *Figure 18* the calculated longitudinal LET_d distributions did not depend on the chosen size of the dose grid´s voxels. A distinction of LET values which were calculated with differing voxel sizes and centered at the same point is expected, since the interval in which the LET was averaged changed. The higher the gradient of the distribution in the area considered was, the higher were the deviations between the LET_d computed with different voxel

sizes. In regions where the LET stayed almost the same those deviations nearly disappeared completely. In those areas the voxel size could be increased without a change in the LET value. To put it straight the observable deviations resulted from different averaging intervals. The unsigned relative deviations were less than 1.2%. Systematic deviations did not occur.

Increasing the number of beams and using orthogonal to contralateral beams had the highest impact on the reduction of maximum LET_d, whereas decreasing the target´s depth and the field size led to a raise of maximum LET_d. Moreover, the voxel size of the dose grid did not influence the LET_d distributions.

Angular dependence

The decrease of maximum LET_d around the PTV with increasing angle separating two SFO beams might be partially explained as follows: If two SFO beams which are separated by a rather large angle are used the peaks at the end of range are diluted by fields entering from the opposite direction. This results in a reduction of maximum LET_d (Grassberger, Trofimov, Lomax, & Paganetti, 2011)

Figure 20, *Figure 21* and *Figure 22* show that using a bigger angular beam spacing reduced in absolute and relative terms the maximum LET_d in the PTV only slightly, but had a larger influence on the maximum LET_d in the rings around the PTV. The second smallest reduction of maximum LET_d occured in the ring from 1.5 to 2.5 cm around the PTV which indicates that changing the separation angle has only a minor impact on regions located sufficiently far from the PTV. It is also illustrated that the use of a small separation angle can lead to an increase of maximum LET_d compared to using contra-lateral beams in some regions around the PTV.

The results for the clinical cases revealed: The bigger the angle between the two irradiation fields the smaller the maximum LET_d, the smaller the maximum dose to areas which are 1 cm or further away from the PTV as well as the smaller the percentage of the $TNTV_B$´s total volume receiving at least 20 and 30 Gy. By increasing the angular beam spacing therefore plans can be generated that are more robust against high LET_ds. The robustness however is always on the cost of raised low dose exposure of normal tissues ($V_{TNTVb,5Gy}$, $V_{TNTVb,10Gy}$).

As already mentioned in section *3.2.2 Angular dependence* irregularities and deviations from the spherical target occurred in the maximum LET_d values to the ring 1.5 to 2.5 cm around the PTV. This is an indication that findings from the phantom case can never precisely represent a clinical situation. Each case must be evaluated individually. The similarity of the geometry between the patient I investigated and the phantom was quite high. In the phantom case a spherical target was centered in a cylindrical water phantom. Consequently, the distance in the water phantom the beam traversed before entering the PTV was the same for all irradiation angles. For the clinical case the distance between the PTV and the patient´s skin surface in the areas, through which the incoming beams passed, just varied slightly. The just small variation, however, might even be noticeable in *Fig. 40* where LET_d values of the clinical and phantom case were compared. For the phantom case the distance the beam traversed before entering the PTV was almost the same for an irradiation angle of 0° and 180°. That´s why the values for the ratio between the maximum LET_d for 180° and the maximum LET_d for 0° obtained for the clinical respectively the phantom case were almost the same for all investigated structures. For irradiation angles between 0° and 180° the PTV was closer to the patient´s skin surface. As shown in section *3.2.3 Depth and size dependence* smaller target depths led to higher maximum LET_d values. Consequently the amounts of maximum LET_d for irradiation angles of about 90°on the maximum LET_d for an angle of 0°were higher for the clinical case than for the phantom case.

In conclusion, it is always important to exactly study the geometry of the individual case in detail before choosing the irradiation angle for a treatment plan. Larger deviations from the values for LET_d and dose I obtained might occur, for instance, for a not centered target or an irregular target shape. Moreover, when creating a treatment plan for clinical application one does not only have

to ensure that the dose to the PTV is high enough but also that dose limits for organs at risk close to the target are observed. In most cases instead of using two contralateral beams, a selection of beams in a way that the beams do not range directly into critical normal structures adjacent and distal to the target might be the better solution. Especially if maximum tolerance doses have to be satisfied for the normal tissue one should choose this approach. Otherwise, the risk for exceeding the maximum tolerance doses might become alarmingly high. Caution is especially warranted for low α/β tissues with higher RBE and high RBE uncertainties (Paganetti, et al., 2019).

Depth and field size dependence

A reason for a smaller maximum LET_d with increasing depth can be explained by the impact of range straggling present when treating deep-seated targets, respectively, using high initial beam energies. The energy distribution becomes broader, the maximum LET_d smaller (Grassberger, Trofimov, Lomax, & Paganetti, 2011).

If the irradiated target is small peaks cannot dilute each other to a great extent. All particles need to stop very close to one another. This results in an increased maximum LET_d compared to larger field sizes.

Number of beam dependence

Since using two beams instead of one had a big impact on the value of maximum LET_d I suggest to apply two fields whenever possible. The reduction of maximum LET_d, of course, might not be as high as presented in this master thesis when, for example, the angle between the two beams is less than 180° (see section *3.2.2 Angular dependence*). If one only considers the results obtained for the phantom case, the usage of more than two beams do not appear to be necessary. The additional reduction of maximum LET_d around the target was negligible. However, in a clinical treatment situation that could look very different. The high LET_d portion of the distal end of the beam is spread to different areas when using multiple beams respectively beam angles. The result is a minimization of the potential influence of a single beam pointing toward one location where probable critical normal structures are located. The use of more beams reduces the weight of each individual beam. Hence, the effect of RBE uncertainties at the distal edge of each beam are lower (Paganetti, et al., 2019).

4.4 Investigation of the influence of different optimization settings on LET_d distributions

As shown in *Fig. 59* and already mentioned in section *3.3.1 Phantom case* maximum LET_d values were more affected than maximum LET_d values to 2% of the PTV when changing the optimization settings. An explanation of this, among other things, could be the high sensitivity of any kind of influences on maximum values. In order to gain values which might be more robust I suggest to use maximum values to 2% of the examined structures instead.

Computations using the Wedenberg et al. model (see section *1.3.4 RBE Models*) depicted (see section *3.3.1 Phantom case*) that the enhanced LET_d values in the distal parts of the irradiation fields had a substantial effect on the biological dose solely in the PTV and the ring from 0.0 to 0.5 cm around the PTV. As a consequence a detailed study of LET_d distributions in clinical cases might be essential whenever OAR are right beside the PTV. Otherwise an overdosage could the outcome. The impact of the LET_d distributions on organs far away from the target are vice versa. The biological-weighted dose determined using an RBE of 1.1 is overestimated according to the Wedenberg et al. model in regions far away from the target. Constraints and clinical goals for those areas defined by radio-oncologist restrict, according to this, the dose optimization process too much. The result might be a suboptimal plan.

The rise of RBE in approximately linear fashion as a function of LET_d determined when calculating RBE values with the Wedenberg et. al model is in consensus with other published RBE models (Paganetti, et al., 2019).

For the presented results for RBE and RBE-weighted dose calculated applying the Wedenberg et al. model a q value of 0.434 Gy µm/keV was used. This value was determined by a fit to cell survival experiments. The relevance of cell survival for TCP considerations seems to be reasonable, for the study of NTCP, on the contrary, seems to be questionable. In the latter case the implementation of other endpoints might be preferable (Paganetti, et al., 2019). Consequently, the received outcomes must be therefore interpreted with caution. For being able to make more reliable statements additional cell experiments as well as clinical studies are needed.

The use of different α/β values elucidated the influence of the tissue´s radiosensitivity on the biological-weighted dose. Whatever optimization settings were used the biological-weighted dose in the PTV was always higher when using the Wedenberg et al. model compared to applying an RBE of 1.1 for the simulation of radiosensitive tissues (α/β of 2 Gy). The biological-weighted doses of radioresistant tissues (α/β of 10 Gy) were affected by the LET_d distributions in the distal regions of the field. The third investigated case, splitting in two areas with different α/β values, reflected a kind of worst case scenario: a radiation resistant tumor, radiosensitive tissues around the target. Typically α/β is lower for healthy tissue than for the target tissue (Paganetti, et al., 2019). Consequently the worst case expressed simultaneously the most common case.

When applying an α/β of 2 Gy for some regions in the target an RBE higher than 1.1 for others an RBE lower than 1.1 was computed. However, all of those values were close to 1.1. The average value inside the target was about 1.1. When using an α/β of 10 Gy the calculated RBE values were higher than 1.1 for all regions inside the target. A conservative choice (smaller RBE values) might avoid underdosage of the target and with this in mind using a constant clinical RBE of 1.1 seems to be reasonable. However, one should be cautious in the case of low α/β or small SOPB widths and tumor targets. Here, the whole volume is affected by the LET_d increase at the distal edge. As a consequence the average RBE might be higher (Paganetti, et al., 2019). Moreover, effects on surrounding normal tissues might be underestimated. Summarizing, an enhanced impact of increased LET_d values is expected for the irradiation of radiosensitive areas. That is why a benefit from precise examination of LET_d distributions is expected in such cases. Additionally, the proton therapy community starts considering clinical use of RBE-models for protons. Moreover, gradients in the RBE-weighted distribution calculated for an α/β of 2 Gy were sharper than those for an α/β of 10 Gy. Sharper gradients lead to a higher sensitivity to small (for instance anatomical) changes.

According to the results obtained for $V_{TNTVb,5Gy}$, $V_{TNTVb,10Gy}$, $V_{TNTVb,20Gy}$ and $V_{TNTVb,30Gy}$ for the phantom cases the use of two beams might in some cases result in a sparing of normal tissue from high dose values.

Comparisons

The applied optimization settings decreased as desired the maximum LET_d values around the target. This statement has to be considered with caution. Of course it is valid for the overall averages. For the particular patient respectively the particular plans, however, no reduction or even an enhancement of maximum LET_d appeared. These results reinforce what was already stated. Examining exemplary a phantom case and some clinical cases can never predict entirely correctly an actual case. To be absolute sure one needs to calculate the LET_d values for the individual case.

At first view the obtained decrease of maximum LET_d not just around but also inside the target might be evaluated as contra-productive. If one considers results from other sections as well this will not be categorized negative in every case anymore. Especially for small superficial as well as for radiosensitive targets the commonly used RBE of 1.1 underestimated the biological

weighted dose in the target. In these cases the underestimation could be reduced by a decrease of LET_d. In these case I cannot see the risk of an overestimation of biological dose inside the target. Moreover, the rather small shifts in average LET_d to the PTV indicated that the variation of maximum LET_d values correlated with a reduction of hotspots but not with a formation of cold spots inside the target. However, for the phantom case the results were considered ideal when using two contralateral beams instead of one. Maximum LET_d to the ring from 0.0 to 0.5 cm was reduced by 55.54%, maximum LET_d to the PTV by 35.87%, minimum LET_d to the PTV increased by 30.23% and average LET_d to the PTV by 3.40%. The parallel increase in minimum and decrease in maximum LET_d to the PTV might lead to a more homogenous biological dose distribution inside the target[52]. The higher average LET_d to the PTV might come along with a better tumor control rate.

The implementation of a minimum spot weight limitation when a maximum spot weight limitation already exists led to changes in LET_d values below ±0.7%, in other words did not have a considerable influence on the LET_d distribution.

In clinical situations where it is not possible to use more than one beam incidence a benefit from increasing distal energy layers combined with limitation of maximum spot weights was seen while the normal-tissue sparing stayed similar. When more than one beam can be used, the respective effects were not pronounced and even slightly increased intermediate doses to normal tissues were observed.

4.5 General aspects

The use of the concept of LET as a surrogate quantity related to biological effect requires particular caution. The characterization of a biological effect at a given dose and for a given tissue endpoint by a single parameter, i.e. LET, is deceptive. Only a crude approximation can be achieved by applying the macroscopic parameter LET. Track structure as well as micro- or even nanodosimetry need to be incorporated additionally (Grassberger, Trofimov, Lomax, & Paganetti, 2011). What is more, a tradeoff between acceptability of physical dose and LET distributions is needed. The achievement of steep dose gradients, for instance, often goes hand in hand with placing stopping protons at field edges which leads to high LET values there, respectively, in the neighboring healthy tissue (Lühr, von Neubeck, Krause, & Troost, 2018).

In this master thesis distributions of the dose averaged LET were examined. The utilization of this mean quantity may not be able to model the biologic effects appropriately when the energy spectrum is broadened like close to the Bragg peak. Using another quantity or the whole LET spectrum distributions might be more precise in such cases. This would, however, make computations of biologics effects much more complicated (Guan & Peeler, 2015).

One reason why I suggest to examine LET_d distributions closely if organs at risks are in close proximity to the target are the numerous sources of uncertainties inherent in the treatment. These can be anatomic as well as computational. They might result in an extension of high LET regions at the end of range at the edge of the PTV into normal tissues. This effect might be even enhanced in or near low-density structures. (Paganetti, et al., 2019)

[52] In this master thesis a homogenous biological dose distribution inside the target is considered as the ideal scenario. However, in clinics a different outcome might be required. Then areas in which the biological dose should be higher respectively lower are defined.

A reduction of high-LET volume applied to the patient in comparison to that predicted by the treatment plan is likely to be a consequence of intra- and interfractional movement[53] as well as anatomical changes. LET hotspots are smeared-out. This may be one possible explanation why, until now, just weak correlations have been established between (computed) LET and observed clinical outcome data. However, in the near future image-guided adaptive proton therapy, which is currently implemented in proton beam facilities, will allow to place the proton beam spots at the same position in the patient on each treatment day. The enhanced precision may result in a greater importance of variable LET, respectively, RBE effects. (Lühr, von Neubeck, Krause, & Troost, 2018).

5 OUTLOOK

Within the scope of this work first an overview of general aspects, physics and radiobiology of proton beam therapy was given. Moreover, the light ion beam therapy facility MedAustron was introduced. With this background information one was able to realize the necessity of studying the biological effect of dose and accurately applying it when using protons in radiotherapy, especially if the target is close to critical organs at risk. As seen in previous studies the RBE of protons is not a constant but increases with increasing LET. Therefore, one has to take special care in regions with high LET regions which are located at the end of the particle range, as the LET of protons used clinically is higher the lower the particle´s energy is.

In a next step, the results obtained can find direct application in biologically motivated treatment planning. It is recommended to use two SFO beams or more instead of single beams and the largest possible angle separating those beams in treatment planning. Moreover, caution must be taken when treating small as well as superficial tumors.

This master thesis can also be seen as an impetus of optimizing not just the RBE-weighted absorbed dose obtained by multiplying the physical absorbed dose by a constant factor but also optimizing the LET distribution in treatment planning. This might help avoiding an underestimation of biological effects and consequently a reduction of harming normal tissue as well as critical organs and consequently acute and late side effects. An optimization algorithm could attempt the movement of elevated LET_d regions away from particular locations respectively organs, for instance from tissues with low α/β. In view of the results obtained within the framework of this master thesis it is highly recommended to optimize LET_d distributions for clinical plans. It transpired improved LET_d distributions did not impair the dose to the target. An introduction of LET_d optimization into clinics does not require a modification of current treatment practice. Moreover, one does not have to decide upon one RBE model. Thereby uncertainties inherent to these models are avoided.

Further in-vitro and in-vivo experiments are suggested to be done to provide more precise information on the dependence of the biological effect of protons on their LET. The rise of RBE with LET is acknowledged. Nevertheless, for an incorporation of data and models a cross-validation against in-vivo studies and clinical outcomes is warranted. The verification of simulated LET values with the use of, for instance, nuclear track detectors might be demandable. That is why for now it is advised to maintain the use of a constant RBE of 1.1 in clinical practice. Anyhow, making an exception is recommended if the end of the beam range is located in a critical structure with low α/β. The potential underestimation of the biological effect on these structures

[53] The entirety of all changes and deviations, which occur between the single treatment sessions (fractions) is called *interfractional movement*. Important variables are: positioning and the mobility of internal organs. Changes within one treatment session are called intrafractional movements. Important variables are: movement caused by the patients themselves and breathing movement (definition according to (Reiser, Kuhn, & Debus, 2004, p. 111)).

could be avoided by, for instance, defining physical dose constraints differing from those applied in photon irradiations or using an increased RBE in these regions (Paganetti, et al., 2019).

It is common knowledge that the dose that needs to be delivered to a patient´s tumor to achieve local control varies from patient to patient. In clinical routine, however, the dose prescribed for patients with the same disease site currently does not vary. For an ideal treatment predictive assays or biomarkers are needed to enable an identification of patients who are more radiosensitive respectively radioresistant. The determination of RBE variations due to both patient- and tumor-specific radiosensitivity would be advantageous (Paganetti, et al., 2019).

Furthermore, the LET distributions for treatment plans of patients who have already been treated and who suffer from acute or late side effects (e.g. radionecrosis[54]) could be calculated. In consequence this will allow to investigate if in areas where normal tissue is harmed the LET values during irradiation were high. In an ideal scenario the LET distributions are not calculated for the planned, but for the actual applied dose distributions. By doing so, the differences between the patient position during each irradiation and that which was used for planning are considered.

Another option of continuing to work on this topic on the basis of this master thesis is inserting the LET distributions in RBE models, which use LET as an input parameter for calculating a varying RBE. Consequently, new optimization strategies using a non-constant RBE might be developed.

Further in the future, after the successful validation and clinical implementation of planning treatments based on new developed LET, respectively, RBE-weighted absorbed dose optimizing strategies the effective benefit of not just using a constant RBE can be evaluated in the course of clinical studies.

In conclusion, even without having a clinical evidence I suggest to try to minimize LET_d to critical structures. By doing so one takes advantage of the exceptional biological characteristics of proton beams and consequently might improve treatment outcome.

[54] *Radionecrosis* is any necrosis caused by radiation. Each tissue has a biological tolerance for radiation prior to the initiation of necrosis. Radionecrosis is typically thought to be a late reaction to radiation (definition according to (Brady & Yaeger, 2013, p. 729)).
Necrosis is a local cell or tissue death in the living organism. Possible causes are i. a. physical (radiation, heat), chemical (acids, alkalis), mechanical (trauma) damage, pathogens (septic necrosis) or oxygen deficiency (avascular necrosis) (definition according to (Reuter, 2007, p. 1262).

DANKSAGUNG

Am Ende dieser Arbeit steht ein großes Danke: Vieles hat zum Gelingen dieser Arbeit beigetragen. Alles davon zu nennen ist unmöglich. Trotzdem ist es mir ein Anliegen einige konkrete Aspekte zu erwähnen.

Dass ich meine Diplomarbeit im Bereich der Medizinphysik schreiben möchte, war für mich bald klar. Dass ich es am einzigen Ionentherapiezentrum Österreichs machen durfte, nicht selbstverständlich.

Danke allen, die unmittelbar zum Gelingen dieser Arbeit beigetragen haben.
Bedanken möchte ich mich bei Karin Poljanc, die mich mit MedAustron in Kontakt gebracht hat. So war sie, wie schon bei meiner Bachelorarbeit und Projektarbeit, meine Vermittlerin und Betreuerin.
Fürs Übernehmen der offiziellen Betreuung der Arbeit möchte ich mich bei Christina Streli bedanken.
Die letzten Monate, das Einlesen und Vertiefen in die Thematik, das Finden, Aufbereiten und Interpretieren der Daten hat mir große Freude bereitet. Markus Stock, möchte ich dafür danken, dass er mir das für mich höchstinteressante Thema der Arbeit vorgeschlagen hat und mich bis zum Abschluss dieser hilfreich begleitet hat. Bedanken möchte ich mich außerdem, dass ich Teil des Medizinphysik-Teams sein durfte, von dem ich herzlich aufgenommen wurde.
Dankbar bin ich ferner, dass ich bei meiner Arbeit auf bereits bestehende Daten von Nicky van Lobenstein und Cristina Ansón Marcos zurückgreifen konnte.
Dank sage ich Andreas Resch für die Zurverfügungstellung der Berechnungen mit GATE8.0/Geant4.10.3.
Für die Einführung ins Thema der Arbeit und in das Programm RayStation bedanke ich mich bei Antonio Carlino und Giovanna Martino.
Gabriele Kragl möchte ich Dank aussprechen für ihre engagierte und großartige Betreuung; dafür, dass sie sich für mich und meine Arbeit viel Zeit genommen hat.

Dankbar bin ich auch dafür, dass ich in den letzten Monaten über meine Diplomarbeit hinausgehend wertvolle Erfahrungen und Einblicke sammeln durfte: Dafür, dass ich die Möglichkeit bekam bei spannenden Vorträgen, Besprechungen und Gesprächen dabei zu sein. Dafür, dass ich einen Einblick in die Welt der Kongresse erhielt und dafür, dass ich den Weg der PatientInnen von der Planung bis zur Behandlung mitverfolgen durfte.

Danken möchte ich dem ganzen MedAustron Team, das in meinen Augen nicht nur beeindruckende Arbeit leistet, sondern auch ein Klima schafft, in dem sich nicht nur PatientInnen sondern auch StudentInnen schnell wohlfühlen können.

Diese Arbeit steht am Ende meines Physikstudium. Ich bin dankbar, dass ich mich für dieses entschieden habe und danke allen, die mein Interesse für die Physik geweckt haben. Danke, meinen MitstudentInnen für das gemeinsame Lösen von Aufgaben, Lernen und Diskutieren. Danke, den ProfessorInnen für spannende Lehrveranstaltungen.

Zu guter Letzt sage ich meiner Schwester und meinen Eltern für ihre stetige und unermüdliche Unterstützung Danke.

A Appendix

A.1 Voxel size dependence - Results

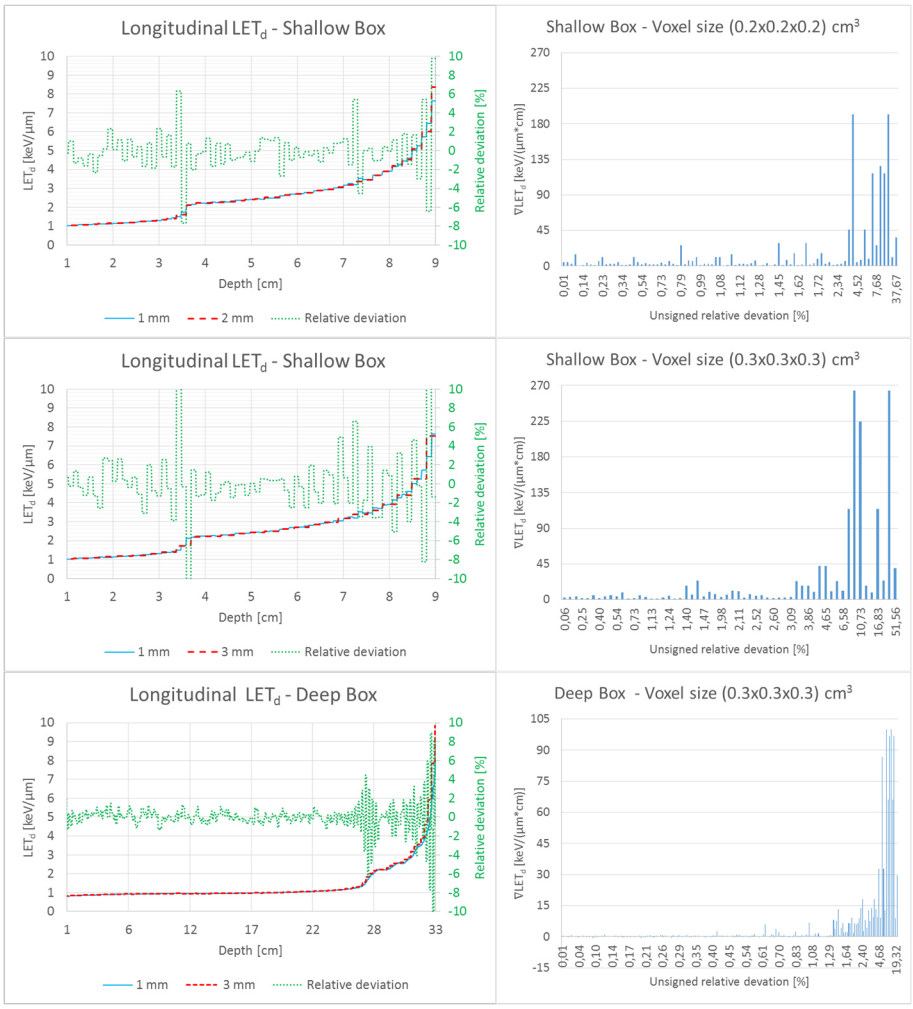

Fig. 97: *Voxel size dependence. LET_d gradient depending on the unsigned relative deviation (pictures on the right) of the LET_d computed with a (0.2x0.2x0.2) cm^3 (image on the top) respectively with a (0.3x0.3x0.3) cm^3 (images in the middle and on the bottom) dose grid from the LET_d computed with a (0.1x0.1x0.1) cm^3 for the shallow box (6 cm in water, images on the top and in the middle) respectively for the deep box (30 cm in water, image on the bottom) in percent and depth LET_d profiles (images on the left) computed with varying dose grid ((0.1x0.1x0.1) cm^3 (solid blue line) and (0.2x0.2x0.2) cm^3 (image on the top) respectively (0.3x0.3x0.3) cm^3 (images in the middle and on the bottom) (dashed red line)) as function of depth for the shallow box (6 cm in water, images on the top and in the middle) and the deep box (30 cm in water, image on the bottom). The relative deviation in percent of the LET_d computed with a (0.2x0.2x0.2) cm^3 respectively with a (0.3x0.3x0.3) cm^3 dose grid from the LET_d computed with a (0.1x0.1x0.1) cm^3 dose grid is also shown (dotted green line).*

A.2 Depth and field size dependence - Results

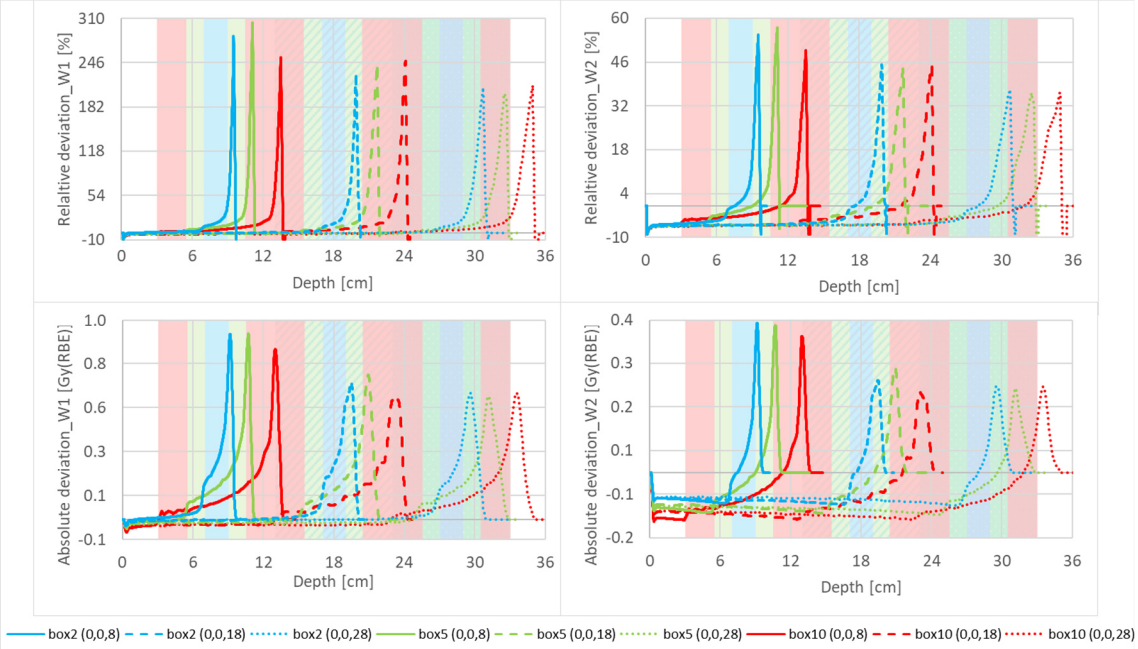

***Fig. 98:**. Depth and field size dependence. Relative (pictures on the top) and absolute (pictures on the bottom) deviation profiles along a line through the center of a (2x2x2) cm^3 (blue lines), a (5x5x5) cm^3 (green lines) and a (10x10x10) cm^3 (red lines) box at a depth of 8 cm (solid lines), 18 cm (dashed lines) and 28 cm (dotted lines) for the RBE-weighted dose calculated using the Wedenberg et al. model and an α/β value of 2 Gy (pictures on the left) respectively 10 Gy (pictures on the right) from RBE-weighted doses calculated using a constant RBE of 1.1 shown. The colors in the background depict the locations of the different boxes.*

***Table 24:** Depth and field size dependence. Investigation of the RBE-weighted dose calculated with the Wedenberg et al. model using an α/β value of 2 (subscript W1) respectively 10 Gy (subscript W2).*

The first column gives the labels of the targets, the second and the sixth columns give the maximum relative deviations of the with the Wedenberg et al. model calculated RBE-weighted doses from the RBE-weighted doses computed using an RBE of 1.1, the third and the seventh the depths at which these maximum relative deviations occurred, the fourth and the eighth the maximum absolute deviation of the with the Wedenberg et al. model calculated RBE-weighted doses from the RBE-weighted doses computed using an RBE of 1.1, the fifth and ninth the depths at which these maximum absolute deviations occurred.

Target label	Max. rel. dev.$_{W1}$	Depth of max. rel. dev.$_{W1}$	Max. abs. dev.$_{W1}$	Depth of max. abs. dev.$_{W1}$	Max. rel. dev.$_{W2}$	Depth of max. rel. dev.$_{W2}$	Max. abs. dev.$_{W2}$	Depth of max. abs. dev.$_{W2}$
	[%]	[cm]	[Gy(RBE)]	[cm]	[%]	[cm]	[Gy(RBE)]	[cm]
box2 (0,0,8)	284.80	9.52	0.93	9.16	54.81	9.51	0.34	9.13
box5 (0,0,8)	303.63	11.13	0.93	10.72	56.98	11.12	0.34	10.71
box10 (0,0,8)	253.73	13.52	0.85	13.01	49.91	13.52	0.31	12.97
box2 (0,0,18)	229.44	19.92	0.68	19.47	45.35	19.92	0.21	19.44
box5 (0,0,18)	244.33	21.71	0.72	20.93	44.17	21.71	0.24	20.92
box10 (0,0,18)	248.75	24.12	0.60	23.46	45.13	24.12	0.18	22.94
box2 (0,0,28)	210.48	30.72	0.63	29.61	37.36	30.71	0.20	29.54
box5 (0,0,28)	201.61	32.52	0.62	31.13	36.08	32.52	0.19	31.12
box10 (0,0,28)	213.15	34.91	0.63	33.57	36.49	34.91	0.20	33.53

A.3 Comparisons - Results

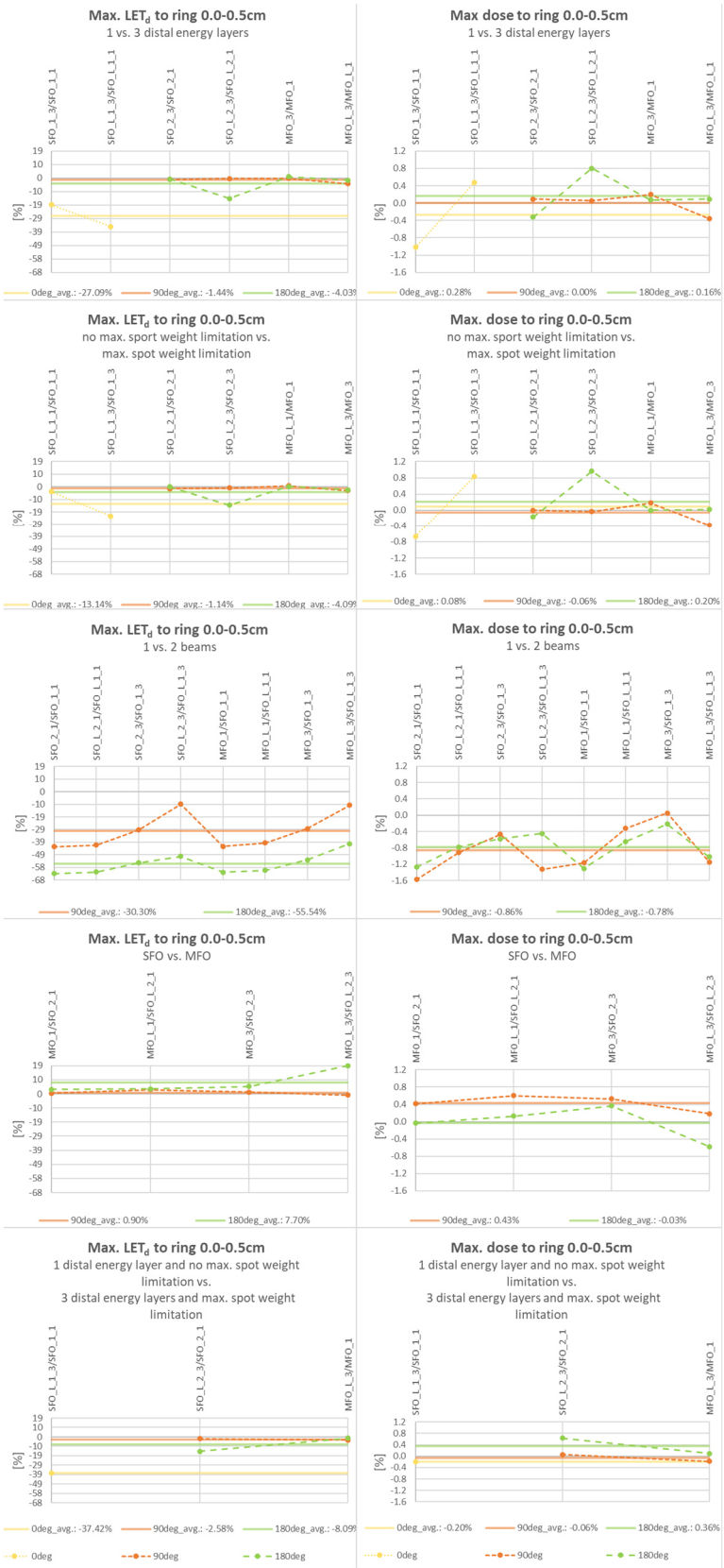

Fig. 99: Change of maximum LET_d (images in the first column) and dose (images in the second column) to the ring from 0.0 to 0.5 cm around the PTV resulting from the change of one optimization setting for the phantom cases in %. The x-axis shows which plans were compared.

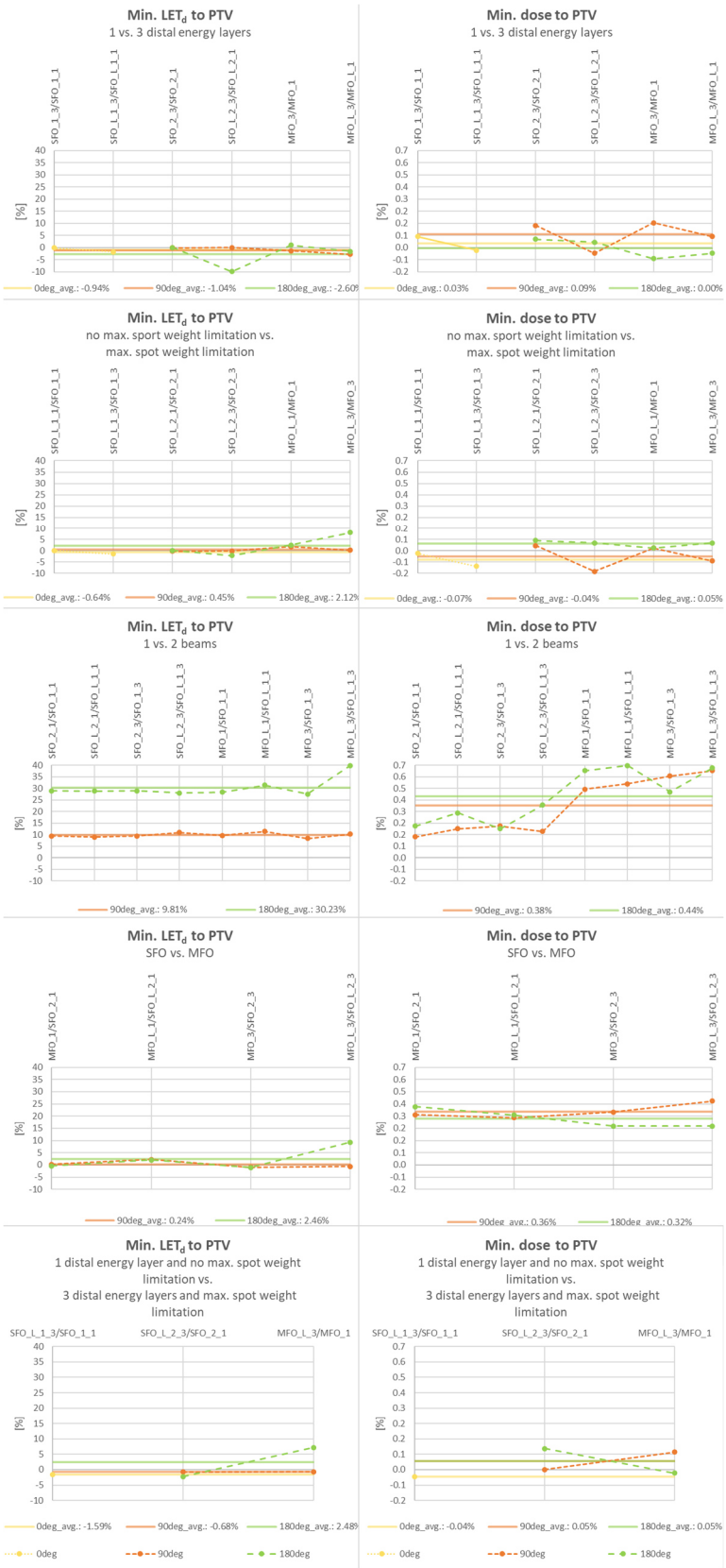

Fig. 100: *Change of minimum LET_d (images in the first column) and dose (images in the second column) to the PTV resulting from the change of one optimization setting for the phantom cases in %. The x-axis shows which plans were compared.*

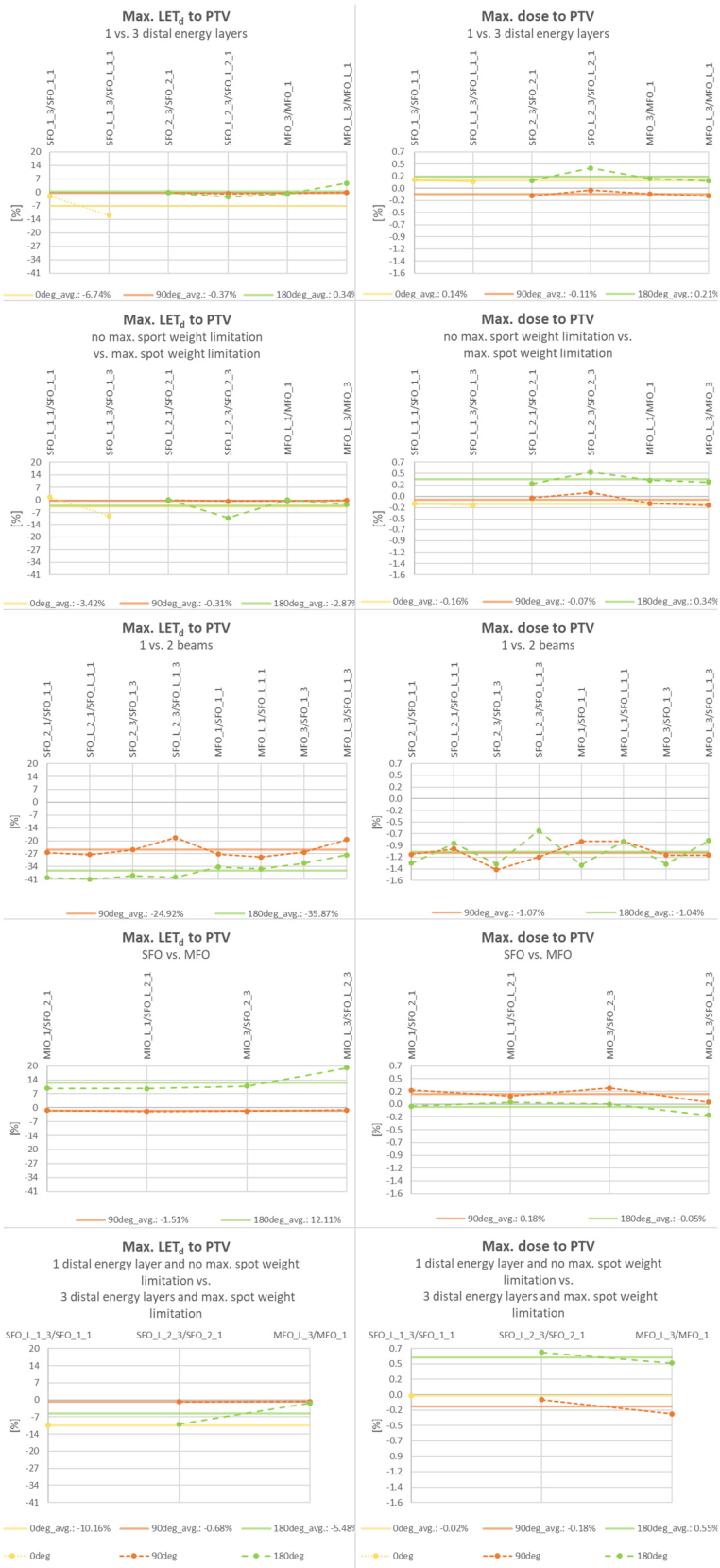

Fig. 101: *Change of maximum LET$_d$ (images in the first column) and dose (images in the second column) to the PTV resulting from the change of one optimization setting for the phantom cases in %. The x-axis shows which plans were compared*

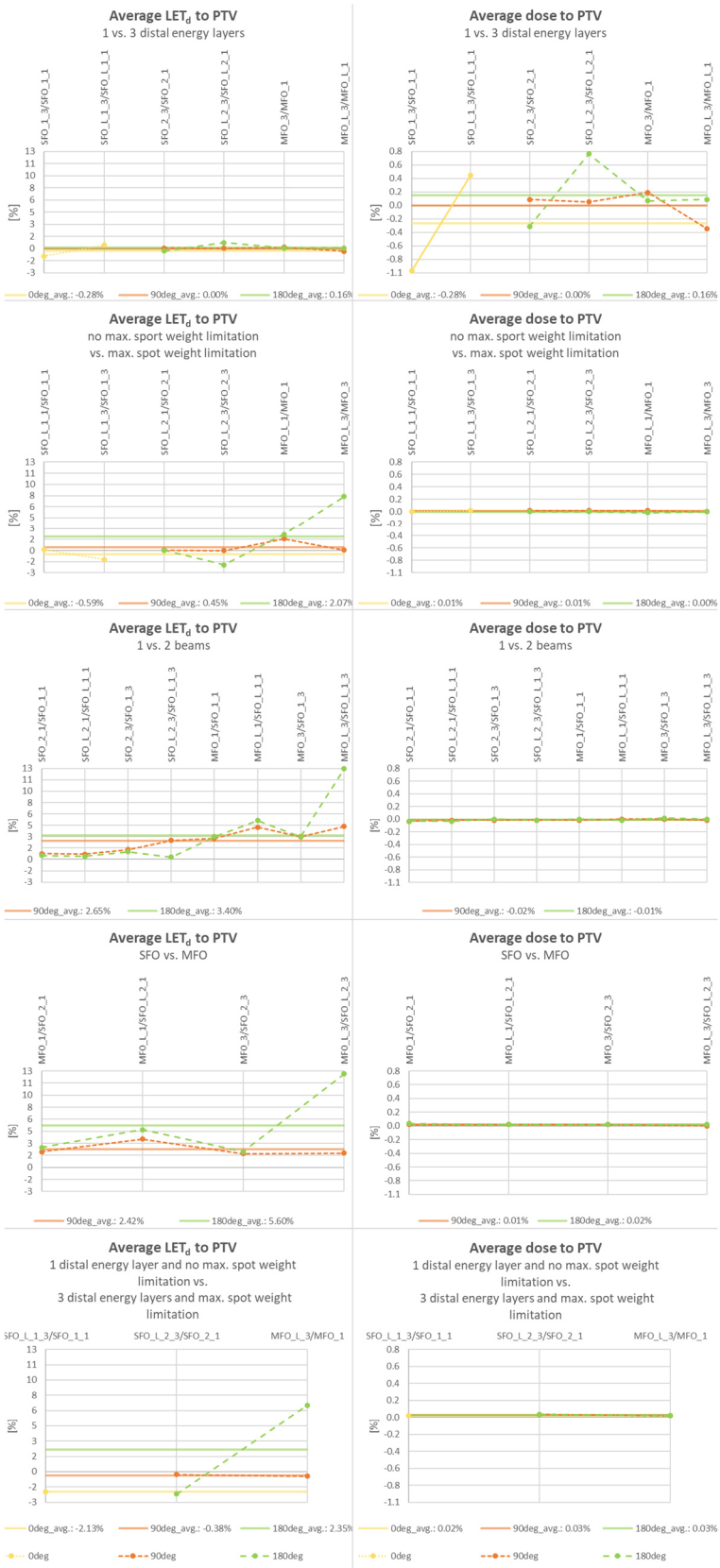

Fig. 102: *Change of average LET$_d$ (images in the first column) and dose (images in the second column) to the PTV resulting from the change of one optimization setting for the phantom cases in %. The x-axis shows which plans were compared.*

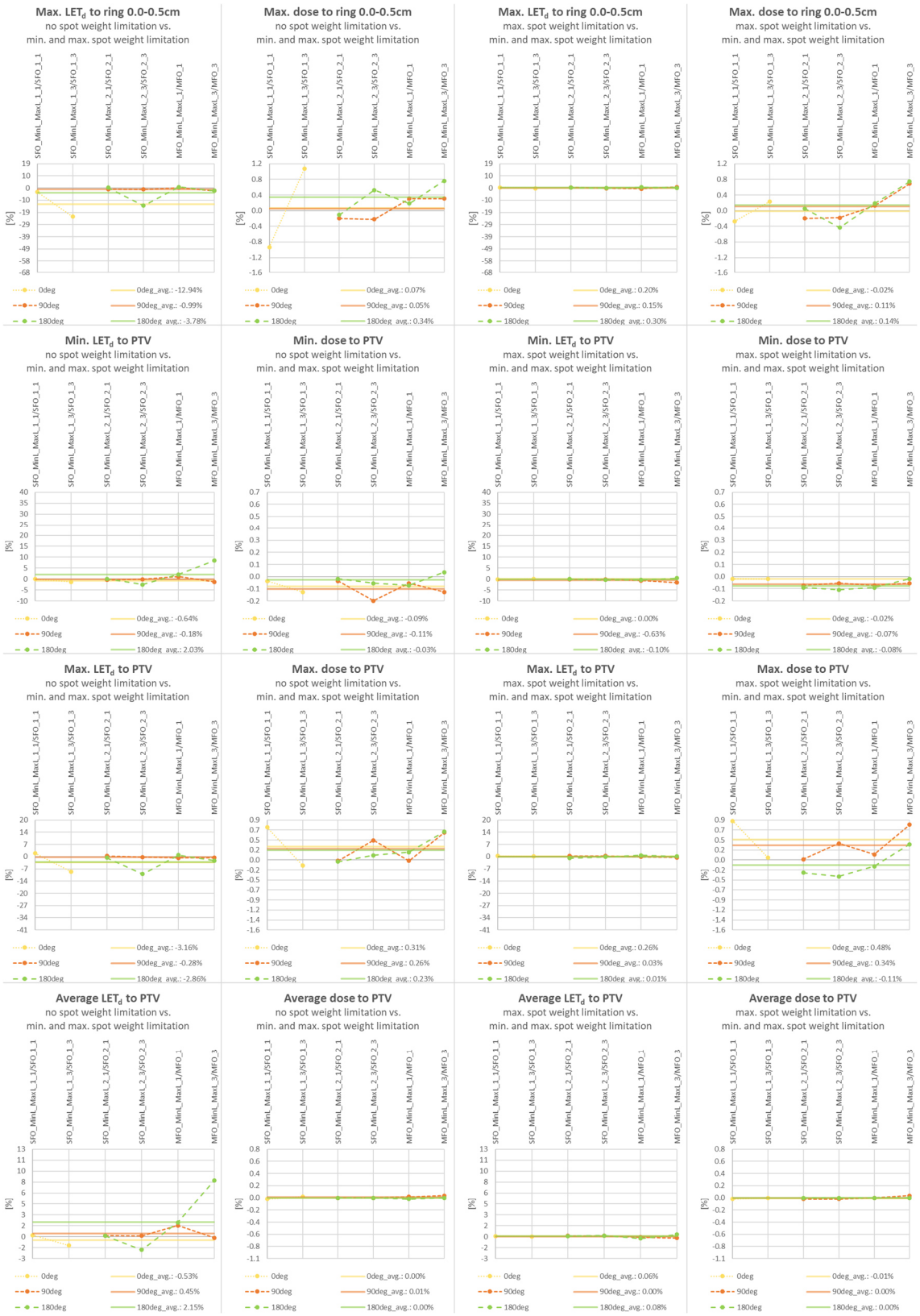

***Fig. 104:**. Change of LET$_d$ (first and third column) respectively dose (second and forth column) values resulting from introducing a maximum and minimum spot weight limitation (first and second column) respectively a minimum spot weight limitation when a maximum spot weight limitation already exists (third and fourth column) for the phantom case. Maximum values to the ring 0.0 to 0.5 cm are shown in the first, minimum values to the PTV in the second, maximum values to the PTV in the third and average values to the PTV in the fourth row. The x-axis shows which plans were compared.*

A.4 Research experience

Contributions to national and international conferences

M. Palkowitsch, G. Martino, A. Carlino, N. van Lobenstein, A. Resch, E. Traneus, M. Stock, G. Kragl: *Influence of treatment plan optimization settings on the dose-averaged linear energy transfer distribution*, Poster presentation: Final MediNet Network Meeting, Wiener Neustadt, AT 2019 & 36. Jahrestagung der ÖGRO, Wiener Neustadt, AT 2019

A. Carlino, G. Martino, **M. Palkowitsch**, N. van Lobenstein, A. Resch, E. Traneus, C. Anson, M. Stock, G. Kragl: *Study on the LET distribution as a function of different treatment planning approaches in proton beam therapy*, Poster presentation: PTCOG58, Manchester, GB 2019

G. Martino, N. van Lobenstein, A. Carlino, A. Resch, **M. Palkowitsch**, E. Traneus, C. Anson, M. Stock, G. Kragl: *LET variation as a function of different optimization approaches in proton beam therapy*, Oral presentation: ESTRO 38, Mailand, IT 2019

LIST OF FIGURES

LIST OF TABLES

BIBLIOGRAPHY

Brady, L. W., & Yaeger, T. E. (2013). *Encyclopedia of Radiation Oncology.* Berlin Heidelberg: Springer-Verlag.

Bray, F. F. (2018). Global Cancer Statistics 2018: GLOBOCAN Estimates of Incidence and Mortality Worldwide for 36 Cancers in 185 Countries. *CA: A Cancer Journal for Clinicians. 68*, pp. 394-424.

Chang, D., Lasley, F., Das, I., & Mendonca, M. D. (2014). *Basic Radiotherapy Physics and Biology.* New York, USA: Springer Science+Business Media.

Cortés-Giraldo, M. A., & Carabe, A. (2015, March 13). A critical study of different Monte Carlo scoring methods of dose average linear-energy-transfer maps calculated in voxelized geometries irradiated with clinical proton beams. *Physics in Medicine & Biology. 60*, pp. 2645-2669.

Exarchos, T. P., Papadopoulos, A., & Fotiadis, D. I. (2009). *Handbook of Research on Advanced Techniques in Diagnostic Imaging and Biomedical Applications.* Hershey, USA and London, UK: Medical Information Science Reference.

Giantsoudi, D., Grassberger, C., Craft, D., Niemierko, A., Trofimov, A., & Paganetti, H. (2013). Linear Energy Transfer-Guided Optimization in Intensity Modulated Proton Therapy: Feasibility Study and Clinical Potential. *International Journal of Radiation Oncology*Biology*Physics. 87(1)*, 216-222.

Grassberger, C., & Paganetti, H. (2011, September 30). Elevated LET components in clinical proton beams. *Physics in Medicine and Biology*, pp. 6677-6691.

Grassberger, C., Trofimov, A., Lomax, A., & Paganetti, H. (2011). Variations in Linear Energy Transfer Within Clinical Proton Therapy Fields and the Potential for Biological Treatment Planning. *International Journal of Radiation Oncology*Biology*Physics. 80(5)*, pp. 1559-1566.

Guan, F., & Peeler, C. (2015, November). Analysis of the track- and dose-averaged LET and LET spectra in proton therapy using the geant4 Monte Carlo code. *Medical Physics. 42(11)*, pp. 6234-6247.

IAEA. (2004). *Technical Reports NO. 430 - Commissioning and Quality Assurance of Computerized Planning Systems for Radiation Treatment of Cancer.* Vienna, Austria: International Atomic Energy Agency.

IAEA. (2005). *Radiation Oncology Physics: A Handbook for Teachers and Students.* Vienna: International Atomic Energy Agency.

IAEA. (2008). *Relative Biological Effectiveness.* Vienna: International Atomic Energy Agency.

ICRU, I. C. (1993). *Report 49: Stopping Powers and Ranges for Protons and Alpha Particles.* Bethesda, USA: ICRU, International Commission on Radiation Units and Measurements.

ICRU, International Commission on Radiation Units and Measurements. (1979). *Report 30: Quantitative Concepts and Dosimetry in Rad iobiology.* Washington, USA: ICRU, International Commission on Radiation Units and Measurements.

ICRU, International Commission on Radiation Units and Measurements. (1993). *Report 50: Prescribing, Recording, and Reporting Photon Beam Therapy.* Bethesda, USA: ICRU, International Commission on Radiation Units and Measurements.

ICRU, International Commission on Radiation Units and Measurements. (1998). *Report 60: Fundamental Quantities and Units for Ionizing Radiation.* Bethesda, USA: International Commission on Radiation.

ICRU, International Commission on Radiation Units and Measurements. (2007). *Report 78: Prescribing, Recording, and Reporting Proton-Beam Therapy.* Glasgow, UK: Oxford University Press.

Koschik, A., Osmić, F., Urschütz, P., & Benedikt, M. (2014). Status of MedAustron the Austrian Ion Therapy and Research Centre. *Presented at: 5th International Particle Accelerator Conference* (pp. 2146-2148). Dresden: JACoW Publishing.

Kraft, G. (2000). Tumor Therapy with Heavy Charged Particles. *Progress in Particle and Nuclear Physics. 45*, pp. 473-544.

Linz, U., & al. (2012). *Biological and Medical Physics, Biomedical Engineering.* Berlin Heidelberg: Springer-Verlag.

Lühr, A., von Neubeck, C., Krause, M., & Troost, E. G. (2018). Relative biological effectiveness in proton beam therapy – Current knowledge and future challenges. *Clinical and Translational Radiation Oncology. 9*, pp. 35-41.

Mayles, P., Nahum, A., & Rosenwald, J. C. (2007). *Handbook of Radiotherapy Physics - Theory and Practice.* Broken Sound Parkway NW, USA: Taylor & Francis Group.

Moyers, M. F., & Vatnitsky, S. M. (2012). *Practical Implementation of Light Ion Beam Treatments.* Madison, WI: Medical Physics Publishing.

Newhauser, D. W., & Zhang, R. (2015, April 21). The physics of proton therapy. 60(8). *Physics in Medicine & Biology*, pp. 155-209.

Nikjoo, H., & Lindborg, L. (2010, April 29). RBE of low energy electrons and photons. *Physics in Medicine & Biology*, pp. 65-109.

Paganetti, H. (2009, June 23). Dose to water versus dose to medium in proton beam. *Physics In Medicine and Biology. 54*, pp. 4399-4421.

Paganetti, H. (2012). *Proton Therapy Physics Series in Medical Physics and Biomedical Engineering.* Boston: Taylor and Francis - Cress Press.

Paganetti, H., Blakely, E., Carabe-Fernandez, A., Carlson, D. J., Das, I. J., Dong, L., . . . Willers, H. (2019). *Report of the AAPM TG-256 on the relative biological effectiveness of proto.* Medical Physics. 46(3).

Paganetti, H., Niemierko, A., Ancukiewicz, M., Gerweck, L. E., Goitein, M., Loeffler, J. S., & Suit, H. D. (2002). Relative biological effectiveness (RBE) values for proton beam therapy. *International Journal of Radiation Oncology*Biology*Physics. 53(2)*, pp. 407-421.

PTCOG. (2019). *Particle Therapy Co-Operative Group*. Retrieved from https://www.ptcog.ch/ [Online, Accessed 16 May 2019]

Quan, E. M., Liu, W., Wu, R., Li, Y., Frank, S. J., Zhang, X., . . . Mohan, R. (2013, August). Preliminary evaluation of multifield and single-field optimization for the treatment planning of spot-scanning proton therapy of head and neck cancer. *Medical Physics. 40(8)*, pp. 081709-1-081709-6.

RAYSTATION 6 - RayPhysics Manual. (2016). RaySearch Laboratories AB.

RAYSTATION 6 - Reference Manual. (2016). RaySearch Laboratories AB.

RAYSTATION 6 - User Manual. (2016). RaySearch Laboratories AB.

Reiser, M., Kuhn, F.-P., & Debus, J. (2004). *Radiologie.* Stuttgart: Georg Thieme Verlag KG.

Reuter, P. (2007). *Springer Klinisches Wörterbuch.* Heidelberg: Springer Medizin Verlag.

Schardt, D., Elsässer, T., & Schulz-Ertner, D. (2010, February 19). Heavy-ion tumor therapy: Physical and radiobiological benefits. 82(1). *Reviews of Modern Physics*, pp. 383-425.

Scholz, M., & Kraft, G. (1996). Track Structure and the Calculation of Biological Effects of Heavy Charged Particles. *Advance in Space Research. 18(1-2)*, pp. 5-14.

Schwarz, M. (2011). Treatment planning in proton therapy. *The European Physical Journal Plus.126(67). Trento: Springer-Verlag*.

Stewart, R. D., Carlson, D. J., Butkus, M. P., Hawkins, R., Friedrich, T., & Scholz, M. (2018, November). A comparison of mechanism-inspired models for particle relative biological effectiveness (RBE). *Medical Physics* , pp. 925-952.

Stewart, R. D., Streitmatter, S. W., Argento, D. C., Kirkby, C., Goorley, J. T., Moffitt, G., . . . Sandison, G. A. (2015, October 9). Rapid MCNP simulation of DNA double strand break (DSB) relative biological effectiveness (RBE) for photons, neutrons, and light ions. *Physics in Medicine & Biology. 60*, pp. 8249-8274.

Stock, M., Dietmar, G., Ableitinger, A., Zechner, A., Utz, A., Mumot, M., . . . Vatnitsky, S. (2018). The technological basis for adaptive ion beam therapy at MedAustron: Status and outlook. *Zeitschrift für Medizinische Physik*, pp. 196-210.

Stock, M., Georg, P., Mayer, R., Böhlen, T. T., & Vatnitsky, S. (2015). Development of Clinical Programs for Carbon Ion Beam Therapy at MedAustron. *International Journal of Particle Therapy*, pp. 474-477.

Traneus, E., & Ödén, J. (2018, October 25). Introducing proton track-end objectives in intensity modulated proton therapy optimization to reduce linear energy transferand relative biological effectiveness in critical structures. *International Journal of Radiation Oncology • Biology • Physics. 103(3)*, pp. 747-757.

Wedenberg, M., Lind, B. K., & Hårdemark, B. (2013). A model for the relative biological effectiveness of protons: The tissue specific parameter a/b of photons is a predictor for the sensitivity to LET changes. *Acta Oncologica. 52*, pp. 580-588.

Wilkens, J. J. (2003, May). Analytical linear energy transfer calculations for proton therapy. *Medical Physics. 30 (5)*, pp. 806-815.

Willers, H., Allen, A., Grosshans, D., McMahon, S. J., von Neubeck, C., Wiese, C., & Vikram, B. (2018, July). Toward A variable RBE for proton beam therapy. *Radiotherapy and Oncology*, pp. 68-75.

World Health Organization - Cancer - Key facts. (2018, September 12). Retrieved from https://www.who.int/news-room/fact-sheets/detail/cancer [Online, Accessed 6 May 2019]